Multifunctional Test Rig for Accelerated Assessment of Electromechanical Characteristics and Failure Mechanisms of Dielectric Elastomer Transducers

Dissertation

zur Erlangung des Grades

des Doktors der Ingenieurwissenschaften

der Naturwissenschaftlich-Technischen Fakultät

der Universität des Saarlandes

von

Daniel Bruch

Saarbrücken

2024

Tag des Kolloquiums:	24. Juli 2024
Dekan:	Prof. Dr.-Ing Michael Vielhaber
Berichterstatter:	Prof. Dr.-Ing Stefan Seelecke
	Prof. Dr. Andreas Schütze
Vorsitz:	Prof. Dr.-Ing Dirk Bähre
Akad. Beisitzer:	Dr.-Ing Attique Bashir

Kurzfassung

Dielektrische Elastomer-Wandler (DETs) eröffnen ein breites Spektrum innovativer Anwendungen. Während DET-Sensoren bereits erste Marktbewegungen verzeichnen, sind Aktor- und Generator Derivate bisher nur Forschungsgegenstand. Ihre weitere Etablierung erfordert umfangreiche elektromechanische Prüfungen unter realistischen Betriebs- und Umgebungsbedingungen, insbesondere bezüglich Zuverlässigkeit und Langzeitstabilität. Jedoch sind die dazu erforderlichen Prüfanlagen nicht kommerziell verfügbar, und bisher vorgestellte Sonderentwicklungen in ihrer Funktion eingeschränkt.

Um diese Lücke zu schließen, wird in der vorliegenden Dissertation ein multifunktionaler Prüfstand entwickelt, der zur beschleunigten Evaluierung des elektromechanischen Verhaltens und der Schädigungsmechanismen von DETs eingesetzt werden kann. Er ermöglicht das Prüfen von DET-Materialien, -Elementen und -Systemen verschiedener Anwendungsfelder und Bauart und bietet vielseitige elektromechanische Prüfroutinen innerhalb kontrollierter Temperatur- und Feuchtigkeitsumgebungen. Tests können individuell programmiert und auf mehreren Stationen simultan ausgeführt werden. Eine automatische Testüberwachung mit Fernzugriff ermöglicht einen unterbrechungsfreien 24/7 Langzeitbetrieb. Im Rahmen der Arbeit erfolgt eine generelle Validierung des Prüfstands. Seine vielseitige Einsetzbarkeit wird anhand der systematischen Charakterisierung eines speziell entworfenen streifenförmigen DETs exemplarisch demonstriert.

Abstract

Dielectric Elastomer Transducers (DETs) open up a wide range of innovative applications. While DET sensors are already in the market, actuator and generator derivatives are still in the research stage. Their further establishment requires extensive electromechanical testing under realistic operating and environmental conditions, especially with regard to reliability and long-term stability. However, the comprehensive test benches required for this purpose are not commercially available, and proprietary developments presented so far are limited in their functionality.

In order to close the above-described gap, a multi-functional test rig is developed and demonstrated in the scope of this dissertation, which can be used for the accelerated assessment of the electromechanical characteristics and the failure mechanisms of DETs. It allows for testing of DET materials, elements and systems of different application fields and construction types and provides versatile electromechanical test routines within various controlled constant temperature and humidity environments. Experiments can individually be programmed and run simultaneously on multiple test stations. Furthermore, automatic monitoring with remote access allows for uninterrupted 24/7 long-term operation. A general validation of the test rig is conducted on the test rig, and its versatility is demonstrated by the systematic characterization of a specially designed rectangular-shaped planar DET.

Acknowledgement

This dissertation was completed during my tenure as a research assistant at the intelligent Material Systems Lab (iMSL) at Saarland University in cooperation with ZeMA gGmbH.

I would like to express my sincere gratitude to my doctoral adviser Prof. Stefan Seelecke for the trust he has placed in me, and for giving me the opportunity to work on exciting and forward-looking scientific topics and to make my own contribution to them in the scope of this thesis.

With this regard, I would like to thank Bürkert GmbH for their generous financial support, which has significantly contributed to the realization of this work.

My appreciation also goes to my colleagues, who have not only supported me with assistance and advice during all this time but have always created an unforgettable warm and friendly working environment. Special thanks go to the iMSL cleanroom team, especially Bettina Fasolt and Tobias Willian, who supported me in the production of the DET samples, and the technical staff, particularly Benedikt Holz, Thomas Würtz, Johannes Feld, Christian Müller, and Julian Taffner, who supported me in setting up the experimental facilities.

I would also like to thank Paul Motzki, Philipp Loew, Sophie Nalbach and Franziska Louia for proofreading early drafts, and in particular Prof. Andreas Schütze for the valuable time he devotes to the review of this dissertation and the doctoral process.

Finally, I would like to dedicate my heartfelt gratitude to my family, especially my beloved Julia, who have been my constant support system, through all the ups and downs. In particular, I would also like to thank my parents, whose love and encouragement not only set me on my career path, but also shaped my character and instilled in me the values that have guided me throughout.

Table of Contents

1 Introduction

The early 21st century faces major challenges in the areas of climate change and globalization - issues in which technology plays a divergent role as both causing factor and potential solution. The industry is experiencing a historic transformation due to the abandonment of fossil fuels, which is currently particularly noticeable in the energy and mobility sectors. The increasing establishment of renewable energies and efforts to provide them emission-free are leading to increasing electrification in these and many other areas. However, generation, storage, distribution, and conversion of electrical energy using conventional technological approaches lead to a high demand for locally and globally limited available natural resources such as rare earths or noble metals. New technologies based on alternative raw materials can provide a remedy by usefully supplementing or replacing conventional solutions. Smart materials, which actively respond to stimulation and thus combine sensory and actuator functions, represent a particularly attractive alternative. The term "smart" is also commonly used to describe a growing technological trend towards ‘smartification’, i.e., the development of intelligent, usually widely interconnected technical systems. In the industrial sector, for example, the “smart factory” refers to a fully digitalized and self-organizing production environment. In consumer environment, on the other hand, "smart phones", "smart wearables" and "smart home" devices facilitate everyday life. Common to all these smart systems is, that their functionality is based on the interaction of a usually large number of sensors and actuators. Hence, due to their responsive characteristics, smart materials provide an excellent basis for developing not only alternatives, but also innovative, highly integrated, and compact smart solutions. Prominent examples of market-established applications based on smart materials are highly dynamic piezoelectric actuators used in diesel engine injector systems, or magnetorheological fluids, whose controllable viscosity is utilized in suspension systems with actively adaptable damping behavior. Other smart materials are already available on the market but are also the subject of research in many respects. Besides the Shape Memory Alloys (SMA), these also include Electroactive Polymers (EAP), in particular the category of Dielectric Elastomer Transducers (DET). Those are highly elastic and polarizable polymers provided with compliant electrodes that undergo a shape transformation when electrically stimulated with high voltage and can thus be used as actuators. Simultaneously, their deformation causes a change in their electrical properties, so that the change in shape can be observed by measuring these quantities, allowing them also to be utilized as sensors. The simultaneous combination of sensory and actuator effects of these DETs is of particular interest, as it enables the development of smart actuators that can be precisely controlled in a closed control loop with no need for external sensors. In quasi-static operation, they are low-noise, proportionally controllable and energy-efficient, as steady-state conditions can be maintained with minimal energetic loss. These properties make them attractive for applications such as valves, switches, servo drives and especially in the soft robotics field due

to their flexibility and light weight. Beyond this, DETs offer a particularly dynamic electromechanical response. Hence, they can be used to operate pumps silently at low frequencies or operate in the audible (kilo)hertz range, making them promising candidates as new types of capacitive loudspeakers. For pure sensor operation, DETs are characterized by their unique flexibility, as well as their high sensitivity and stretchability, making them promising candidates to detect large deformations along with forces in soft structures, particularly in gaming or medical or textile sectors.

In recent years, the trend has increasingly been towards application and process-oriented research and initial efforts have been made to establish the technology on the market, with initial successes being achieved in the field of DET-based sensor technology. The market maturity of sensor applications before actuator and generator applications has various reasons. Those particularly include the fact that pure sensors do not require high voltage control and are therefore not exposed to the complex electromechanical loads that can lead to failure depending on the operating and environmental conditions. This underlines the importance of reliability and lifetime as critical factors in assessing the market competitiveness of DET technology, alongside with general properties such as sensor accuracy, actuator performance, or generator efficiency. All these attributes are influenced across all product levels, e.g. material, compound, and system, and at all development phases, e.g. concept, design, and production. Their assessment and improvement necessitate comprehensive electromechanical testing, including both short-term and particularly long-term experiments within various operational and environmental conditions, as well as simultaneous testing of various test objects for accelerated statistical evaluation.

As will be shown in the literature review conducted in the scope of this dissertation, no comprehensive standardized or proprietary test rigs have yet been available with this regard, as most of them are limited in their testing capability, i.e. focusing on specific testing conditions, application fields or designs. However, a corresponding multifunctional device can significantly advance research and development of DET technology. This dissertation addresses this deficiency by developing and demonstrating a comprehensive multifunctional electromechanical test rig for DETs, that is suitable for accelerated assessment of statistically relevant data for both short-term and especially long-term testing. It aims to assist scientists and engineers within a wide range of application fields, product levels, and development phases in bringing the technology to market maturity.

The structure of this dissertation is as follows: Chapter 2 presents the fundamentals of DET technology and typical electromechanical experiments applied to them for characterization purposes. This is followed by a literature review of the state of the art in long-term testing and related test systems, pointing out the lack, that motivates the development of the test rig presented in this thesis. Chapter 3 explains the development of the test rig along with the exemplary DET test

samples which are tailored to the test rig's sample grips and used for demonstration purposes. For this, motivation and objective are discussed in greater detail first, then presenting conceptualization, design and construction, electronics and wiring as well as control and software. Subsequently a comprehensive electromechanical validation is given, providing general information about test rig accuracy i.e. depending on load or temperature. Chapter 4 demonstrates the versatile electromechanical testing capabilities of the test rig by conducting various mechanical, electrical, and electromechanical controlled experiments on the specially developed DETs. Finally, in Chapter 5 a brief conclusion and outlook for future work is provided.

2 Fundamentals and State of the Art

The essential physical actuation principle of Dielectric Elastomer Transducers (DETs) has already been documented by Wilhelm Conrad Röntgen [1] in the late 19th century but has not been further considered in research or become relevant in technological development for over 100 years. It was not until the early 1990's that Pelrine et al. [2] returned to the subject, identifying the 'electro strictive response of elastomeric polymers' [3] as promising actuation technology for artificial muscle approaches. This was followed by fundamental modeling of the electromechanical actuation, and first experiments on materials and manufacturing processes, with regard to electro-mechanic performance and potential applications including sensors and smart devices [4], [5], [6], [7]. Complemented by consideration of generator functionality of DEs utilizing energy harvesting methods [8], the foundation for a new field of research was established, that quickly gained increasing attention due to the promising and versatile properties of the technology, and which is nowadays being investigated by research groups all over the globe. The character of research is thereby gradually changing from basic research to application and process-oriented research, motivated by the desire to establish the technology on the market. In order to evaluate the suitability of the technology with this regard, experimental investigations on properties such as electromechanical performance, reliability, as well as long-term and fatigue characteristics under realistic environmental conditions are thus increasingly coming to the fore.

2.1 Fundamentals of Dielectric Elastomer Transducers

This section provides an overview of DET technology, focusing on the fundamental basics, that are most relevant in the context of this thesis. It introduces the general composition of DETs, commonly employed materials and manufacturing processes, and explains the basic sensing and actuation principles with examples for typical applications. As this work primarily focuses on linear uniaxially operated DETs, corresponding design variants typically applied in sensor and actuator systems are introduced, and the actuator system layout of planar DET types, that are typically provided with preload elements, are explained. Thereby, particular focus is given on rectangular shaped planar designs used as exemplary test object for demonstration purposes in this work. Finally, this section provides an overview of the general mechanical and electrical characteristics of DETs to facilitate a thorough understanding of electromechanical transduction, including time-, load-, and temperature-dependent phenomena along with failure mechanisms.

2.1.1 Materials, Transducer Compound and Manufacturing

Dielectric elastomers (DEs) are in general highly elastic, stretchable, and electrically polarizable polymers that belong to the group of Electroactive Polymers (EAPs). Embedded as thin dielectric layer (typically $20 - 200\ \mu m$) in between two compliant electrodes, the result is a highly flexible transducer compound, that changes its shape through electrical stimulation (refer to Section 2.1.4),

and changes its electrical properties through deformation (refer to Section 2.1.3) (Figure 1). Due to this reversible electromechanical effect, this compound is referred to as a Dielectric Elastomer Transducer (DET), which can be used for sensor, actuator, and generator applications [9], [10].

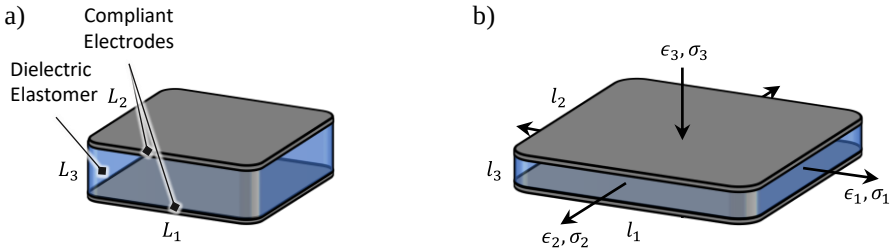

Figure 1: DET in undeformed configuration (a), and deformed configuration (b).

Dielectric Elastomers

The DE material is generally required to feature high elasticity combined with low viscosity, high permittivity, as well as high dielectric breakdown strength for high voltage driven actuator and generator applications [7], [11], [12]. The most commonly used DE materials are natural rubbers [13], [14], synthetic rubbers [14], [15], polyurethanes [16], [17], silicones [18], [19] and polyacrylates [14], [20]. In addition to the wet-chemical production and deposition of uncured dielectric and electrode material using fabrication techniques such as spin-coating [21], [22], 3D-printing [23], [24], [25], or blade casting [26], commercially available film materials are frequently utilized and provided with thin compliant electrode coatings. Due to their commercial availability, particularly acrylate-based adhesive tapes from the *3M Corp.* (i.e. *VHB 4910*) and polydimethylsiloxane films (PDMS films) from *Wacker-Chemie AG* (i.e. *Elastosil 2030*) are widely employed. Acrylate-based materials typically feature a higher permittivity then silicone materials, enabling for particularly higher actuation strains at lower actuation voltages, but also a lower dielectric breakdown strength limiting maximum applicable voltage, along with a notably higher viscosity, resulting in lower actuation rates and higher viscoelastic losses [11], [27].

Compliant Electrodes

The electrodes are generally required to provide high flexibility, combined with low viscosity and high conductivity over large strains, along with sufficient adhesion to the dielectric layer. They are usually either based on coherent metal thin films, or on conductive micro and nanoparticles that are deposited in powder form or embedded in inherently compliant materials. Metal thin films typically achieve highest conductivity along with lowest viscosity e.g. achieved by electrode deposition on pre-strained dielectric elastomer films, i.e. using sputtering processes [28], [29], [30]. Upon release of the pre-strain, the elastomer relaxes, causing the electrodes to fold up. Corresponding DET compounds therefore exhibit high compliance when they are stretched, enabled by the unfolding of the wrinkled electrode. Conductive nanoparticles are deposited in powder form [31], dispersed in solvents to provide conductive inks [32], or used as fillers in greases [7], (uncured) elastomeric

materials [33], [34], or combinations of both [35], to provide conductive pastes. Commonly used conductive nanoparticles are carbon black (CB) [7], [32], [33], [35], carbon nanotubes (CNT) [31] or silver (Ag) [34]. Frequently utilized depositions processes comprise inkjet printing [32], [36], spray coating [26], pad-printing [37], or screen printing [33], [38]. In contrast to powder and grease-based electrodes, the elastomer-based electrodes are commonly cured subsequently, resulting in a fully elastomeric DET compound with particularly high electrode adhesion [11], [27].

2.1.2 General Assumptions on Geometry and Constraints

For common analytical description of the mechanical characteristics, simplifying ideal assumptions are commonly made considering a thin elastic membrane, i.e. refer to [9], [10]. In its undeformed state, this typically exhibits a much smaller thickness L_3 compared to its length L_1 and width L_2 (refer to Figure 1a). Thus, a single layer structure can only absorb compressive forces in the thickness direction and tensile forces perpendicular to it. Furthermore, DETs behave approximately incompressible, maintaining a constant volume during deformation, resulting in a shorter deformed thickness l_3 and increased deformed surface area $l_1 l_2$ (refer to Figure 1b). The deformation is commonly described by the spatial strains ϵ_1, ϵ_2 and ϵ_3 and the corresponding principal stretches $\lambda_1, \lambda_2, \lambda_3$:

$$\lambda_1 = \frac{l_1}{L_1} = 1 + \epsilon_1 \qquad \lambda_2 = \frac{l_2}{L_2} = 1 + \epsilon_2 \qquad \lambda_3 = \frac{l_3}{L_3} = 1 + \epsilon_3 \tag{2.1}$$

Considering these stretches, volume consistency can be simply formulated:

$$\lambda_1 \lambda_2 \lambda_3 = 1 \tag{2.2}$$

Despite generally isotropic material properties, DETs do not deform homogeneously in reality due to constraints, but exhibit anisotropic strain and stress distribution, particularly when large deformations are considered. This is typically modeled and computed by means of numeric continuum mechanical simulation, e.g., using the Finite Element Method (FEM) [39], [40]. For simplified analytical analysis and experimental considerations, additional simplifications are typically introduced based on geometry and kinematic constraints, i.e. refer to [41], [42]:

$\lambda_2 = \lambda_3$	$\lambda_2 = 1$	$\lambda_1 = \lambda_2$	(2.3)
uniaxial	pure shear	equi-biaxial	

Uniaxial and pure shear deformation represent limiting cases in which λ_1 is controlled, and λ_2 and λ_3 remain unconstrained. Uniaxial-like conditions prevail for long and narrow designs ($L_1 \gg L_2$), whereas pure shear-like conditions apply to short and wide designs ($L_1 \ll L_2$). Equi-biaxial conditions prevail for designs of similar length and width, with either identical control of λ_1 and λ_2, or control of λ_3, assuming that λ_2 and λ_3 remain unrestricted.

2.1.3 Sensing Principle

The deformation of a DET causes a change in its electrical capacitance.

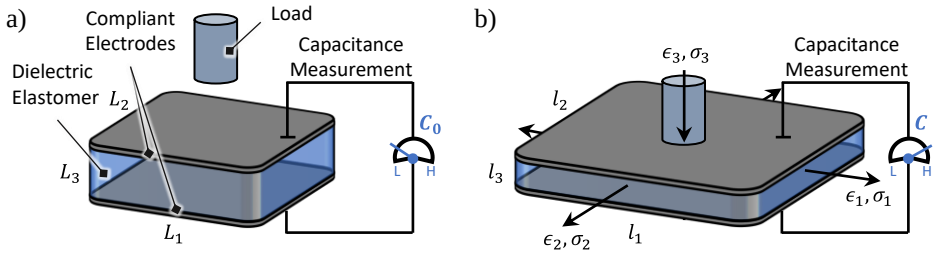

Figure 2: Sensor function principle illustrated by comparison of a DET in its unloaded condition (a), to its loaded condition, resulting in a deformation induced increase in capacitance (b).

To explain the sensing principle, a single DET layer is considered as thin and flexible plate capacitor, with electrode area $L_1 L_2$ and plate distance L_3 in the non-deformed state (Figure 2a), i.e. refer to [9], [10]. With vacuum permittivity ε_0 and dielectric constant ε_r, the nominal capacitance C_0 is obtained:

$$C_0 = \varepsilon_0 \varepsilon_r \frac{L_1 L_2}{L_3} \tag{2.4}$$

Due to the mechanical properties given in (2.1), deformations of the capacitor induced by an external load result in an increased surface area $l_1 l_2$ and a reduced thickness l_3 (Figure 2b). Both effects result in an increased capacitance C:

$$C = \varepsilon_0 \varepsilon_r \frac{l_1 l_2}{l_3} \tag{2.5}$$

By supplementing (2.1) into (2.5) this can also be expressed using the principal stretches:

$$C = \varepsilon_0 \varepsilon_r \frac{\lambda_1 L_1 \lambda_2 L_2}{\lambda_3 L_3} = \frac{\lambda_1 \lambda_2}{\lambda_3} C_0 \tag{2.6}$$

From the volume consistency given in (2.2), it follows that the capacitance increases quadratically with the surface expansion or with the reciprocal of the square of the decrease in thickness:

$$C = C_0 \frac{1}{\lambda_3^2} \tag{2.7}$$

For in-plane strain control with further simplifications from (2.3), a linear strain sensor characteristic curve is thus obtained for uniaxial conditions, a quadratic characteristic curve for pure shear conditions, and a fourth order characteristic curve for equi-biaxial conditions:

$C = \lambda_1 C_0$	$C = \lambda_1^2 C_0$	$C = \lambda_1^4 C_0$	(2.8)
uniaxial	pure shear	equi-biaxial	

Corresponding designs enable the development of proportional capacitive strain sensors. Those are characterized by properties such as high flexibility, biocompatibility, and excellent sensitivity. By

integrating them into wearables, such as gloves [43], [44], shoes [45], or wristbands [46], [47], they are particularly suitable to capture human motion, and forces exerted on the human body. They can thus be used as human-machine interfaces, e.g. for gesture communication and control [43], [44], [46], or for virtual and augmented reality applications [48], and also provide data relevant to the medical and sports sectors, e.g. for detecting incorrect posture or improving athletic performance [45], [47]. For technical applications, DET strain sensors are generally well suited for detecting large and complex movements, e.g. those of robotic joints [49]. They are additionally utilized as pressure sensors in various designs, e.g. to monitor the compression load of battery packs for electric vehicles [50].

2.1.4 Actuation Principle

Connecting the electrodes of the DET to a controllable high voltage source enables it to be utilized for actuation purposes (Figure 3a).

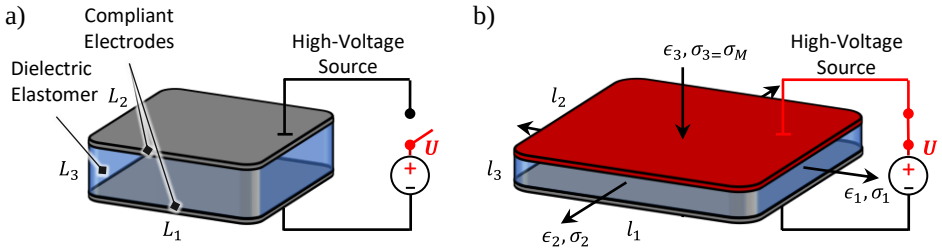

Figure 3: Actuator function principle illustrated by comparison of a DET in its non-activated condition (a) to its activated condition (b).

By activating the electric potential U, charges are distributed over the electrode surface and an electric field E is generated through the dielectric. Depending on the permittivity $\varepsilon_0\varepsilon_r$, the electric field exerts a mechanical (compressive) Maxwell stress σ_M on the material, [9], [10]:

$$\sigma_M = \varepsilon_0\varepsilon_r E^2 \tag{2.9}$$

The soft elastomeric material is thus compressed in thickness direction and simultaneously expanded in surface area due volume consistency. The reduction in thickness increases the electric field, whereas an increase in the electric field in turn leads to a further reduction in the thickness. This self-reinforcing effect lasts until the exciting Maxwell stress is in equilibrium with the mechanical stress opposed by the material (Figure 3b). In this equilibrium, the DET exhibits steady state deformation of thickness l_3 with electrode surface area $l_1 l_2$:

$$\sigma_M = \varepsilon_0\varepsilon_r \frac{U^2}{l_3^2} \tag{2.10}$$

By supplementing (2.1) into (2.10) this capacitance can also be expressed using the principal stretches:

$$\sigma_M = \varepsilon_0 \varepsilon_r \frac{U^2}{L_3^2} \frac{1}{\lambda_3^2} \tag{2.11}$$

Maxwell stress and the corresponding actuation force in thickness direction of the DET is thus quadratically proportional with the voltage control if no deformation is considered. However, due to the electromechanical coupling, it is also inversely quadratically affected by the voltage induced thickness change ($\lambda_3 < 1$), resulting in even higher stresses with a nonlinear stress-voltage function, as a result of the non-linear material properties. For in-plane strain control with further simplifications from (2.2) and (2.3), σ_M can be expressed with λ_1:

$$\sigma_M = \varepsilon_0 \varepsilon_r \frac{U^2}{L_3^2} \lambda_1 \qquad \sigma_M = \varepsilon_0 \varepsilon_r \frac{U^2}{L_3^2} \lambda_1^2 \qquad \sigma_M = \varepsilon_0 \varepsilon_r \frac{U^2}{L_3^2} \lambda_1^4 \tag{2.12}$$

uniaxial pure shear equi-biaxial

It is evident, that under pure shear conditions, higher Maxwell stresses are generated in comparison to uniaxial conditions, as they are quadratically affected by λ_1, and even higher actuation stresses are obtained for equi-biaxial conditions. The spatial deformation of the DET increases proportionally with the inducing Maxwell stress. The induced deformation cannot further be described using simple analytical terms due to the typically non-linear material properties and the electromechanical coupling. The specific electromechanical actuator characteristics are usually determined experimentally, or by means of advanced mathematical models, e.g. based on free-energy approaches, that are solved using numerical methods [51]. Actuators, that simultaneously utilize sensing and actuation principle are referred to as ‘smart actuators’, which utilize the so called ‘self-sensing effect’ enabling them to identify and react to their deflection state without external sensors [52], [53]. The corresponding operation principle is illustrated with a single layer DET, which is controlled to maintain a constant thickness $l_3 = l_{3d}$ during load variation, e.g. if subject to a single load element (Figure 4a), and transitioning to two load elements (Figure 4b).

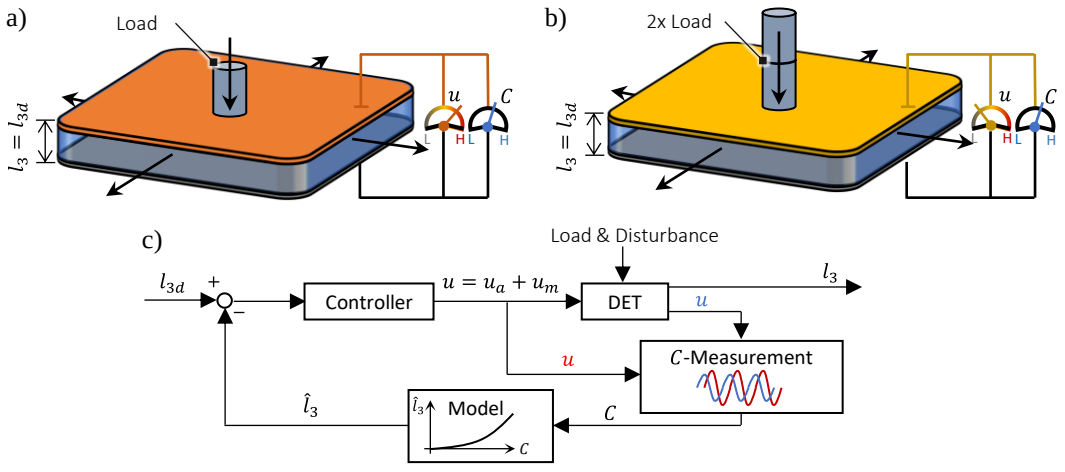

Figure 4: Function principle of a smart DET actuator, which maintains constant thickness during load variation if subject to a single load element (a), and transitioning to two of these elements (b). For closed loop control, capacitance is typically measured via high-frequency measurement voltage signal superimposed to the control voltage signal and correlated with deformation on a model base (c).

Thereby, capacitance is typically measured via an alternating current voltage u_m (AC-voltage, low voltage, small signal) which is superimposed to a quasi-stationary actuation voltage u_a (high voltage, large signal) resulting in a combined voltage u. It is correlated with the deformation on a model base, resulting in an equivalent thickness $\hat{l}_3$, that is used as control variable in the closed control loop (Figure 4c). In addition to the illustrated displacement control, there are also advanced approaches reported in the literature, e.g. enabling force control, i.e. refer to [54], [55], and the simultaneous self-sensing of displacement and force, i.e. refer to [56].

DET actuators can be used in a wide range of applications. In quasi-stationary operation, they are particularly suitable for the proportional control of valves [57], [58] and positioners [59], [60]. Compared to conventional drives such as solenoids, DETs have particularly low energy losses and thus heat dissipation in this operating mode due to the low leakage currents (see Section 2.1.7). Due to their thin and flexible structure, they also offer novel and particularly compact design possibilities. Due to their softness, they can also be used for safety-critical human-machine interactions, e.g. in soft robotics applications [61]. When controlled in the lower frequency range, DEAs can be used for silent pump drives, e.g. classical membrane pumps [62], or peristaltic pumps [63]. When controlled in the high frequency range, they can also be used as loudspeakers, either as drivers only [64], or as a combination of driver and acoustic membrane [65].

2.1.5 Design Variants

Due to the high design flexibility many individual DET design variants have been established in the past decades. Standard types for uniaxial operation are particularly common in the field of actuators but can also be considered for sensor applications. They can be divided into two classes: DETs that primarily utilize the thickness reduction effect and DETs that primarily utilize the surface area expansion effect.

Operated in the thickness direction, single DET layers can only be subject to compressive loads and are suitable for direct use as pressure sensors. High voltage actuation of a single DET in this configuration results in relatively low actuator forces that scale with the footprint size, but only small strokes in the lower µm-range. To scale the actuator stroke, several layers are usually stacked in so-called stack actuators (Figure 5a) [66].

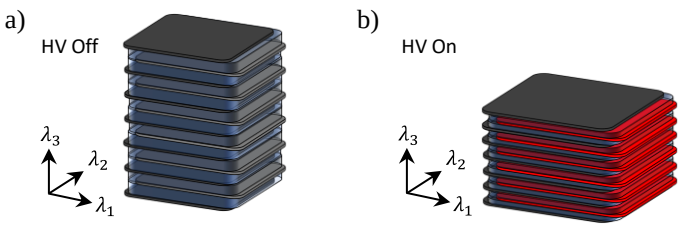

Figure 5: Multiple DET layers configured as stack actuator (a), which reduces in thickness when activated by high voltage (b).

These are reduced in length when activated by high voltage (Figure 5b), and suitable for actuating compressive and tensile loads [67]. Other designs that primarily utilize the thickness reduction effect and have properties similar to stacked actuators include folded planar actuators [68] and helical dielectric elastomer actuators [69].

DETs that primarily utilize the surface area expansion effect are referred to as planar DETs. They are operated in longitudinal direction (λ_1-direction) either in the surface plane, or perpendicular to the surface plane. Single layers can only be subjected to tensile loads and are suitable for direct use as strain sensors. For actuator operation, they are usually biased with preload elements, e.g. coil springs, to generate significant strains in the higher percentage range. A simple design variant is a rectangular shape that is uniaxially operated in the plane, referred to as strip-in-plane DET (SIP) [70]. The two edges perpendicular to the stretching direction of a SIP have a fixed width. This constraint results in inhomogeneous deformation and typical necking characteristics when stretched (Figure 6a) [71]. With long and narrow SIP designs, approximately uniaxial conditions prevail, resulting in a linear sensor characteristic curve and relatively low actuation force. With short and wide designs, approximately pure shear conditions prevail, resulting in a quadratic sensor characteristic curve and relatively high actuation force. In contrast, more complex diamond-shaped planar DETs, which are clamped within a 4-bar linkage mechanism, show a homogeneous stress-strain characteristics [72].

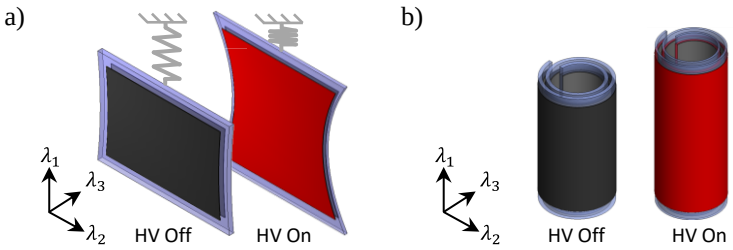

Figure 6: Actuation principles of typical in-plane operating DETs; with rectangular-shaped planar DETs (SIPs) biased with a coil spring (a), and hollow-rolled free-standing DETs (b).

Rolled and tubular DET variants are obtained when the surface of a strip is considered as the lateral surface of a cylinder (Figure 6b). They can also be operated linearly in the longitudinal direction, whereby their overall deformation and force characteristics strongly depend on their specific design and dimensioning. For example, thin and tightly rolled versions exhibit strong uniaxial behavior, therefore provide a linear characteristic for sensor operation [73], [74]. Wider multi-layer versions can also be free-standing and subjected to compressive and bending loads [75], [76]. The inside of the rolled versions can also be hollow and accommodate a biasing element such as linear springs, e.g. to increase the stroke output [76], [77]. Tubular DETs can also be operated radially, e.g. for active fluid control by feeding a liquid through the tube. When a liquid is passed through the interior, pressure-dependent tube expansion can be sensed [78], and pressure and flow can be controlled by actuation or generated by pumping motion [79]. Circular planar DETs can be

operated perpendicular to the surface plane, thus referred to as cone-out-of-plane DETs (COPs) (Figure 7). Their deformation can be approximated with a pure shear characteristic, resulting in relatively high voltage induced forces, which scale with the outer radius, whereby the stroke scales with the distance between inner and outer radius [80]. Due to the vertical movement out of the plane, force and stroke are transmitted non-linearly, resulting in lower force and higher stroke output. In general, the strip and rolled DETs can also be operated out of the plane and then exhibit similar force-displacement behavior. Strip-shaped DETs configured in this way are referred to as strip-out-of-plane DETs (SOPs) [81].

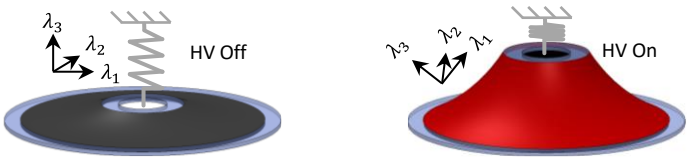

Figure 7: Actuation principles of typical cone-shaped and out-of-plane operating DETs (COP), biased with a coil spring.

2.1.6 System Layout

Planar DETs in particular are preloaded to provide significant stroke when actuated. Preload elements, such as conventional tensile or compressive coil springs, exert increasing force as they are deflected, therefore referred to as positive stiffness bias elements (PBS). In contrast, elements such as inclined buckled beam springs [59] or magnets [82] exhibit nonlinear force-displacement characteristics with a negative stiffness branch, therefore referred to as negative bias stiffness elements (NBS). The combination of DET actuator and preload element is referred to as the DET actuator system. The layout of a quasi-statically operated system, e.g. based on a SIP combined with a coil spring PBS or an inclined buckled beam NBS, is a consideration of the balance of forces between DET and biasing elements (Figure 8a) [83]. The individual force-displacement characteristics of the biasing elements, e.g. $F_{PBS}(x_{PBS})$ or $F_{NBS}(x_{NBS})$, and of the DET are determined separately either experimentally with tensile tests or based on numeric simulations. Two characteristics curves are required for the DET, one with maximum applicable voltage applied, e.g. $F_{DHV}(x_{DET})$, and one without, e.g. $F_{D0V}(x_{DET})$. All curves are transformed into the DET coordinate system, resulting in the DET actuator system layout diagram, thereby neglecting hysteresis for simplicity (Figure 8b). The space between the DET curves span an area, which represents the maximum amount of energy (mechanical work), that can be converted within one actuation cycle. If the motion is blocked, a blocking force ΔF_B is built up corresponding to the force gap in between the DET curves. If the system is not blocked, the respective free system stroke, e.g. Δx_{NBS} and Δx_{PBS}, is obtained directly from the intersection points of the DET curves with the corresponding preload curves. From this, it is apparent that preloading the DET with an NBS achieves significantly higher stroke than a PBS (Figure 8b, c). As the stroke also limits the

amount of energy that is actually converted, system designs with NBS biasing elements are typically particularly efficient [59].

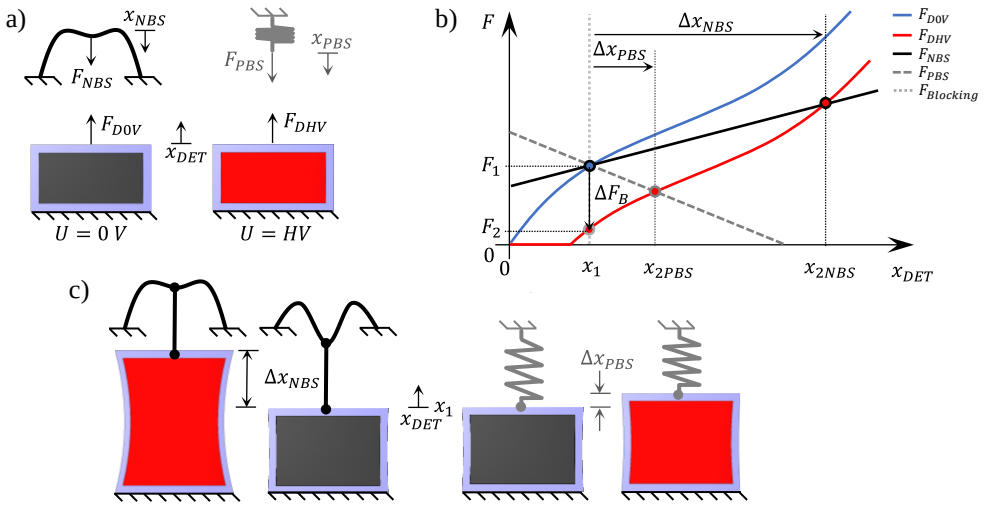

Figure 8: Individual DET actuator system components and their cut-free forces (a), which are transformed into a typical DET actuator system layout diagram for quasi-static system design (b), showing that NBS biasing elements achieve significantly higher stroke than PBS biasing elements (c).

Actuator system curves are obtained by subtracting the preload curves from the DET curves (Figure 9a). The area in between these curves represents the mechanical work available for actuating external loads. It is slightly reduced if the hysteresis behavior of the DETs is taken into account (dashed lines). As no deformation occurs, the typical blocking force-voltage curves exhibit no hysteresis and an approximately quadratic trend (Figure 9b). The displacement-voltage curve is typically hysteretic and non-linear due to non-linear and hysteretic force-displacement characteristics of the DET and the non-linear electromechanical coupling (Figure 9c).

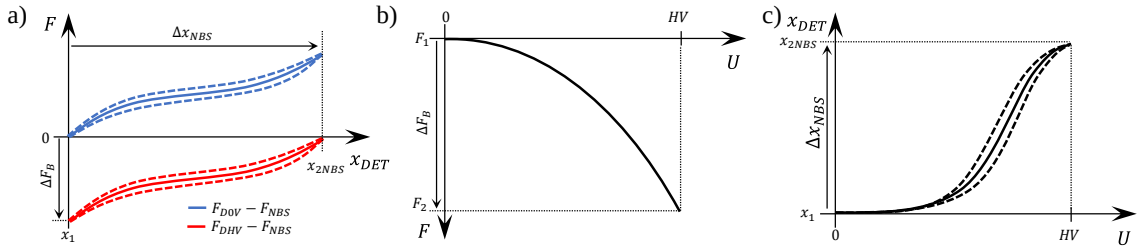

Figure 9: Typical quasi-stationary DET actuator system curves spanning the mechanical work available to actuate an external load (a), and corresponding quadratic blocking force-voltage curve (b), as well as hysteretic and non-linear displacement-voltage curve (c).

For dynamic design, the DET actuator system can be mechanically considered as a spring-mass-damper system. A simplified design approach is limited to solving the equation of motion for a spring-mass system, neglecting damping and electrical parameters [84]. It considers inertia as displacement and rate-dependent stiffness, resulting in a force $F_{in}(x, f)$ that is subtracted from the preload force. This results in a set of bias curves for different frequencies, e.g. $f_3 > f_2 > f_1 = 0$,

which can be used to estimate frequency-dependent system stroke using the quasi-static DET system design curves (Figure 10).

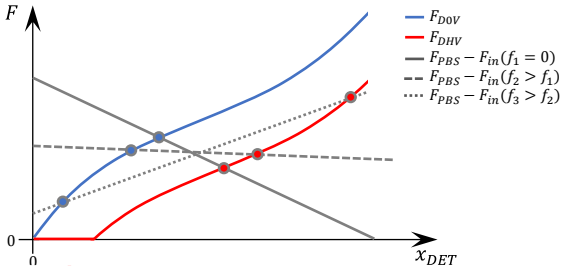

Figure 10: Rate dependent layout of a PBS-preloaded DET system, using the quasi-static DET system design diagram, thereby considering inertia as a rate-dependent stiffness that is subtracted from the preload stiffness.

2.1.7 Mechanical Characteristics

Analyzing the mechanical properties of DETs facilitates a thorough comprehension of electromechanical transduction principles, along with, time-, load-, rate-, and temperature-dependent phenomena, which is crucial for application-oriented development, testing and characterization purposes. The mechanical characteristics of DETs are predominantly determined by the dielectric layer, as the electrode layers are usually significantly thinner and their stiffness is further reduced during manufacturing, e.g. by using pre-stretching techniques [28], [29]. Particularly for fully polymeric DETs, i.e. PDMS-based dielectric films provided with CB-PDMS-electrodes, the mechanical properties correspond closely to the general mechanical properties of elastomers well known from polymer science. In this context, the viscoelastic load-, rate- and temperature-dependencies are typically characterized under the assumption of small deformations, which is discussed below.

Small Deformation Mechanical Material Properties

Assuming quasi-static deformation, as is common for tensile tests, the stress σ as a function of strain ϵ of elastomers is approximated as linear. This resulting stress-strain curve exhibits identical mechanical loading and unloading paths (Figure 11a). The linear-elastic characteristics is described by a single parameter, the Young's modulus of elasticity Y according to Hooke's law:

$$\sigma = Y\epsilon \tag{2.13}$$

This simple model is utilized for comparison of DET materials, with the Young's modulus typically in the lower MPa-range, e.g. $0.4 - 2.3$ MPa for polyacrylates or $0.09 - 2.5$ MPa for silicones [27]. However, in reality, elastomers exhibit viscoelastic properties, resulting in inherent damping and limited frequency response, as well as rate-dependent energy losses during cyclic operation, as shown by characteristic hysteresis curves in the stress-strain diagram (Figure 11b). By introducing the viscosity constant η which depends on the strain rate $\dot{\epsilon}$, a time-dependent variant of

(2.13) is obtained, known as the Kelvin-Voigt rheological model, offering a simple description of the viscoelastic behavior[85]:

$$\sigma'(t) = Y'\epsilon(t) + \eta\dot{\epsilon}(t) \tag{2.14}$$

Therein σ' denotes the rate-dependent material stress and Y' the rate dependent storage module. Rheological models consisting of lumped spring and dashpot elements are frequently utilized to describe this time-dependent viscoelastic characteristic of elastomers. Common examples include the Voight-Kelvin model, the Maxwell model, the Standard Linear Solid model, and the Burger model, along with their modifications and combinations [86], [87]. Stiffness and viscosity are highly temperature and rate dependent, therefore usually determined experimentally using dynamic mechanical analysis (DMA), by subjecting the material to sinusoidal strains at various frequencies ω and temperatures T, and measuring the stress response [85], [86]. By segregating the stress components that are in phase with strain from those that are out of phase, the complex dynamic modulus Y^*can be derived, with the real part representing the storage modulus Y' as elastic component, while the imaginary part (imaginary unit j) represents the viscous component, known as tensile loss modulus Y'':

$$Y^* = Y' + jY'' \tag{2.15}$$

From this, the viscosity η can be obtained [85]:

$$\eta(t) = \frac{Y''}{\omega} \tag{2.16}$$

For filled elastomers, beyond a critical strain, the storage modulus shows a decreasing trend with increasing strain, whereby the loss modulus shows a maximum in that strain range (Figure 11c). This phenomenon is known as the Payne effect [88], [89], [90]. Measuring at constant frequency, elastomers exhibit energy-elastic properties similar to rigid solids for temperatures lower than the glass transition temperature T_G, but soften to an entropy-elastic, rubber-like behavior for temperatures higher than T_G (Figure 11d) [91], [92].

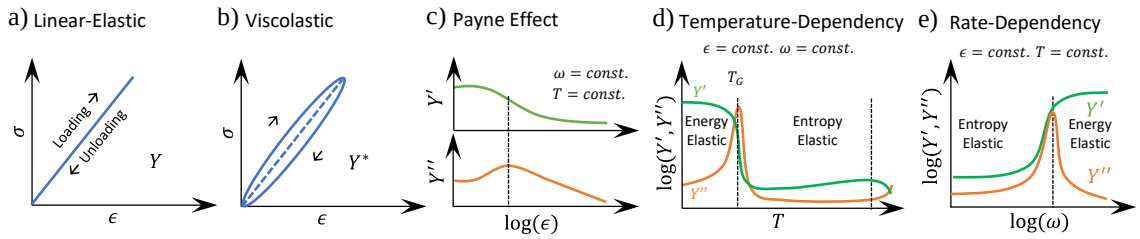

Figure 11: Typical qualitative stress-strain curves of elastomers for small deformations, showing linear stress-strain characteristics for quasi-static deformation (a), viscoelastic hysteresis for dynamic deformation (b), and the Payne effect for filled elastomers (c). At constant frequency, the storage modulus changes from a stiff energy elastic characteristic to a soft entropy elastic characteristic when exceeding the glass transition temperature range, in which the loss modulus shows a peak (d). Due to frequency-temperature equivalence, converse trends are observed with increasing frequency at constant temperature (e).

The entropy-elastic range represents the common operating range for DET applications. Within this range, elastomers typically show an increase in stiffness with temperature [91], [92], [93], e.g. observed for PDMS materials [94], [95]. Time and temperature behavior of elastomers are interdependent, thus measuring at constant temperature and increasing frequency, the moduli typically show a converse trend, with transition from entropy-elastic to energy-elastic properties (Figure 11e). This frequency-temperature equivalence is commonly utilized to extend the DMA temperature and frequency range through time-temperature superposition [86], [96].

Above explanations illustrate typical mechanical properties of elastomers, and thus DETs, under the assumption of small deformations. However, these properties vary depending on factors such as the specific elastomer composition, crosslinking density, and filler content, making it difficult to make generalized statements.

Large Deformation Mechanical Material Properties

Due to the tendency of DETs to undergo large deformations, they exhibit rather nonlinear than linear material properties. Nominal stress-strain curves considering large deformations typically show an initial decreasing stiffness for increasing strains, followed by a relatively constant stiffness in the mid-range, which is finally increasing again for higher strains, until rupture occurs (Figure 12a). While this nominal stress refers to the undeformed cross-sectional area of the DET, the true stress refers to the deformed cross-sectional area, typically exhibiting progressively increasing stiffness in the lower strain range, with a tangent slope similar to that of the nominal stress. To adequately account for both stresses, Young's modulus is determined from the slope of the tangent at zero strain [41]. Since linear stress-strain considerations become inadequate for large strains, their use is limited to rough estimates. Instead, the strain-stress correlation is usually described by higher order hyperelastic material models, e.g., Neo-Hooke, Mooney-Rivlin, Ogden or Yeoh [39], [51]. The stress-strain hysteresis can either be closed for reversible deformation (Figure 12b), or open for irreversible deformation, showing permanent set with a pronounced residual strain, that is visible as zero-stress plateau along the strain axis (Figure 12c). Furthermore, the slope of the stress-strain curve depends on the previous maximum strain, which leads to a strain-induced softening phenomenon, the so-called Mullins effect [97], [98] (Figure 12d).

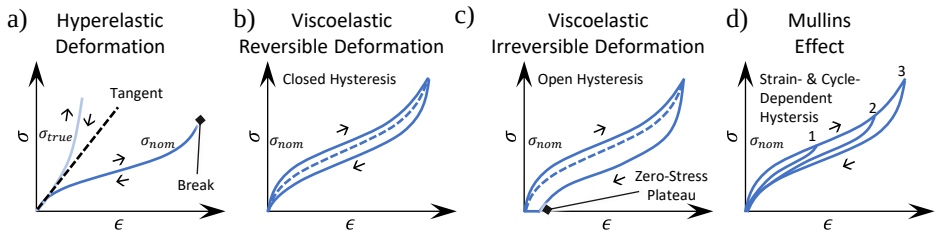

Figure 12: Typical large deformation stress-strain curves of DETs, exhibiting highly non-linear hyperelastic behavior (a), along with viscoelastic characteristics with either reversible deformation (b) or irreversible deformation (c), accompanied by a strain-and cycle-dependent stress softening known as Mullins effect (d).

Also, for large deformations, the viscoelastic behavior of elastomers is typically modeled using rheological models consisting of lumped spring and dashpot elements [51], [99].

Molecular Effects

The nonlinear and viscoelastic entropy elastic behavior of elastomers is typically explained by their macromolecular structure, representing a network of widely meshed cross-linked polymer chains, which, according to rubber conformation theory, can be considered as entropic springs [100]. In an unloaded state these chains arrange themselves in a coiled configuration to maximize mobility according to the principle of entropy maximization (Figure 13a). Under tension, the entangled network gets untangled, whereby it can be exerted to high strains (Figure 13b). Further stretching after untangling, results in a stiffer solid-like behavior, as now the interatomic bonds of the fully stretched chains become stretched until rupture. Even though elastomers generally exhibit a positive coefficient of thermal expansion, they contract in load-direction when heated under tensile stress due to the increased entropy, resulting in an increased stiffness with temperature [92], [93].

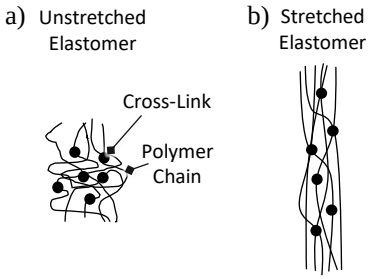

Figure 13: Schematic illustration of an unstretched cross-linked elastomer network, exhibiting a short, entangled structure resulting from the entropy-elastic characteristics (a), in contrast to its stretched configuration, in which the elastomer chains are stretched (b).

The viscous behavior of elastomers is explained at the molecular level by several mechanisms resulting from the interaction of molecular chains, which occur in addition to the covalent bonds and entanglements within the cross-linked network. These mechanisms include frictional effects between elastomer chains, van der Waals forces between them, and the formation of weak and reversible bonds such as hydrogen bonds [101]. The strain-induced softening observed with the Payne effect only occurs with filler-reinforced elastomers for low and moderate strains and is attributed to strain induced breaking of the filler agglomerates bound in the elastomer matrix and restructuring of the polymer-filler network [88], [89], [90]. For higher strains, however, an increased stiffness can still be observed compared to unfilled elastomers, which is explained by the immobility of the filler particles, which affects the mobility of the polymer chains [102]. Gilormini et al. [98] have summarized the findings of the recent years on the Mullins effect. Their literature research reveals that the effect is not limited to filler-reinforced elastomers, but also occurs in unfilled crystallizing rubbers. The phenomenon is reversible, as materials can heal when exposed to high temperatures in a vacuum or through solvent swelling. Physically motivated theories to

explain the effect include bond ruptures, molecule slipping, filler-cluster rupture, chain disentanglement, chain retraction, network rearrangement, and composite microstructure formation, but no general agreement has been gained so far [98].

2.1.8 Electrical Characteristics

DETs are either operated by applying low voltage electrical measurement signals, high voltage control signals or combinations of both. Consequently, their frequency response and energetic losses are influenced not only by their mechanical, but also by their electrical properties.

Equivalent Circuit Representation

The electrical characteristic of DETs is typically described with a simplified equivalent circuit diagram of deformation-dependent electrical components, i.e. refer to [103], [104]. In this, the DET is considered as flexible capacitor of capacitance C, complemented with a parallel leakage resistance R_l and two serial resistances R_e, which are representing the flexible electrodes. These are connected to a voltage signal source via constant contacting resistance R_a (Figure 14a).

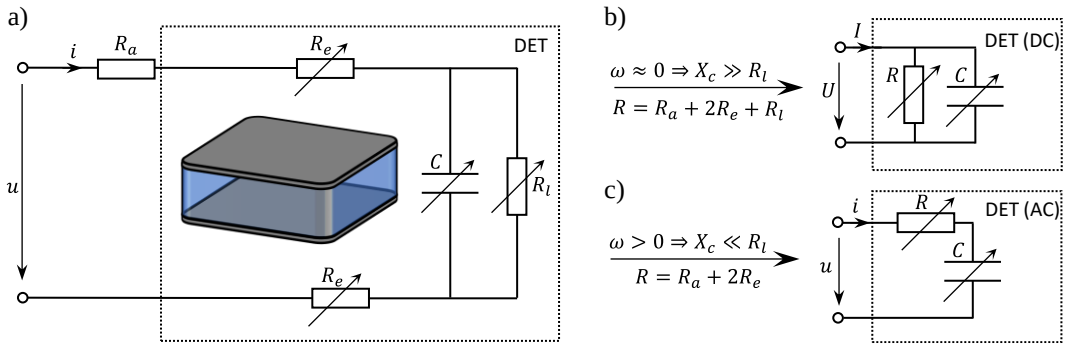

Figure 14: Common equivalent circuit of a DET, and lumped models for DC-operation and quasi-stationary operation, neglecting current through the capacitor; and AC-operation neglecting leakage current.

The capacitance depends on the permittivity ε_r of the material and the deformed geometry, as described in (2.5). The parallel leakage resistance also depends on the (deformed) geometry and the specific film resistivity ρ_l, for simplicity assuming ideal homogeneous materials and no change of ρ_l due to deformation:

$$R_l = \rho_l \frac{l_3}{l_1 l_2} \tag{2.17}$$

Exemplary values for a PDMS dielectric film (e.g. *Elastosil 2030*) are $\varepsilon_r = 2.8$, and $\rho_l = 10^{16}\Omega\text{m}$ and $l_3 = 20 \ldots 100\ \mu\text{m}$ [105]. With typical DET lengths and widths in the cm-range, this results in single-layer leakage resistances in the lower TΩ-range, and in capacitances in the lower nF-range. Similarly to the leakage resistance, the electrode volume resistance R_e in length-direction of (compliant) electrodes is obtained from the specific resistivity ρ_e and the thickness l_{3e} of the electrode, with the same simplifying assumptions:

$$R_e = \rho_e \frac{l_1}{l_2 l_{3e}} \tag{2.18}$$

Furthermore, a sheet resistance is defined independently of the electrode surface:

$$R_{es} = R_e \frac{l_2}{l_1} = \frac{\rho_e}{l_{3e}} \tag{2.19}$$

Sheet resistance is a commonly used metric for quantifying the electrical properties of a thin electrode layer along the surface plane to compare different electrodes and electrode materials, as it is often difficult to accurately measure the electrode thickness [41]. For sputtered metal electrodes, for example, this is in the sub-kΩ range (e.g. 400 Ω), while for CB- PDMS based electrodes it is in the low kΩ-range (e.g. 50 kΩ) [28].

From this equivalent circuit, further simplified lumped models for either direct current (DC-) operation (Figure 14b) or alternating-current (AC-) operation can be derived, used to approximate quasi-stationary, or higher frequency and dynamic operation (Figure 14c). Quasi-stationary operation implies frequencies $f \approx 0$, resulting in voltages U, that are approximately DC. The lumped model consists of a capacitor C in parallel to a resistor R, which represents the sum of series and parallel resistors. This is postulating, that no charging current is flowing through the capacitor, as this has an infinite reactance X_c.

$$X_c = -\frac{1}{2\pi f C} \tag{2.20}$$

Therefore, resulting constant current I is only attributed to leakage, which is limited by the total resistance R, resulting in Ohmic losses of active power P_{ea}:

$$P_{ea} = RI^2 \tag{2.21}$$

Since typical R is in the lower TΩ-range and typical U in the lower kV-range, I is in the lower nA-range, resulting in very low ohmic losses in the lower µW-range, which makes DET actuators particularly efficient for quasi-stationary operations. A lumped model for dynamic or frequency operation with time-dependent (AC-) voltages u, is obtained, postulating that all current is flowing through the capacitor and no leakage occurs. Thus, R_l is neglected and R only comprises the sum of the series resistors, with typical values for DETs in the lower kΩ-range. Since typical values for C are in lower nF-range, and typical R_l is in the lower TΩ-range, this characteristic is approximated, as the reactance X_c is significantly lower than R_l, also for lower frequencies (e.g. $f = 1$ Hz). The model represents a simple RC-series element of complex impedance $\underline{Z}$:

$$\underline{Z} = R + jX_c \tag{2.22}$$

and time constant τ

$$\tau = RC \tag{2.23}$$

With this, the time t_c to charge a standard capacitor by approximately 99 % is obtained, which is used as a rough estimate of the (minimum) charging time of a DET, if a voltage is applied:

$$t_c = 5\tau \tag{2.24}$$

The RC-series represents a lowpass of cut-off frequency f_c at which the phase angle between voltage and current is $\theta_c = -45°$, and the voltage over the capacitor is attenuated by approximately 3 dB, or 70.7 %:

$$f_c = \frac{1}{2\pi\tau} \tag{2.25}$$

The cut-off frequency represents a transmission limit for the electric stimulation of DETs, which must be considered for high frequency operated actuators and for high frequency impedance measurement. The highly simplified RC-series model is used in particular as an equivalent circuit diagram for the derivation of capacitance and electrode resistance of DETs from impedance measurements, e.g. for self-sensing methods [103], [104]. As this is also implemented in the scope of this work, further details are discussed in Section 3.5.3. Furthermore, it is noteworthy that the simple RC-series model does not take into account the local distribution of R and C, which leads to inhomogeneous voltage distributions that affect actuation and measurement, especially with large DET surfaces, high electrode resistances, and high measurement and actuation frequencies. This must be considered with more sophisticated models, e.g. for high frequency actuator applications [106] or sensing of locally distributed resistance or capacitance changes within a single DET structure [107]. As this must also be taken to in account in the scope of this work, further details are discussed in Section 4.1.

Dielectric Permittivity

The electromechanical transduction principles of any DETs are fundamentally controlled by the permittivity ε_r of the DET (refer to Section 2.1.3, and 2.1.4). A review on typical dielectric elastomer materials is given in [27], covering a range of permittivity ranging from $\varepsilon_r = 2.8$, i.e. for PDMS (*Elastosil 2030*), to $\varepsilon_r = 12.5$, i.e. for Hydrogen Nitrile Butadiene Rubber (HNBR). Permittivity arises from the alignment of dipoles within the polarizable material due to an applied electric field. From equation (2.9) it can be observed that a higher value of the dielectric constant leads to an increase in the induced Maxwell stress, and thus higher actuator performance, and from equation (2.4) it is evident, that this also goes along with a higher sensitivity. Efforts are therefore being made to increase permittivity, with various approaches being pursued, as shown reviewed in [9]: Besides the synthesis of new polymers, these include random composites in which fillers, e.g. ferro- and piezo-electrics, conductive particles, or organic mono- and polymers, are embedded into

the elastomer matrix, and field-structured composites, where crosslinking is carried out in presence of an electric field.

Electrode Conductivity

Two approaches have generally been established to make conductive electrodes compliant, either utilizing pre-stretching techniques during electrode deposition to achieve an unfolding structure, or using conductive micro- or nanoparticles, usually embedded into inherently compliant materials (refer to Section 2.1.1). The advantage of coherent wrinkled metal thin-film electrodes resulting from the first approach is, that they exhibit comparatively low viscosity along with a high conductivity, that is consistent over the permissible stretch range [28], [29]. However, their deposition, e.g. with the aid of sputtering processes, is complex. Conductive particles are therefore used more frequently in the literature, i.e. embedded in elastomers such as PDMS [34], [38], [108], which are then cross-linked, to obtain sufficient adhesion to the dielectric layer. The conductivity of these filled elastomer electrodes is explained by the percolation theory, i.e. refer to [108], [109]. It states that the conductivity is given at a certain degree of filling, the percolation threshold, at which the first coherent conductive paths are established, and increases only slightly with a further increase of the filler content. For typical carbon-based conductive particles, the percolation threshold for CNT is typically lower than for CB due to their high aspect ratio [109]. A negative temperature coefficient is frequently reported for CNT-filled PDMS, i.e. [110], [111], [112], but also for CB-filled PDMS, i.e. [113], [114], [115]. This characteristic is explained by an increased mobility of the charge carriers and tunneling currents with increasing temperature, that is counteracting the increase in resistance due to thermal expansion of the material [110], [111], [114]. Beyond the mechanical influences of the fillers (refer to Section2.1.7), CB-filled elastomeric PDMS electrodes usually also exhibit a complex electromechanical behavior, frequently exhibiting non-linear, and often bi-modal hysteretic behavior depending on the utilized materials and filler concentration, i.e. shown in [108]. Potential explanations of these effects consider the behavior of the CB clusters within the silicone matrix and their changing ratio of loss and formation of conductive paths.

2.1.9 Failure Mechanisms

As discussed in Section 2.1.7, (dielectric) elastomers and especially filled variants i.e. CB-PDMS based electrodes, exhibit a variety of mechanical phenomenon, such as load amplitude- and cycle-dependent permanent set and softening phenomena, as well as time-, rate- and temperature-dependent non-linear hysteresis characteristics. This assumes that no load is applied above the yield point, at which the material immediately tears. Many load-related effects typically subside after a few cycles, so that a reproducible mechanical behavior can be achieved, which is crucial for the specification of DET sensors, actuators, and corresponding systems. Accordingly, the corresponding sensors and actuators must be trained during production, and it must be ensured that

they are not loaded beyond the specification during operation, as this can lead to a reduction in performance, accuracy, or even total failure. In the specified operating range, it must also be ensured that minor temperature, time, and rate-dependent changes can be tolerated.

Mechanical Degradation and Failure

Long-term and high-cycle operation usually goes along with a decrease in residual strain or residual stress until mechanical failure (crack / tearing) occurs. The service life specified by the number of load cycles usually decreases with increasing strain amplitude, strain rate and temperature. An overview of relevant studies in the context of DET technology is given in Section 2.3.

Conductivity Degradation and Failure

Along with mechanical degradation, the strain amplitude and cycle-dependent fracture of continuous electrode areas leads to a degradation of the electrical conductivity. Coherent wrinkled metal electrodes, typically exhibit widely consistent conductivity during cyclic operation i.e. shown in [28], [30], however a steep decline in conductivity can occur after fatigue fracture of the electrode surface, e.g. shown in [116]. For conductive particle-based electrodes, i.e. CB-PDMS electrodes, the breaking of agglomerates can lead to the formation of partially or completely isolated islands and thus to a gradual degradation of the electrical conductivity [10], [41].

Dielectric Breakdown

DE materials are limited in their electromechanical actuation performance by their maximum electrical breakdown strength. This is characterized by a sharp increase of current, occurring when a critical voltage or electric field threshold is exceeded, usually creating a permanent conductive path through the elastomer, preventing it to be charged again [10], [41]. A review on typical dielectric elastomer materials is given in [27], covering a range of dielectric breakdown field strengths from $17 \ldots 35\ V/\mu m$ for *VHB 4910*, over $100\ V/\mu m$ for *Elastosil 2030* up to $235\ V/\mu m$ for *Nusil CF19-2186*, which represents another silicone material. However, these breakdown strengths cannot be considered as material constant, but also depend on thickness and pre-stretch of the sample, the rigidity, geometry, size and surface properties of the electrode, and extrinsic factors such as humidity, temperature, type, and rate of the electrical stimulation [33], [41], [117].

Electromechanical Instability

With reference to Section 2.1.4, the actuator effect usually results in an equilibrium between the voltage induced stress and the material stress acting against it. However, for some materials, e.g. VHB acrylates, the increase in reacting material stress is lower than the increase in Maxwell stress, resulting in a continuously decreasing thickness of the dielectric, until breakdown occurs [41]. This electromechanical Instability (EMI) phenomenon can be counteracted, for example, by pre-stretching the material, i.e. refer to [118].

2.2 Fundamentals of Testing and Characterization of DETs

Testing and characterization of DETs, their underlaying materials and derived systems involve both, controlling mechanical and electrical quantities and measuring mechanical and electrical quantities in response. To ensure reproducibility and study the effects of temperature and humidity, tests are typically conducted under (various) controlled environmental conditions. They can generally be categorized as mechanically, electrically, and electromechanically controlled experiments, conducted under either short-term (low-cycle) or long-term (high-cycle) test conditions. The categories and the general test principles are explained below, by means of two generic electromechanical test setups which enable to conduct typical characterization experiments within temperature and humidity-controlled environments (Figure 15). One setup enables to conduct mechanically, electrically and combined electromechanically controlled experiments, e.g. on DET elements (Figure 15a). The second setup is suitable to conduct purely electrically controlled experiments, e.g. on DET actuator systems including biasing mechanisms (Figure 15b). The SIP design together with the NBS preload mechanism is considered as a test object example, as this configuration is particularly relevant in the context of this work.

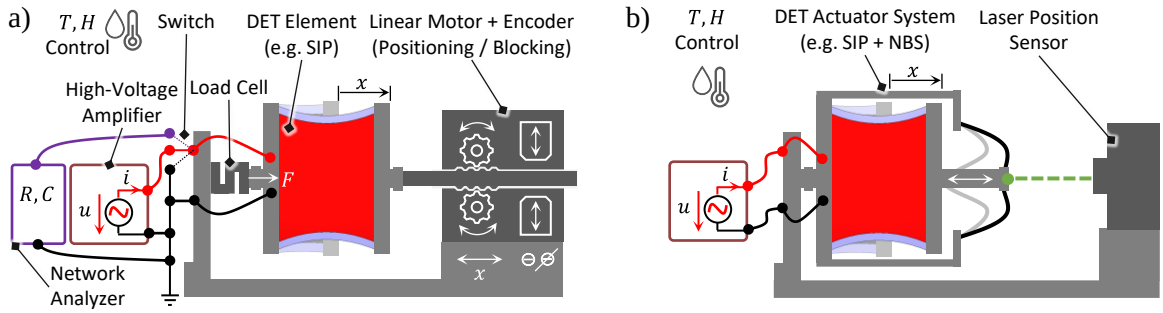

Figure 15: Schematic illustration of generic electromechanical test setups located in temperature and humidity-controlled environments, suitable to conduct either mechanically, electrically, and electromechanically controlled experiments, e.g. on SIP compounds (a), or purely electrically controlled experiments, e.g. on SIP actuator systems including buckled beam NBS preload mechanisms (b).

2.2.1 Mechanically Controlled Experiments

In mechanically controlled experiments, active control is provided to control either force (stress) or displacement (strain) and measuring the respective remaining variable. Thereby, the electrical status of the DET is usually not indifferent, but subject to specific constraints, such as grounding or constantly applied high voltage. Common complementary measurements include the simultaneous investigation of electrical properties, such as electrode resistance, or dielectric permittivity measurement [41].

Typical mechanically controlled tests for planar DETs are uniaxial tensile tests (Figure 16a), planar tension tests (Figure 16b), and equi-biaxial tensile tests (Figure 16c), including bubble inflation tests (Figure 16d). The test variants can be either displacement controlled, or force controlled.

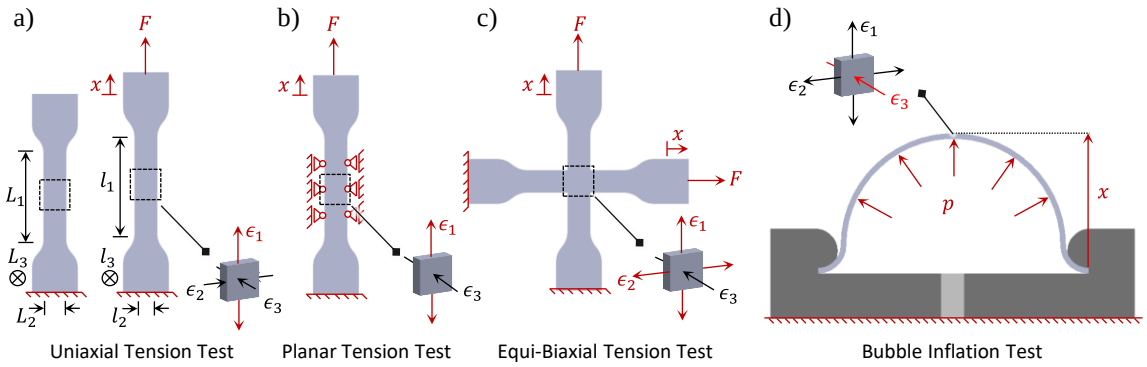

Figure 16: Typical mechanical tests on DE materials, i.e. uniaxial tension tests (a), planar tension tests (b), equi-biaxial tension tests (c), and bubble inflation tests (d).

Multiaxial Testing

The bubble inflation test is a common biaxial test performed on elastomers pioneered by Treloar [119] and Rivlin et al. [120] in the mid-20th century. It involves inflating a circular membrane mounted on a frame to a known pressure and measuring its expansion optically to calculate the stress-strain curve from the applied pressure, geometry, and expansion data, i.e. refer to [41], [121], [122]. In the field of DETs, these tests are relevant to identify constitutive parameters for hyperelastic material models, i.e. refer to [122], [123]. They also serve for experimental investigations on biaxially (pre-)loaded DET types, in particular bubble-like inflated membrane designs, i.e. to investigate their actuation performance and EMI [124], [125], [126].

Equi-biaxial tests can also be conducted on rectangular or cross-shaped planar samples, by actively controlling two perpendicular axes. Corresponding tests are particularly conducted to obtain constitutive material parameters, i.e. refer to [121], [127]. However, the design of the samples and test setups is relatively complex in comparison to the bubble inflation test.

Similarly complex setups are used for planar tension tests, also referred to as pure shear tests, i.e. refer to [121], [127]. For this reason, simplified tests are therefor usually conducted by using pure shear-like samples in uniaxial tensile tests.

Uniaxial Testing

Uniaxially mechanically controlled tests are particularly used to characterize and design uniaxially operated DET compounds and systems (refer to Sections 2.1.5 and 2.1.6). Assuming uniaxial- or pure shear-like test objects, corresponding tests can also be utilized to investigate general material characteristics, i.e. to determine constitutive material parameters, thus avoiding the more complex design of test setups with multiple control axis to enable planar or biaxial testing and using standardized universal setups instead. In particular, uniaxial tests serve as a basis for determining the modulus of elasticity and the complex mechanical modulus as a function of temperature and frequency using DMA (refer to Section 2.1.7). However, in the context of research and development on DETs, mostly quasi-static investigations with large strain amplitudes are

conducted, that are particularly relevant with focus on sensing and actuation with large strains. Corresponding tests are also relevant to investigate long-term and fatigue characteristics of DETs and underlying materials, as explained in more detail in Section 2.3.1.

Typical test setups for uniaxially controlled tensile tests basically consist of a linear motor, which can either be displacement controlled, e.g. via the position signal of the motor internal encoder, or force-controlled via the force signal provided by the load-cell (refer to Figure 15, left). Both standardized universal test devices and proprietary developments, are typically utilized for this purpose, some of which are also installed in climate chambers, to investigate temperature and humidity impacts.

To obtain comparable test results, Carpi et al. [41] defined standardized test conditions for uniaxial testing. Therein, a minimum (tensile) length-to-width aspect ratio of 5:1 is specified for uniaxial characteristic sample designs, and minimum aspect ratio of 1:5 for pure shear characteristic sample designs. The typical variations in the strain rate are a tenfold increase or decrease if the change strain rate results in more than 10 % change of the stress-strain curves. In addition, ambient test conditions are defined with a room temperature of 23 ± 2°C and humidity of 50 ± 5 %rh. Test results of continuous cyclic experiments are commonly presented with stress-strain curves (see Figure 12), with strain and stress described as nominal (engineering) quantities, related to the undeformed geometry. Hence, strain ϵ_{nom} is described as ratio of the stretched length l_1 to the initial length L_1:

$$\epsilon_{nom} = \epsilon_1 = \frac{l_1 - L_1}{L_1} \tag{2.26}$$

The corresponding nominal stress σ_{nom} is described as ratio of the applied force F to the undeformed cross-section area $L_2 L_3$:

$$\sigma_{nom} = \sigma_1 = \frac{F}{L_2 L_3} \tag{2.27}$$

The experiments carried out as part of this work (refer to Section 4) are also evaluated using these nominal quantities, whereby they are only referred to as $\epsilon_{nom} = \epsilon$ and $\sigma_{nom} = \sigma$ for the sake of simplification.

2.2.2 Electrically Controlled Experiments

In electrically controlled experiments, active control is provided by controlling the actuation voltage. The mechanical constraints are commonly not indifferent and depend on the respective test type. The most relevant electrically controlled experiments are dielectric breakdown tests, blocking force tests, and free-stroke tests.

Blocking Force Tests

Blocking force experiments are conducted to evaluate uniaxially operated DET actuators for their actuation force. For this purpose, the DET is pretensioned against a load-cell with a specific constant pre-strain, i.e. using a linear motor which is blocked at a corresponding position (refer to Figure 15a). By controlling the DET with a slow voltage profile, the blocking force-voltage curve can be acquired, which typically exhibits an approximately quadratic characteristic (refer to Figure 9b). By providing frequency sweeps, the dynamic behaviors of DET actuators can additionally be characterized in terms of force as a function of excitation frequency, given that the stiffness of the test setup is significantly higher than this of the DET [41].

Free-Stroke Tests

Free stroke experiments are conducted to evaluate uniaxially operated DET actuators for their actuation stroke. For this purpose, the corresponding free-standing test object is mounted on a rigid test platform and its stroke output is measured with a displacement measurement sensor, e.g. laser position sensor (refer to Figure 15b). By providing frequency sweeps, the dynamic behavior of DET actuators can additionally be characterized in terms of stroke as a function of excitation frequency [41].

Dielectric Breakdown Tests

Dielectric breakdown tests are conducted to evaluate DETs and their underlaying materials for their breakdown strength (refer to Section2.1.9). During dielectric breakdown tests, the DET compound, or to the pure film is provided with constant pre-stretch, and a continuously increasing voltage signal is applied until dielectric breakdown occurs, which is detected by a steep increase in current. A corresponding test can generally be carried out, using a similar setup as for the blocking force (refer to Figure 15a, motor locked), with focus on current measurement for dielectric breakdown detection, instead of force measurement. If DET compounds with compliant electrodes are tested, breakdowns can occur in the entire electromechanically active area. The test bench developed within the scope of this dissertation also follows this approach (refer to Section 4.3.2). However, breakdown tests are often carried out point-by-point on pure film material, which is firmly clamped between two rigid metal electrodes of the test device [41]. Commercially available equipment can serve for this purpose, but comprehensive proprietary developments are proposed in the literature, that offer improved systematic experimentation and wider test variations. For example, they enable automatic point-by-point scanning of film samples at multiple local points, utilization of various electrode geometries, adjustment of electrode contact pressure, and execution of experiments under controlled ambient conditions, i.e. refer to [128], [129].

2.2.3 Electromechanically Controlled Experiments

In electromechanically controlled experiments, active control is provided by both, strain (or stress) and voltage (refer to Figure 15a, motor unlocked). Corresponding test benches can be used in

particular for hardware-in-the-loop (HIL) experiments. To name some examples, Hodgins et al. conducted HIL experiments by simulating various (pre-) load profiles in combination with a DET, therefore applying sinusoidal voltage signals and control the motor to obtain a constant force or a desired stiffness [83], [130]. Moretti et al. conducted HIL simulations on DET generator prototypes, that includes dedicated power and control electronics, with a real-time model that emulates oscillating water column plant hydrodynamics[131], [132].

HIL approaches generally offer the possibility of simulating realistic operating conditions. They therefore also represent a promising approach for the long-term testing of DETs with realistic electromechanical load scenarios. Two HIL approaches that can be carried out with the developed test rig are also demonstrated as examples in this dissertation. These methods do not rely on a closed control loop but instead utilize feed-forward techniques, operating under simplified assumptions. With this approach, a constantly controlled electric field is generated across a DET over a wide strain and voltage range (refer to Section 4.4.1), or the strain-voltage behavior of a DET-NBS system is simulated (refer to Section 4.4.2).

2.3 State of the Art: Long-term Testing of DETs

In general, mechanically, electrically, and electromechanically controlled tests can be carried out under both short-term and long-term operating conditions. Long-term tests and short-term tests generally require similar test setups with regard to attributes such as functionality and precision. In this respect, long-term tests and short-term tests can be carried out, using similar test rigs. However, long-term tests involve further challenges for the test system, such as low wear and maintenance, automatic condition monitoring, as well as failure detection. Due to the long test duration, they also require the simultaneous execution of several tests under equal testing conditions for the accelerated assessment of statistically relevant data. These additional requirements particularly apply to the test rig developed in this work. Therefore, the following literature review offers an overview of long-term tests conducted in scope of DET research, including discussions on the associated test setups. It shows the wide range of testing options that have already been implemented and reveals the gap that this work aims to close.

2.3.1 Mechanically Controlled Long-Term Experiments

Mechanically controlled long-term tests typically use universal test benches located in temperature-controlled laboratories and measuring rooms. Corresponding investigations mainly focus on changes in the stress-strain behavior and electrode degradation characteristics of DETs.

The long-term behavior of elastomers in general is covered in detail in the polymer science literature mostly with regard to stress-strain behavior for different environmental conditions. Mechanical lifetime is mainly studied by the crack initiation (nucleation) and the crack propagation (growth) method [133], [134], [135]. With the crack initiation method, a decrease in material

stiffness is typically observed, and the occurrence of cracks or fractures is defined as the end of the service life. With regard to this, Cadwell et al. [136] conducted pioneering uniaxial strain-controlled experiments on rubber, reporting a dependency between maximum strain and number of cycles until failure, and thus strain-based life cycle prediction. In the crack propagation method, fatigue life is defined as the number of cycles required for a crack of a given initial size to propagate to the maximum crack size under the influence of the external energy release rate. With this regard, Lake et al. [137] conducted pioneering experiments on razor-cut crystallizing (natural) rubber and non-crystallizing styrene–butadiene rubber (SBR), also reporting significant increase in the cut growth rate for increasing temperature. Dogadkin et al. [138] conducted first investigations on the effect of electrical charges on carbon-reinforced rubber, reporting higher mechanical lifetime in fatigue experiments if the test specimen grips are grounded.

Only a few high cycle mechanical lifetime experiments can be found in the literature, which have been conducted in the context of DET technology in the past decades. Fan et al [139] investigated crack growth of pure shear like DE samples (*VHB 4910*), by conducting cyclic strain-controlled uniaxial tests with various maximums stretches and more than 10^5 cycles. From the results they derived a simple power law to describe the relation between crack growth rate and energy release rate to predict the lifetime of these DEs. Iannarelli et al. [140] investigated, how the pure mechanical cyclic strain affects the dielectric integrity of DEs (*Elastosil 2030* film), by monitoring the partial discharge activity after applying up to 10^4 cycles of various stretches. For their studies, they used a fatigue test bench that enables to test five samples in parallel. For higher stretches (200 %) they report generally larger discharge moduli for the fatigued samples in comparison to non-fatigued samples, but no difference for lower or moderate stretches. Won et al. [116] investigated electrode degradation of acrylate and PDMS based DET samples (*VHB 4910* and *Sylgard 184kit*), with spray-coated silver ink electrodes combining interpenetrating network and wrinkle surface methodology. With uniaxial strain-controlled tensile tests for rectangular shaped DETs (1 Hz sinusoidal strain of 76.5 %), they proved approximately constant electrode conductivity for up to 10^3 cycles, although severe cracks are obtained in the electrode surface. Hubertus et al. [30] conducted similar experiments on PDMS DET samples (*Elastosil 2030*), with sputtered NiCr-based thin-film electrodes also using the wrinkle surface methodology, varying layer configuration, pre-stretching, and cyclic stretches. From their studies, they report only minor changes in conductivity for 10^7 cycles (20 Hz sinusoidal strain of up to 65 %). Taine et al. [129] investigated the relationship between silicone film strain and its breakdown strength through strain-controlled cyclic uniaxial tensile tests at varying strain levels, followed by an assessment of dielectric breakdown. Their findings indicate that the initial stretching, characterized by the Mullins effect, predominantly diminishes the breakdown strength.

2.3.2 Electrically Controlled Long-Term Experiments

For electrically controlled long-term tests, either blocking force with different constant pre-strains or free-stroke tests with different pre-strain mechanisms are typically conducted. For long-term operation, corresponding test benches are equipped with automatic breakdown detection and shutdown mechanisms for the high voltage source. Carrying out free stroke tests within a climate chamber offers application-oriented test scenarios for evaluating DET actuators in real operation. Kornbluh et al. [141] summarizes pioneering lifetime investigations mainly on VHB-based DETs (e.g. *VHB 4910* or *4905*) under varying electrode materials, actuation or generation strains, electric fields, pre-strain, and humidity conditions. They generally show that higher electric fields and environmental humidity significantly reduce the lifetime of these materials. However, lifetimes higher than 10^7 cycles are achieved, e.g. when operating 300% biaxially pre-stretched in-plane operating circular DET samples with a 5 Hz rectangular signal and electric field strengths up to 100 V/µm. Matysek et al. [142], [143] present a lifetime setup for characterization of stacked DETs, which comprises a total of 16 individual test stations divided into four channels, each provided with a programmable high voltage amplifier and voltage monitor (Figure 17 a).

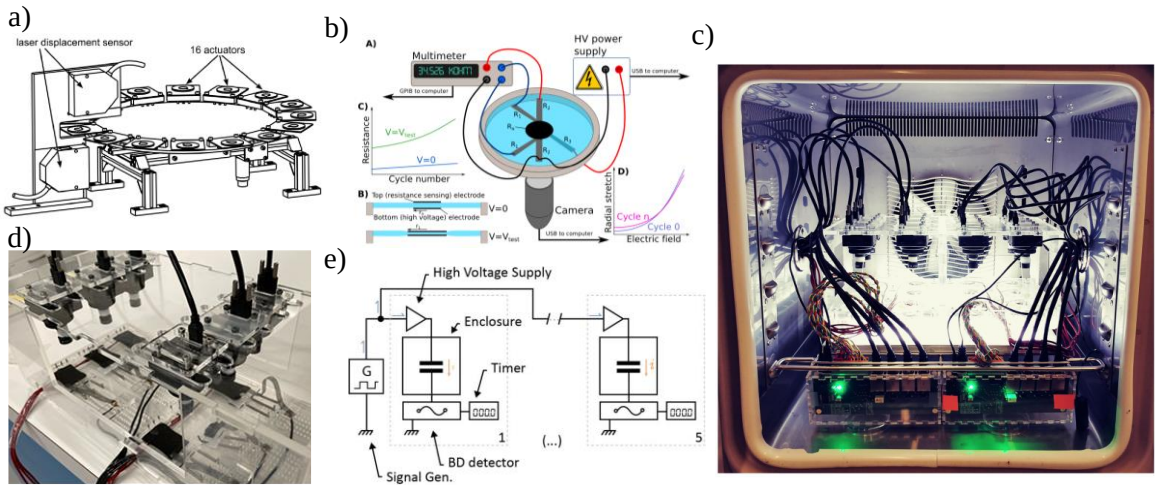

Figure 17. State of the art electrically controlled lifetime investigation setups; with stack DET testing device [142] (a), the NERD setup [144] (upper mid), two MAPLE Setups within a climate chamber [145] (c), one MAPLE setup adapted to rectangular shaped DETs pre-stretched with coil springs [146](d), and the ALT setup [147] (e).

Each test station provides individual current measurement, and individual high voltage relays, to detect electrical breakdowns and disconnect the test station from the respective high voltage amplifier. One test station provides laser position measurement, to investigate the voltage induced thickness change of the DET stacks. The setup is also capable of being operated at higher temperatures, e.g. 80 °C and 50 % relative humidity. From their studies, they report that 30-layer silicone DETs (*Elastosil P7670*) with graphite powder and silver grease electrodes achieve up to 10^9 cycles, when operated at a 10 Hz sinusoidal signal, with electric fields between 15 V/µm and 30 V/µm. Rosset et al. [144], [148], [149] introduce the *novel electrode resistance degradation*

(NERD) setup, which stresses in-plane expanding DET actuators with a programmable high voltage amplifier, measuring the in-plane surface area expansion with a digital camera and the electrode resistance with a multimeter, using four-wire resistance measurement (Figure 17 b). Providing square wave signals up to 1 kHz, this setup enables to carry out accelerated aging tests to investigate electrode resistance degradation. For studies with 50 Hz square wave voltage excitation, they report a lifetime higher than 10^7 cycles for circular DET actuator samples (*Elastosil 2030* with CB powder or CB-PDMS based electrodes), with progressive electrode degradation and gradual strain reduction. Chen et al. [150], [151] present a lifetime test setup consisting of a high voltage source, which is connected to 16 in-plane circular DET samples via individual high voltage relays. The setup provides voltage and current measurement capabilities, but no force or displacement measurement. In their studies, lifetimes higher than 10^6 cycles are reported for silicone DETs (*Elastosil 2030*) with blade-casted CB-PDMS based electrodes at 75 V/µm, with dielectric breakdown as the main failure mechanism. Iannarelli et al. [147], [152] investigate the effects of static pre-stretching of in-plane circular silicone DETs (*Elastosil 2030* with CB-PDMS based electrodes) on their long-term reliability, by conducting accelerated static lifetime tests under gradually increasing DC voltage. Their results show that the lifetime decreases considerably with increasing pre-strain, although the critical breakdown stress increases significantly. Corresponding studies are carried out on a setup with 16 test stations, each provided with an individual high voltage amplifier, a timer, and a fuse, which disconnects the samples after electrical breakdown and stops the timer (Figure 17 c). Inspired from the *NERD* setup Kühnel et al. [145], [153] introduce the *Multi-Sample Actuation Performance and Lifetime Evaluation* (*MAPLE*) setup (Figure 17 d). This includes six test stations, each equipped with a camera, a common multimeter for all samples, and a common high voltage amplifier, which can be connected to and disconnected from each test station via individual high voltage relays. The setup is placed in a climate chamber providing varying environmental conditions up to up to 85 °C and 85% relative humidity. Conducting lifetime investigations on silicone-based (*Elastosil 2030*) and slide-ring material-based (SRM-based) DET actuators, they report, that reversing high voltage can improve the lifetime of SRM-based DETs more than tenfold, with no comparable effect to the silicone DETs.

2.3.3 Electromechanically Controlled Long-Term Experiments

Previous sections refer to work in which long-term tests are controlled either mechanically or electrically. While the mechanically controlled tests are limited to tests without applied actuation voltage, the electrically controlled tests are conducted under either free or constant mechanical constraints. However, mechanically controlled tests only enable limited interpretation of the measurement results on the actuator characteristics, whereby electrically controlled tests only enable a limited interpretation on the sensor characteristics of DETs. So far, only one comprehensive test bench has been reported by Hill et al. [154], [155], [156], [157], in which both mechanical and electrical variables can be controlled independently of each other simultaneously

on 15 DET samples (SOPs) within long-term testing conditions and controlled environments (Figure 18).

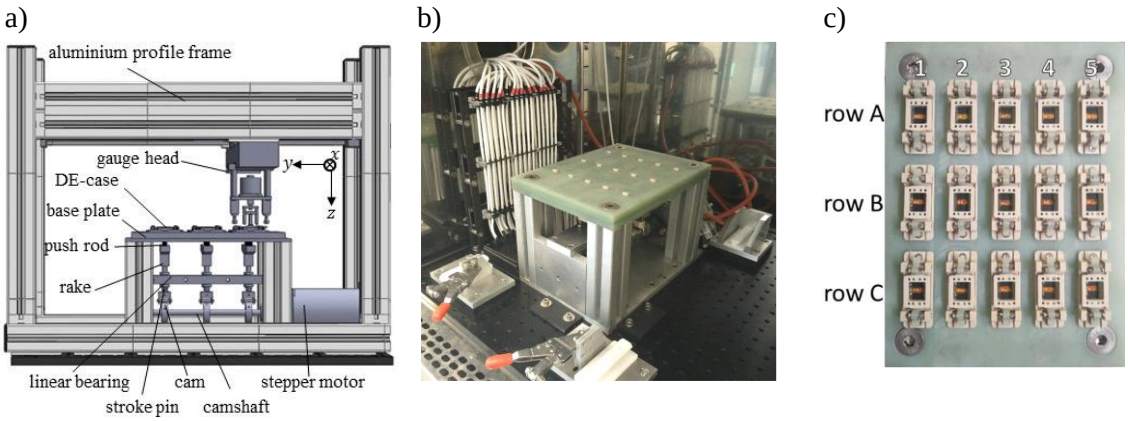

Figure 18: Electromechanical fatigue setup [154], [155], [156], [157]; with CAD side view perspective to the setup including electromechanical control unit and force measuring unit (a), photo of the electromechanical control unit inside a climate chamber (b), and photo with top view perspective to the 3x5 SOP test samples mounted to it (c).

The test bench comprises an electromechanical test unit and a separate force measurement unit installed within a climate chamber. The test unit features three channels, providing five test stations each. Each channel is provided with identical displacement and voltage control. Out-of-plane displacement control is achieved with a camshaft that converts the rotating movement of a robust rotary motor into sinusoidal linear movements. Due to the respective cam geometry, identical and varying linear displacement trajectories can be generated on the channels. Furthermore, each channel is equipped with one high voltage amplifier connected to five individual test stations via dedicated relays and current monitors. This enables simultaneous voltage control across five DET samples, and individual current measurements and voltage shutdown functionality. Capacitance and resistance measurements can be performed consecutively on the test samples by switching them from the high-voltage amplifier to a common proprietary measuring device. The mechanical measurement unit provides force-measurements, that can be carried out consecutively by automatically moving a load-cell from one test station to the next. The mechanical control unit can be operated in a climate chamber in a temperature range between -20°C and 100°C, whereby the force measurement unit can only be used in room-ambient conditions. The setup enables a wide range of comprehensive electromechanical long-term tests to assess fatigue and lifetime of DET sensors and actuators with simultaneous displacement and voltage control of 15 DET samples in a wide temperature and humidity range. To date, no electromechanically controlled test bench has been proposed that features comparatively far-reaching test capabilities. However, also this setup has limitations in many regards:

- The displacement control based on cam drives requires a considerable amount of manual test preparation and limits trajectory design capabilities, thus the ability to design more sophisticated tests scenarios.
- As the force measurement can only be carried out under room ambient conditions, temperature, and humidity influences on the DET force characteristics cannot be investigated. Moreover, for random measurements during a long-term test, the test must be interrupted accordingly in order to install or uninstall the force measuring unit manually.
- Due to simultaneous control, but only successive measurement of force, capacitance and resistance, fully simultaneous permanent monitoring of all samples is not possible. This Random monitoring is sufficient for long term tests, but less effective to provide statistically significant data for shorter test durations with low cycles.
- Capacitance and resistance measurement is only possible if no high voltage is applied to the samples for actuation. Consequently, the pure sensor and actuator properties of the samples can be characterized, but not the self-sensing properties of smart DET actuators.
- The test rig is limited to testing DET types, that are deflected out of the plane, i.e. SIPs and SOPs.

This dissertation aims to develop a test rig with comparable testing capabilities, but to overcome the limitations described above. Early versions of the setup have already been presented at scientific conferences [158], [159]. It represents a flexibly user-configurable tool, allowing full testing capabilities simultaneously on numerous DET samples within various controllable environments, thereby providing capacitance and resistance measurements during applied high voltage. It thus enables testing of DET sensors, actuators, and smart actuators of various construction types, allows comprehensive investigations on temperature and humidity impacts, and is not only specialized for long-term tests but also generally enables the acquisition of statistically relevant data for short-term tests. A more detailed elaboration on the motivation and objectives is given in Section 3.1 and Section 3.2.

3 Test Rig Development

This chapter elaborates on the development of the multifunctional test rig created within the scope of this thesis. Based on the literature review described above, the need for this innovation is first motivated, and the objectives are formulated. Subsequently, the design of the test rig is explained and an overview with details on construction, electronics and software is given. This is followed by an experimental validation and discussion of the test rig's control and measurement capabilities.

3.1 Motivation

The research and development (R&D) of DETs and their derivatives in the field of sensors, (smart) actuators and generators require comprehensive testing and electromechanical characterization procedures on several product levels ranging from the basic material, over transducer compound up to the system and application level (Figure 19a,b).

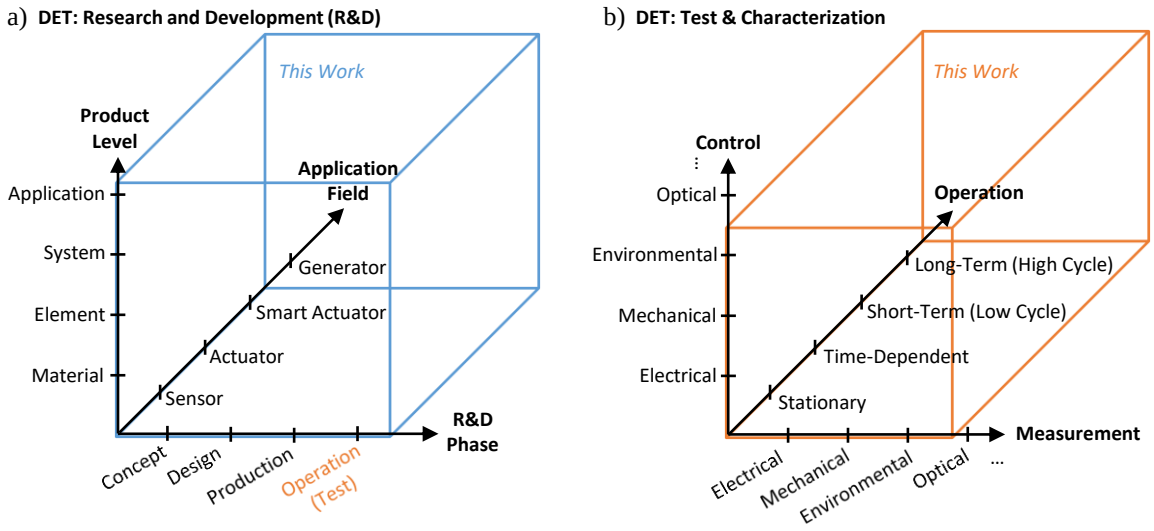

Figure 19: Overview of R&D phases, product levels, and application fields of DET technology (a), and corresponding control variables, measurement variables and operational conditions demanded for comprehensive electromechanical testing (b); with highlighted delineation of the scope addressed in this work.

The test focus varies depending on the respective R&D phase. In the concept and design phase, testing primarily aims at identification, evaluation, and improvement of mechanical, electrical, and electromechanical properties, i.e. to gain a fundamental understanding of transducer effects, ensure functionality, and optimize performance. For this purpose, individual short-term and low-cycle tests are usually sufficient. In contrast, for the production phase, the focus of testing shifts towards establishing, evaluating, and optimizing production processes, i.e. in order to ensure a specified quality, reproducibility, and production yield. Random short-term testing may be sufficient for established production processes. However, many products require 100 %-testing and characterization, i.e. to produce a sensor calibration data sheet. Moreover, the development and

evaluation of new processes requires statistical evaluation based on the results of numerous experiments. Particularly, after general product and process feasibility evaluation, reliability, long-term stability, and service life must be evaluated with respect to the respective application's operational and environmental conditions, by performing long-term and high-cycle tests. The specification of these attributes enables the assessment of product's applicability and direct comparison with competing technologies and products, which is essential for marketing purposes. By monitoring electrical, mechanical, and electromechanical properties during a long-term test, degradation and fatigue mechanisms can be investigated and the findings can be incorporated into product and process development. Resulting data can also serve as the foundation for condition and health monitoring algorithms, offering the potential to integrate further smart features into DET products.

For comprehensive electromechanical testing and characterization of DETs and their derivatives, there are currently no standardized test rigs available. The literature review (refer to Section 2.3) shows, that the standard test rigs and enhanced custom developed setups are mostly limited in their functionality, aiming at specific materials, construction types and application fields. They are mostly confined to either mechanically controlled, or electrically controlled experiments with either constant electrical constraint or constant mechanical constraint. However, mechanically controlled tests generally only enable a limited interpretation of the measurement results on the actuator characteristics, whereby electrically controlled tests only enable a limited interpretation on the sensor characteristics of DETs. Moreover, numerous complementary tests reported in the literature primarily focus on short-term evaluations without statistical analysis, whereas many long-term tests only gather limited complementary measurement data and mainly aim to assess service life. So far, only one test bench has been reported, that enables simultaneous mechanical and electrical control on multiple test objects with complementary electromechanical measurements under controllable operating and environmental conditions. It specializes in electromechanical fatigue testing of 15 out-of-plane operated DET types, by simultaneously controlling displacement and voltage, but measuring force, capacitance, and resistance sequentially, whereby force measurement can only be conducted in room-ambient conditions. Its operability is thus limited, particularly for investigating electromechanical properties under varying climatic conditions, short-term operational scenarios, and uninterrupted long-term conditions (refer to Section 2.3.3).

To date, no test rig has been proposed that provides both, flexibly configurable electrical and mechanical control, and corresponding measurement at multiple test stations in parallel for simultaneous electromechanical testing of different DET designs and applications, which is equally suitable for both, short- and (uninterrupted) long-term experiments, under different constant controllable environments. In particular, no such test rig has been reported that is capable of

simultaneously measuring electrical properties such as capacitance and resistance of DETs during the application of high voltage, i.e. to investigate the self-sensing properties of smart actuators.

However, as DET research becomes more application and process-oriented, there is a growing need for corresponding universal utilizable test rigs, with particular emphasis on accelerated acquisition of statistically relevant data and long-term testing, i.e. to evaluate reliability and lifetime performance.

3.2 Objective

The aim of this work is to fill the gap described above by developing the first multifunctional electromechanical test rig for DETs, providing comprehensive electrical and mechanical control and corresponding measurement on multiple test stations for simultaneous electromechanical testing of various DET types and applications, which is suitable to both short- and particularly uninterrupted long-term experiments under various controllable environments (Figure 20).

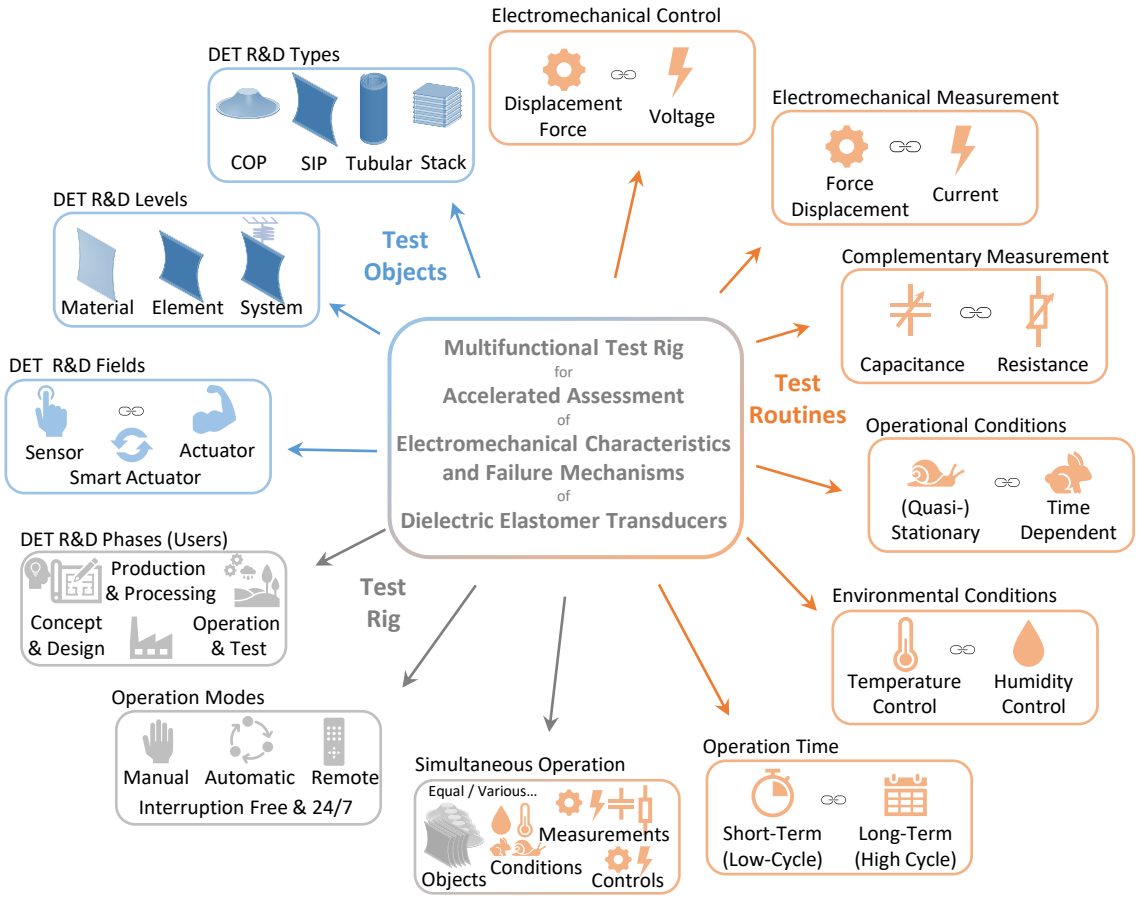

Figure 20: Overview of the objectives for the multifunctional electromechanical test rig for DETs under various controlled environmental conditions.

The test rig is intended to support scientists and engineers in a wide range of R&D phases, product levels, and application fields in bringing the technology to market maturity. It aims to enable the experimental investigation of fundamental electrical, mechanical, and electromechanical effects,

the experimental evaluation of DET product concepts and designs, as well as the evaluation of new production processes and the quality control of existing production processes. Application fields of interest are thereby ranging from pure DET sensors and pure DET actuators to smart DET actuator applications that utilize the self-sensing effect. The R&D levels of interest are ranging from basic material investigation over studies on transducer compounds up to the DET system level, i.e. with consideration of preload mechanisms. As the test rig is particularly aimed at application and process-oriented research, focus is set on uniaxially operated DET types such as COP, SIP, tubular or stack-DETs, which are common and promising variants in the field of sensors and actuators.

To serve the demanded application fields, both, mechanical and electrical control variables must be provided by the test rig, i.e. strain, stress, and (high) voltage. The respective mechanical and electrical measuring variables must be measured in response, i.e. stress, strain and current. Moreover, electrical properties such as dielectric permittivity or corresponding capacitance, and electrode resistance must be acquired simultaneously, also during high voltage actuation of the test samples. Control and measurement of all variables must provide high rates of generation and acquisition as well as synchronization to effectively study both, quasi-stationary operating conditions, and time-dependent effects. Demanding simultaneous continuous control and measurement of all variables must be provided, to enable highest freedom in the design of experiments. Moreover, all control and measurement variables should be able to operate in a wide temperature and humidity range to allow continuous investigation of the influence of different environmental conditions without interruption or manual intervention and modification of the test rig. All experiments must be adaptable to both short-term and long-term testing conditions. In order to obtain a maximum of statistically relevant data, full parallelization across several test stations must be possible without restrictions, e.g. controlling several test samples while simultaneously measuring the reaction of only one sample. Additionally, the aim is to test multiple samples or operating scenarios simultaneously, allowing the study of corresponding variations within a single test run under equal environmental conditions, to accelerate the acquisition of statistically relevant data. Long-term tests require uninterrupted operation over several days or weeks, which must continue even if no personnel are on site for monitoring, i.e. overnight or during the weekend. This requires automation of the test routines and monitoring of the test and safety statuses, as well as the possibility of remote access.

3.3 Concept

This section first outlines the overarching conceptual strategy that guide the development process of the test rig, discusses individual conceptual approaches based on it, and provides a comprehensive overview on the overall conceptual design and control.

3.3.1 Conceptual Strategy and Approaches

The conceptual strategy is guided by four fundamental principles, namely programmability, robustness, efficiency, and modularity. The conceptual approaches are systematically identified in accordance with these principles to meet the demanded requirements of the test rig, which is explained in more detail below (Figure 21).

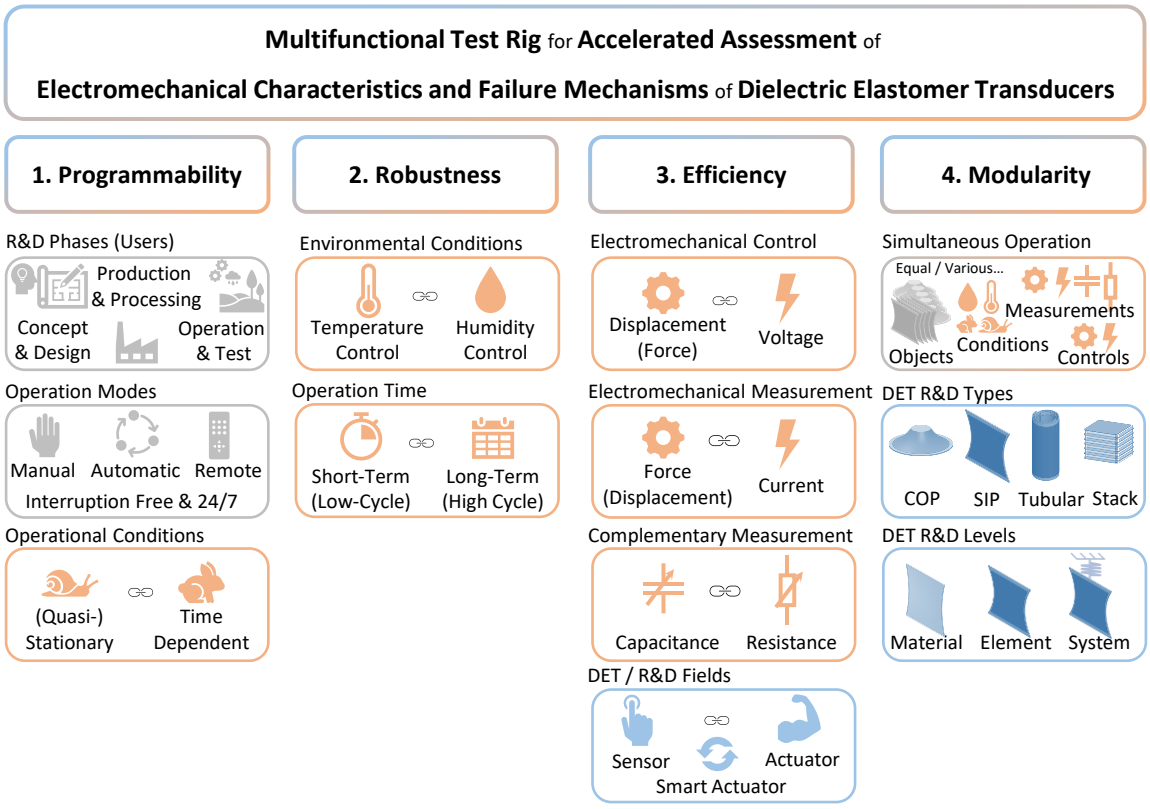

Figure 21: Overview on the conceptual strategy, which is based on four fundamental principles, namely programmability, robustness, efficiency, and modularity, and used to systematically derive conceptual approaches to fulfill the demanded requirements for the test rig.

Programmability

A fully programmable, digitally controlled test rig configuration offers many advantages in meeting the operational requirements: It provides maximum freedom in experimental design, including the ability to customize control trajectories for both, mechanical and electrical control in either quasi-stationary and time-dependent tests, as well as short- and long-term tests. Additionally, different test scenarios can be run in automated test sequences without the need for manual user intervention, resulting in less susceptibility to error and better timing and reproducibility of experiments. For long-term tests that cannot be personally monitored on-site, flexible digital

programmable control allows for event-driven status monitoring as well as automated control and remote control. Thus, in advancing concept and design, emphasis is placed on minimizing manual configuration of test scenarios while favoring programmable, configurable, and controllable sensor and actuator components equipped with interfaces designed for seamless integration into a unified digital control system.

Robustness

Generally, there are two conceptual approaches of testing DET objects under various environmental conditions: On the one hand, a climate chamber can be built around them in such a way that sensitive test rig instruments are located outside and shielded from the climatic conditions (Figure 22a). On the other hand, sensors and actuators can be installed inside of the climate chamber, if they can withstand the climatic test conditions (Figure 22b).

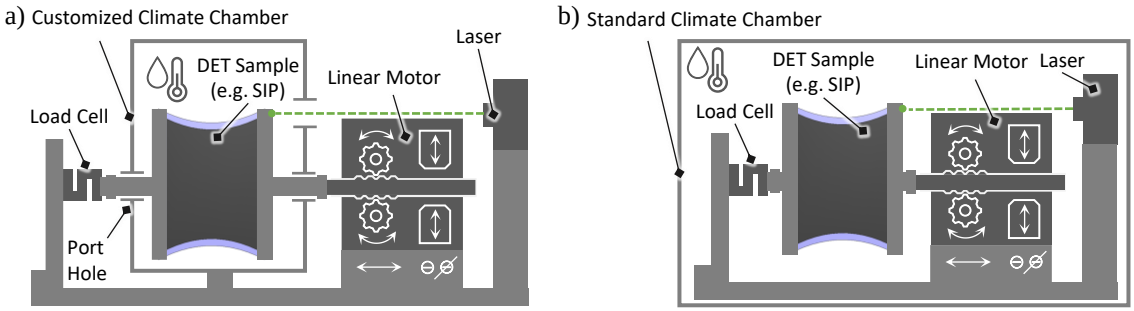

Figure 22: Comparison of concepts for testing DETs under different environmental conditions; with sensors and actuators outside the climate chamber, allowing the use of sensitive test equipment, but requiring a high degree of custom engineering (a), or with sensors and actuators inside the climate chamber, allowing the use of a commercially available climate chamber, but requiring robust test equipment (b).

The first approach potentially allows a very wide temperature and humidity range but is not pursued further as it requires a high degree of customized engineering, especially as moving parts have to be led out of the climate chamber and to be sealed against the testing environment.

The second conceptual approach enables the simple use of a commercially available climate chamber with programmable temperature and humidity profiles. However, in order to cover a wide range of climatic test conditions, sensor and actuator components must be selected for the test rig, that are robust against corresponding temperature and humidity levels. Components with non-integrated but external power-, instrumentation- and control units generally offer operation over a wider temperature range, as the electronics can be shielded from temperature, e.g., by installing them outside the climate chamber. This robust design approach is followed for the entire test rig by housing all electronics in control cabinets outside the climate chamber. Thereby cable routing in the climate chamber must be carefully managed to protect the cables from environmental conditions and to prevent crosstalk due to magnetic or electrical fields. With regard to robustness, all mechanical components, sensors, and actuators inside the test room must be selected to

withstand stationary and cyclic loads for long-term operation. In particular, the moving parts are selected to be wear-resistant and designed for facilitated maintenance.

Efficiency

Wear-related failure of test rig components is inevitable in long-term continuous operation, even with careful maintenance. Replacement of test rig components can be a costly and time-consuming process. Moreover, individual simultaneous control and measurement of each test sample results in a large number of sensor and actuator components, requiring large construction space and also cause high costs. An efficient conceptual test setup is therefore being identified, that is minimizing the required number of control and measurement variables, and the corresponding number of required sensor and actuator components (Figure 23). This is essentially based on 4 approaches:

- Simultaneous electromechanical control, but individual measurements.
- Proprietary impedance measurement methods.
- Focus on voltage and strain control.
- Proposal of alternative designs of experiments (DOEs).

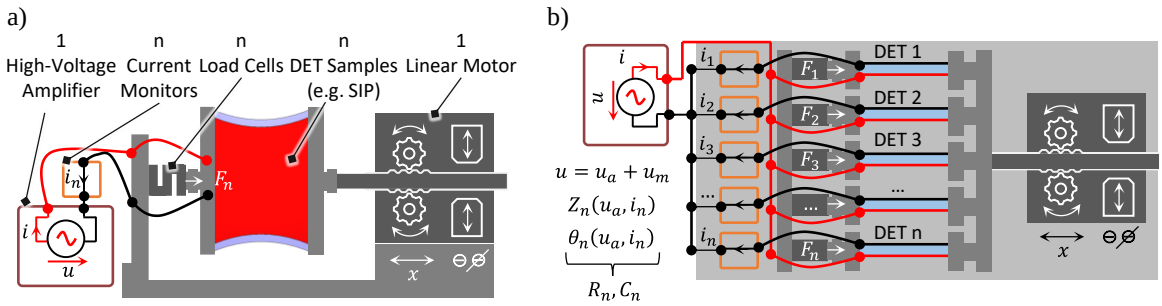

Figure 23: Efficient test setup concept, providing one linear motor and one high voltage amplifier, with dedicated load-cells and current monitors for simultaneous testing of multiple DET element test objects; from side-view perspective (a), and from top-view perspective (b).

Simultaneous Electromechanical Control with Individual Measurements

The conceptual setup comprises a programmable linear motor for continuous mechanical control (control variables x) and a high voltage amplifier for continuous voltage control (control variable u) of multiple (n) DET test samples in parallel. Apart from measuring the motor displacement with the motor internal encoder, there are no dedicated displacement measurements of the test samples provided, and only the individual forces F_n and currents i_n are measured via dedicated load-cells. This approach basically enables the simultaneous testing of several samples under the same operating conditions and individual evaluation of the test results for statistical evaluation purposes.

Proprietary Impedance Measurement Methods

Proprietary impedance measurement methods can be employed to determine impedance magnitudes $Z_n(u, i_n)$ and phases $\theta_n(u, i_n)$ and derive capacitances C_n and resistances R_n of the DET samples, utilizing the high voltage amplifier in combination with the current monitors. For

this purpose, the quasi-stationary high voltage actuation signal u_a for actuation is superimposed with an AC low voltage signal u_m. This method is common for self-sensing approaches of DET actuators (refer to Section 2.1.4). It enables parallel measurement of their electrical properties without the need for additional instrumentation in the setup. It also allows measurements to be made at high actuation voltages, a capability not available in commercially available instruments.

Voltage and Strain Control.

In general, the design enables simultaneous continuous control of the electrical voltage in combination with either displacement- or force control, whereby the superimposed impedance measurement always allows the resistance and capacitance properties of the samples to be investigated simultaneously. Due to the limitation that force-controlled tensile tests can only be carried out with respect to the sensor signal of one load cell, it is not possible to test several specimens in parallel with this type of test. Apart from this testing variant, all other tests can be carried out in parallel on all DET test objects at the same time. A tabular overview of the control- and measurement variables and their possible combinations demonstrates the testing capabilities of the proposed conceptual setup, if only displacement control and no force control is considered, to allow parallel testing on multiple DET samples (Table 1).

Table 1: Tabular overview over electrical, mechanical, and complementary control- and measurement variables and their possible combinations provided within the conceptual setup, demonstrating sufficient testing capabilities to fully characterize pure DET sensors, pure DET actuators and smart DET actuators.

Control \ **Measurement**	**A) Mechanical**: $\boldsymbol{F(t)}$ *Force*	**B) Electrical:** $\boldsymbol{i(t)}$ *Current*	**C) Combined:** $\boldsymbol{F(t), i(t)}$ *Force & Current*
1) Mechanical & Complementary $\boldsymbol{x(t), u_m(t)}$ *Displacement, Measuring Voltage*	$F(x, u_m)$ $\boldsymbol{F(x)}$	$i(x, u_m)$ $\boldsymbol{C(x), R(x)}$	$F(x, u_m)$, $i(x, u_m)$ $\boldsymbol{F(x), C(x), R(x)}$ ***Sensor***
2) Electrical & Complementary $\boldsymbol{u = u_a(t) + u_m(t)}$ *Actuation and Measuring Voltage*	$F(u)$ $\boldsymbol{F(u)}$	$i(u)$ $\boldsymbol{C(u), R(u), i(u)}$	$F(u)$, $i(u)$ $\boldsymbol{F(u), C(u), R(u), i(u)}$
3) Combined & Complementary $\boldsymbol{x(t), u(t) = u_a(t) + u_m(t)}$ *Displacement, Voltage*	$F(x, u)$ $\boldsymbol{F(x, u)}$ ***Actuator***	$i(x, u)$ $\boldsymbol{C(x, u), R(x, u), i(x, u)}$	$F(x, u)$, $i(x, u)$ $\boldsymbol{F(x, u), C(x, u), R(x, u), i(x, u)}$ ***Smart Actuator***

Therin all variables are defined as time-dependent, to emphasize that control and acquisition hardware is generally aimed to also study time-dependent besides quasi-stationary effects. From this table, the properties of a pure DET sensor are obtained by considering line 1, and are fully characterized in cell C1, only considering control of displacement and complementary measuring voltage, and the measurement of both, force and current, from which the capacitance is derived. In contrast, the properties of a pure DET actuator are obtained by considering column A, and are fully characterized in cell A3, only considering measuring forces in response to displacement control and voltage control. The properties of a smart DET actuator are obtained by considering line 3, or

column C respectively, and are fully characterized in cell C3, considering control of both displacement and voltage, and the measurement of both, force and current, from which the capacitance is derived. The remaining cells represent partial tests that aim at specific properties of DETs or their underlying materials. These considerations show that the proposed test setup offers sufficient capabilities for the complete characterization of multiple DET sensors, actuators, and smart actuator in parallel, despite the lack of individual displacement measurement and the exclusive consideration of displacement control and no force control. Particularly typical test scenarios for DETs, such as tensile tests, blocking-force tests, or dielectric breakdown tests, can be performed either under short-term or long-term conditions, with either quasi-stationary or time-dependent control.

Alternative DOEs

Tests can also be conducted to DET systems including the preload mechanism. In principle, no functional changes to the test setup are required for this purpose, as only the sample grips need to be adapted. For example, the DET actuator system can be investigated for their characteristic system force-displacement characteristics, using the linear motor for positioning (Figure 24a), or free-stroke measurements can be conducted to it, using the motor in blocking mode (Figure 24b).

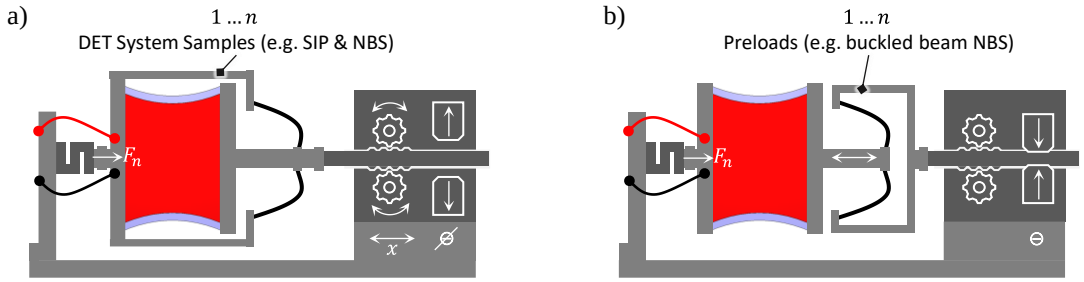

Figure 24: Conceptual test setup equipped with DET actuator system test objects, enabling to perform tensile tests, e.g. to identify the DET actuator system characteristic curves (a), or to conduct free stroke tests, which must be evaluated by force measurement (b).

Due to the lack of individual stroke measurement, free-stroke experiments must be evaluated by means of the force. For quasi-static operation, the corresponding stroke can be calculated using the force-displacement curves of the individual components within the DET system, as determined from the system design diagram (refer to Figure 8), assuming that the preload characteristics remain constant throughout the test. As these tests are of particular interest for long-term investigations, two possible DOEs are suggested, which enable a feasible evaluation:

A DET actuator system with physically installed preload-mechanisms can be tested with purely electrical control, enabling high testing rates and the investigation of dynamic effects (Figure 24b). In order to obtain interpretable results with respect to changes in the electromechanical properties of the DET using this approach, it is essential to ensure that the preload mechanism is fatigue resistant during long-term testing and that its force-displacement behavior remains constant.

On the other hand, for slower testing rates, the preload element must not be installed on the test bench, but the displacement-voltage characteristics known from the design diagram (refer to Figure 8) can be used to plan displacement- and voltage control trajectories in such a way, that they approximately match to the theoretical DET system behavior. With this HIL-approach, the preload element characteristic is simulated by the linear motor, ensuring that it maintains consistent mechanical properties throughout the test duration.

With these alternative DOEs, the proposed setup covers comprehensive capabilities for characterizing and testing DETs, thereby requiring a minimal amount of instrumentation. In particular, the elimination of dedicated displacement measurement contributes to the robustness of the test rig, as the corresponding optical sensors (e.g. laser position sensors) are often sensitive and prone to error in changing temperatures and humidity.

Modularity

The conceptual test setup introduced above is featuring a multi-channel (n-channel) design, which facilitates parallel testing of multiple test samples. This configuration is primarily intended to acquire statistically relevant data in an accelerated manner. Customization of the individual sample grips generally enables simultaneous testing of different DET test objects under the same environmental and operational conditions. However, different test objects (e.g. different DET types) rarely require identical control conditions. Hence, to test different test objects in parallel within their respective required control conditions, multiple similar setups (modules) can be run in parallel to enable different electrical and mechanical controlled operation at the same time. A holistic modular approach thereby integrates standardized, scalable, and interchangeable components, alongside with unified physical- and communication interfaces (Figure 25).

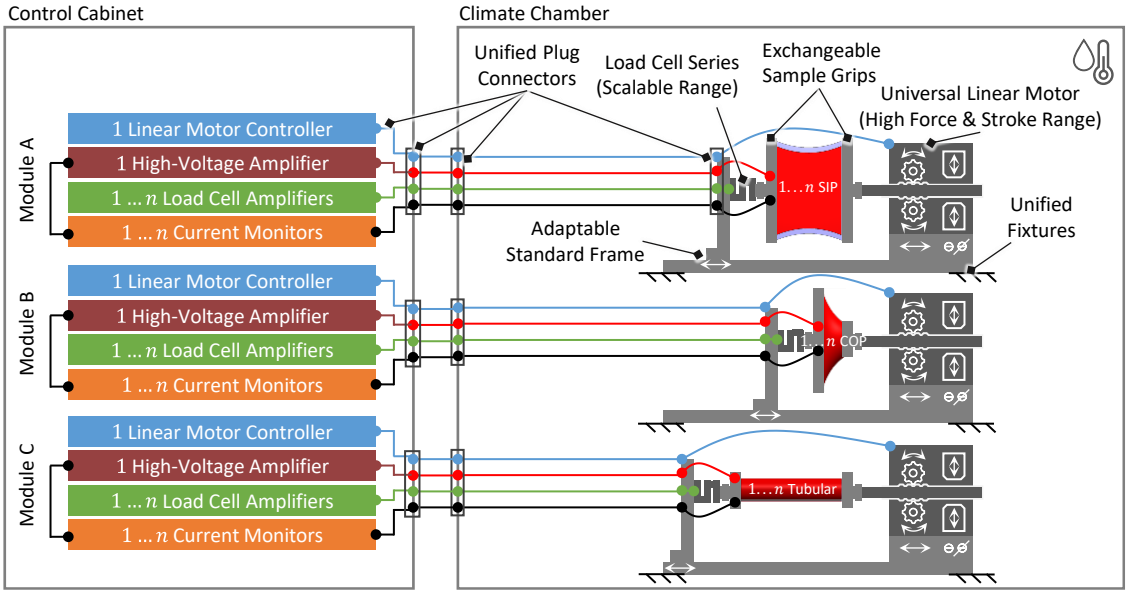

Figure 25: Modular test rig concept, featuring standardized, scalable, and interchangeable components and unified physical and communication interfaces, allowing to test different DET test objects in parallel within different operational and equal environmental conditions.

This approach enables the use of the generally identical setup design for testing different DET test objects in parallel, requiring modifications only to the sample grips. A compact design featuring standardized connectors and fixtures enables user-friendly maintenance, as well as test preparation and operation. Furthermore, simultaneous operation of multiple modules generally allows multiple force-controlled tests to be performed simultaneously under the same environmental conditions, thus satisfying the last open requirement.

3.3.2 Overall Conceptual Design

The specific overall conceptual test rig design is based on the above approaches and supplemented by additional features required for safety and fully automatic operation, as well as for calibration and validation of the proprietary implemented impedance measurement (Figure 26).

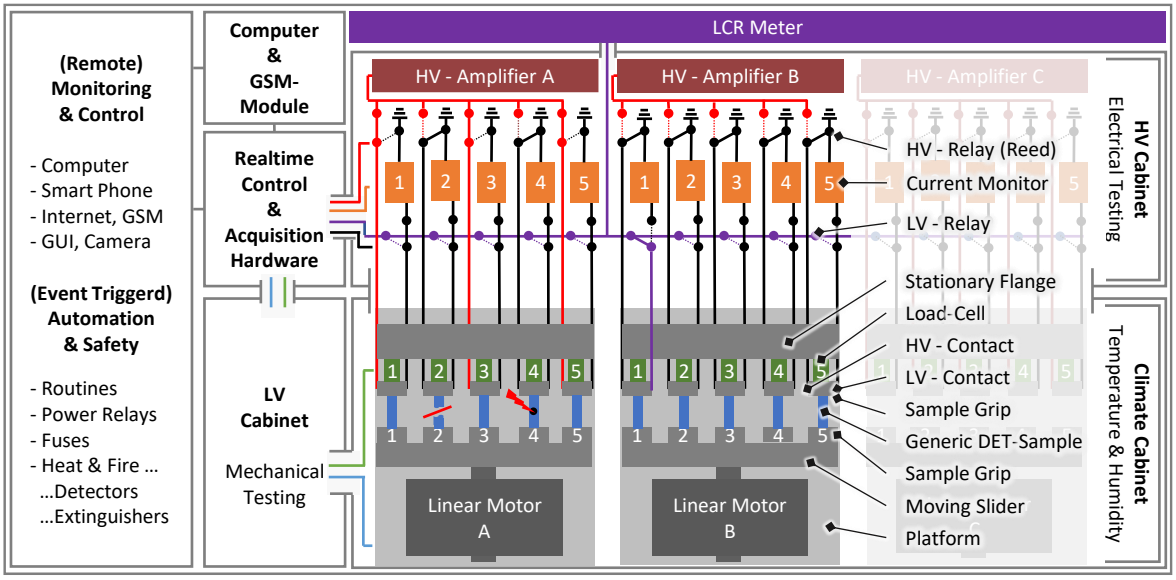

Figure 26: Overall conceptual design of the multifunctional electromechanical test rig for DETs, with module A configured for high voltage testing and module B for low voltage testing.

The basis of the setup is the climate chamber, that contains three test modules (module A, B and C) in its test room. The modules each consist of a rigid platform with a programmable linear motor and an opposing stationary flange to which five load-cells are mounted equidistantly. Each load-cell is equipped with a stationary sample grip. Together with its movable counterpart, which is mounted directly to the motor slider in opposite, the two sample grips form one test station (station 1…5). The stationary sample grip is equipped with two electrical contacts connected to high voltage cables, which serve to transmit, electric measurement and actuation control signals. Supply cables from motors and load-cells are routed to a control cabinet (LV-cabinet) outside the test chamber, where they are connected to their corresponding supply and control electronics. The high voltage cables are routed from the climate chamber to a separate control cabinet (HV-cabinet) containing electronics for voltage control, current measurement, and active signal routing. Thus, all electronic components are located outside the test room and not exposed to any harsh climatic test

conditions. In addition, the high voltage electronics are electrically isolated from the rest of the electronics to prevent crosstalk from electric or magnetic fields.

A closer look to the HV-cabinet shows, that one electric contact (HV-contact) of each test station is connected to the common high voltage amplifier of the module via a separate controllable reed relay (HV-relay). This can be operated during applied high voltage, switching the test station to ground. The opposite electric contact (LV-contact) of each test station is connected to a separate current monitor via a separate standard relay (LV-relay). This can only be operated when no high voltage is applied, switching the test station to a common LCR-meter.

To achieve high data rates as well as transmission stability and synchronization, the entire control and measurement electronics are connected to a real-time capable control and data acquisition system, that provides deterministic timing and low jitter. This in turn is connected to a conventional host computer, which enables (user-) control of the real-time system, as well as management of (post-)processing and data saving routines. Together with an additional control-module connected to the Global System for Mobile Communications (GSM), it also enables remote monitoring and control with a second computer or smart phone via the Internet or GSM-network. Moreover, IP-capable cameras, e.g. directed at the test room and the entire setup, enable visual surveillance.

The test rig concept incorporates numerous event-driven and passive safety devices. These include programmable power relays connected to the main power supply that allow automatic or remote shutdown. Arc-fault protection switches and lead fuses allow local or collective disconnection of power in the event of electrical faults. Fire detectors and automatic fire extinguishers detect flames, heat, and smoke and trigger relays to switch off power and extinguish flames in the event of a fire. All safety and fire protection devices are aimed to also report an alarm via the GSM-module if they are triggered, ensuring that operators are notified immediately to take further action.

3.3.3 Overall Conceptual Control

The conceptual control of the test bench generally provides two different modes of operation, namely manual mode, and experiment mode (Figure 27a). Manual mode enables the configuration of all individual control variables, e.g., for functional tests, or the configuration of starting conditions for test routines. Experiment mode enables the programming of several (n) sequentially running test routines and their multiple (m-fold) repetition, whereby a distinction is made between high voltage test programs (HV-testing) and low voltage test programs (LV-testing).

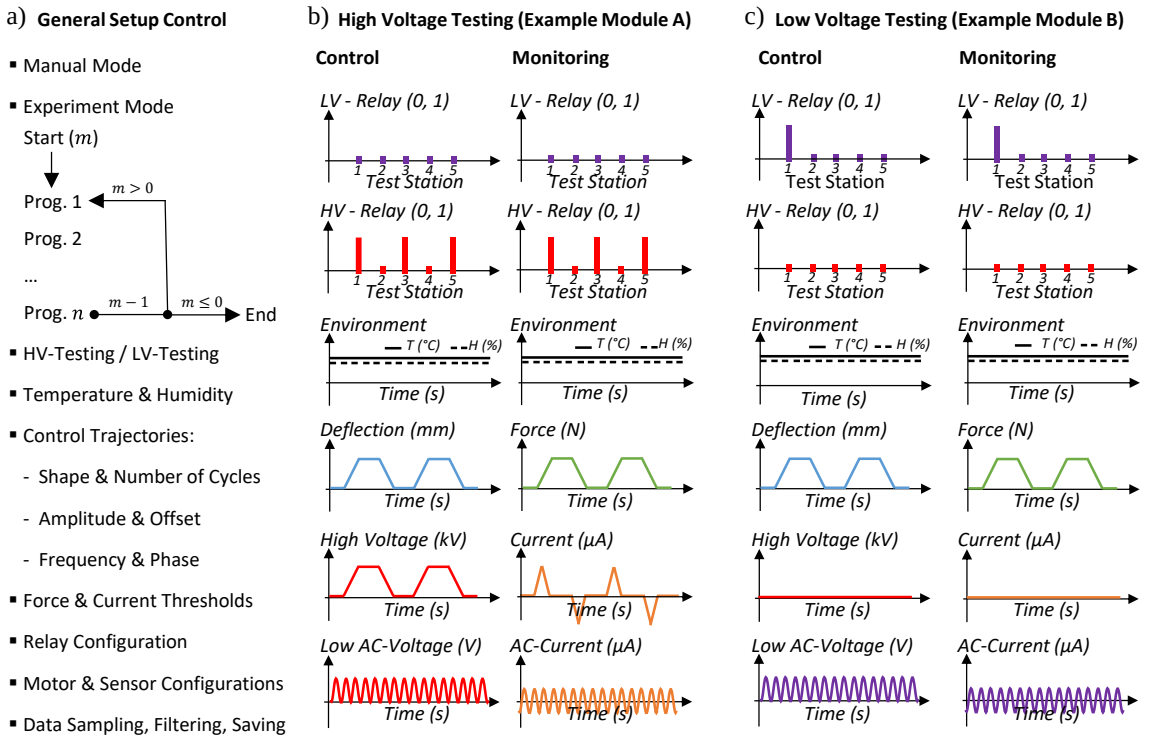

Figure 27: Conceptual control- and monitoring variables of the multifunctional electromechanical test bench for DETs (a), with distinction in high voltage testing (a), and low voltage testing (b).

High Voltage Testing

For high voltage testing (Figure 27b, referring to module A in Figure 26), up to five DET samples can be simultaneously subjected to a voltage waveform provided by the common high voltage amplifier with each test module, and the individual current can be measured with the respective current monitor. Simultaneously, all test objects can be deflected by the respective motor with the same displacement trajectory and the individual reaction force can be measured via the respective load-cells. Voltage waveforms and displacement trajectories are synchronized and can be configured in terms of shape, amplitude, offset, frequency, and phase, as well as the number of stimulation cycles. A sample defect, such as a mechanical tear through (e.g. test station A2) or an electrical breakdown (e.g. test station A4), is detected via permanent force and current measurement and comparison with configurable threshold values. In this event, the relevant HV relay is automatically disconnected from the high voltage amplifier, and the sample is discharged to ground to prevent fire damage or voltage supply collapse, thus avoiding induced crosstalk to the remaining intact samples.

In addition to testing the DET actuators with continuous waveforms of relatively slow rates, the high voltage amplifiers and current monitors are also used to measure the resistance and capacitance of the samples by employing proprietary impedance measurement. For this purpose, a high-frequency control voltage with low voltage amplitude (small signal) is generated with the high voltage amplifier and the individual current signal is measured at the respective test station.

Impedance is calculated from both signals and used to determine resistance and capacitance of the sample on a model-base. Modulation of the small signal to the quasi-stationary high voltage actuation waveform also enables measurement with applied and continuously varying high voltage stimulation for (smart) DET actuators. Another advantage of this method is, that the impedance of all samples can be measured simultaneously, as a separate current measurement is obtained for each sample. In this way, time- or stimulation cycle-dependent effects (e.g. training effects) can be investigated simultaneously on all samples for accelerated acquisition of statistically significant data. However, compared to conventional LCR-meters, a higher measuring voltage is required with this method, and a lower measuring accuracy and a limited measuring range are achieved.

Low Voltage Testing

Therefore, during low voltage testing (Figure 27c, referring to module B in Figure 26), the samples (e.g. test station B1) can be switched individually to a common standardized LCR-meter via the low voltage relays, if they have previously been disconnected from the high voltage amplifier and discharged to ground. This enables particularly precise low voltage impedance measurement over a large measuring range. It can be used in particular to characterize low voltage operated DET sensors, and as a reference and calibration option for the proprietary implemented impedance measurement methods. However, as the samples can only be measured consecutively and not simultaneously, this method is only suitable to a limited extent for the simultaneous characterization of multiple samples and the determination of time- or stimulation cycle-dependent effects. This applies in particular if a displacement excitation occurs during the measurement that is also experienced by the other samples on the same module. To avoid this, only one sample per module can be installed, so that the displacement excitation can be controlled individually, allowing three samples to be tested consecutively within the same environmental conditions. Fully equipping a module with test samples is useful if random measurements are conducted between large time or control cycle intervals, so that the measurement time or number of measurement cycles is negligible, e.g., for long-term and fatigue tests.

3.3.4 Conclusion on Test Rig Concept

The overall conceptual strategy that guides the development process of the test rig is based on four guiding principles, namely programmability, robustness, efficiency, and modularity.

Based on this strategy, a low-maintenance and modular design is derived, comprising programmable and durable components resilient to wear and harsh environments. With control and measurement electronics installed in separate control cabinets, this enables testing within harsh environmental conditions inside the test room of a standardized climate chamber. Efficiency and robustness are enhanced by minimizing the utilization of wear- and climate-sensitive components. This includes controlling multiple test samples simultaneously with just one control unit, utilizing proprietary impedance measurement without requiring additional test instruments, and eliminating

the need for individual displacement measurement for each test station by proposing alternative DOEs to maintain full testing capability.

The conceptual design features the following key properties:

- Simultaneous electromechanical testing of 15 DETs within various controlled environments
- Modular design with 3 individual test modules, equipped with 5 test stations, each:
  - Standardized interfaces enable adaptation to several DET types
  - Individually configurable strain and voltage control for each module.
  - Individual force and current measurement for each test station.
  - Individual capacitance and resistance measurement for each test station.
  - Individual electrical and mechanical failure detection and shutdown mechanisms.
- Simultaneous control and measurement of all test variables in parallel across all test stations.
- Fully automatic operation with programmable, sequential, and repeatable test routines.
- 24/7 continuous operation with remote control, automatic safety measures and fire protection.

Providing that quantitative specifications are met, the concept presented in this section enables comprehensive electro-mechanic test and characterization of various DET types within controlled constant environmental conditions, with focus on accelerated assessment of statistical relevant data for either short-term and particularly for long-term experiments.

3.4 Design and Construction

The test bench concept refers to uniaxial operated DETs in general but does not consider any specific design variant. However, it is constructed in such a way that only the sample grips need to be specifically adapted to the respective design variant, and thus minor changes to the overall setup are required. For demonstration purposes, the test rig design presented below is adapted to rectangular DETs that are operated perpendicular to their thickness direction and are therefore referred to as strip-in-plane DETs (SIPs). In this section, the design and manufacturing of the exemplary test samples is first introduced, before the construction of the test rig is explained subsequently.

3.4.1 Test Sample

The SIP test sample is designed to showcase the testing capabilities of the test rig developed within the scope of this work, thus required to be investigated within a wide range of test scenarios, aiming to observe various typical electromechanical phenomena of DETs. The corresponding design and the tailored manufacturing and assembly processes are explained in the following.

Design

The SIP test sample is based on a PDMS film (*Elastosil 2030/20*), that is screen-printed on both sides with CB-PDMS-based electrodes (Figure 28a). The T-shaped facing electrodes are arranged in mirror symmetry. They form a rectangular sandwich structure in the center, which represent the electromechanically active area, and two electrical contact surfaces on each side (Figure 28b). Those are not part of the electromechanically active area, to prevent the mechanical and electrical contacting from affecting the electromechanical properties of the transducer.

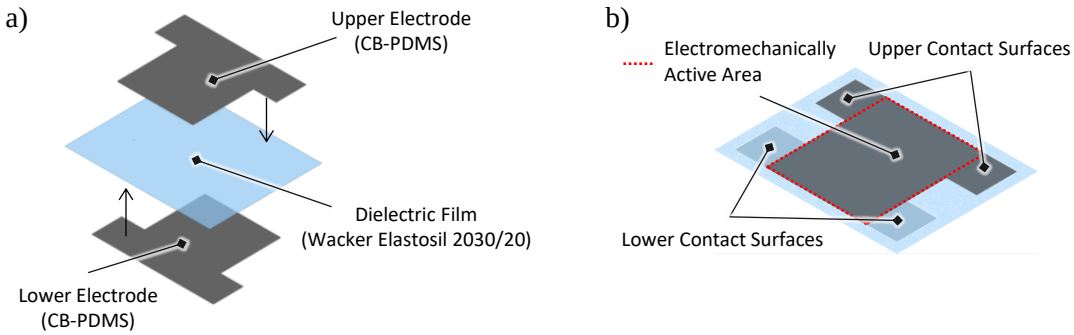

Figure 28: CAD Design of SIP film and electrode shown as explosion (a) and compound (b).

The SIP is provided with two rigid fixtures on the opposite edges perpendicular to its working direction, both serving for mechanical and electrical connection. To prevent adhesive bonds from altering the material properties of film and electrode, a force-fit connection is implemented, with each fixture consisting of a pair of T-shaped solid clamping bars in between which the film is clamped via screw clamping (Figure 29a). The aspect ratio of the mechanically and electromechanically active areas in between the clamps is deliberately chosen to neither result in uniaxial nor pure shear behavior of the SIP, as these are special cases in which the necking effect in particular cannot be observed for demonstration purposes (Figure 29b).

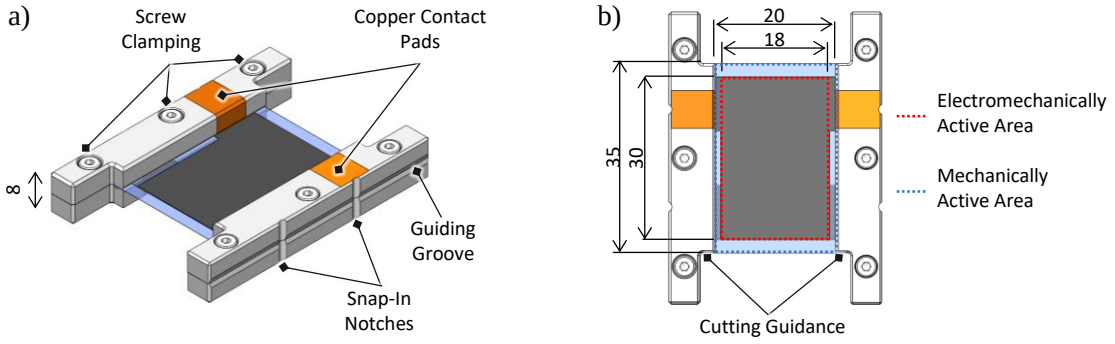

Figure 29: CAD Design and dimensions of SIP provided with clamps in a 3D perspective (a), and top view perspective (b).

The width of the narrow clamping part exactly corresponds to the width of the SIP, so its lateral edges serve as cutting guidance, which is used to cut the exposed edges of the SIP free. The wider

rear part of the T-shaped clamps provides the screw connection with the screws in the upper and the recessed nuts in the lower clamp (Figure 30a). The back side of the clamp is provided with a longitudinal guiding groove and two transverse snap-in notches, which serve to guide and fix the sample to the sample grips of the test rig (refer to Section 3.4.2). Dimensions and insulation distances of the SIP are designed to tolerate production variations, and thus reduce the risk of failure under electromechanical load: A 1 mm gap between the electromechanically active area and the clamps prevents compression of the active electrode-elastomer sandwich, reducing the risk of localized electric field increase and potential failure during high voltage actuation. Furthermore, an insulation distance of 2.5 mm between electromechanically active area and free SIP edges prevents high actuation voltage from jumping across the exposed edges due to ionization of the air. The clamps are manufactured based on a temperature-resistant epoxy material (*Formlabs High-Temp Resin*) using a highly resolved stereolithographic printing process (*Formlabs Form3* Printer). They provide a well-defined surface pressure, controlled by the tightening torque of the screws used to assemble the clamping pair. To obtain a homogeneous outgoing clamping pressure, which follows a straight horizontal line, the narrower frontal part of the T-shaped clamps is provided with a well-defined tongue-and-groove structure within the clamping surface, with tongue at the upper clamp and groove at the lower clamp (Figure 30a, b).

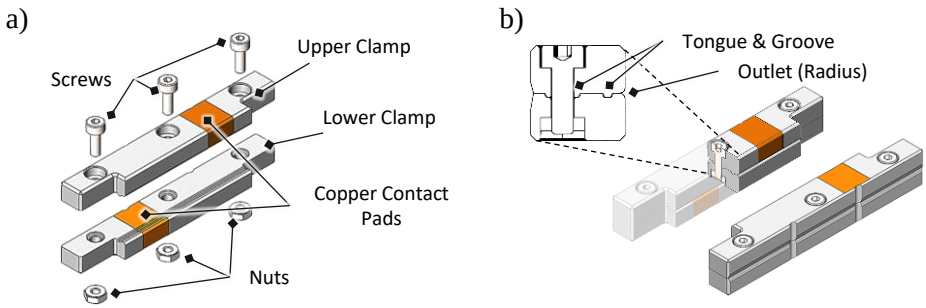

Figure 30: CAD design of SIP clamps in exploded view (a) and assembly with details of tongue and groove assembly in cross-sectional view (b).

The through holes for the screws are also provided with tongue and groove structures in the clamping surface, to prevent twisting and tearing of the film when through piercing and tightening the screws. Furthermore, to avoid shearing of the clamped film over sharp edges, the clamping outlet on the frontside of the clamps feature a defined and smooth fillet radius. Rectangular recesses are provided within the clamping surface, into which self-adhesive copper strips of similar dimension are embedded. They are flush with the inner clamping surface and lead over the frontal face to the outer side of the clamp, to provide an electrical contact pad. When clamped together, the surface of the copper strips is firmly pressed onto the SIP's imprinted electrode contact surface, ensuring robust electrical contact, with the tongue-and-groove connection also providing a reliable strain relief.

Screen Printing Process

Screen printing as a manufacturing process itself generally offers high precision and reproducibility. However, since two opposite sides of the specimen are printed consecutively, they must also be exactly aligned with each other. For this reason, the PDMS films are fixed on rigid rectangular metal frames before printing to ensure facilitated handling (Figure 31a). In the operating direction of the SIP, which corresponds to the squeegee direction of the screen printer, a defined pre-stretch of ~10 % is applied to achieve a reproducible and high-quality print pattern (Figure 31b). The direction perpendicular to this is not pre-stretched, to minimize the mechanical stress peaks in the rigidly fixed edges of the SIP due to transverse stretching. After this preparation, 3x4 SIP electrodes are printed on one side of the pre-stretched film in one printing pass and then cured at 150 °C for 10 min (Figure 31c). The mirror-symmetrical electrode design of a single SIP, as well as the print pattern allows the same screen to be used for both SIP electrodes. This enables convenient and particularly accurate alignment and thus reproducibility by simply rotating the metal frame by 180 ° (Figure 31d), to print the second (facing) electrode on top, which again is cured at 150 °C for 1 h (Figure 31e).

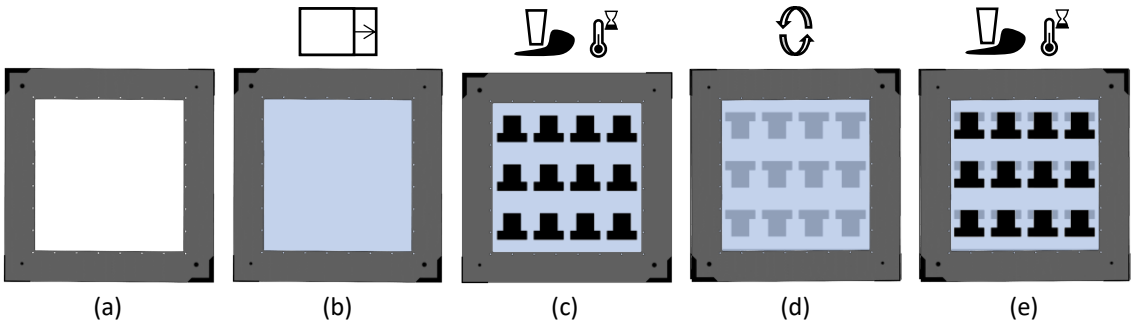

Figure 31: Schematic illustration of the step-by-step screen-printing process starting with a metal frame (a) which is provided with a pre-stretched PDMS film (b), printed, and cured with the first electrode (c), flipped (d) and finally printed and cured with the opposite electrode (e).

Assembly Process

To maintain the safety distances between the electrode and the clamps, or the electrode and the exposed edge of the SIP respectively, a systematic and repeatable procedure for the assembly is developed. A 3D-printed assembly stencil made of grey polyethylene terephthalate (PETG) is fabricated as an assisting tool for assembling the samples. Its design is based on the footprint of the screen-printed layout with 3x4 patterns, as well as the dimensions of the metal frames on which the film is mounted. The stencil contains 24 positive recesses for the lower clamping elements, two of which are arranged in mirror-symmetrical pairs with a fixed spacing of 22 mm. 3D-printed soft cutting pads made of thermoplastic polyurethane (TPU) with a thickness of 1 mm are applied to the area in between these pairs (Figure 32a). The procedure developed for assembling the SIPs using this assembly stencil comprises four steps. First, all lower clamps (orange) are inserted into the recesses of the assembly stencil (grey) so that their clamping surfaces face upward and are flush with the surface of the TPU cutting pads (blue) (Figure 32b). In the second step, the metal frame

with the screen-printed film is aligned on the assembly stencil to center the electrodes of all samples vertically and horizontally between the clamps (Figure 32c). Attention is also paid to ensure that the lower electrode pads are in contact with the corresponding copper contacting surfaces of the clamps. When aligned properly, the film is firmly pressed against the TPU cutting pads and adheres to them, thus remaining in a fixed position. In the third step, the upper clamps are screwed to the lower clamps so that the film is clamped in between them (Figure 32d). Before and during screwing, the upper clamps are firmly pressed onto the lower clamps with the finger and automatically align themselves properly due to the tongue and groove structures in the clamping surface. The screws are then pushed through the through holes and pierced through the film in between the clamps until they contact the thread of the lower clamp. They are then tightened with a torque wrench with 0.2 Nm, always starting with the inner screw. This is carried out consecutively for each pair of clamps, starting from the edge of the assembly stencil towards the center, in order to achieve homogeneous deformation of the film. In the last step, the now clamped specimens are cut free (Figure 32e).

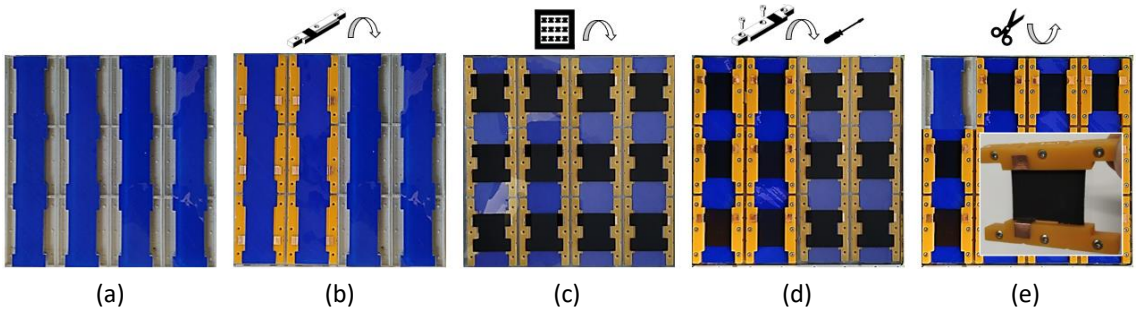

Figure 32: Assembly process starting from assembly stencil provided with TPU-cutting pads (a), putting lower SIP clamps in its recesses (b), aligning metal frame with printed elastomer film on top (c), fastening upper clamps by torque-controlled screwing (d), and cutting out samples (e).

For this purpose, the exposed edges of the SIP are first cut free with a sharp custom-made blade, which is of a rectangular shape with a length of 26 mm. This allows it to be guided from above past the cutting edges of two opposing clamps, and pressed vertically onto the film until both the film and the TPU cutting pad are cut straight through. As a result, the exposed edges of the SIP exhibit defined high-quality cutting profile without fringes that can cause a tear propagation when subjected to mechanical stress. The remaining edges of the clamp are then cut free by hand using a surgical scalpel. Finally, the individual SIP samples can then be removed from the assembly stencil and be used for testing.

3.4.2 Test Rig

Design, construction and wiring of the test rig are described below, starting with an overview of the exterior setup, followed by the modular setup that is implemented in the test room. The focus is then placed on a single test module and finally on the sample grips, which are specially designed for the exemplary developed SIP samples.

Exterior Structure

The test setup is built around the climate chamber (*CTS C-70/350*). It provides temperature control within $-70 \ldots 180\,°C$ and climate control within $10 \ldots 95\,°C$, thereby comprising relative humidities within $10 \ldots 98\,\%$ [160]. Host computer, electronic cabinets and safety components are installed on a peripheral structure made of aluminum profiles, which is form-fitted around the left and rear sections (Figure 33).

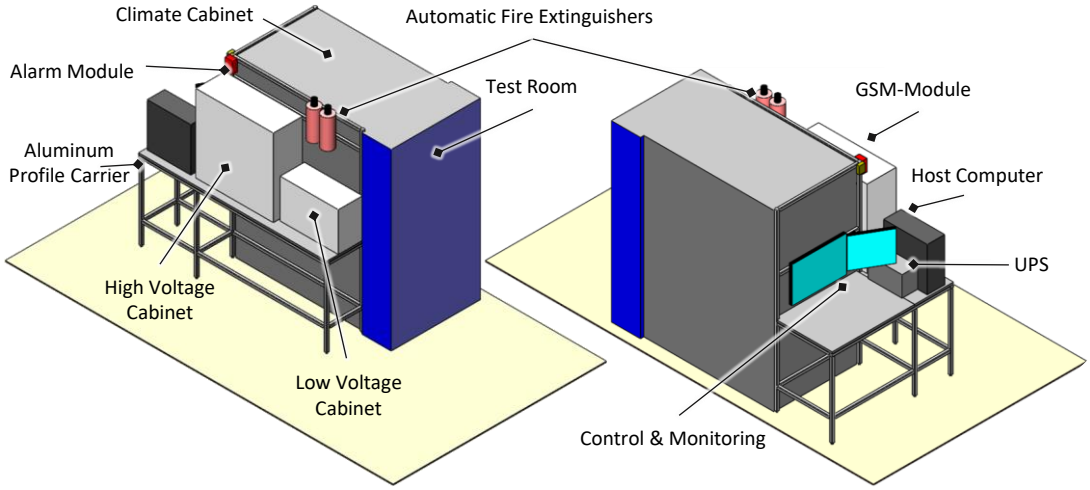

Figure 33: Exterior setup CAD-design front (left) and rear (right).

Two remotely accessible IP-based cameras (*D-Link DCS-2330L*) are directed to it, one to the electrical cabinets and one to the test room window (Figure 34).

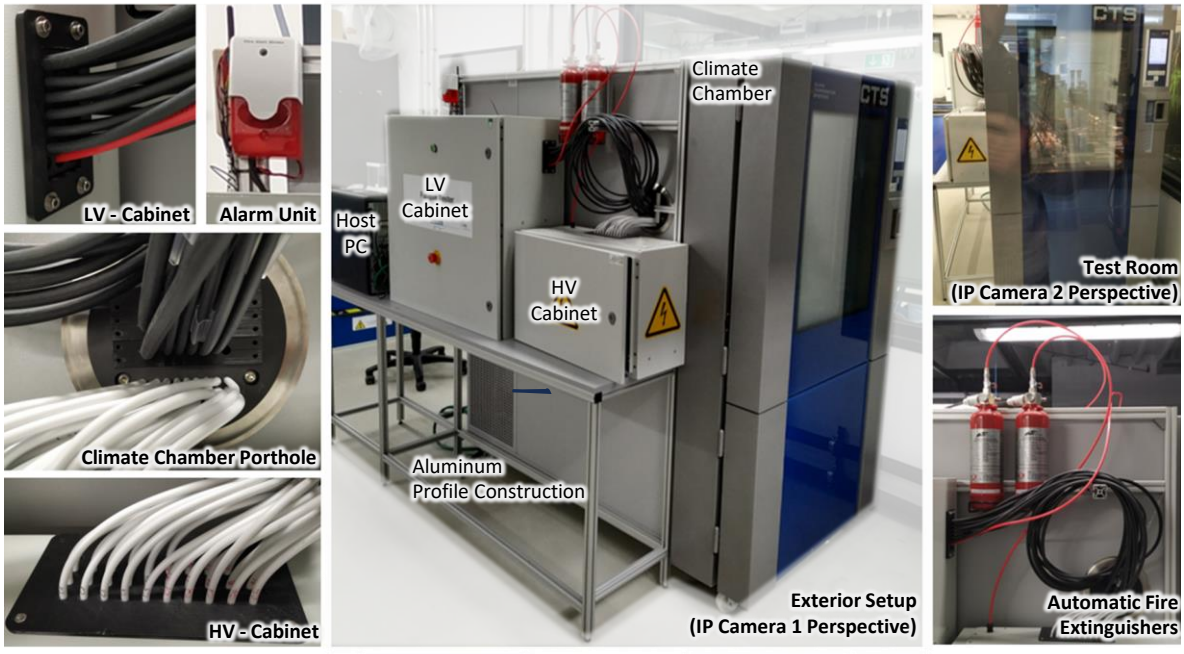

Figure 34: Exterior setup from IP-camera 1 perspective (mid), IP camera 2 perspective with closer look into to the test room window (upper right), as well as detailed view to automatic fire extinguishers (lower right), cable management and visible/audible alarm unit and GSM-Module (left).

Two automatic fire extinguishers (*SAE FALCON DLP*) are installed between the control cabinets, from each of which a hose is fed into one of the cabinets. These hoses passively burst on contact with a heat source and emit a gas (*HFC 227ea*), extinguishing the fire locally without causing additional damage. Moreover, each control cabinet is equipped with a heat and smoke detector (*Gira Dual Q*), which is triggered in the event of smoke development or overheating. Each fire extinguisher and heat/smoke detector come with event-controlled relays that are activated when one of these safety devices is triggered. The relays are connected to a GSM-module (*WiLARM FIVE GSM*), featuring digital inputs and outputs as well as programmable switching relays. Those trigger the main power supply relays as well as a visible and audible alarm unit in the event of error or fire. Computer and safety equipment are all connected to an uninterruptible power supply (*UPS*), which takes over the supply in case of power fluctuations and failure of the main supply, so that all safety-related measures are maintained. High voltage cables, as well as control and measuring cables from the respective control cabinets are shielded against electric and magnetic fields and are guided in a well-organized manner with a customized and sealed guide through the porthole of the climate chamber into the inner test room of the climate chamber.

Interior Structure

From interior perspective, the test rig comprises three identical test modules, guided on aluminum rails, and mounted on a common stainless steel plate using aluminum mounting angles (Figure 35).

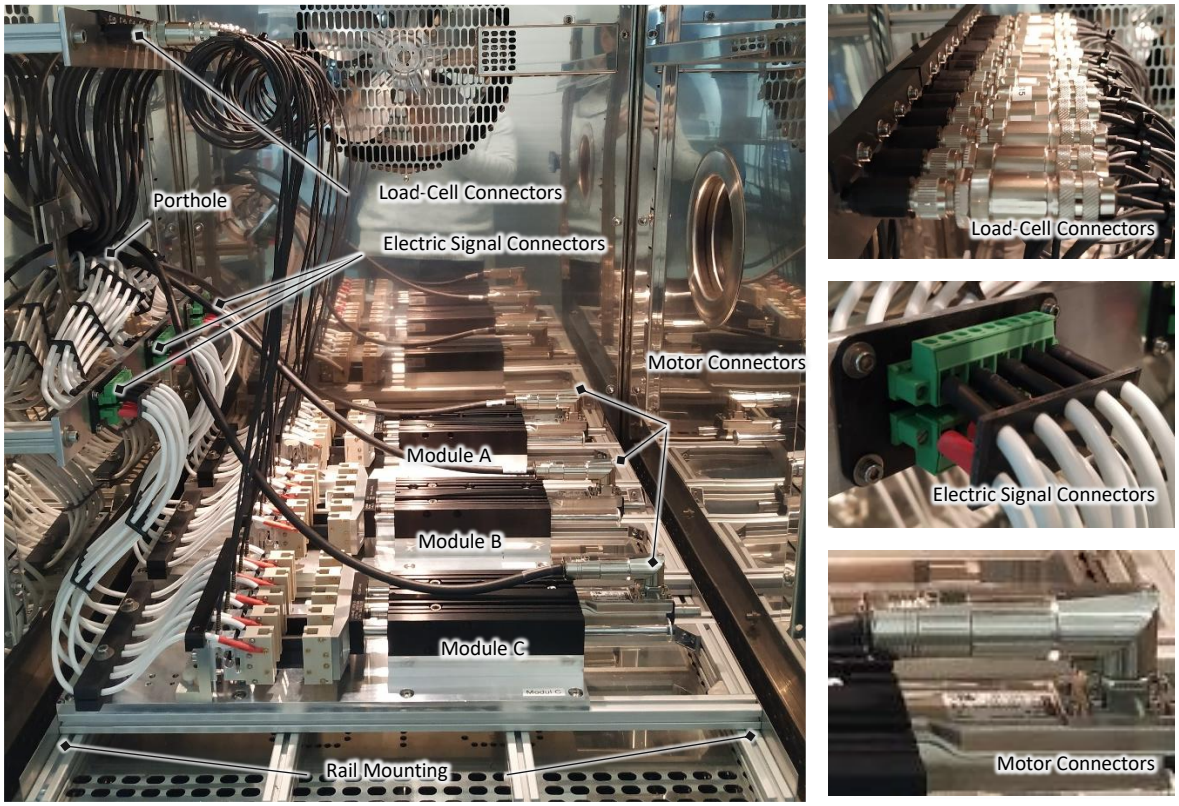

Figure 35: Photo of the test room, in which three test modules are mounted on a common stainless steel base plate via aluminum guiding rails and mounting angles (left); with detailed view to the cable management and connector plugs (right).

The common base plate is form-fittingly installed into the test chamber with the help soft and temperature-resistant polymeric buffers, which passively damp vibrations induced by climate compressor or motors. Cables passing through the porthole of the climate chamber are distributed on rail fixtures, attached to the left side wall of the test room. Thereby, the electrical connections belonging to the individual test modules are combined in bundles with pluggable connectors. This allows the test modules to be easily removed and reinstalled e.g., for maintenance purposes, which occur regularly, especially with long-term tests, e.g., for lubricating the bearings of the linear motors.

Test Module

The foundation of each module is an aluminum base plate fixed to an aluminum profile frame, through which the module can be mounted to the common steel plate in the climate chamber (Figure 36).

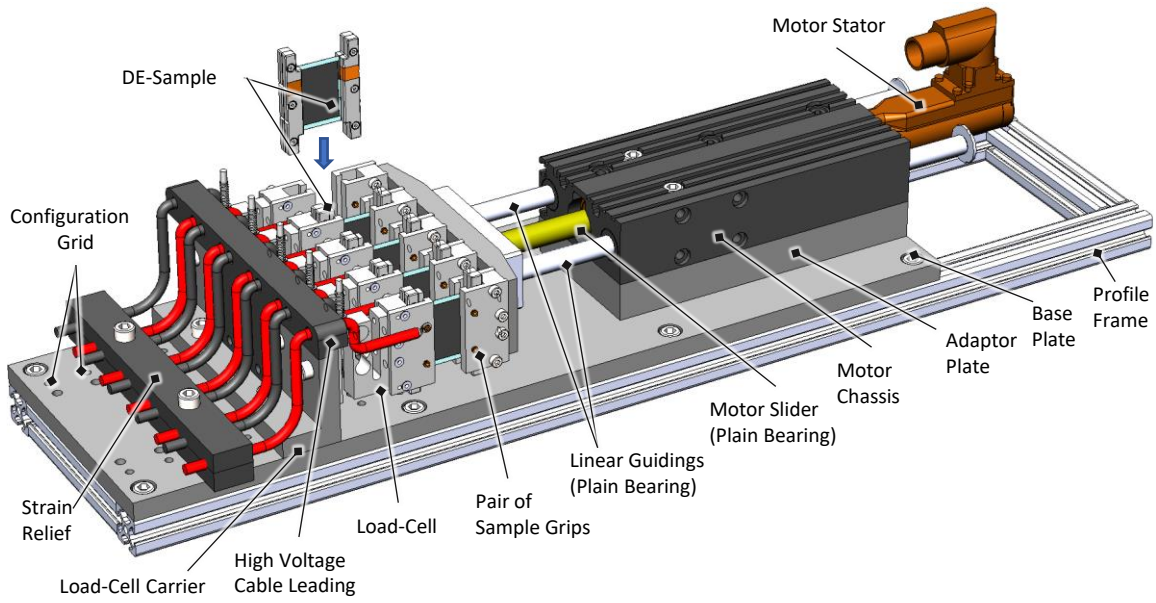

Figure 36: CAD design and description of a single test unit with five test stations on which five exemplary SIP samples are installed.

A programmable linear motor (*LinMot PS01-23x160H-HP-R*) equipped with an H-shaped linear guide (*LinMot H01-23x166/80*) is mounted slightly elevated on the right side of the base plate via an aluminum adaptor plate. The combined linear drive offers a stroke range of up to 80 mm and is designed to generate relatively large static forces of up to 138 N and velocities up to 5.2 m/s [161], [162]. Despite this, it maintains a low moving mass of only 610 g, making it suitable for dynamic operations, such as high-cycle and high-rate tensile tests. The motor is certified to IP67, thus dust-tight and safe against splash water and occasional submersion. This feature, combined with a maximum permissible operating temperature of 120°C, makes it particularly suitable for testing in harsh test environments. Its cylindrical guidings are equipped with low-wear, smooth-running plain bearings that require little maintenance other than occasional re-greasing and can be

easily replaced in the event of a defect. Five identical DET sample grips are attached to the slider output side of the motor via a common aluminum motor flange, which is also designed to be lightweight so as not to significantly increase the moving mass. On the opposite side of the motor, identical sample grips are attached mirror-symmetrically via individual load-cells (*ME-Meßsysteme KD40s*) to an angled aluminum carrier. These load-cells are suitable for measuring tensile and compressive forces in the range up to 10 N with 0.1 % accuracy [163]. They are specified for a temperature range of -10°C to +85°C and are certified to IP65, hence dust and splash-proof and thus well suited for harsh test conditions as well. The aluminum load-cell carrier can repeatably be fixed to the base plate at various distances from the motor using a 20 mm hole grid. On the one hand, this allows longer DET samples to be tested. On the other hand, samples of the same length can be tested within different active areas of linear motor and guiding, which distributes the wear of these parts and makes the test setup more durable.

Sample Grips

The opposing DET sample grips are constructed in a two-part structure and consist of an L-shaped and a U-shaped part milled from polyetheretherketone (PEEK), a polymeric material that has particularly high rigidity, as well as temperature and humidity resistance and provides in addition good electrical insulation (Figure 37).

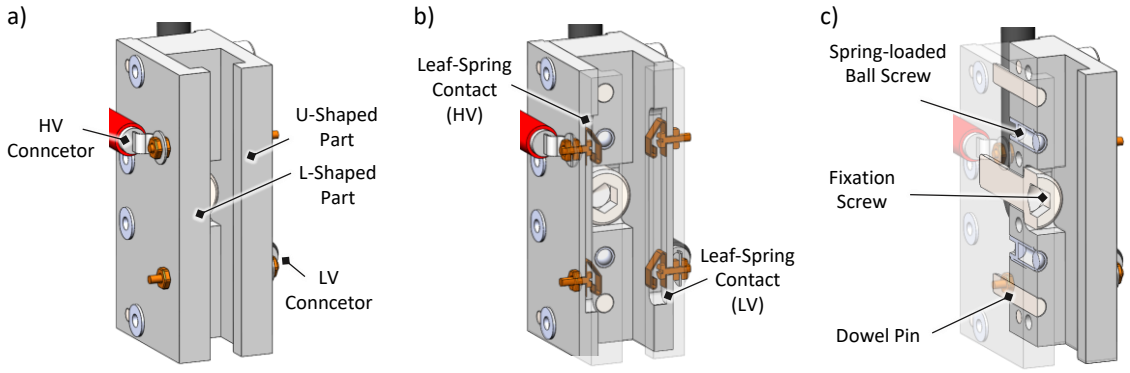

Figure 37: CAD design of DET sample grips with electrical leaf spring contacts and mechanical lock-in mechanism via spring-loaded ball screws as an overall 3D view (a), with frontal cross-section view (b), and with lateral cross-section view (c).

The two parts are aligned with dowel pins and screwed together to form a sample grip unit, which exhibits a slot-shaped insert for receiving the SIP sample. This is backed with two further dowel pins, and a fixation screw for attachment to the corresponding load-cells, or motor flange. Furthermore, two spring-loaded ball screws are countersunk in the back of the sample grip, which protrude with their spring-loaded spherical end into the sample insert. These are pushed back when the form-fit clamps of the SIP are inserted into the holder top down, until they meet the fixation notches of the sample and snap into place, enabling facilitated and reproducible insertion of the test samples. For the electrical contacting, two leaf springs made from sintered copper-bronze are embedded in the inner recesses of the side walls of the specimen holder and protrude slightly into

the specimen insert. As the SIP sample is inserted from top to down, these leaf springs are pushed back slightly so that they rest against the sample with a defined pressure. As soon as the SIP is locked in place, the leaf spring of the sample grip and the copper contact of the sample form an electrical contact with reproducibly defined contact area and contact pressure. This electrical connection is led to the outside of the sample grip by means of brass screws soldered to the leaf springs. Supply and measuring cables are attached and contacted with ring cable lugs to the further protruding screws on the outside of the specimen holders. Since each sample grip is equipped with four electrical contacts, there are potentially eight electrical contacts available for each SIP sample. In the following, only two of these contacts of the respective sample grip on the load-cell side are used to contact the opposite electrodes of the SIPs (refer to Figure 36). The cables serve simultaneously as a supply line for the high voltage control, and for the measurement signal transmission of the impedance measurement. For this reason, shielded high voltage cables with a thick insulating layer are used to protect against electric fields during high voltage excitation and to prevent crosstalk from magnetic fields during measurement. The respective cables are passed through a cable guide mounted to the angled aluminum carrier and then secured with a strain relief, which is also attached to the 20 mm grid of the base plate. Cable guidings and strain reliefs are 3D-printed from a temperature-resistant acrylonitrile-styrene-acrylate polymer (ASA). They prevent temperature-induced expansions in the setup or ventilation inside the climatic chambers from being transmitted via the cables to the load-cells and distorting the force measurements. In general, all electrical cables are fixed to stationary parts of the setup to avoid vibration-induced changes or defects in the electrical contact.

3.4.3 Conclusion on Design and Construction

The test rig is designed to allow the investigation of different planar DET types with minimal modifications, primarily adjustments to the sample grips. For demonstration purposes, the design presented in this work is adapted for exemplary SIP types specifically developed for this purpose, aiming to observe various typical electromechanical phenomena of DETs.

The SIP test samples are based on an *Elastosil 2030/20* dielectric film, screen-printed on both sides with CB-PDMS electrodes and provided with rigid 3D-printed high temperature resistant fixtures for mechanical and electrical connection. The sample is designed to undergo a reproducible step-by-step manufacturing and assembly process with minimal tolerance deviations, and to allow for facilitated handling and reproducible mounting on the test rig. Dimensions, isolation clearances and mechanical and electrical connection interfaces of the SIP aim to provide a robust design that can withstand production variations and reduce the risk of failure under electromechanical load.

Control, electronics and safety equipment of the test rig are installed on a peripheral aluminum structure surrounding a standardized climate chamber. Therein three test modules are mounted on a rail fixture, utilizing convenient plug and screw connections, enabling facilitated installation and

maintenance. The test modules are based on an aluminum platform on which a robust programmable linear drive is mounted opposite to a stationary load-cell carrier, which comprises 5 equidistant mounted load-cells. The load-cell carrier can be moved reproducibly along a defined grid, on the one hand to extend the testing range, and on the other hand to reduce wear on the motor. The load-cells and the motor slider are each equipped with 5 oppositely aligned sample grips. Each sample grip features mechanical snap-in mechanisms and electrical spring contacts that are tailored to the SIP test samples and enable facilitated sample installation with reproducible alignment and reliable electrical contacting.

3.5 Electronics and Wiring

This chapter describes layout, design, and wiring of both the low voltage and high voltage test electronics of the test rig, providing detailed specifications of the utilized components. It particularly provides detailed explanations of the proprietary circuit boards used for filtering, signal routing and current measurement. A separate section explains the implementation of the proprietary impedance measurement methods, with a detailed discussion of their accuracy as a function of load and measurement parameter configuration.

3.5.1 Low Voltage Test Electronics

The larger LV-cabinet (refer to Figure 34) includes power supplies, motor controllers, load-cell amplifiers, real time data generation and acquisition system (RT-system), as well as safety components such as fuses, fire detectors and fire extinguisher hoses (Figure 38).

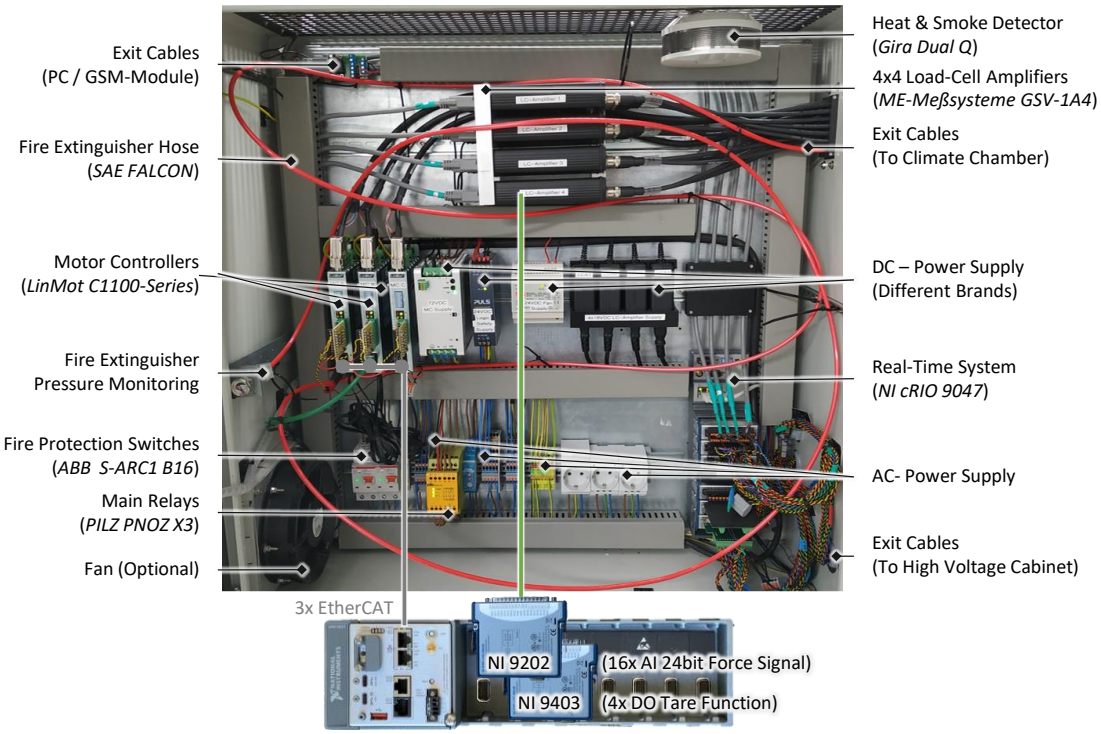

Figure 38: View into the LV-cabinet, containing power supplies, motor controllers, load-cell amplifiers, RT-system, and safety components such as fuses, fire detectors and extinguisher hoses.

All devices are mounted via DIN rail mounting, whereas the cables are arranged in a way to minimize signal crosstalk between power, logics, and control and measurement signals. The 230 V AC power supply is fed through a cable feed-through in the lower left of the cabinet where the corresponding supply components are located. Two separate supply phases are provided and protected with arc fault protection switches (*ABB-S-ARC1B16*), one for the logics, and one for the power electronics. The logics supply runs via the external UPS (*APC SMC1000I*), which is also connected to the host computer and GSM-module, enabling them to be safely terminated in the event of a power failure. The power electronics are supplied via a triggerable main relay (*PILZ PNOZ X3*) enabling the power to be switched off, either program-controlled using the RT-System (*NI cRIO 9047*) or the GSM-module, or manually by pressing the emergency stop button on the outside of the cabinet door. From the main relay, the AC power supply is distributed to the individual DC power supplies, which are arranged in the cabinet center. To avoid crosstalk, each device is provided with its individual DC power supply unit. As the motor controllers also generate switching power signals, they are placed directly next to them. However, the sensitive load-cell amplifiers are mounted on the top level of the control cabinet at a certain distance from the switching components in order to be protected from interfering electrical and magnetic fields. For the same reason, the RT-system is also located with a certain distance to those components but located in the lower right of the cabinet, in order to keep the cable length of signal lines to the neighboring high voltage control cabinet short. These cables are routed through a corresponding cable feed-through right next to the RT-system. Two more cable feedthroughs are leading in or out of the control cabinet. One (upper left) routes connection cables from controller and safety components to the host computer and GSM-module. The second (upper right) routes control and measurement cables from motor controllers and force measurement amplifiers to the climate chamber. The RT-system is used to control and synchronize the entire test bench hardware in real-time within a *NI LabVIEW* programming environment. For this purpose, it features two combinable real-time controllers, namely a real-time controller (RT-controller) and a field programmable gate array (FPGA) within the same chassis, both of which are synchronized and used simultaneously in the setup. The controller chassis is equipped with analog and digital input and output modules which are collectively controlled via the FPGA. An analog voltage input module (AI-module *NI 9202*) is used to acquire the force measurement signals. It features 16 channels of simultaneous acquisition of signals in a range of $\pm 10\,\mathrm{V}$ with a 24-bits resolution and a sample rate of 10kS/s. The inputs are connected to the outputs of four four-channel full-bridge measuring amplifiers (*ME Meßsysteme GSV-1A4*), which are designed to also provide $\pm 10\,\mathrm{V}$ at their output, within the entire measuring range of the load-cells (*ME Meßsysteme KD40s 10N*). In addition, a configurable 32-channel digital input/output module (DIO-Module *NI 9403*) featuring a $5\,\mathrm{V}$ logics level with quick response times is used control the logical function of these amplifiers and taring the measurement signal. The motor controllers (*LinMot C1150-EC-XS*), on the other hand, are directly

connected to the RT-system via an Ethernet port and can thus be controlled and monitored via the RT-system using a digital EtherCAT protocol, allowing a maximum sample rate of 1 kS/s when controlled via the NI Scan-Engine.

3.5.2 High Voltage Test Electronics

A larger number of modules and control system interfaces are provided for the electronics in the neighboring LV-cabinet (refer to Figure 34). It houses high voltage electronics including high voltage amplifiers, switching relays, and current measurement circuits. It is placed close to the porthole of the climate chamber, to keep electrical wiring to the samples short, and thus to keep electrical interference fields during high voltage control or parasitic effects during impedance measurement low. The custom developed electronics are of modular design and distributed on six circuit boards (double Eurocard), which are arranged in a rack-mounted housing (Figure 39).

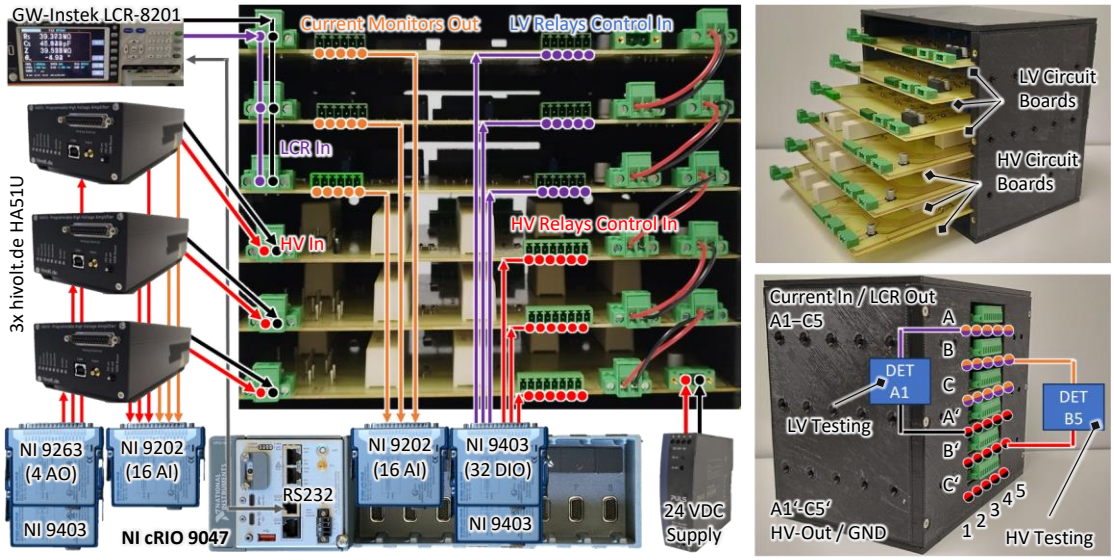

Figure 39: Rack mounted circuit boards connected to power supply, RT-system, high voltage amplifiers, and LCR-meter (left), with detailed view to the modular design (upper right), as well as signal in/out-side with LV- and HV-testing examples illustrated (lower right).

The 24 V DC supply voltage of the circuit boards is provided via a common power supply unit and passed on from one board to the next. Logical functions of the circuit boards and of the high voltage amplifiers are controlled via the RT-system using DIO-modules (*NI 9403*). Furthermore, two additional AI-modules (*NI 9202*) are used to acquire the signals of the customized current monitoring devices as well as those of the inherent voltage and current monitors of the high voltage amplifiers (*hivolt.de HA51U*), which also cover an output range of ± 10 V. Voltage waveforms are controlled with a 4-channel analog voltage output module (AO-Module *NI 9263*), providing voltage signals within a range of ± 10 V with 16-bit resolution and a maximum sample rate of 100 kS/s. The high voltage amplifiers provide analog input control within a range of $0 \ldots 10$ V, enabling voltage stimuli of up to $0 \ldots 3$ kV and a maximum current of 10 mA. As with the motor controllers, the LCR-meter (*GW-Instek LCR-8201*) is connected directly to the RT-System via an

Ethernet port, but in contrast is controlled via a serial *RS232* protocol, which only enables relatively slow (stable) acquisition rates of ~50 S/s.

High Voltage Circuit Board Layout

The high voltage reed relays (*cynergy³ DAT72410*), capable of switching high voltage of up to 10 kV within 3 ms [164], are installed on three of the six high voltage circuit boards on the lower side of the rack. Corresponding high voltage circuit boards (HV-boards) features a high voltage input on the supply side for connecting a separate high voltage amplifier (e.g. *hivolt.de HA51U*), and six digital inputs for relay control (0 V: open, 5 V: closed) (Figure 40).

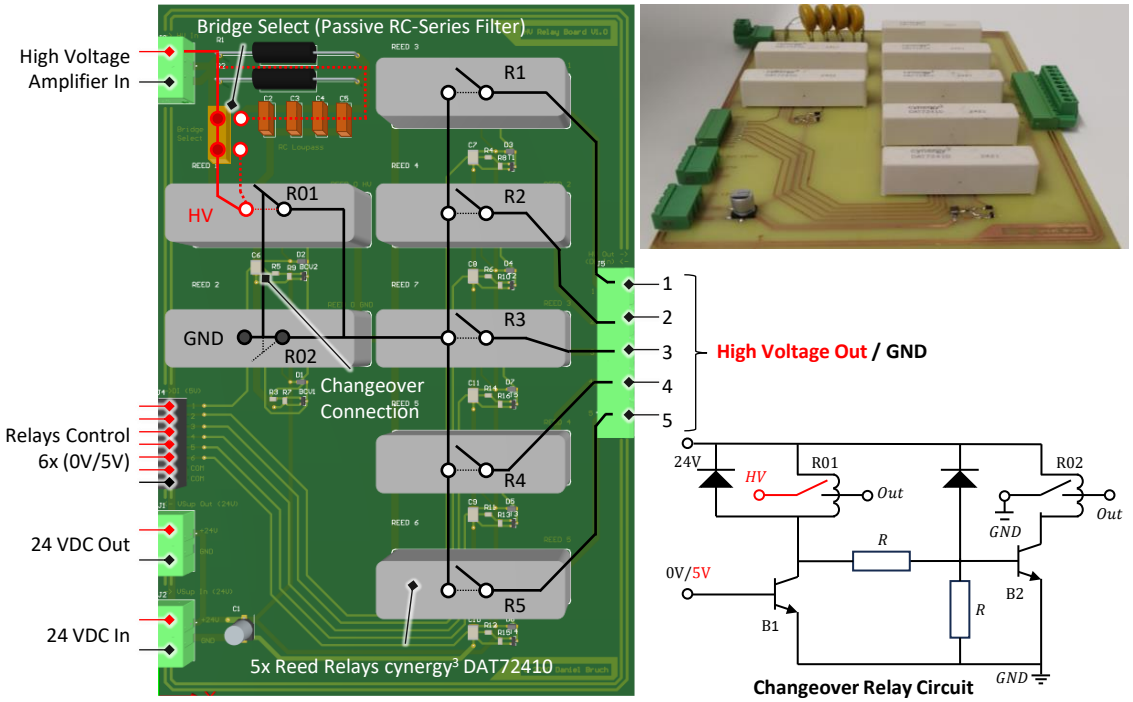

Figure 40: HV-circuit board layout, highlighting normally open state reed relays and no RC-filter bridge select (left), circuit board photo (upper right), and schematic of the changeover circuit obtained with two normally open relays (lower right).

On the opposite side, they provide five configurable in-/outputs that can be switched between common ground (in) and high voltage signal (out). As the reed relays are single normally open contacts, two of them are required to enable a changeover characteristic. In the multi-channel design of the HV-board, a corresponding changeover contact realized using this approach is connected in series with five single normally open relays (0 V: common ground, 5 V: high voltage amplifier). Consequently, each channel can be opened individually on the output side, but on the input side all channels can only be switched collectively between high voltage or ground signal. As a result, simultaneous high voltage and low voltage testing with the same test rig module is neither feasible nor intended due to the risk of damaging the LCR measuring device and potential interference from electrical fields during low voltage testing. The high voltage board also includes a user-configurable RC-series lowpass filter using high voltage resistors and capacitors on the high

voltage input side. This filter is selectable via jumper settings. In scenarios where constant voltage control is required, this setup enables smoothing and buffering of the voltage signal, effectively preventing voltage spikes and dips during operation, i.e. in the case of short circuits due to electrical breakdown of a connected DET.

Low Voltage Circuit Board Layout

The low voltage relays (*OMRON G2R1*) together with the custom-designed current monitors are installed on the three low voltage circuit boards (LV-boards) on the upper side of the rack (refer to Figure 39). Each of them is equipped with an input for connecting the common LCR-meter (e.g., *GW-Instek LCR-8201*), five digital inputs for relay control (0 V: current monitor, 5 V: LCR-meter), as well as five analog outputs (± 10 V) for acquisition of the current signal detected with the current monitors (Figure 41).

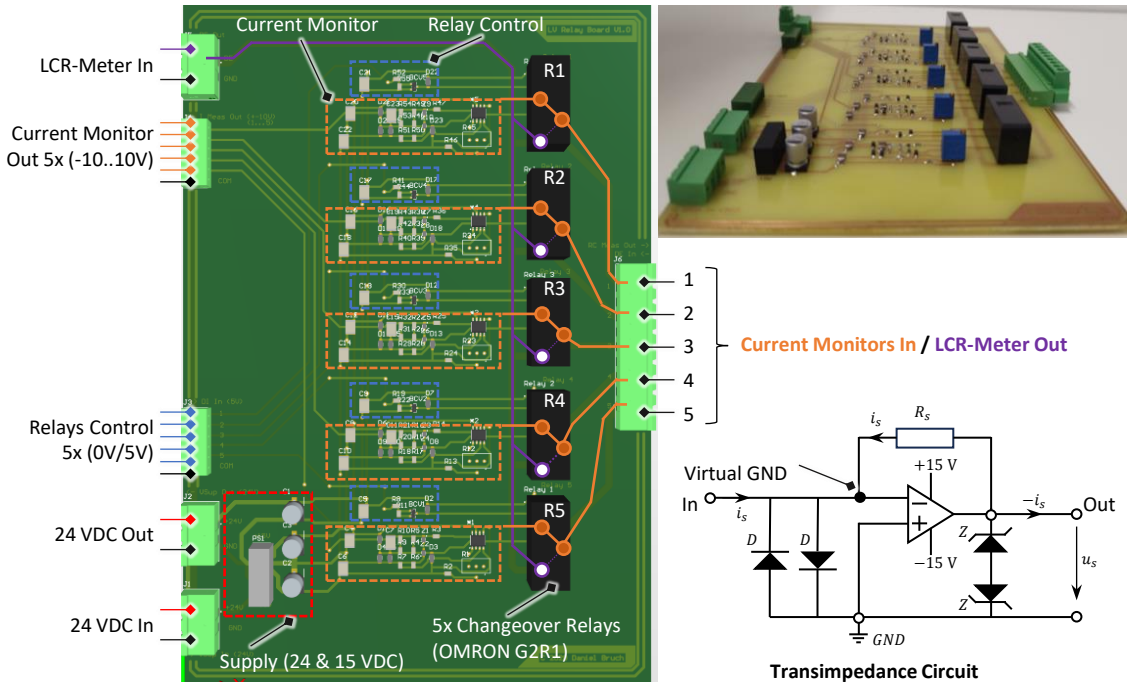

Figure 41: LV-board layout, highlighting normal relay status (left), low voltage circuit board photo (upper right), and schematic of the transimpedance circuit with safety diodes for current measurement (lower right).

On the opposite side, they provide five configurable in-/outputs that can be switched between current monitor signal (in) and LCR-meter signal (out). The current measurement is implemented using transimpedance circuits. They are realized with operational amplifiers whose output is fed back to the inverting input via a configurable shunt resistor R_S, with the non-inverting input set to ground. The operational amplifier thus also regulates the non-inverting input to ground for potential equalization between the two inputs and generates the same, but negative current on its output, as applied to its inverting input. This current i_S is measured via voltage u_S across the shunt resistor:

$$i_S = -\frac{u_S}{R_S} \tag{3.1}$$

Hence, the inverting input of the operational amplifier represents a “virtual” ground, where the low voltage side of a DET can be connected to, to measure a high voltage induced current. High voltage diodes are connected between inverting terminal and ground to prevent high voltage from being fed to the operational amplifier in the event of a short circuit, e.g., due to electrical breakdown of a DET. The output of the operational amplifier is equipped with Zener diodes providing voltage limiting to protect the connected acquisition hardware from overvoltage.

3.5.3 Impedance Measurement Electronics

A total of three different impedance measurement methods are implemented on the test bench to measure the capacitance and the electrode resistance of the DET samples, namely LCR-Meter, LV-Method, and HV-Method: LCR-Meter and LV-Method are used for low voltage testing. The standardized LCR-meter generally features a large measuring range and high accuracy and can be used in particular to precisely measure individual DET sensing capabilities, and to calibrate the proprietary impedance measurement methods. The proprietary LV-method enables similarly precise measurements over a smaller measuring range, but with higher data rates, which are required in particular for the acquisition of time-dependent effects. The proprietary HV-method is used for high voltage testing. It generally enables measurements of lower precision, but with similar measuring ranges and data rates compared to the LV-method. However, it particularly enables measurements with a superimposed high voltage for actuation, as well as simultaneous measurements on all test stations. Details on the implementation of the individual methods are given below.

LCR-Meter Measurement

For low voltage testing, the high voltage amplifier is disabled, the normally open high voltage relays are closed, and the high voltage changeover relays are switched to ground to fully discharge the DET samples. In this configuration, the low voltage relays are used as a multiplexer, and one test station is switched to the LCR-meter, while the others remain switched to the respective current monitors (Figure 42a, b). In this configuration, impedance magnitude Z, phase-shift θ, capacitance C, and resistance R of the DET sample applied to this test station can be continuously acquired. Thereby, the sample can simultaneously be deflected by the motor with a continuous deflection trajectory to investigate the change in these measurands in response to the mechanical stimulation. Once the test is complete, the low voltage relays can be used to multiplex to the next test station until all samples have been tested. By using a standardized LCR-meter (*GW Instek LCR-8201*), this test method enables precise measurements over a large measuring range.

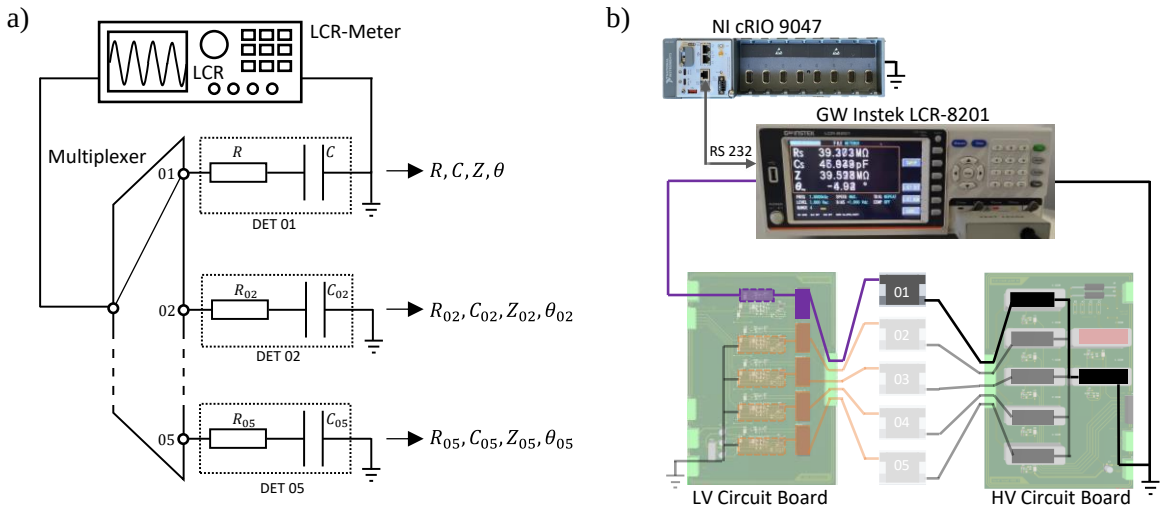

Figure 42: Low voltage impedance measurement with LCR-meter via multiplexer, considering one test module illustrated as circuit diagram (a), and schematic wiring within the setup (b).

However, testing time-dependent effects in combination with mechanical stimulation is restricted due to the limited transmission rate between the LCR-meter and the RT-system via the *RS232* interface (~50 S/s). Furthermore, all samples mounted to the test module are deformed if the samples are mechanically deflected during the test, but impedance measurement is only conducted to one sample. Consequently, changes due to cyclic loading in particular cannot be accessed for the remaining samples. Moreover, the LCR-meter cannot be used in combination with applied high voltage, thus the self-sensing properties of smart DET actuators cannot be investigated.

Fundamentals on Proprietary Impedance Measurement Methods

These limitations are addressed by implementing proprietary impedance measurement methods, namely LV-Method and HV-Method, using the RT-system to control and acquire the corresponding measurement signals with high sampling rates. Both methods utilize a standard AC measuring principle, which can be described with fundamental AC theory. This is briefly explained in the following to support the description of the methods implemented on the test rig.

For impedance measurement, a sinusoidal voltage signal u with constant frequency is applied to a generalized electrical network with a complex impedance $\underline{Z}$ (e.g. a DET sample), and the current signal response i of the network is measured (Figure 43a). As these signals represent constant sinusoidal waveforms, they can be described by the measurement frequency f_m, their respective magnitudes U and I and their respective zero phase angles θ_u and θ_i (Figure 43b).

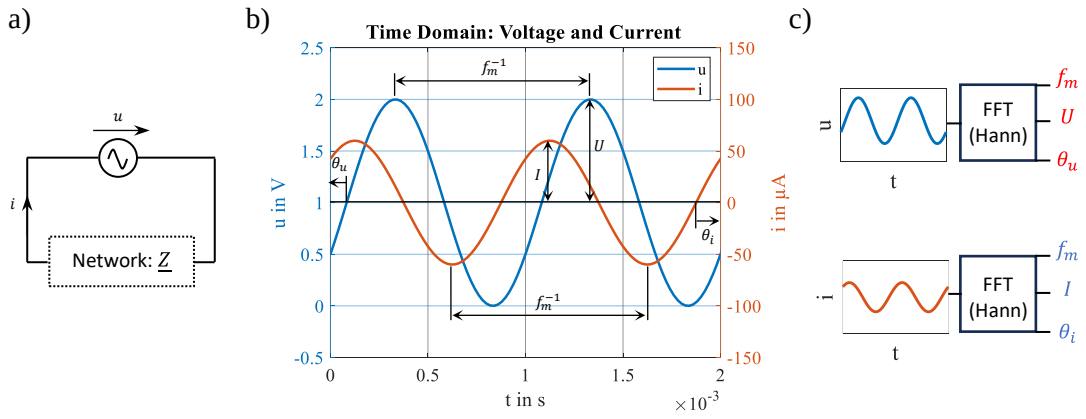

Figure 43: Impedance measurement of a generalized electrical network via sinusoidal voltage control and measurement of the current response; with schematic illustration of the generalized network (a), exemplary control and measurement signals in time domain (b), and schematic illustration of Hann-windowed FFT, used to identify respective signal magnitudes in frequency domain (c).

These quantities can be accessed by transforming the time-domain signals to the frequency domain using Hann-windowed Fast Fourier Transform (FFT) (Figure 43c), and determining the peak values within the resulting amplitude spectrum (Figure 44a) and phase spectrum (Figure 44b), obtained at the known measuring frequency.

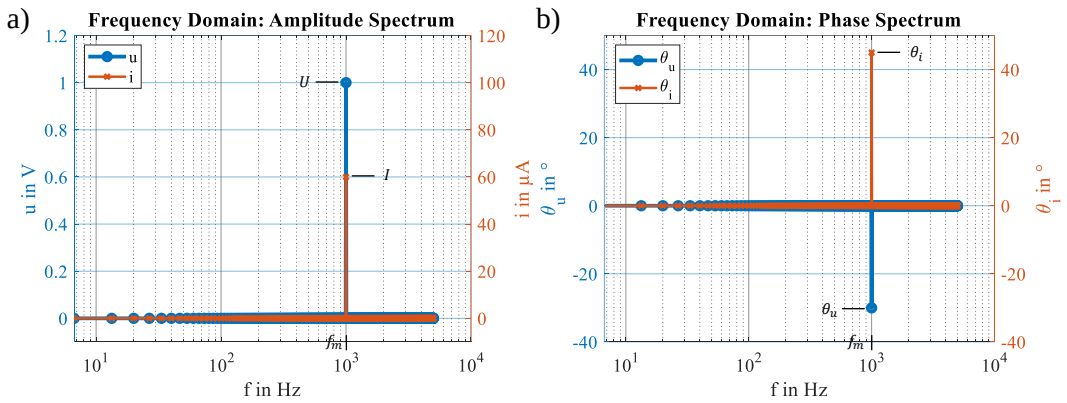

Figure 44: Amplitude spectrum (a) and phase spectrum (b), obtained by Hann-windowed FFT of the time-dependent voltage and current signals.

Considering stationary measurements at constant frequency, voltage u and current i can be described in complex notation using phasors $\underline{U}$ and $\underline{I}$ respectively:

$$\underline{U} = Ue^{j(\theta_u)} \qquad \underline{I} = Ie^{j(\theta_i)} \tag{3.2}$$

The corresponding impedance $\underline{Z}$ of the network results from Ohm's law:

$$\underline{Z} = \frac{\underline{U}}{\underline{I}} = \frac{U}{I}e^{j(\theta_u - \theta_i)} = Ze^{j\theta} \tag{3.3}$$

The measurands impedance magnitude Z and phase-shift θ of the network thus result from the magnitudes and zero-phase angles of voltage and current measurement signals:

$$Z = \frac{U}{I} \qquad \theta = \theta_u - \theta_i \tag{3.4}$$

If the general impedance network is replaced by the equivalent circuit diagram of a DET as a simple RC-series element (Figure 45a) (refer to Section 2.1.8), resistance R and capacitance C can be determined by relating the pointer diagram of the measurement signals (Figure 45b) and the pointer diagram of the equivalent circuit (Figure 45c) to each other.

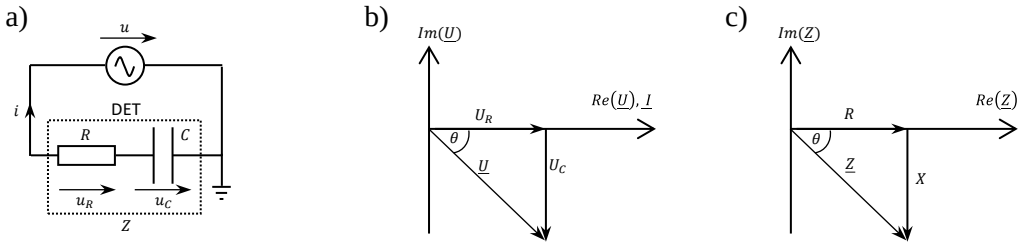

Figure 45: DET considered as RC-series equivalent circuit (a), and pointer diagrams of the measurement signals (b), and the equivalent circuit (c).

The latter diagram shows, that (3.3) can also be described using geometric expressions:

$$Ze^{j\theta} = Z(cos\,\theta + j\,sin\,\theta) \tag{3.5}$$

From this resistance R and reactance X_c are obtained by considering the real and imaginary parts:

$$R = Zcos\,\theta \qquad X_c = Zsin\,\theta \tag{3.6}$$

By supplementing X_c in equation (2.20), the capacitance can be obtained.

$$C = -\frac{1}{Zsin\,\theta\omega} \tag{3.7}$$

This method is implemented on the test bench using the *NI-cRIO 9047* RT-system, equipped with a *NI 9263* AO-module for voltage control, and a *NI 9202* AI-module for voltage and current measurement.

For the LV-Method these components are solely supplemented by an additional shunt resistor for current measurement, while directly utilizing the voltage output module to provide the measurement voltage signal. In contrast, for the HV-Method the measurement voltage provided by the voltage output module is amplified by the high voltage amplifier and the current signal is acquired via the individual current monitors of each test station. Details on the corresponding methods are given below.

LV-Method

For LV-Method, the measurement voltage directly provided by the *NI-9263* AO-module is applied via the LCR-meter input of the LV-board, and current is measured via a shunt resistor between the AO-module and this input (Figure 46a, b).

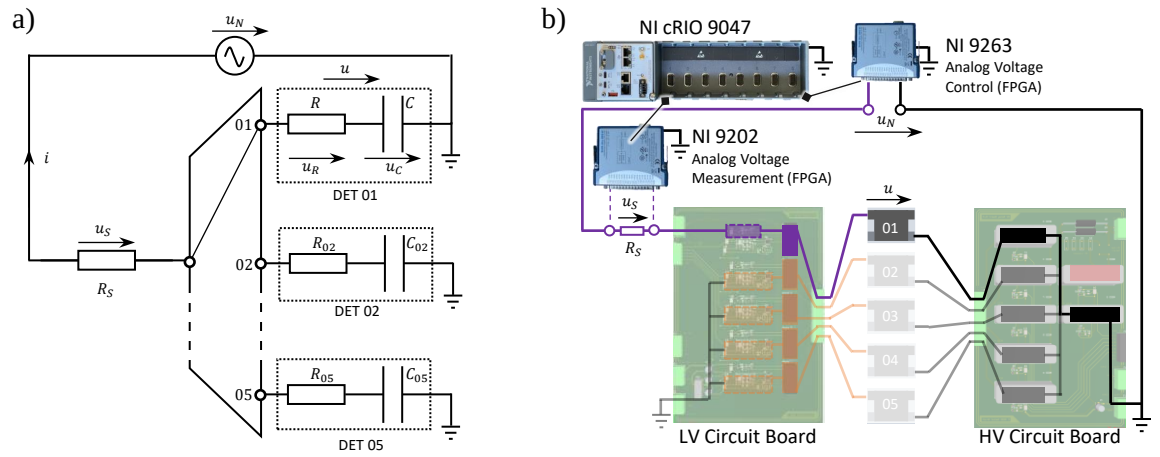

Figure 46: Low voltage impedance measurement with current measurement via shunt resistor, considering one test module illustrated as circuit diagram (a), and schematic wiring within the setup (b).

The voltage input module is used to measure both, control voltage u_N over the entire network, and voltage u_S over the shunt resistor. From these signals the measurands U_N, U_S and θ_N are determined, utilizing a high-level Hann-windowed FFT-function provided in *NI LabVIEW*. Since the shunt resistor R_S is part of the network, it must be considered within the pointer diagrams of the network (Figure 47).

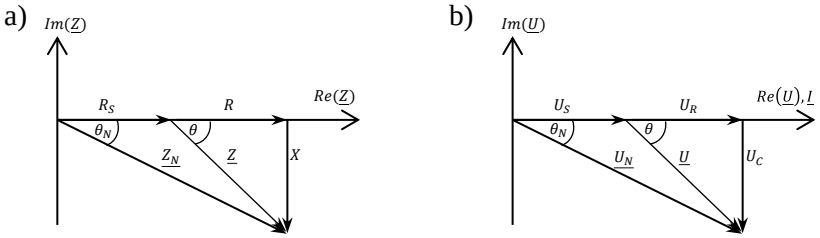

Figure 47: Pointer diagrams of low voltage impedance measurement via shunt resistor, considering the measurement signals (a), and the equivalent circuit (b).

From this, the current magnitude I through the DET is directly obtained:

$$I = \frac{U_S}{R_S} \tag{3.8}$$

Furthermore, the voltage magnitude U over the DET is derived from U_N and U_S and θ_N:

$$U = \sqrt{U_N^2 + U_S^2 - 2U_N U_S \cos\theta_N} \tag{3.9}$$

The corresponding phase-shift θ also depends on these measurands:

$$\theta = arctan\frac{U_N sin\ \theta_N}{U_N\, cos\, \theta_N - U_S} \tag{3.10}$$

Substituting (3.8) and (3.9) into (3.4) results in the impedance magnitude Z. With this and the phase-shift θ obtained from (3.9), resistance R and capacitance C result from (3.7). In principle, this approach enables the same measurement procedures as with the LCR-meter. However, direct implementation on the FPGA enables a much higher acquisition rate and better synchronization with the other setup components. Since at least two sinusoidal periods are required for the Hann-windowed FFT to reliably determine amplitudes and phases of current and voltage, the maximum achievable acquisition rate f_a results in:

$$f_a = \frac{f_m}{2} \tag{3.11}$$

As the voltage input module only enables a maximum sample rate $f_s = 10\,\mathrm{kS/s}$, the measuring frequency f_m can be set to a maximum of 5 kHz according to the Nyquist-Shannon sampling theorem. Thus, the theoretical maximum acquisition rate of the impedance measurement results in $f_a = 2.5$ kHz. As this can be processed robustly by the RT-system, the hereby introduced method enables ~50-times higher acquisition rate within the setup compared to the LCR-meter.

HV-Method

HV-Method is utilized to determine capacitance and resistance during high voltage testing. In this testing mode, the individual high voltage relays are closed, and the high voltage changeover relays are connected to the high voltage input of the HV-board. The low voltage relays are switched to the individual current monitors of each test station, representing virtual ground (Figure 42a, b).

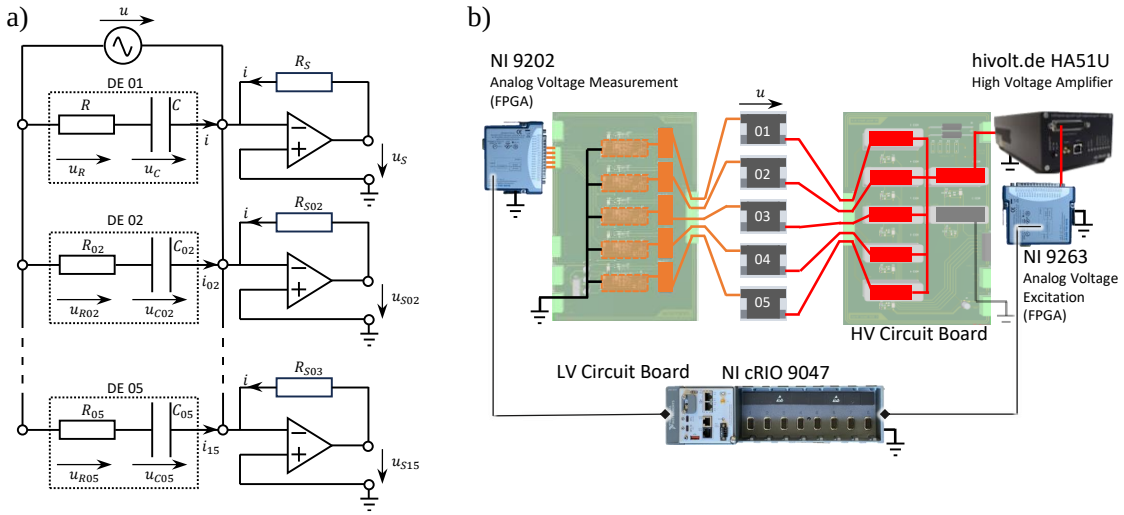

Figure 48: High voltage impedance measurement with current measurement via transimpedance circuits, considering one test module illustrated as circuit diagram (a), and schematic wiring within the setup (b).

The measurement voltage is applied via the high voltage input of the HV-board with the signal from the *NI-9263* AO-module being amplified by the high voltage amplifier (*hivolt.de HA51U*). The current is measured via the individual current monitors (transimpedance circuits) and acquired

by the *NI 9202* AI-module. The bandwidth of both the current and voltage monitors exceeds 10 kHz (refer to Section 3.7.2), ensuring they do not limit the maximum measuring frequency. Consequently, with this approach, measurements and data acquisition can theoretically be performed at the same frequency as with the LV-method. Moreover, the individual current measurement enables simultaneous impedance measurement on all test stations of one module. Finally, it also enables the impedance measurement of the samples with applied high voltage by modulating the (small) AC measuring signal onto the (large) quasi-stationary high voltage signal. A drawback of this method is the lower accuracy with regard to the signal-to-noise (SNR) at low measurement voltages. On the one hand, this is caused by the comparatively large signal ripple of the high voltage amplifier. On the other hand, it is also due to the less suitable measuring range of the current monitors, which are primarily dimensioned for the detection of electrical breakdowns. The general influence of load and measurement configuration on the accuracy of the proprietary measurement methods, especially in terms of sensitivity and SNR, is discussed below.

Discussion on Proprietary Impedance Measurement Accuracy

In order to achieve a sufficient measuring signal quality, electrical circuit boards and wiring are designed in a symmetric design with large safety distances and shielding to minimize interference with surrounding electric and magnetic fields (refer to Section 3.5.2). LV-method and HV-method do not utilize AC measuring bridges, as common with standard LCR measuring devices. Consequently, they are potentially more susceptible to disturbances. However, permanent parasitic effects in setup and wiring are eliminated by means of a four-step load calibration of the individual test stations, enabling sufficient accuracy within a limited measuring range (refer to section 3.7.3). Apart from parasitic effects and interference, the measurement accuracy generally depends on the configuration of the AC measurement voltage (i.e. amplitude and frequency) and its combination with the impedance characteristics of the electrical network under test (i.e. RC-series elements). This fact is particularly important for the continuous characterization of DETs, as they do not represent a constant load, but significantly change their capacitance and resistance under mechanical deformation. Since no further (automatic) measurement range adjustments are implemented for LV-method and HV-method, the measurement voltage must be user-configured with regard to the impedance characteristics of the DET sample, to achieve measurement results of sufficient accuracy. To gain a better understanding of this configuration, the relations between measuring signal and impedance characteristics of RC-series loads are discussed in the following with regard to noise and measuring sensitivity.

In general, the measurement signal quality of measurands C and R depends on the quality of the lower level measurands Z and θ, which in turn depend on the quality of the measurands u and i on lowest level. As these are generated with DAC-converters and measured with ADC-converters, they have a fixed sample rate and a fixed amplitude quantization error. With f_s, the maximum

reproducible measuring frequency f_m is limited to the corresponding Nyquist rate $f_s/2$. Since the amplitude of the measurement voltage is usually constant during measurement, the corresponding quantization noise will also remain constant. However, since RC-series elements represent high-pass current filters, the amplitude of current i is decreasing with decreasing f_m or with increasing Z. Therefore, the measurement of i is critical with respect to quantization noise, which changes accordingly with a nonlinear characteristic, if the properties of the RC-series changes during continuous measurements. In addition to other potential noise sources and interferences, this error trend is proportionally propagated to the parent quantities Z and θ according to equation (3.4). From there, they are nonlinearly propagated to the quantities C and R, e.g. according to equation (3.6) and (3.7) for HV-Method.

To explain the nonlinear characteristics, the generic frequency responses of RC-series elements are considered and varied within a range of typical capacitance and resistance values of DETs, (e.g. $R = 4\ \text{k}\Omega \ldots 100\ \text{k}\Omega$ and $C = 0.5\ \text{nF} \ldots 10\ \text{nF}$). Thereby, once R is fixed (e.g. $R = 4\ \text{k}\Omega$) and only C is varied (Figure 49a, b), and once the C is fixed (e.g. $C = 5\ \text{nF}$) and only the R is varied (Figure 49c, d).

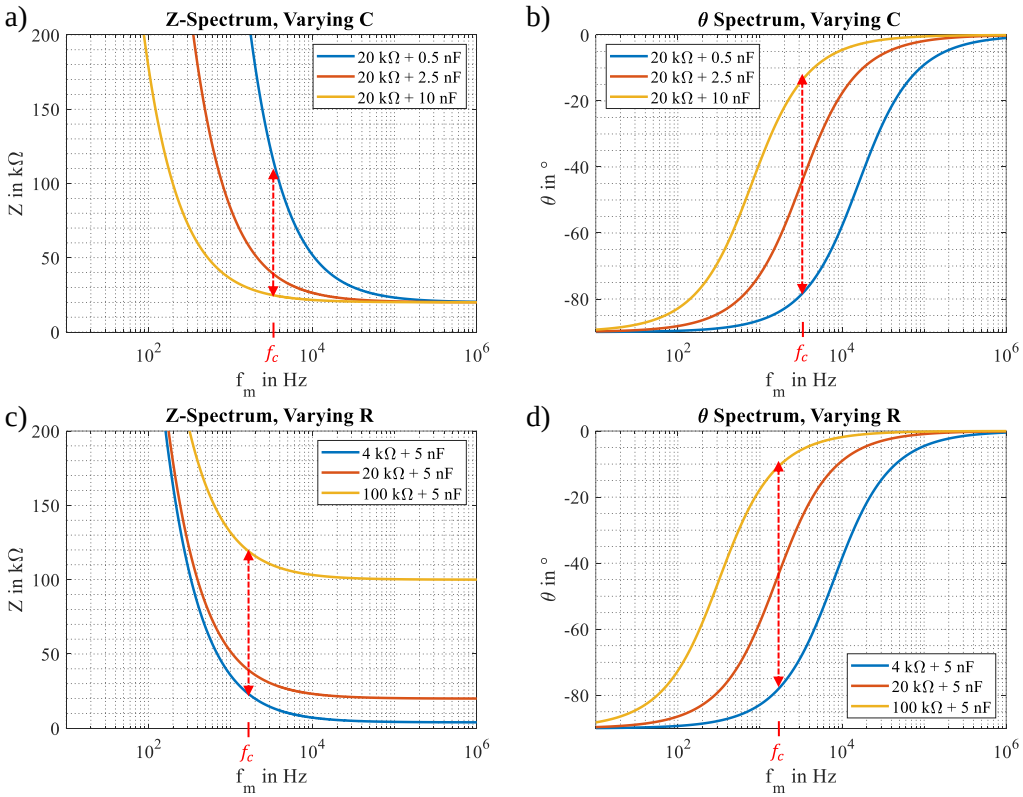

Figure 49: Generic frequency response of RC-series elements with fixed resistance and varying capacitance and resulting impedance spectrum (a) and phase spectrum (b); and with fixed capacitance and varying resistance and resulting impedance spectrum (c) and phase spectrum (d).

When varying C and observing the resulting Z-curves it is observed that they converge towards each other for increasing f_m, resulting in a decreasing measurement sensitivity (Figure 49a). In

contrast, varying resistance R only results in a vertical shift of the Z curves, thus maintaining constant sensitivity for increasing f_m (Figure 49c). Consequently, considering Z as measuring variable, and C and R as derived variables, robust measurement results with sufficient sensitivity and low noise are therefore achieved for R with higher f_m, as these frequencies result in lower Z and thus higher i-amplitudes with minor (quantization) noise. However, for C, better results are obtained within the lower frequency range, whereby an optimum frequency is expected, that provides the best signal quality as a compromise between noise and sensitivity. When considering the phase spectra accordingly, the θ-curves converge for increasing f_m towards $\theta = 0\,°$ and for decreasing f_m towards $\theta = -90\,°$. Variation of C (Figure 49b) and R (Figure 49d) results in the same trend of the curves, which are shifted to the left, as C or R increase. Highest measurement sensitivity for both quantities is given at $\theta = 45\,°$. The corresponding measuring frequency is the cutoff frequency f_c (refer to equation 2.25). It thus represents an optimum for both capacitance and resistance measurement with regard to sensitivity.

To sum up, it is generally recommended to aim for a phase-shift $\theta \approx -45°$, or to configure $f_m \approx f_c$ respectively, in order to achieve good measuring quality for both measurands, C and R. If one measurand is prioritized, $f_m < f_c$ must be configured for the capacitance measurement, and $f_m > f_c$ for the resistance measurement. Thereby, it must be ensured that the lower-level quantities Z and θ, and thus u and in i also feature sufficient signal quality. With regard to this, in the low frequency range, it is important to ensure sufficient i-amplitudes, while sufficient sample resolution must be achieved in the higher frequency range.

In electromechanical characterization experiments for DETs, C and R usually increase with applied strain or voltage. With regard to sensitivity, it is thus reasonable to select $f_m < f_c$, or $\theta < -45°$ respectively, as θ increases during the measurement. However, DETs generally represent much more complex RC networks than a simple RC-series element. Therefore, high measurement frequencies in particular can lead to areas further away from the electrical contact no longer being detected in the measurement signal. This applies in particular the exemplary investigated SIPs in this work, which is explained in more detail in section 4.1. It is thus generally recommended to characterize a DET sample with the LCR-meter as a reference prior to the first electromechanical loading, and then determine a suitable frequency f_m for an electromechanical test using LV-method or HV-method. Since both methods are calibrated using a load calibration (refer to Section 3.7.3), this approach can be integrated into the calibration process. Additionally 3D-spectra of Z and θ over the desired capacitance range (Figure 50a, b), or over desired resistance range (Figure 50c, d) can assist to estimate suitable measurement frequencies depending on the load. Therein, the visualization of the lowest and highest resistance and the lowest and highest capacitance of the desired ranges respectively, result in two curved surfaces that span the entire measuring range in each diagram.

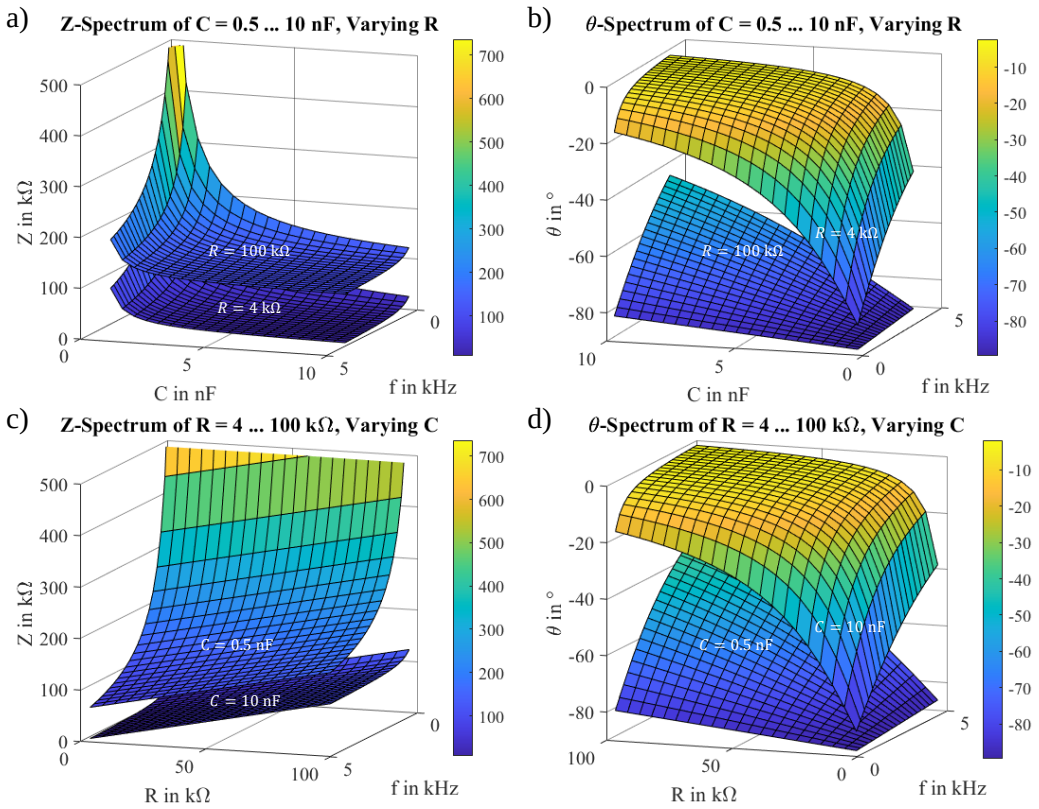

Figure 50: 3D-spectra of impedance magnitude and phase-shift over the desired capacitance range (a, b), and over demanded resistance range (c, d).

3.5.4 Conclusion on Electronics and Wiring

Detailing the layout, design, and wiring of both the low voltage and high voltage test electronics of the test rig, this section offers comprehensive specifications of the utilized components and explanations on the realized impedance measurement methods.

Low voltage electronics in the LV control cabinet include standardized supply, logic, measurement, control, and safety components arranged and shielded to prevent interference from power electronics.

Electrical signal routing via low and high voltage relays, signal filtering with passive filter elements, and individual current monitoring based on transimpedance circuits are realized on proprietary developed circuit boards, namely the LV- and HV-boards. Together with the high voltage amplifiers, these are rack-mounted in the HV control cabinet, thus shielded from the low voltage control and measurement electronics.

Three impedance measurement methods are employed to determine the electrical properties of DET samples: LCR-meter, LV-method, and HV-method. LCR-meter and LV-method are used for sequential low voltage testing. The standardized LCR-meter, providing wide measurement range and high accuracy, is ideal for accurately measuring individual DET sensing capabilities and calibrating the proprietary impedance measurement methods. The proprietary measurement

methods are based on fundamental AC theory, whereby sinusoidal measurement voltages and currents are analyzed using a Hann-windowed FFT. The LV-method provides similar accurate measurements over a smaller range, but higher data rates in comparison to the LCR-meter, which is essential for capturing time-dependent effects. The HV-method, designed for high voltage testing, provides measurements with lower accuracy but similar ranges and data rates to the LV-method, allowing measurements with superimposed high voltage for actuation and simultaneous measurements on all test stations. Measurement accuracy, analyzed with respect to load using simple RC-series elements as an example, highlights the importance of keeping the measurement frequency close to the cutoff frequency of the RC-series element. However, this can only be achieved if the measured impedance allows sufficient measurement currents while preventing the DET regions further away from the electrical contact from being cut off.

3.6 Control and Software

With numerous test stations, various test routines, and the need for automated operation, this work presents a test rig with extensive measurement and control variables that require a user-friendly control interface. Moreover, well-structured, and efficient data management is essential to prevent high-resolution and long-term experiments from memory overflow and provide facilitated data evaluation. These challenges were overcome by appropriate hardware embedding, software implementation and data management, which are described in the following sections.

3.6.1 Hardware Embedding

The central operating unit of the test bench is the host computer (*Microsoft Windows 10*, and *NI LabVIEW*). This is connected to real time data generation and acquisition system (RT-System, *NI cRIO 9047*), embedding the test hardware, and to the GSM-module (*WiLARM FIVE*), embedding the safety hardware (Figure 51).

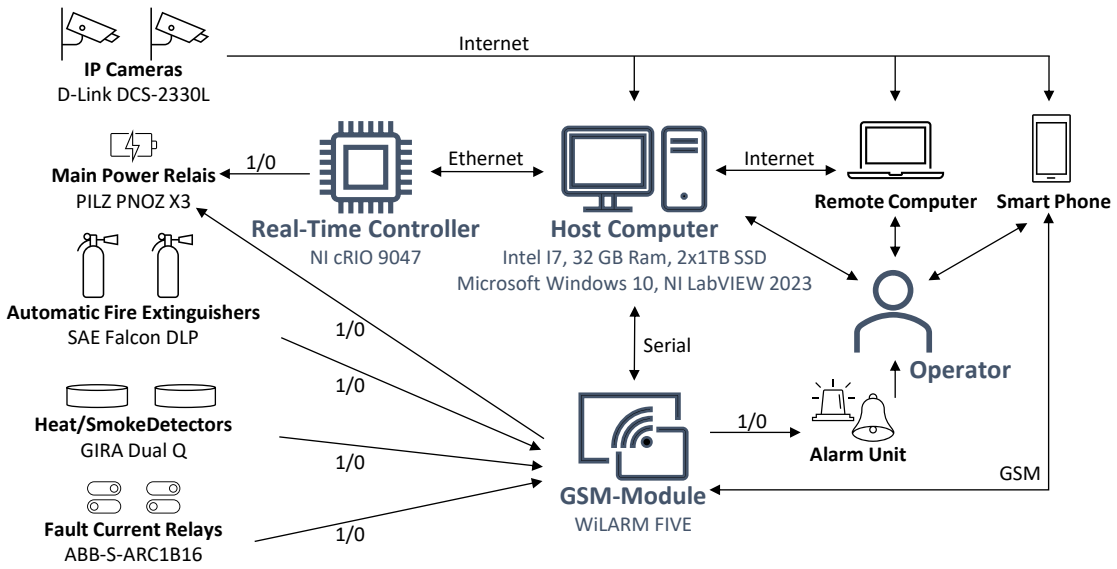

Figure 51: Schematic illustration of the interconnection of control units, safety devices and operator of the test rig.

Embedding of Safety Hardware

The GSM module is directly powered through the fault current relay (*ABB-S-ARC1B16*), which also supplies power to the main supply relay (*PILZ PNOZ X3*) of the test rig. Equipped with a backup battery, the GSM module monitors its own voltage status, enabling it to detect a relay shutdown caused by a fault current while remaining powered itself. The fire detectors (*GIRA Dual Q*) and the automatic fire extinguishers (*SAE Falcon DLP*) each are equipped with event-controlled relays that switch over when activated. These are individually connected to the digital inputs of the GSM-module, which thus recognizes exactly which safety device has been triggered. The GSM module additionally provides two programmable output relays, one of which is used to control the main power relay and one for the visual and audible alarm unit. In the event of fire or fault current the module is thus programmed to initiate automatic safety routines. These always involve switching off the main power supply relay, and activating the alarm module, which is also supplemented with an additional backup battery. In addition, the operator receives a phone call via the GSM network and a text message describing the alarm reason. The operator then has the option of accessing the two IP cameras (*D-Link DCS-2330L*) one of which is aimed at the electronics cabinets and one at the test room, via smartphone or (mobile) computer. This enables to obtain an overview of the situation and initiate further measures manually. The camera facing the test room is also used to support remote control of the test bench via Microsoft *Windows Remote Desktop*, allowing access to the test bench's graphical user interface from a remote computer. In addition to monitoring and configuring running tests, the GSM-module can also be used to shut down the power supply via the RT-system connected to the main power relay of the setup. This feature allows the safe shutdown of the entire test bench, i.e. at the end of a test or in the event of a fault.

Embedding of Test Hardware

With the exception of the climate chamber (*CTS C-70/350*), which is connected to the computer via serial connection, all test hardware components are controlled via the RT-system (Figure 52). It is equipped with a field programmable gate array (FPGA-controller) and a real-time controller (RT-controller).

The RT-controller provides deterministic access to the digital communication interfaces offered by the RT-system, which include various industry-standard data protocols. In particular, the *EtherCAT* interface is used for communication with the motor controllers (*LinMot C1150-EC-XS*), and the serial *RS232* interface for communication with the standardized LCR-meter (*GW-Instek LCR-8201*). Both are programmed within a *NI LabVIEW* real-time environment, but only the *EtherCAT* connection enables high and deterministic data transfer rates limited to 1 kS/s when controlled by NI Scan- Engine, whereas the *RS232* transfer rate is only stable at ~50 S/s.

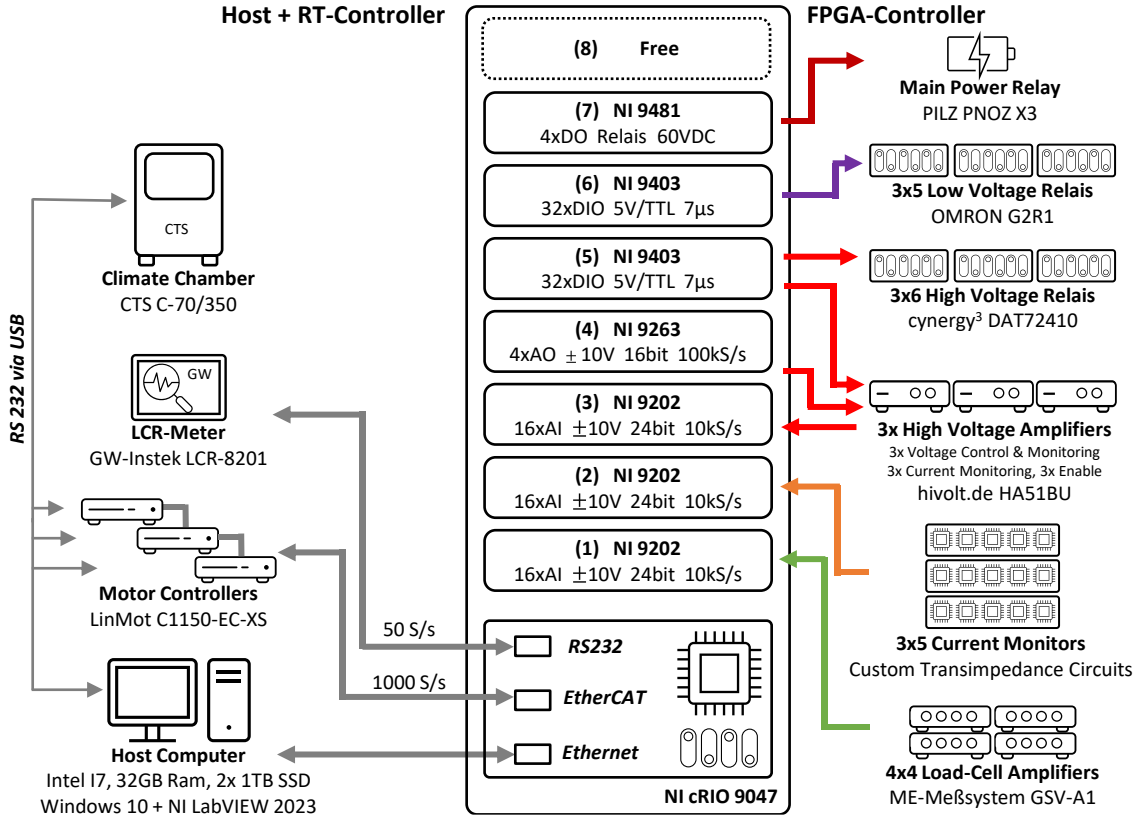

Figure 52: Schematic illustration of the test hardware embedding, with a focus on the real time data acquisition system and its analog and digital modules and interfaces.

The FPGA-controller is used to control and measure analog signals and digital states via seven configurable input and output modules. Three *NI 9202* AI-modules are used for analog inputs, each providing 16 channels with 24-bit amplitude quantization and a simultaneous sample rate of 10 kS/s over a voltage range of ±10 V. They are connected to the analog outputs of the load-cell amplifiers (4x4 channels *ME-Meßsysteme GSV-1A4*), the proprietary developed current monitors (3x5 channels transimpedance circuits) and the current and voltage monitors provided by the high voltage amplifier (3x *hivolt.de HA51U*). As these devices also provide ±10 V outputs over the respective measuring range, the full quantization range of the analog input modules is utilized. A *NI 9263* AO-module is used for the analog voltage output, which offers four channels with +10 V output voltage each, at a 16-bit quantization resolution and transmission rate of 100 kS/s. This module is used to control the operating voltage of the high voltage amplifiers with nominal gain 1:300. The high voltage relays (21x *cynergy*^{3} *DAT72410*) and the low voltage relays (15x *OMRON G2R1*) are triggered using two *NI 9403* DIO-modules, each providing 32 channels, which can be configured as digital input or output at a 5 V digital level with response times of 7 µs. Those modules are furthermore used to trigger digital functions of the load-cell amplifiers and the high voltage amplifiers, such as enabling high voltage output or taring the force signal. Finally, the *NI 9481* DO-relay-module is connected to the main power relay, which enables program-controlled shutdown of the power supply.

3.6.2 Software Architecture

The software architecture consists of three interconnected program components, executed on the individual processing systems (Figure 53). The top-level component is the host program, that is executed on the host computer (Figure 53, top). It controls the general program flow and provides the user with input and output functionality. The second component is a real-time program (Figure 53, lower right), which is executed by RT-controller, ensuring deterministic program sequences with a fixed cycle time. It provides direct access to the motor controllers and the LCR-meter, which are connected via the controller chassis using digital data transfer protocols (*EtherCAT* and *RS232*). The third program component is implemented on the FPGA. It enables the analog and digital input and output modules to be programmed deterministically as well, but furthermore offers increased programming flexibility and the use of higher data rates. Data transfer and synchronization between the programs is achieved (beyond other methods) by using real-time FIFOs (e.g. FIFO1-FIFO3) and global trigger variables (e.g. GV1-GV3).

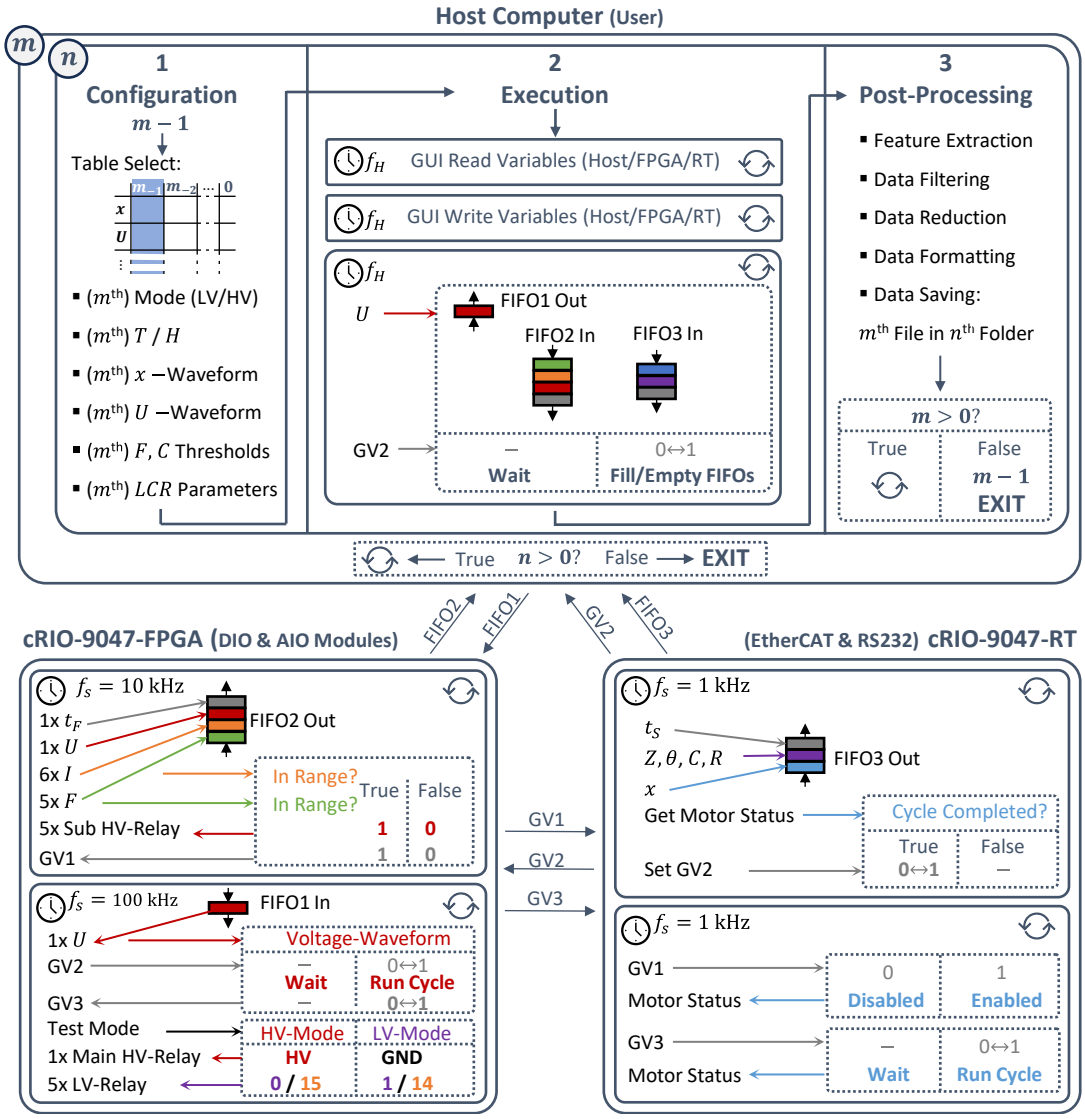

Figure 53: Schematic of general software architecture, consisting of three interconnected program components with the host program (top), the FPGA program (lower left) and the RT-program (lower right).

Host Program

The host program (Figure 53, top) is designed to execute the same sequence of m different configured test programs n-times in the main loop before it is terminated. Each of the m programs basically runs through three steps, namely (experiment-) configuration, (experiment-) execution and (experiment data-) post-processing. In the configuration step, m is decremented first. Based on the result, the m^{th} column containing the configuration of the m^{th} experiment is then selected from a configuration table, which is created by the user, and which contains full definition of all experiment variables e.g., testing mode or voltage trajectory. In the execution step, the experiment is executed based on this configuration, with three program loops of different functionality running simultaneously. The first loop continuously reads out all control and measurement variables during the experiment and displays them on the graphical user interface. The second loop waits continuously for input from the user, who can intervene in the test procedure, e.g. cancel the experiment. The third loop interacts with RT and FPGA programs that primarily execute the experiment program. It continuously transfers the voltage excitation waveform data array through FIFO1 to the FPGA and receives all measurement data transferred from the FPGA via FIFO2 and from the RT via FIFO3. It is thereby triggered by GV2, which is inverted by the RT- program after each control cycle, thus preventing the FIFO buffers from overflowing during long-term tests. Once a test has been completed, the data is post-processed and saved in the final step of the host program (refer to Section 3.6.5). If m is not zero after this post-processing, the host program returns to the configuration step, decrements m and selects the next experiment. If m reaches zero, the program decrements n, restarts the m-loop from the beginning and repeats the experiment sequence of m experiment programs, until also n is zero and the entire program is terminated.

FPGA Program

The FPGA-program (Figure 53, lower left) continuously reads the analog signals from voltage monitors, current monitors, and load-cells with a stable sample rate of $f_s = 10\ \text{kS/s}$, and transmits this data with timing information to the host via FIFO2. Furthermore, current and force values are continuously compared with user-defined threshold values. If those are exceeded for a configurable time, the high voltage relays of the corresponding channel or the motor (via GV1) of the corresponding module are switched off. The voltage waveform is generated in a separate loop with a stable generation rate $f_s = 100\ \text{kS/s}$. The status of the high voltage changeover relays and the low voltage changeover relays is thereby determined by the specification of the respective testing mode (LV / HV). After generation of each voltage control cycle, the program waits for the status of the global trigger variable GV2 to change before generating the next cycle.

RT Program

This variable change is set by the RT-program (Figure 53, lower right) after the motor has completed a full cycle. When the FPGA-program detects the state change of GV2, it immediately

alters the state of GV3, which in turn triggers a new displacement control cycle within the RT-program. Thus, voltage and displacement waveforms are synchronized each individual control cycle, ensuring that the signals do not drift apart. Unlike the generation of the voltage waveform, the displacement trajectory is not generated via an analog output signal. Instead, it is configured by the motor controller through the host program in advance. Consequently, only the execution of each individual stimulation cycle is triggered via the RT program within a control-loop, which is timed with a stable sample rate $f_s = 1\ kS/s$, and which is also used to control the motor safety shutdown via GV1. Additionally, the RT-program continuously reads motor position and motor status, as well as the values of the LCR-meter with a constant and stable sample rate $f_s = 1$ kS/s, transmitting them with timing information to the host via FIFO3.

3.6.3 Waveform Generation and Synchronization

The configuration of periodic voltage and displacement control signals is designed to enable a large number of control signals with just a few configuration parameters: offsets (voltage offset U_1, displacement offset x_1), amplitudes (voltage amplitude U_2, displacement amplitude x_2), as well as holding times (t_1, t_3), and ramping up and down times (t_2, t_4) (Figure 54).

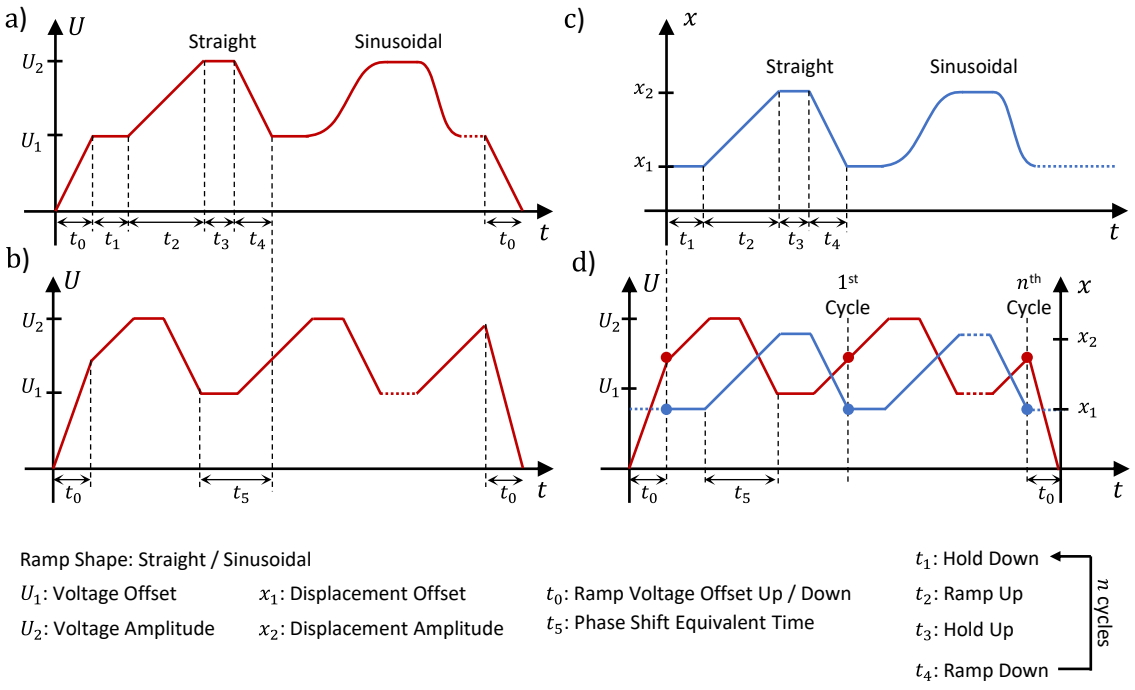

Figure 54: Generation of periodic control voltage signal with no phase-shift (a), with phase-shift (b), as well as generation of periodic displacement control signal (c), and combination of both signals highlighting phase-shift and triggers (d).

By configuring the ramp shape to be straight or sinusoidal, these parameters enable the configuration of typical symmetrical and asymmetrical signal shapes, such as square, sine, triangle, trapezoid and sawtooth, as well as many customized shapes. Two additional timing parameters t_0 and t_5 are given for voltage signal generation. Parameter t_0 allows the voltage to be ramped up to

the initial value of the voltage trajectory within a specific time before starting a periodic test and ramped down again at the end. Thus, dynamic effects of a stepwise voltage increase are avoided, which might lead to an undesired electrical breakdown of a DET test sample. The initial value can be represented by the voltage offset (Figure 54a), but also differ from that due to the configuration of a timing parameter $-t_p < t_5 < t_p$ (Figure 54b), resulting in a phase-shift $-360° < \phi < 360°$, of the periodic signal with periodic time t_p:

$$\phi = \frac{t_5}{t_p} \times 360\,° = \frac{t_5}{t_1 + t_2 + t_3 + t_4} \times 360\,° \tag{3.12}$$

In contrast to voltage generation, the displacement trajectory starts directly from the absolute position previously defined in manual mode, and no phase-shift is provided within the configuration (Figure 54c). However, if both control variables, voltage, and displacement have the same periodic time, they can be defined as phase-shifted via parameter t_5 (Figure 54d). Synchronization is maintained by retriggering each cycle, ensuring that this phase-shift is maintained even during continuous stimulation with a high number (n) of cycles, despite differences in the controller and timing reference of the two signals.

3.6.4 Graphical User Control

The test bench provides a GUI that is generally divided into three permanently displayed areas: One for user-defined control inputs, one for displaying the post-processed results of an experiment, and one for real-time monitoring of all sensor values and device states (Figure 55).

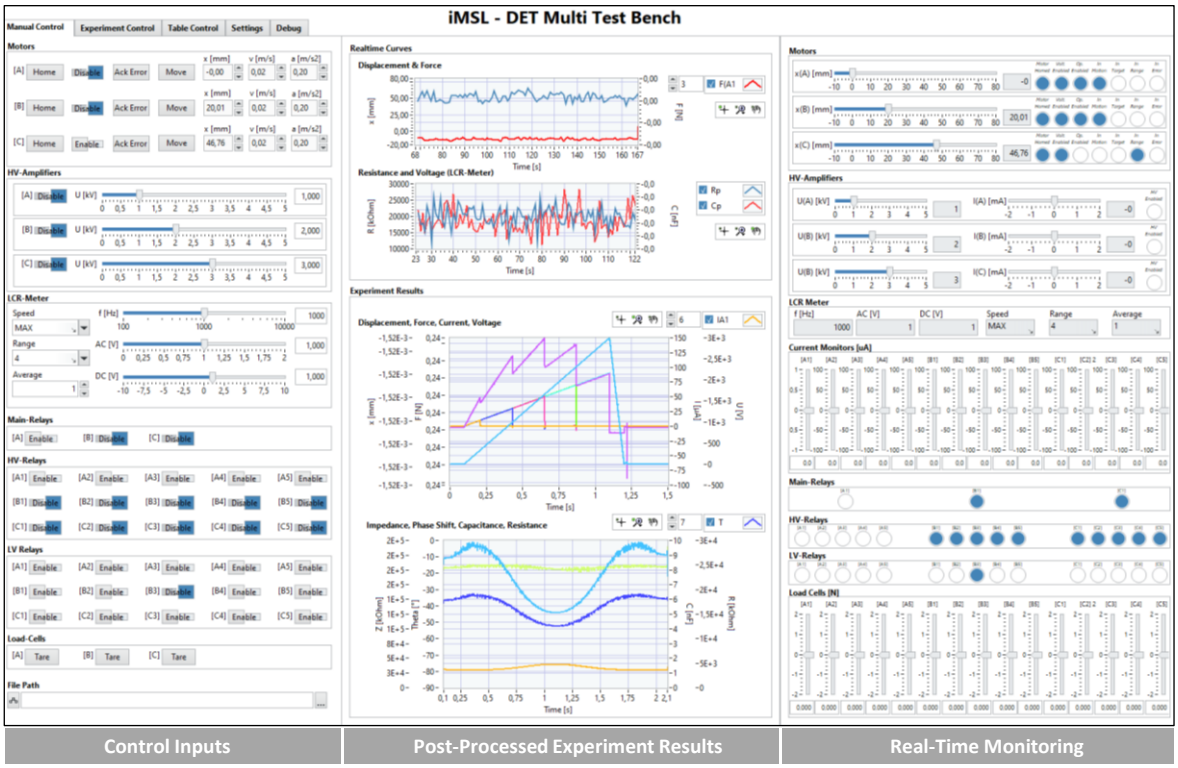

Figure 55: Test rig GUI, divided in three sections: Control inputs with ‘Manual Control’ tab selected (left), post-processed results (center), and real-time monitoring of all measuring quantities and relay states (right).

The control inputs section features a tab control, switching between ‘Manual Control’, ‘Experiment Control’, ‘Table Control’, and ‘Settings’.

The ‘Settings’ tab contains general settings that affect all operation modes of the test rig. These include post-processing settings, calibration values for sensors and actuators, and force and current thresholds for each test station.

‘Manual control’ (Figure 55, left) allows motors, HV-amplifiers, LCR-meter, and force-amplifiers to be operated manually in real-time. This enables the setting of test run start conditions, quick functional testing, and taring of load-cells and current monitors with direct feedback in the real-time monitoring section. Since current and force thresholds are also monitored in this mode, relays and motors will automatically shut down if one of them is exceeded for safety reasons.

‘Experiment Control’ (Figure 56a) enables a single experiment to be configured either for HV-testing using the high voltage amplifier or for LV-testing using the LCR-meter. Individual configuration of motor controller parameters, displacement trajectories, and voltage waveforms allows multiple test conditions to be run simultaneously. During configuration electrical and mechanical control signals are displayed in a preview diagram. The configured experiment can either be executed directly or transferred to the control table with a defined test number. During a test, the only permissible user intervention is to abort the test prematurely. In this case, all motors and high voltage amplifiers are immediately shut down and all relays are connected to ground. After the regular end of a test, the post-processed data is saved and displayed (Figure 55, center).

a)

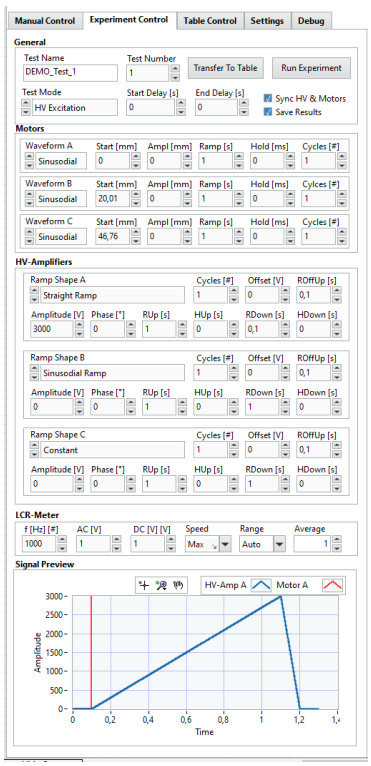

b)

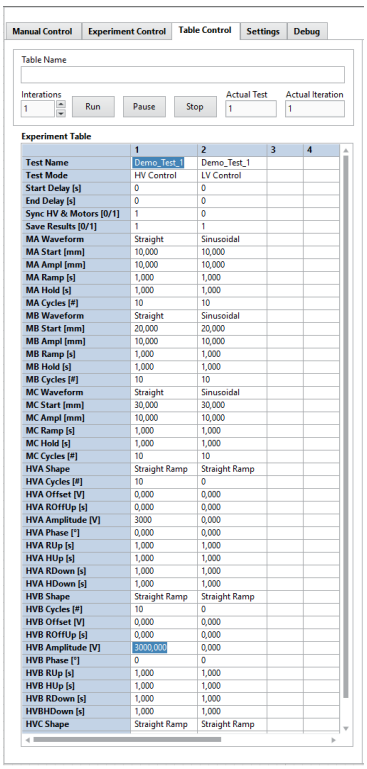

Figure 56: GUI control inputs with selected "Experiment Control" tab (left), and ‘Table Control’ tab (right)

'Table Control' lists all configured experiments according to their test number in a control table (Figure 56b). When the table is executed, all experiments are performed in sequence and the entire sequence is repeated for the configured number of iterations. The data is saved in a corresponding folder and file structure (refer to Section 3.6.5). It is thereby possible to configure whether or not to save data for each individual experiment. This allows, i.e. performing long accelerated fatigue tests without data saving, alternating with short, slow, and precise measurements with data saving and thus saving memory space. The automatic table control process can be paused or aborted, and in either case the current experiment will be completed.

3.6.5 Data Management

At the end of each experiment, the high-resolution raw data is subject to post-processing, which is performed in the host program in consecutive steps before the data is finally saved (Table 2).

Table 2: List of successive post-processing steps, which are conducted to the raw data after each experiment, containing feature extraction (1.), memory size reduction (2.-5.), formatting (6.), and saving (7.).

Post Processing Step (Folder m, File n)	**Before Step**	**After Step**
1. Feature Extraction Impedance Measurement Method	t, x, F, i, u	$t, x, F, i, u, Z, \theta, R, C$
2. Data Filtering (User Configurable) Zero-Phase Butterworth Filter	No Filtering	e.g.: 100 Hz Cutoff
3. Sample Reduction (User Configurable) Save each k-th Sample, Discard Rest	10 kS/s	e.g.: 200 S/s ($k = 50$)
4. Change of Datatype Reduce Bit-Size, Maintain Range & Precision	e.g.: Double 64 bit	e.g.: Single 32 bit
5. Result Filtering		
Delete Data Arrays of Broken DET-Samples		
via Status (Test Station A1...C5)		
$n-1$: Electrical Status 1	F, i, R, C	F, i, R, C
$n-1$: Electrical Status 0	F, i, R, C	F
$n-1$: Mechanical Status 0	F, i, R, C	---
via Status (Module A...C)		
$n-1$: Electrical Status 1	t, x, u	t, x, u
$n-1$: Electrical Status 0	t, x, u	t, x
$n-1$: Mechanical Status 0	t, x, u	---
6. Formatting Structure Data in Common Data Container	Data Arrays	TDMS File
7. Saving Save File in File & Folder Hierarchy	Root (Configurable)	Root / Folder n / File m

In the first step, a feature extraction is conducted in which the measured quantities Z and θ, as well as C and R are derived from the highly resolved raw voltage signals u, and the raw current signals i, if not acquired by the LCR-meter.

The four subsequent steps serve to reduce the amount of data to a reasonable level, as it may require significant memory space, as well as computing resources and time during evaluation, especially for long-term tests.

First, the data is lowpass filtered to eliminate noise, by using a zero-phase digital Butterworth filter using forward-backward filtering, which is user-configurable in terms of filter activation, filter order, and frequency. Thereby, the filter frequency must be set high enough, that the frequencies examined in the experiment are not cut off, leading to a loss of information.

Subsequently the filtered data is reduced by a factor of k, with every k-th sample being stored in a new array and the samples in between being discarded. Based on the fixed data acquisition rate of 10 kHz, k must be selected so that the data reduction matches the previously defined lowpass filter, in order to avoid information loss.

In addition to this sample reduction, the memory usage of the data is further reduced by converting the data types into suitable data types with lower range or precision (e.g. 64-bits double to 32-bits single). A suitable choice of units ensures, that the necessary minimum range and precision of data are maintained.

In the final data reduction step, data arrays that do not contain any relevant information are sorted out and deleted. This is achieved for the actual iteration m by considering the electrical and mechanical (Boolean) states of the individual test stations, that have been obtained in the previous iteration $m - 1$. These are set to zero, if the user-defined current and force thresholds respectively have been exceeded in that experiment. Thus, the DET samples applied to these test places are assumed to be defective, i.e. due to electrical breakdown or mechanical tear-through, and the corresponding measurands do not contain any relevant information and must not be further considered for evaluation purposes. However, this approach ensures that the last measurement in which the sample was not yet defective is saved. It is applied to both, the quantities that are acquired individually for each test station (A1…C5), and to the quantities that are related to the modules (A…C).

The reduced data arrays are then converted into a well-structured common file container (Figure 57, right) and saved in a defined file and folder hierarchy (Figure 57, left). Therein, the user-defined name of one experiment sequence corresponding to the name of the configuration table is assigned to the common main folder. According to the number of m iterations with n individual

experiments, this folder contains n subfolders (automatically named: ‘I1’, ‘I2’, …, ‘In’), each of which contains m files (automatically named: ‘E1’, ‘E2’, …, ‘Em’).

The *NI-TDMS* file format (Technical Data Management Streaming) enables the storage of large amounts of data of different data types in a well-structured data container. The file format is structured using three levels of hierarchy, namely file, group, and channel. The top level (file) contains metadata with information on the file name, file path, author (operator), saving date and time, as well as an overview of the data, which is organized in groups and channels and provided with information on data type, unit, and size. On the group level, data arrays of the same measurand, unit and device-order i.e. individual test station (A1, A2, …, C5) or entire module (A, B, C), are grouped together, whereas each data array represents one channel.

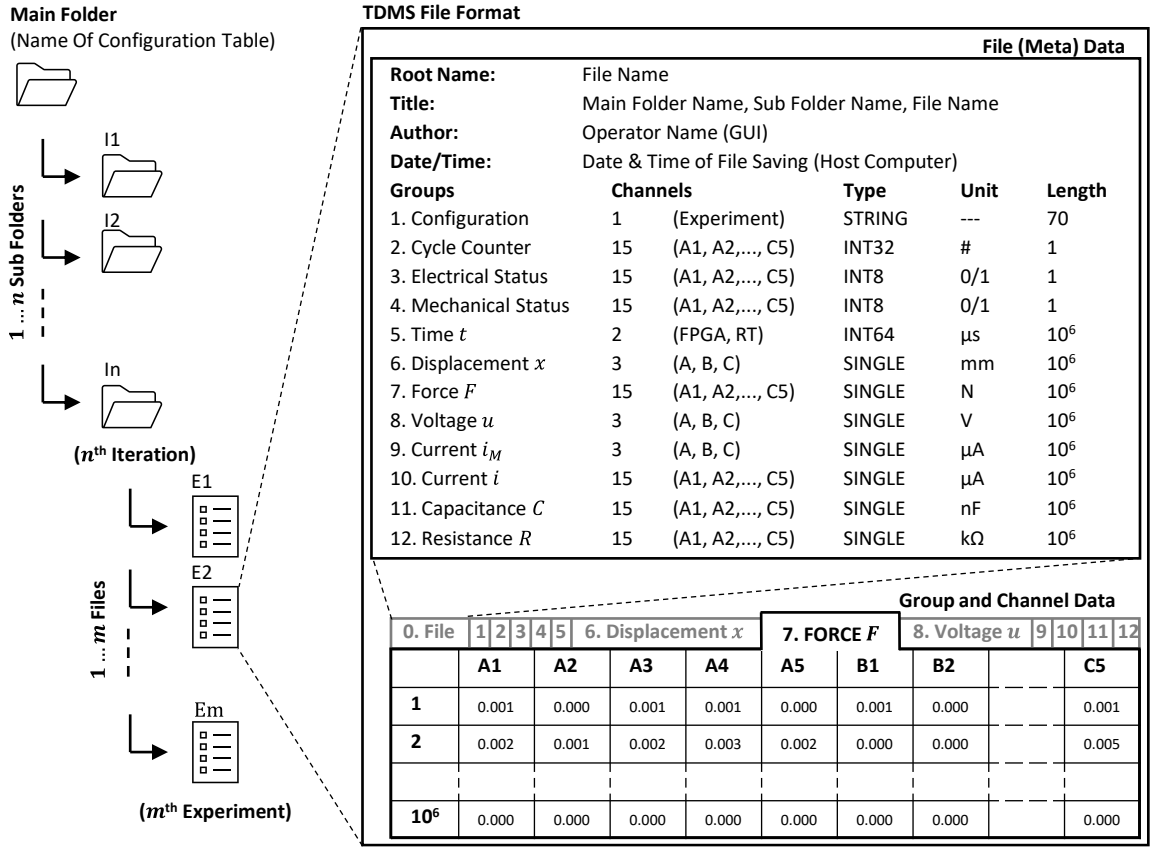

Figure 57: Schematic illustration of folder and file hierarchy for saving experiment results (left), and of a TDMS file, providing a clear structure of the data acquired for one experiment, while maintaining the defined data types (right).

For example, the "Voltage u"-group contains three data arrays (channels) with voltage values, each of which has been acquired with the common voltage monitor of the respective modules (A, B, C). The "Force F"-group, on the other hand, contains 15 data arrays (channels) with force values, each of which has been acquired with the individual load-cell of the respective test station (A1, A2, …, C5).

Tools are provided to import the TDMS file into common data analysis programs such as *Microsoft Excel* and *MathWorks MATLAB*, which enable further processing and evaluation of the data outside of the *NI LabVIEW* environment. In *Excel*, each group is represented by a sperate tab-selected worksheet, in which the individual channel data is provided in table columns next to each other (Figure 57, lower right). An additional worksheet is created to provide an overview of the metadata (Figure 57, upper right). Similarly, the groups are converted into a cell array in *MATLAB*, whereby each cell contains a table with the individual channel data provided in table columns next to each other. Since irrelevant data arrays and thus channels are sorted out in the post-processing, the number of channels per group can be reduced in the progress of an experiment series, as the data from defective DET samples are no longer saved. It is therefore important that the channels are selected by name and not by location during data extraction.

3.6.6 Conclusion on Control and Software

Hardware embedding, software architecture, user control, and data management of the test rig, aim to achieve flexible experiment configuration, high precision, and throughput, along with safe and robust automatic long-term operation, user-friendly control, and efficient data saving.

The central control units of the test rig consist of a standard host computer connected to a GSM-module, primarily integrating safety instruments, and a RT-System, primarily integrating test instruments. The RT-system is equipped with an FPGA-controller, used to control and measure analog signals and digital states, and a RT-controller, used for communicating with test instruments via digital transmission protocols.

Accordingly, the software architecture, implemented in a *NI-LabVIEW* programming environment, consists of three program parts: Host-program, FPGA-program, and RT-program. The host-program facilitates user control and monitoring, manages general program flows, and enables configuration, execution, post-processing, and data saving of test routines. FPGA- and RT-program facilitate deterministic communication with the respective connected test instruments, ensuring data transfer rates via real-time FIFOs and real-time synchronization via global variables.

The test rig GUI features three sections: One for user inputs, one for displaying experiment results, and one for real-time monitoring of sensor values and device states. It provides the user with manual real-time control and monitoring of all test instruments, as well as the configuration of automatically running test routines. These can be transferred to a control table, enabling sequential execution of multiple experiments for a specified number of iterations, which is particularly beneficial for fully automatic long-term testing.

Experimental data is post-processed with configurable feature detection, filtering, data reduction, and formatting. The data is packed into a well-organized and space-efficient container file format and stored in an automatically generated folder structure.

3.7 Experimental Validation

Mechanical and electrical control and measuring devices are validated and calibrated through experimental procedures, thereby utilizing standard reference components, including tensile springs, resistors, and capacitors. This approach is essential, as the complex electromechanical characteristics of DETs undermine the reproducibility and comparability of the experimental findings, making them unsuitable to be used as references.

3.7.1 Displacement Control and Force Measurement

For mechanical control and measurement, validation primarily targets the load and temperature dependency of the test rig and its components, focusing on measurement accuracy, repeatability, and reproducibility across different test stations. For this, load-cells and motors are individually tested across their entire control and measuring range. Subsequently, they are integrated into the measurement platform, where exemplary measurements are conducted to evaluate their combined characteristics.

Load-cells

The load-cell signals (*ME KD40s 10N*) are amplified by the signal amplifier (*ME GSV-1A4*) and transmitted to a 24-bit voltage acquisition module (*NI 9202*) of the RT-System (*NI cRIO-9047*). To exemplary validate temperature dependency and linearity, one representative load-cell is attached to a horizontally aligned aluminum cantilever inside the climate chamber (Figure 58a). Precision weights ranging from $0.05\,\mathrm{kg}$ to $1.00\,\mathrm{kg}$ are consecutively attached to the load-cell through the climate chamber's porthole, and static force measurements are conducted, beginning with the lowest and progressively increasing to the highest weight. These measurements are repeated at various temperatures between $0\,°\mathrm{C}$ and $80\,°\mathrm{C}$ in $20\,°\mathrm{C}$ increments, with a waiting period of $15\,\mathrm{min}$ after a temperature change (Figure 58a). Plotting measuring force F_{LC} against the nominal force F_N yields temperature-dependent characteristic sensor curves (Figure 58b). From a linear fit of the corresponding sensor gains over temperature, a linear temperature dependency $c_{TL} = 0.012\,\%/\mathrm{K}$ is derived (Figure 58c). The absolute linearity error is determined by subtracting the measured force from the temperature-corrected nominal force (Figure 58d). The error shows consistent trends across all temperatures within a range of $\pm 2\,\mathrm{mN}$, whereby systematic deviations probably occur due to factors such as deformation of the experimental setup or inaccuracies in the calibration weights. The exemplary determined linearity and temperature characteristics obtained with these experiments closely align with the data sheet values and represent the typical properties of the load-cell [163]. This also validates that no measurement signal errors are induced within the signal transmission chain of the test rig. The remaining load-cells undergo less extensive validation measurements and are only verified for their sensor characteristic constant.

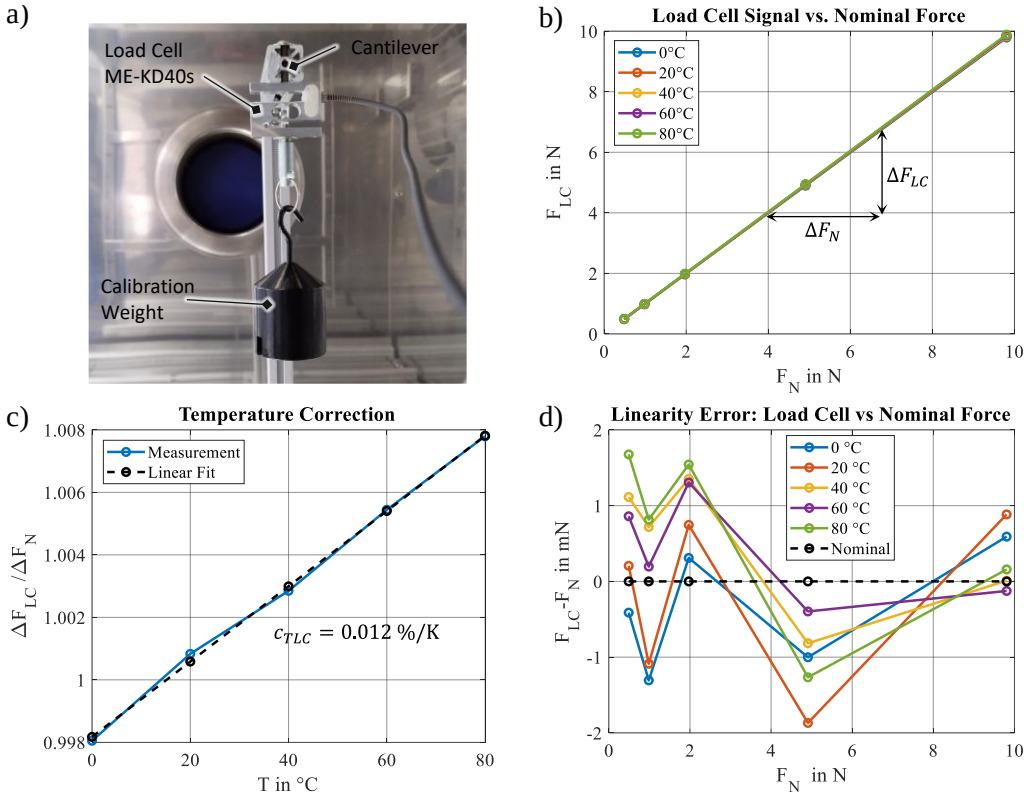

Figure 58: Exemplary load-cell validation, by conducting measurements on various calibration weights within various temperatures in the climate chamber test room (a), plotting resulting measuring force over nominal force curves (b), and determining temperature coefficients (c), as well as and linearity (d).

To specify general linearity error and temperature dependence of the force measurement, the confirmed typical values from the load-cells' datasheet are anticipated, thus an absolute linearity error margin of ± 2 mN, and a temperature correction $c_{TL} = 0.01$ %/K. However, this level of accuracy is applicable only during short loading and unloading durations. For longer constant loading, sensor creep, typically in the range of 0.1% of the applied force, needs to be considered.

Motors

The motors used for mechanical control (*LinMot PS01-23x160H-HP-R & H01-23x166/80*) are connected to the RT-System (*NI cRIO 9047*) via a real-time capable *EtherCAT*-interface. Since no alternative position sensor is installed in the setup to measure the displacement, the motor positioning via motor-internal position sensor is examined for its temperature characteristics and linearity error over the full travel range. For this purpose, the motor is operated with a 0.2 Hz sinusoidal waveform inside the climate chamber over its entire travel range, and the displacement is measured with a laser sensor (*Micro-Epsilon optoNDCT 1900-100*). The laser is located outside the climate chamber and the laser beam is directed through the port opening onto the motor slider (Figure 59a). These measurements are repeated at various temperatures between 0°C and 80°C in 20°C increments, with a waiting period of at least 30 minutes after a temperature change. Plotting the laser position signal x_L against the demanded motor position signal x_D yields temperature-dependent characteristic motor positioning curves (Figure 59b). Through a linear fit of the

corresponding gains over temperature, a linear temperature correction factor $c_{TM} = 0.003\,\%/\mathrm{K}$ is obtained (Figure 59c). The linearity error is determined by subtracting the measured laser position signal from the demanded position signal (Figure 59d). The error shows consistent trends across all temperatures within a range of $\pm 0.3\,\mathrm{mm}$. Plotting the motor's internal position sensor error demonstrates, that the linearity error mainly arises from sensor imprecision of the motor, as the motor reliably follows the specified trajectory within $\pm 0.02\,\mathrm{mm}$ error margin (Figure 59e). The absolute positioning error is decreased for shorter travel distances by addressing systematic linear error trends through adjustment of the motor gain using the least squares error method. This method can, for instance, reduce the error range by half within the first $5\,\mathrm{mm}$ of travel (Figure 59 f).

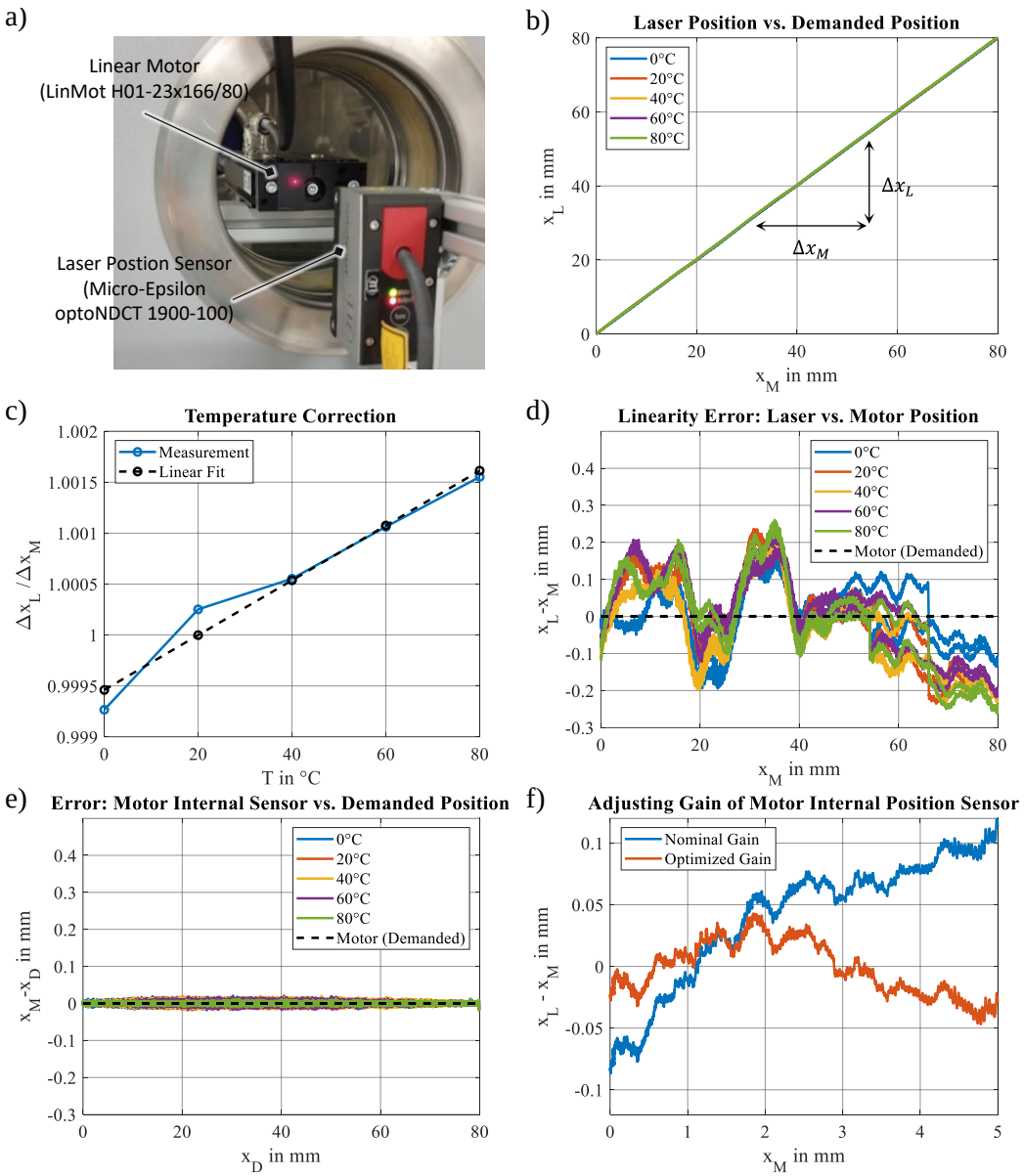

Figure 59: Motor validation by measuring the full motor travel at different temperatures in a climate chamber using a laser (a), acquiring curves of measured displacement over nominal displacement (b), determining temperature correction coefficients (c) and linearity (d), as well as assessing motor positioning control error (e). Adjusting the motor's internal position sensor gain results in a reduced linearity error (f).

In general, utilizing this method yields a positioning accuracy of approximately 1 % of the travel distance. Thus, this gain is implemented as user-configurable in the test bench GUI. Additionally, there is the option to select between two different PID controller configurations for motor positioning: A precision optimized parameter set for stiff control characteristics ensures highly accurate positioning but only at low travel speeds, for instance, a maximum of 0.1 Hz sinusoidal for 10 mm travel, as higher frequencies lead to instability (Figure 60a). Conversely, the second parameter set is designed to enable higher travel speeds, for instance allowing for a 10 Hz sinusoidal waveform for 10 mm travel, with precision being sacrificed (Figure 60b).

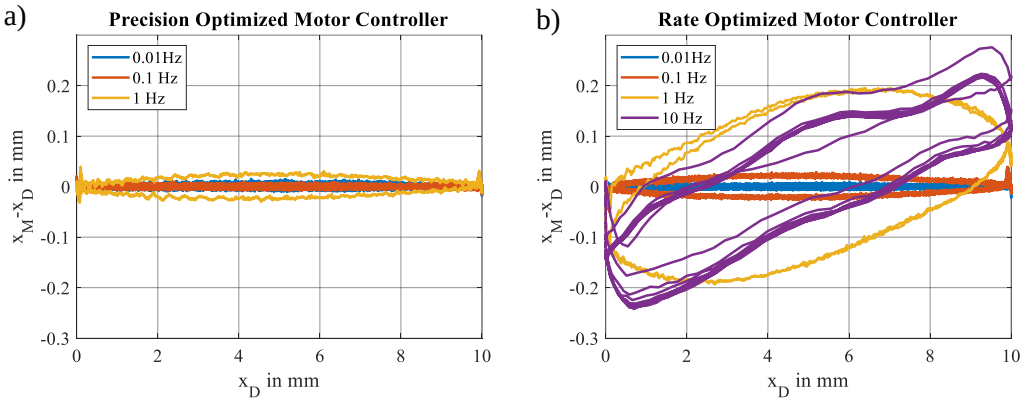

Figure 60: Motor positioning error using the precision optimized motor controller parameter set results in high precision positioning, but low travel speeds (a), whereby the rate optimized motor controller parameter set enables higher travel speeds, but less accuracy (b).

Mechanical Compliance

The stiffness of the test setup is evaluated by short-circuiting the opposing sample grips with a rigid 3D-printed dummy 3D-printed from glass-filled epoxy material (*Fromlabs Rigid 4000*) and conducting a displacement-controlled tensile test (sinusoidal, 0.1 Hz, 75 µm) (Figure 61a).

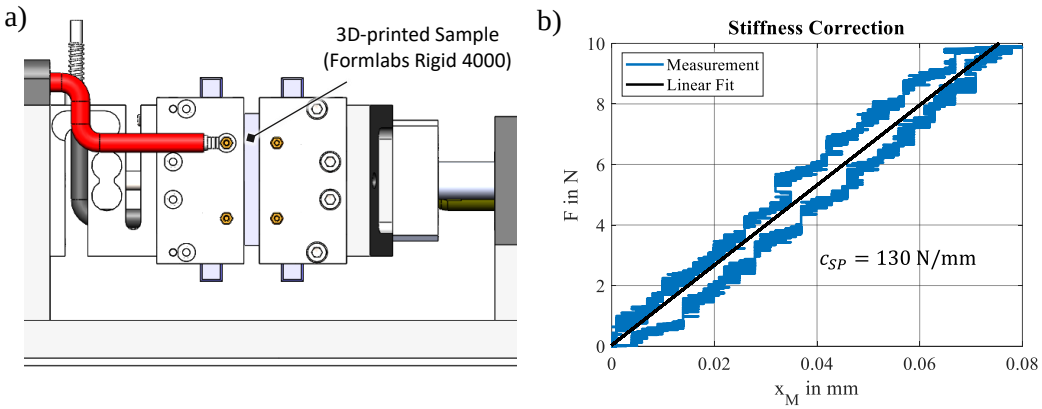

Figure 61: Stiffness test by mechanically short circuiting the opposing sample grips with a rigid 3D-printed dummy (a), followed by conducting a tensile test to derive the stiffness correction factor from the resulting force-displacement curve (b).

The gradient of the resulting force-displacement curve yields a typical stiffness correction factor of $c_{SP} = 130\ \mathrm{N/mm}$.

Thermal Expansion

The expansion of the mechanical platform due to temperature variations affects the distance of the clamps, thereby influencing the (pre-) strain applied to the samples. This effect is compensated for, by determining the corresponding thermal expansion correction factor c_{TP}. This factor is obtained by measuring various clamping distances using a caliper (*Holex 150HM*), starting from 20 mm and increasing in 40 mm increments up to 140 mm, both at 20 °C and after heating the platform to 80 °C (Figure 62a). The results indicate a regressive thermal expansion over increasing clamping distance, resulting in a temperature correction factor c_{TP} ranging from 4.2 %/K to 2.5 %/K (Figure 62b). This may be attributed to measurement inaccuracies at small clamping distances, but also to the fact that the construction materials have different coefficients of thermal expansion, especially the aluminum platform and the steel motor and guide elements, which affect the clamping distance to different degrees at different clamping distances.

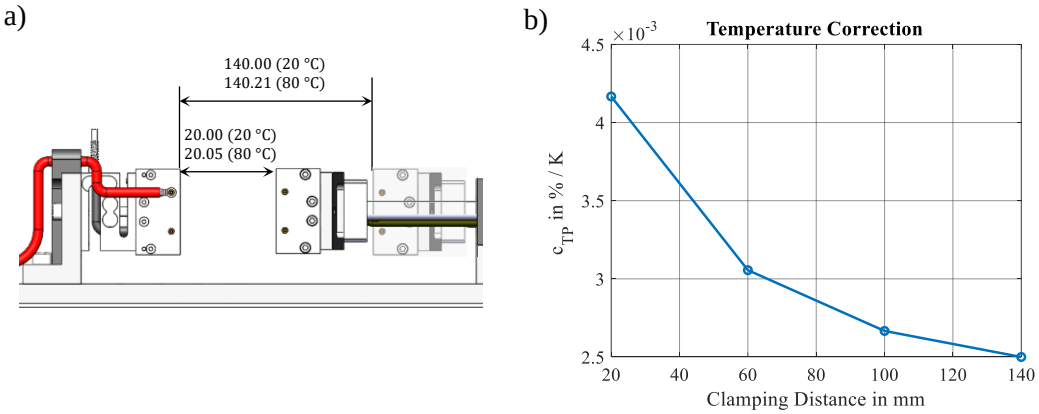

Figure 62: Thermal expansion test by measuring various clamping distances for both, at 20 °C and after heating the platform to 80 °C (a), resulting in a regressive thermal expansion over increasing clamping distance (b).

Combined Force-Displacement Measurements

All components of the mechanical platform are precision-manufactured and consistently aligned during assembly. The use of dowel pins guarantees the reproducibility of alignment, facilitating disassembly and reassembly while maintaining precision. Apart from the manufacturing and assembly-related tolerances, the mechanical setup is subject to a slight bearing clearance of the linear motor. The opposing sample grips therefore have minor deviations in clamping distance, height offset, width offset, and tilt (Figure 63a). These tolerances typically fall within the lower µm-range and may exhibit slight variations depending on the alignment, slider position and load. Due to the challenges associated with direct measurement, repeatability and reproducibility are evaluated experimentally. This is achieved by evaluating the force-displacement characteristics of a linear tension spring, which is connected at both ends to similar clamps as those of the SIPs to also account for the test sample mounting (Figure 63b).

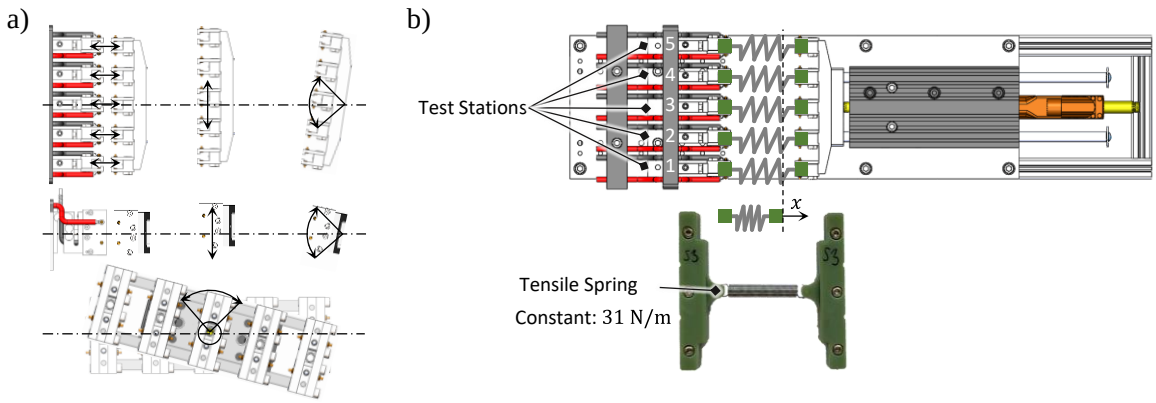

Figure 63: Qualitative illustration of position tolerances of test stations with minor deviations in clamping distance, height offset, width offset, and tilt (a); and test stations equipped with tensile springs, to experimentally evaluate repeatability and reproducibility, which could potentially be influenced by these tolerances (b).

To evaluate repeatability, the spring is measured consecutively five times on the same test station (test station 1). During these measurements, the spring undergoes a 5 mm pre-stretch and is deflected by 15 mm with a constant stretch rate of 3 mm/s (Figure 64a). The resulting force-displacement curves are consistent, and the spring constant 31.3 N/m is obtained from their slope in each case, which is close to the nominal value of 31.0 N/m (Figure 64b). The deviations of the measurement repetitions become visible by averaging the force-displacement curves over all measurements and plotting the absolute error against this mean value (Figure 64 c).

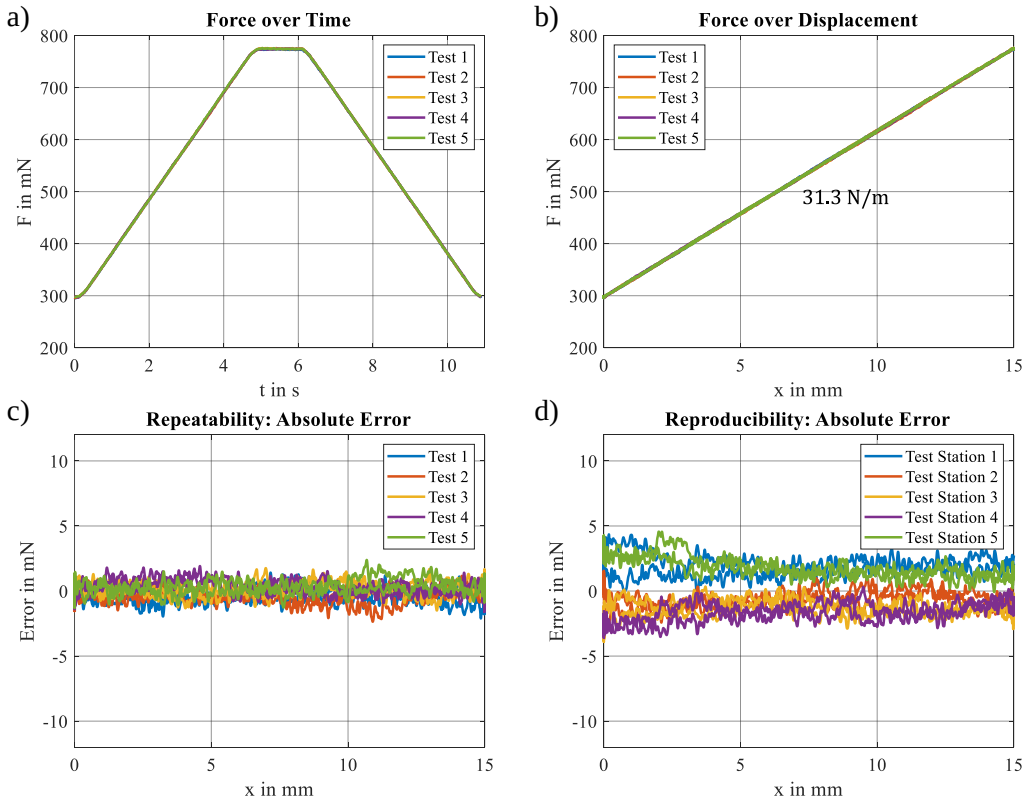

Figure 64: Results of repeatability and reproducibility experiments performed on a linear spring sample, showing force-time curves (a), force-displacement curves (b), absolute error in repeatability (c), and absolute error in reproducibility (d).

The errors show linear and horizontally distributed pattern scattering around the mean within a narrow range of ± 3 mN. Assuming that this error is only due to the positioning error of the motor, dividing it with by the spring constant, results in a total positioning error of ± 90 µm. Conducting the same experiment consecutively at each of the five test stations, rather than repeating it at the same station, allows absolute errors to be assessed in terms of the reproducibility of measurements at each specific test station (Figure 64d). The resulting force errors also show a horizontally distributed pattern without systematic gradients, scattering with an offset from the mean within an absolute error range of approximately ± 5 mN. Assuming that there is no error due to the different calibrated load-cells, dividing this error with the spring constant results in a total positioning error of ± 160 µm. These results show that repeatability and reproducibility errors are in the same order of magnitude as the accuracy of the force measurement and the positioning themselves, thus indicating satisfactory values.

Strain Rate Dependency

Conducting the above-described test at different strain rates (e.g. 0.3 mm/s, 3 mm/s, and 30 mm/s) shows in consistent force-displacements curves (Figure 65a). A minimal increase in hysteresis becomes visible for higher stretch rates only if the absolute error of the corresponding measurements with respect to a linear fit of the respective curves is considered (Figure 65b). This is possibly attributable to friction in the spring attachment, but negligible in comparison to hysteresis of DETs, which are typically in a higher order of magnitude.

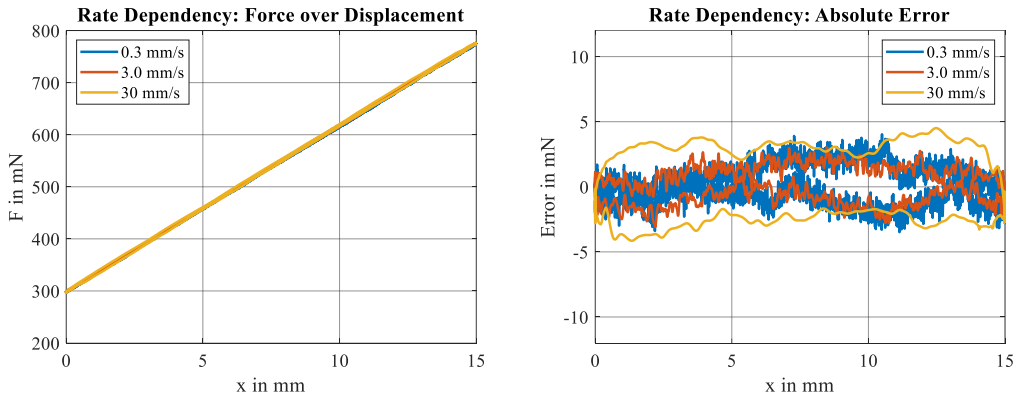

Figure 65: Results of rate dependency experiments performed on a linear spring sample; with force-displacement curves (a) and absolute error relative to a linear fit of the respective curves showing minimal increase in hysteresis (b).

3.7.2 Voltage Control and Current Measurement

Considering one test station of a test rig module, the individual current monitor is connected to the common high voltage amplifier via one low voltage relay and two high voltage relays, with the respective wiring, and sample grips in between. A closed signal channel is only created, if a test sample, i.e. a SIP, is electrically connected between the leaf spring contacts of the (left side) sample grip. The channels are located next to each other and electrically connected in parallel via the

common high voltage amplifier and the common reference potential. This makes them susceptible to signal crosstalk due to reference potential fluctuations as well as electric and magnetic interference fields. Since the common reference potential is connected to ground (earth) and all components are connected in a star configuration with equal-length leads, most parasitic currents flow off and fluctuations are avoided. In addition, design elements such as sufficient safety distances, shielding and twisted pair wiring prevent signal crosstalk (refer to Section 3.5) However, all components and connectors of the individual channels are potential sources of error, leading to minor deviations in their electrical properties (i.e. parasitic lead resistance, capacitance, and inductances), which can further change during operation. These deviations are compensated by means of a calibration.

The components of each signal channel, in particular current monitors and high voltage amplifiers, are calibrated individually. The gains of the proprietary developed current monitors (i.e. nominal 10 µA/V) slightly vary mainly due to the tolerance of the shunt resistors utilized in the transimpedance circuits. Hence, they are calibrated by applying a reference current on their input with a function generator (*Keysight 33250A*) and measuring the output with an oscilloscope (*Keysight DSXO2004A*).

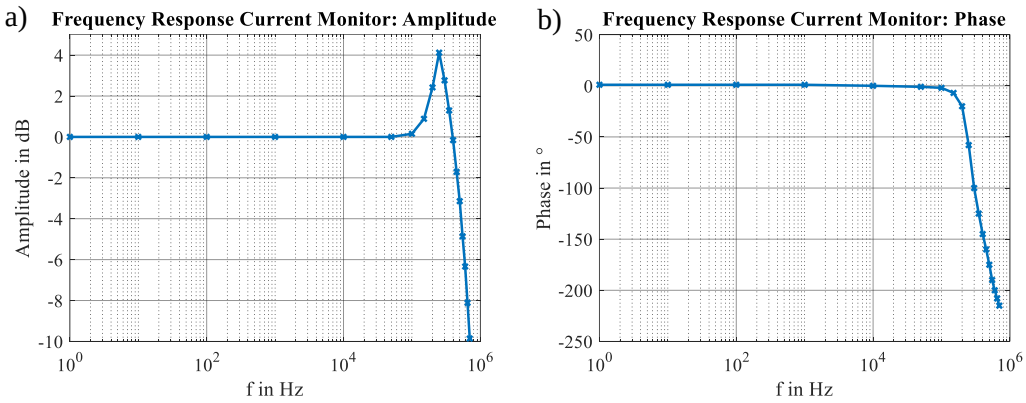

Figure 66: Typical frequency response of proprietary current monitors (transimpedance circuits); with current amplitude response (a), and phase response (b).

As the current monitors are also used for impedance measurement using the HV-method, they are tested for their frequency response with the same setup, by applying sinusoidal voltage curves subsequently with increasing constant frequency. The resulting Bode diagrams of amplitude (Figure 66a) and phase (Figure 66b) demonstrate constant characteristics beyond 10 kHz, which is consistent to the specified voltage monitor bandwidth of the high voltage amplifier [165]. Hence both devices, high voltage amplifier, and current monitors feature similar and sufficient bandwidth since the maximum utilized testing frequency is limited to 5 kHz (refer to Section 3.5.3).

The voltages applied to the test objects of the individual channels vary slightly and are usually lower than the value specified by the common voltage monitor, as the parasitic resistances of

relays, wires and connectors create voltage dividers. As these voltages are not measured individually, the parasitic resistance R_P for each channel can be determined with an additional calibration step. In this, the entire signal path of each channel is considered, by connecting a (high voltage) shunt resistor between the electrical contacts of the (left side) sample grip, to create a closed circuit. The shunt is soldered between the copper contacts of a (left side) SIP clamp, enabling it to be inserted into the sample grip, and to be electrically connected via the leaf spring contacts (Figure 67a). This ensures, that the contacting of the sample itself is included in the calibration. The shunt is dimensioned in order to widely utilize the measuring range of the current monitors (i.e. 33 MΩ for measuring range ± 100 µA). By applying constant high voltage U with the high voltage amplifier and measuring resulting current I in the signal path with the individual current monitor, the true voltage U_S over the shunt resistor is given (Figure 67b).

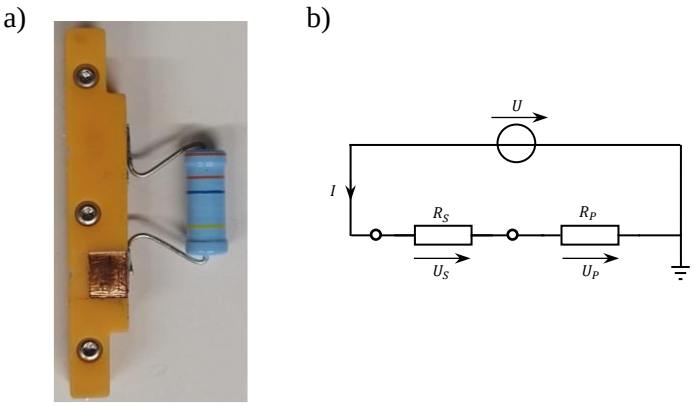

Figure 67: Photo of high voltage resistor Vishay VR68 soldered to a SIP clamp (a), enabling it to be inserted to the test station sample grips, to determine true measuring voltage and parasitic measuring voltage via current measurement as shown with an equivalent circuit (b).

Hence, the parasitic resistance R_P is obtained:

$$R_P = \frac{U - U_S}{I} \tag{3.13}$$

Assuming a constant R_P, this can be used as voltage correction factor to determine the true voltage U_S over the test sample (i.e. SIP), by rearranging (3.13) accordingly. For high voltage control, describing voltage amplitudes is sufficient since it is based on quasi-DC signals and the signal path is considered to be purely resistive. For AC impedance measurement with LV-method and HV-method, however, parasitic capacitances and inductances must also be considered. Hence a separate calibration is carried out for this purpose (refer to Section 3.7.3).

Accuracy of Current and Voltage Signals

Accuracy of voltage control combined with current measurement is evaluated by means of an exemplified experiment conducted to a high voltage resistor sample (Vishay VR68, 33 MΩ) mounted to a calibrated test station (refer to Figure 67a). A commanded voltage u_D is applied to it covering the entire amplifier output range (1 Hz, 0 ... 3 kV). The corresponding measured voltage

signal u is obtained by the voltage monitor of the HV-amplifier and a current i by the individual current monitor (Figure 68a).

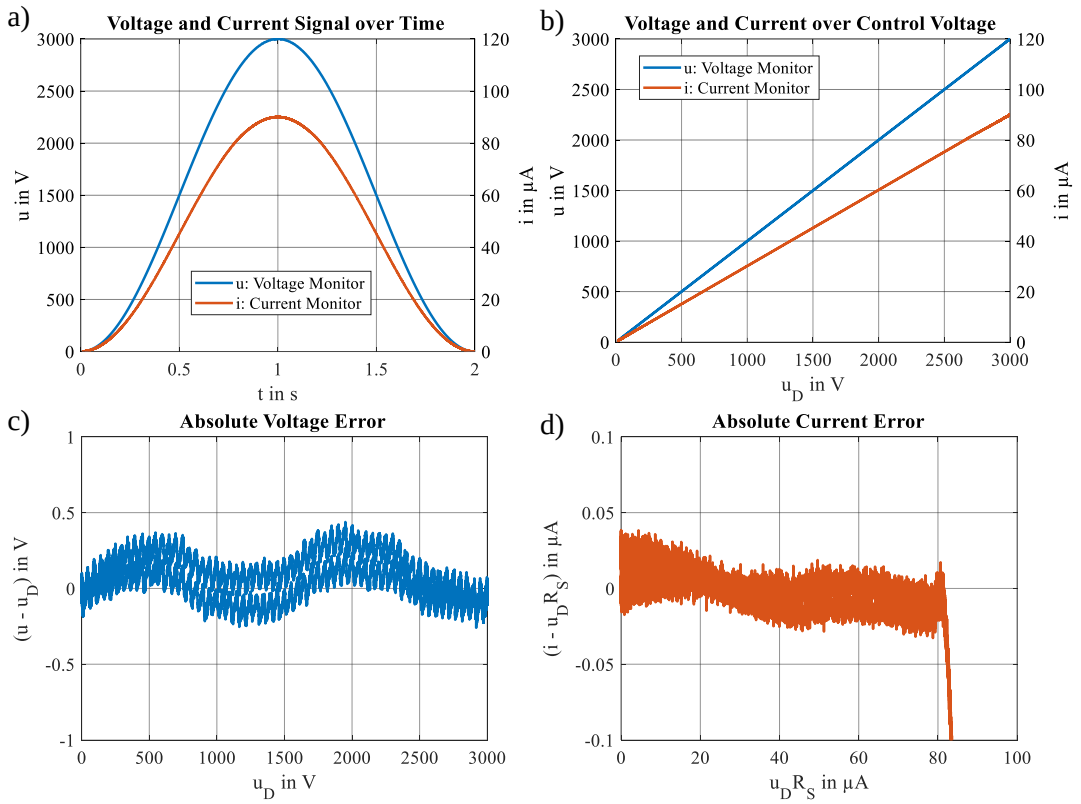

Figure 68: Typical voltage and current obtained with voltage monitor and individual current monitor of one test station, by applying a sinusoidal voltage to a high voltage resistor sample inserted to the sample grip; with results over time (a), control voltage (b) and respective errors (c, d).

Plotting u and i over u_D, both measurements exhibit a linear characteristic (Figure 68b). Considering the absolute error between u_D and u (Figure 68c), the amplifier ripple is clearly visible, which aligns with data sheet value of ± 150 mV [165]. Linearity shows no systematic trend, resulting in a typical total error margin within ± 0.5 V. If the current monitor error is considered in the same way, using the product of R_S and u_D as current reference, it shows sufficient linearity with a slightly decreasing trend until 80 µA is reached. This characteristic is obtained for each channel, various resistive loads, and measuring ranges. It is attributed to the limits of operational amplifiers and diodes utilized within the current monitor circuits, which affect the signal output if it is higher than 80 µA. Up to that point the typical total error margin is within ± 0.05 µA. However, the range between 80 µA and 100 µA can also be used if higher errors are tolerable.

In order to further reduce the error for both measurands, u and i, signal ripple and higher frequency noise can optionally be low pass filtered. For filtering with passive elements, the common high voltage input of the respective HV-boards and the outputs of the individual current monitors of the respective LV-boards are provided with bridges and placeholders for resistors and capacitors (refer to Section 3.5.2). However, as with digital filtering, these filters change the

frequency response of the signals and thus must be designed carefully, especially for experiments that include impedance measurement using HV-method.

Repeatability and Reproducibility of Current and Voltage Measurement

To demonstrate and compare the repeatability of voltage and current measurements of one test station, the above experiment is carried out five times in succession, with the same sample placed to the same test station. The standard deviations are calculated from the measurement results, and the error of these standard deviations from their mean value is used to assess the repeatability of the experiments: a narrower spread of these errors indicates better repeatability. The errors are normalized by the respective maximum current (100 µA) and voltage (3 kV), to obtain a relative representation for comparison of both quantities. With a similar error within ± 20 ppm, the results show that voltage and current measurements are highly repeatable (Figure 69a). If this experiment series is carried out by placing the same test sample from one test station to the next, the result gives information about the reproducibility of the experiments with regard to different test stations. It shows that the error spread of the current measurements is significantly higher than this of the voltage measurements, and the current measurement reproducibility thus lower (Figure 69b). This is attributed to the calibration errors of the individual current monitors, while the voltage measurement results all refer to a single calibrated device. It also shows that the signal path (parasitic effects due to relays, connectors, and wiring) has less influence on the reproducibility of the experiments than the calibration of the devices themselves. However, an error range of ±0.04 % provides sufficient reproducibility for the use of the test rig.

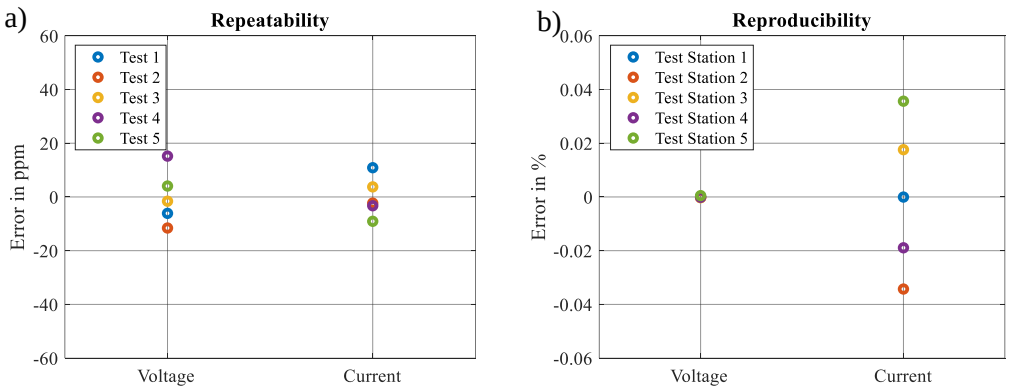

Figure 69: Error of the standard deviations from their mean value for full range voltage and current measurements consecutively conducted to the same high voltage resistor sample; carried out on the same test station to evaluate repeatability (a), and on five different test stations to evaluate reproducibility (b).

Switching Characteristics and Crosstalk of High Voltage Relays

To test and validate the switching characteristics of the HV-relays, all test stations of a test module are equipped with similar high voltage resistor samples (Vishay VR68, 33 MΩ). Each test station is configured such, that the sample is connected to the HV-amplifier via the respective HV-relay, and to the individual current monitor via the respective LV-relay. Thus, in the experiment, the same

voltage ramp (0 ... 3 kV) is simultaneously applied to all samples and similar individual current measurements are obtained for each sample. However different current threshold values are configured as switching conditions for the relays, increasing from one test station to the next (10 µA, 30 µA, 50 µA, 70 µA, 90 µA). Consequently, the HV-relays disconnect the sample from the HV-Amplifier successively during the experiment. If this voltage ramp is applied slowly, e.g. with a rising time of 10 s, the samples are disconnected with high precision and negligible delay, when reaching the respective threshold (Figure 44a). The result shows that the detection is very robust, and all relays switch off at the correct threshold value. This robustness is attributable to the low signal crosstalk, and to the detection algorithm, which does not consider single threshold violation, but a configurable number of violations within a configurable number of samples, i.e. 5 out of 10 within a sample rate of $f_S = 100$ kHz (refer to Section 3.6.2). Detailed view to the switching of one relay (number 3) shows, that disconnection of the sample does not affect the voltage signal, and only slightly affects the signals of those current monitors, that are still connected (Figure 44b, c). As their current signal is pulled down during the switching event, it does not affect threshold detection. The influence of the switching process on the already disconnected current monitors is increased due to their floating state (Figure 44c), but as they are not connected to a sample, this is of no significance.

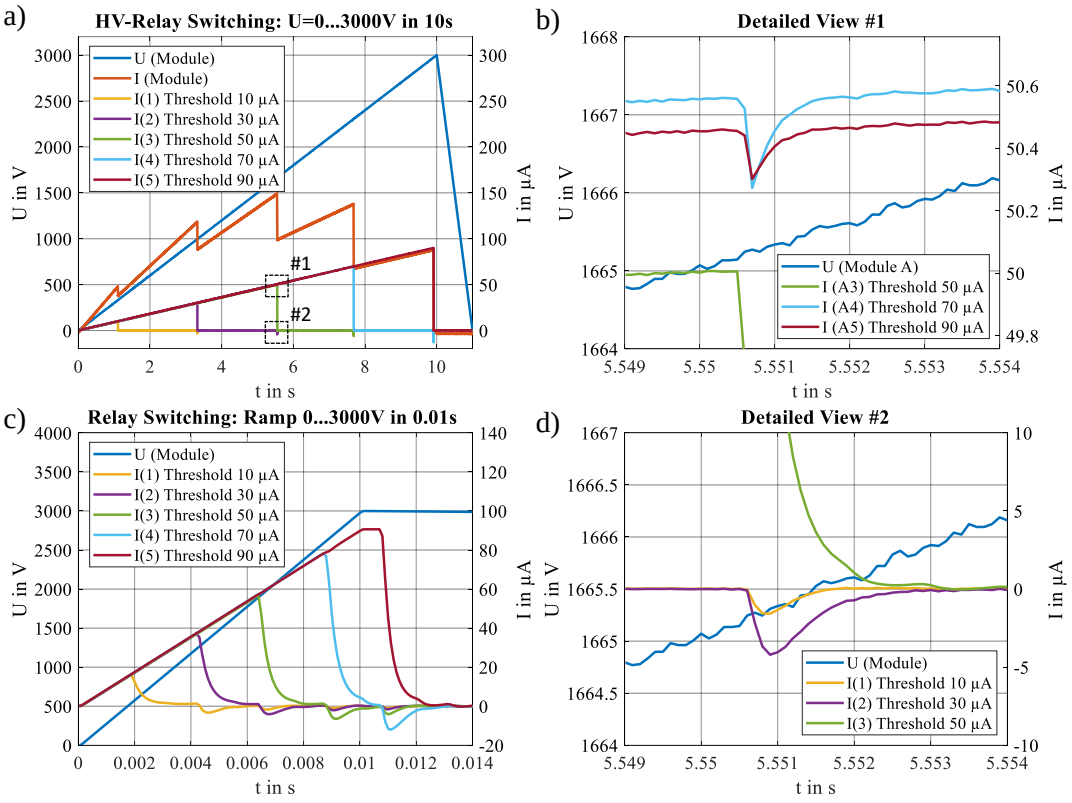

Figure 70: Current response to voltage ramp simultaneously applied to all tests stations, equipped with similar resistor samples and configured with different current thresholds as relay switching condition; with slow rising time (a), and high rising time (b), as well as detailed view to one switching occurrence (b, d), as well as with fast rising time.

If the experiment is performed quickly, such as with a rise time of 0.1 s (Figure 44c), the samples are also correctly disconnected with minimal crosstalk, but the apparent ∼1 ms release time becomes non-negligible and leads to the thresholds being exceeded. The fact that the release time is below the value specified in the datasheet (2 ms) [164] confirms the minimal impact of threshold detection, validating a highly effective implementation.

Synchronization of Voltage and Displacement

Since the periodic trajectories for high voltage and displacement control are generated by different devices and thus based on different timers, they are synchronized after each period (refer to Section 3.6.23.6). Moreover, voltage trajectories can be customized with user-defined positive or negative phase-shifts (e.g. $\phi = +45°$ and $\phi = -45°$) relative to displacement trajectories, with start and end values approached using user-defined ramps (Figure 71a). Measuring the absolute phase-shift error between synchronized sinusoidal trajectories of various frequencies (e.g. 0.1 Hz, 1 Hz, 10 Hz) over longer time (e.g. 100 s) proves, that the signals do not drift apart, but are continuously corrected, resulting in a positive mean error (Figure 71, b).

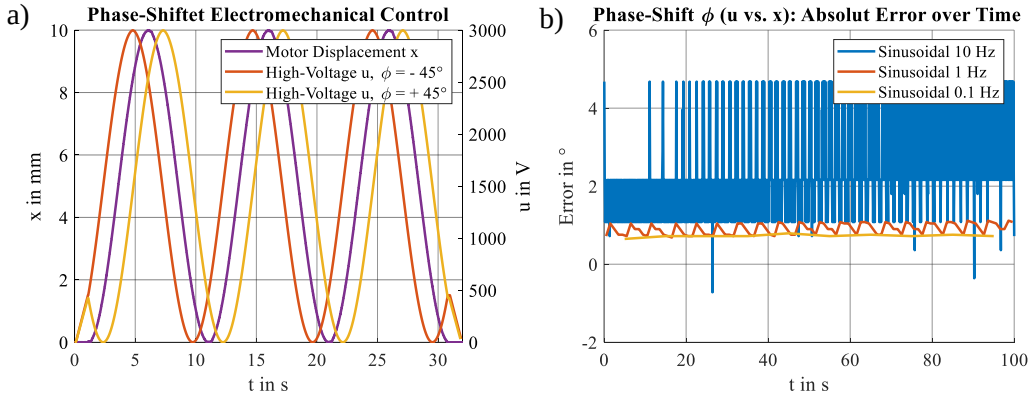

Figure 71: Voltage waveforms provided with user-defined phase-shifts relative to the displacement trajectories (a); with synchronization preventing the signals from drifting apart, as shown by the continuous phase-shift error of synchronized sinusoidal trajectories for different frequencies (b).

The resulting error margin is within an expected range, e.g. within 3.6 ° for a 10 Hz sinusoidal. It primarily results from a theoretical maximum timing error of ∼1 ms between voltage and displacement due to the limited acquisition and control rate of the motor of 1 kHz via the *EtherCAT* interface (refer to Section 3.6.1 and 3.6.2). Thus, the experiment demonstrates, that with the realized implementation maximum achievable precision with regard to synchronization of the periodic control signals is achieved, limited by the transmission rates of the available hardware. However, to achieve high precision with particularly low phase-shift errors less than 1 °, a slow experiment frequency (e.g. 1 Hz or 0.1 Hz) must be configured.

3.7.3 Impedance Measurement

The impedance measurement methods utilized in this work (LCR-meter, LV-method, and HV-method) are calibrated and validated using equivalent circuit load samples, each consisting of a

series of a standard capacitor and resistor. They are soldered to the copper contacts of the (left-side) SIP clamps (Figure 72a), so they can be placed and electrically connected to the sample grips of the test bench (Figure 72b). While the resistance of each test sample is constant with a nominal value of $20\,\mathrm{K\Omega}$, the capacitance varies within a nominal range $0.47\,\mathrm{nF} \ldots 4.7\,\mathrm{nF}$ ($R_{20}C_{4.70}$, $R_{20}C_{2.20}$, $R_{20}C_{0.47}$). Moreover, for calibration purposes, one clamp is provided with open contacts (R_∞) and one with only a resistor (R_{20}).

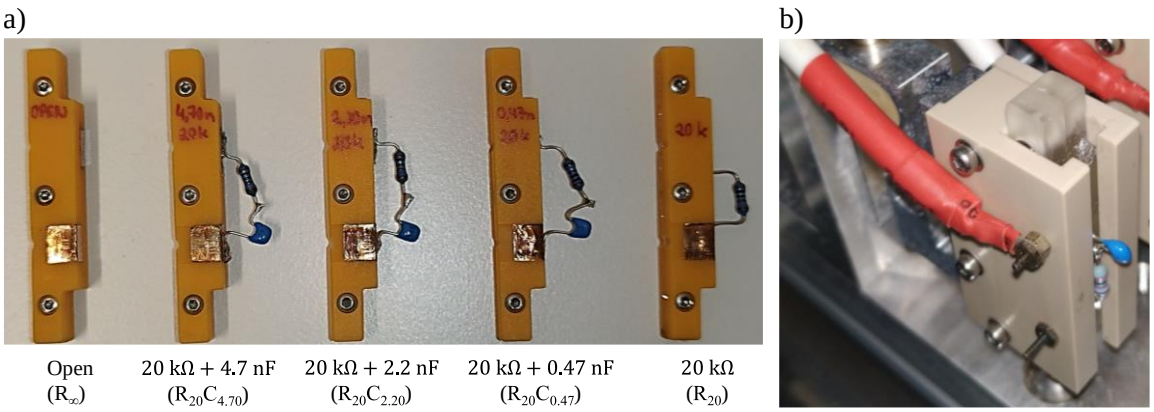

Figure 72: Photo of the RC-series test samples, soldered to SIP-clamps (a), enabling them to be inserted and electrically contacted for calibration and validation purposes on the sample grips of the test rig (b).

Calibration

Calibration of the test stations eliminates currents caused by parasitic resistances, capacitances and inductances of electronic components, cables, and contacts, which impact the measurement results. For conventional LCR-meters, AC-measuring bridges calibrated via open-circuit and short-circuit calibration, ensure robust compensation of these parasitic effects. Since LV-method and HV-method do not utilize any measuring bridges, a four-step load calibration is conducted instead to each test station (Figure 73).

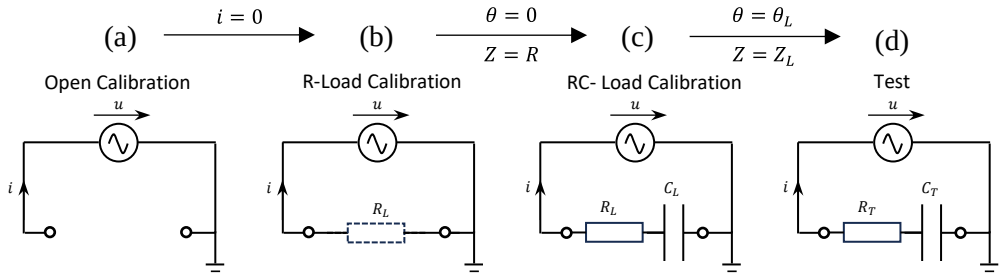

Figure 73: Schematic illustration of four-step calibration of the proprietary implemented impedance measurement methods, with open calibration (a), R-load calibration (b), RC-load calibration (c) and test (d).

In the first calibration step an impedance measurement is carried out, with the R_∞-sample inserted into the sample grip of the respective test station (open calibration, Figure 73a). Since theoretically no current can flow in this experiment, the measured current i is attributed to parasitic effects. Hence, it is subtracted from the subsequent current measurements. In the second step, a further impedance measurement is carried out, with the R_∞-sample replaced by the R_{20}-sample (R-load

calibration, Figure 73b). Due to the purely resistive load, the impedance magnitude Z theoretically corresponds to the known resistance value, and a zero phase-shift. Deviations from these expected values are compensated for, by adjusting the current measurement gain accordingly and subtracting the measured phase-shift. After these calibration steps, impedance can already be roughly determined, when measuring RC-series samples. However, higher accuracy is achieved by matching current and phase-shift to the corresponding values of an RC-element previously determined with an LCR-meter, to ensure that they are within the desired measurement range (RC-load calibration, Figure 73c). This procedure is conducted on the RC-series sample with the lowest capacitance ($R_{20}C_{0.47}$) and then tested with the two remaining samples with higher capacitance ($R_{20}C_{4.70}$, $R_{20}C_{2.20}$) (test, Figure 73d).

Linearity

To obtain comparable results for all impedance measurement methods, they are carried out with the same measurement frequency $f_m = 2$ kHz. Measurement voltage amplitude U_m and offset are always configured identically, resulting in a sinusoidal waveform in the range of $0\,\text{V} \dots 2U_m$. They are set to $U_m = 1\,\text{V}$ for LCR-meter and LV-method, and $U_m = 20\,\text{V}$ for the HV-method, as this method requires higher voltages due to the lower signal quality of the high voltage amplifier. The window size W_m is set to 20 sinusoidal periods for both, LV- and HV-method.

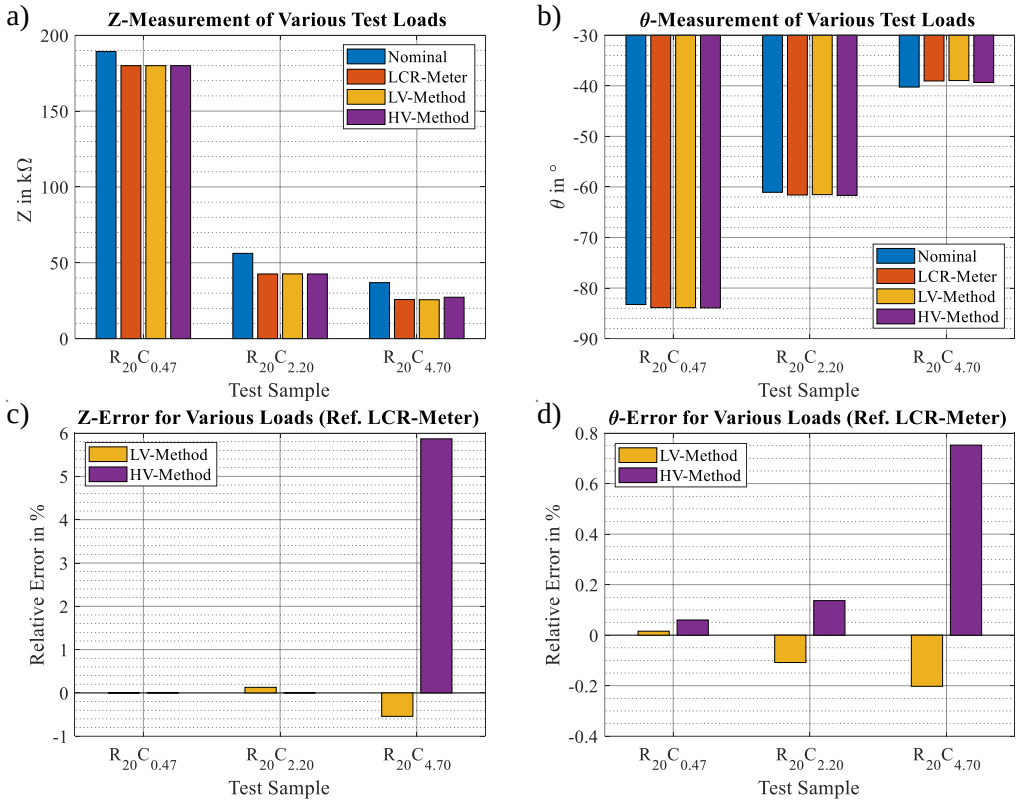

Figure 74: Measurement results obtained with LV-method, HV-method, and LCR-meter compared to nominal values of the resistors and capacitors; with impedance magnitude (a), phase-shift (b), and corresponding relative errors of the proprietary implemented methods with respect to LCR-meter (c, d).

Comparison of the measurement results obtained with LV-method and HV-method with those of the LCR-meter as a reference shows, that the error of Z and θ increases with increasing C (Figure 74a, b). This is particularly evident, if the error in relative to the LCR-meter is considered (Figure 74c, d). However, the results also demonstrate that the observed error of the experiments is sufficiently low, e.g. below $\pm 1\,\%$, especially for test samples with capacitances close to the calibration value, and particularly for the LV-method. The deviations of Z and θ are propagated to the derived measurands C and R (Figure 75a, b), but due to the non-linear correlation (refer to Section 3.5.3), no clear error trend is apparent when considering these quantities.

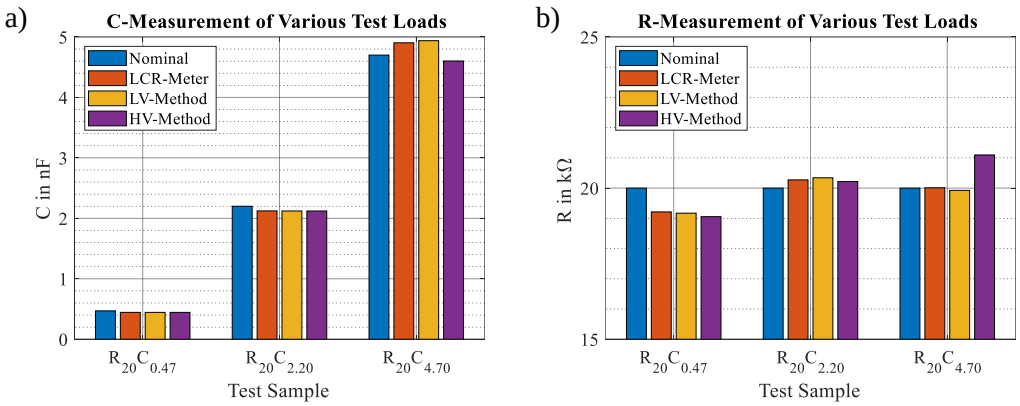

Figure 75: Measurement results obtained with LV-method, HV-method and LCR-meter compared to nominal values; with capacitance (a), and resistance (b).

Noise

An exemplary examination of the continuous measurement signal over time for test sample $R_{20}C_{2.20}$ shows significantly higher noise with the HV-method compared to LV-method and the LCR-meter for both measurands, C and R (Figure 76a, b).

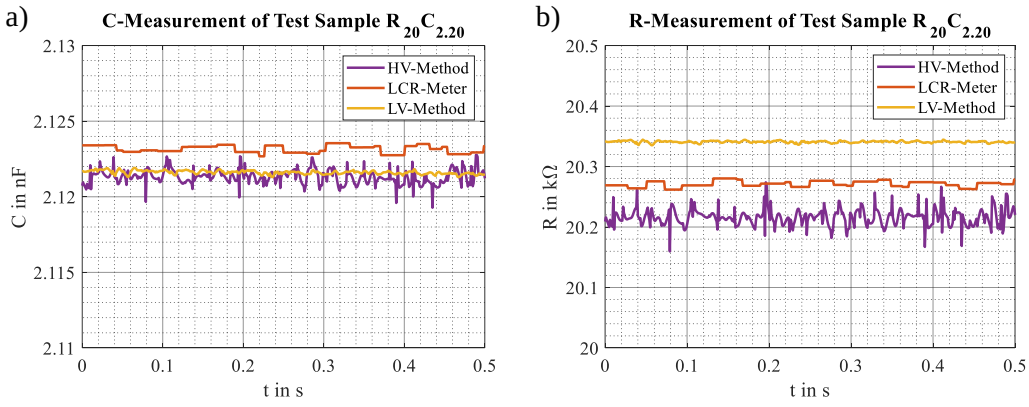

Figure 76: Continuous measurement signals over time obtained by LV-method, HV-method, and LCR-meter; with capacitance measurement (a), and resistance measurement (b).

In addition, the LCR-meter signal shows a step-like characteristics, which is caused by the limited transmission rate between LCR-Meter and *NI cRIO-9047* RT-system. The quality of all output signals C, R, Z and θ is quantified by means of the SNR, which results from the distance between the respective signal power P_S and noise power P_N, if considered on the logarithmic scale:

$$SNR = 10\log_{10}(P_S)\,\mathrm{dB} - 10\log_{10}(P_N)\,\mathrm{dB} \tag{3.14}$$

Assuming that these signals are proportional to a measuring voltage with a root mean square amplitude A_{RMS}, the respective signal power P is proportional to the square of this amplitude:

$$P \sim A_{RMS}^2 \tag{3.15}$$

Normalizing P by P_S, the average SNR is obtained from the ordinate of the corresponding power diagram, by considering the mean of the noise power curves. In this example ($R_{20}C_{2.20}$) a higher average SNR is achieved for C (Figure 77a) than for R (Figure 77b) with each measuring method.

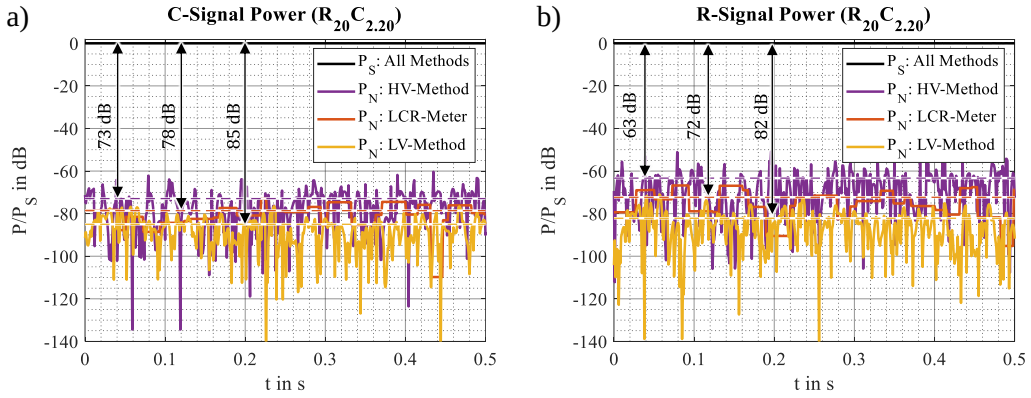

Figure 77: Normalized signal and noise power for LV-method, HV-method, and LCR-meter, highlighting the average SNR for each signal; with capacitance signal (a) and resistance signal (b).

Furthermore, both measurands show highest SNR for the LV-method and lowest for the HV-method, with the LCR-meter in between. However, providing average $SNR > 60\,\mathrm{dB}$ for all measurands and methods, high quality measurement signals are ensured in any case. Separation of the normalized power signals into their spectral components shows, that higher frequencies result in lower noise values for both, C and R (Figure 78a, b).

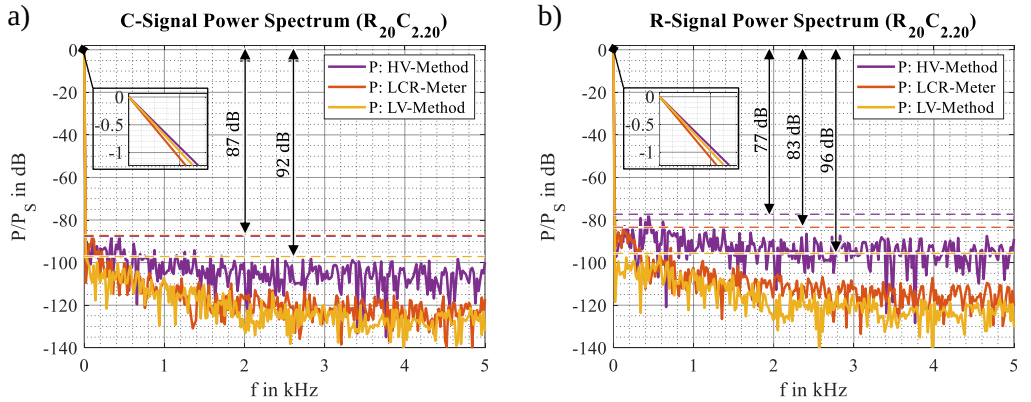

Figure 78: Normalized power spectrum for LV-method, HV-method, and LCR-meter, highlighting the lowest SNR; with capacitance signal (a) and resistance signal (b).

Besides this attenuation characteristics, no noticeable interference is observed in any signal. On the contrary, the (minimum) SNR of the individual frequencies (refer to Figure 78) always shows

higher values than the average SNR (refer to Figure 77). In particular, the LCR-meter signals exhibit low SNR in the lower frequency range, caused by the step-like signal characteristics (refer to Figure 76).

Repeatability and Reproducibility

To evaluate and compare the repeatability of the implemented impedance measurement methods, for each of them five identical measurements are successively conducted to the same test station with the same test sample ($R_{20}C_{2.20}$). For each measurement the mean value of 0.5 s continuously acquired data is considered as one result value. Due to calibration errors, these results slightly differ between the measurement methods (refer to Figure 75). Therefore, the relative error between the individual measurements and the mean value over all measurements for the respective method is considered to obtain comparable results. The corresponding error diagrams for both measurands, C and R, show a uniform error distribution for all methods, with the LV-method exhibiting the lowest error margins (Figure 79a, b). The HV-method exhibits similar error margins for capacitance measurement but significantly higher ones for resistance measurement compared to the LCR-meter. However, all error margins are within a narrow range of ± 0.15 %, providing sufficient repeatability for all methods and measurands.

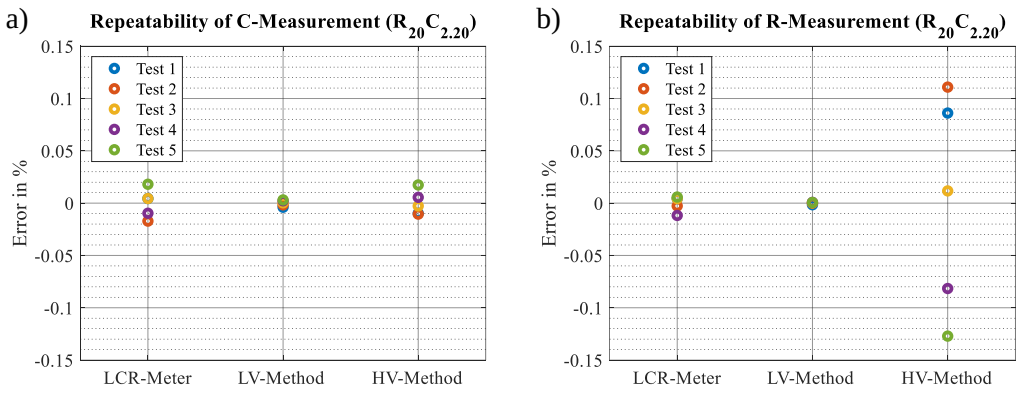

Figure 79: Repeatability evaluation of LV-method, HV-method, and LCR-meter, considering the relative error of five individual measurements conducted to the same test load at the same test station in relation to the mean value over all measurements for the respective method; with measurand capacitance (a) and resistance (b).

By successively mounting the same test sample ($R_{20}C_{2.20}$) from one test station to the next and conducting the same impedance measurements as above, the reproducibility of the measurements with regard to the test stations is evaluated. The corresponding error diagrams for both measurands, C and R (Figure 80a, b) show a less uniform error distribution and higher error margins when compared repeatability error diagrams (refer to Figure 79).

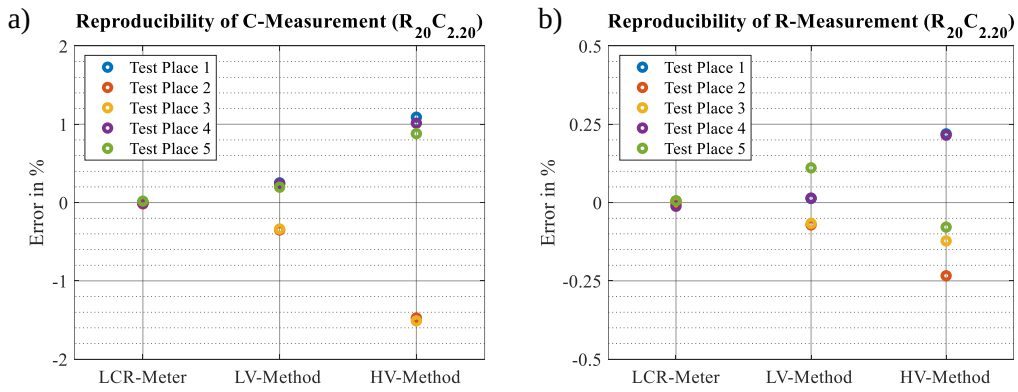

Figure 80: Reproducibility of LV-method, HV-method, and LCR-meter, considering the error of 5 individual measurements conducted to the same test load at 5 different test stations in relation to the mean value over all measurements for the respective method; with measurand capacitance (a) and resistance (b).

Furthermore, they exhibit a clear trend with lowest error margins for the LCR-meter, and significantly higher error margins for LV- and HV-method. This is attributed to the high sensitivity of those methods to deviations from their calibration, i.e. due to placing a new test sample to the sample grip. Thus, resulting errors can reach the lower percentage range, which is acceptable for experiments, in which the relative change in R and C of DET samples is investigated. However, for comparison of absolute values, i.e. if DET samples are investigated on their manufacturing reproducibility, this error can be too high to obtain interpretable results. Thus, it is recommended to use the LCR-meter for these experiments.

Signal Quality – Effects of Different Loads and Measurement Settings

Based on the previous discussion of signal quality, all implemented impedance measurement methods give satisfactory results. However, it's important to note that the assessment based on a single test sample cannot be extrapolated to the entire measurement range, as the signal quality depends significantly on the configuration of the measurement parameters and the specific load, as discussed in Section 3.5.3. To substantiate the theoretical considerations made therein, experimental validation is conducted subsequently. Since the HV-method represents the most critical and at the same time the most promising variant, these impacts are examined for it in the following.

Varying the load with fixed R and various C ($R_{20}C_{4.70}$, $R_{20}C_{2.20}$, $R_{20}C_{0.47}$), while keeping the measurement settings constant ($f_m = 2$ kHz, $U_m = 10$ V, $W_m = 20$ Periods), results in a decrease in Z and increase in θ for increasing C (Figure 81a). The average SNR of the corresponding measurement increases first, showing a maximum at $C = 2.2$ nF, and then start decreasing for higher C (Figure 81b). However, these minor changes have no influence on the generally monotonic SNR characteristics of the derived quantities C and R, which decrease and increase with increasing θ respectively, and cross each other at $C \approx 4$ nF ($\theta \approx 45°$). Absolut measurement values of Z and θ, and qualitative curves of the SNR thus correspond to the expectations resulting

from the theoretical considerations and are therefore valid and sufficient within the considered range (refer to Section 3.5.3).

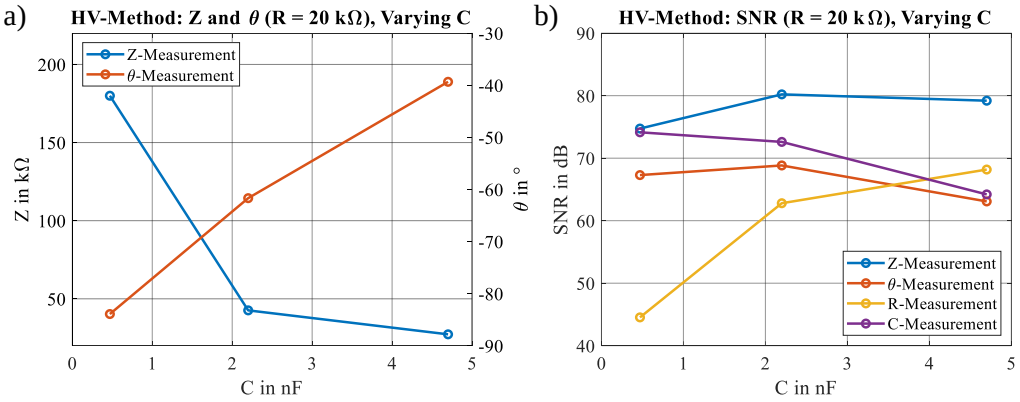

Figure 81: HV-method applied to various test loads with constant resistance and various capacitances; with impedance magnitude and phase-shift (a) and average SNR of all measurands (b).

Varying the measurement frequency f_m, while keeping the remaining measurement settings and the load constant ($U_m = 10$ V, $W_m = 20$, sample $R_{20}C_{2.20}$), results in decreasing Z and increasing θ for increasing f_m (Figure 82a). Setting $f_m > 4$ kHz no longer yields plausible results due to sampling limitations with a theoretical limit at $f_m = 5$ kHz. Since the cut-off frequencies of high voltage amplifiers and current monitors are considerably higher and no current limit is exceeded, those devices do not have a major impact to the frequency response. The average SNR of Z and θ increases first and then start decreasing for higher f_m, with a maximum at $f_m = 2$ kHz (Figure 82b), thus showing similar characteristics as for increasing C (see Figure 81). Also in this measurement, these minor changes do not influence the generally monotonic SNR characteristics of the derived quantities C and R, which decrease and increase with increasing θ respectively. and cross each other at $f_m \approx 3.4$ kHz ($\theta \approx 48°$). Absolut measurement values of Z and θ, and qualitative curves of the SNR thus correspond to the expectations resulting from the theoretical considerations and are therefore valid and sufficient within the considered range (refer to Section 3.5.3).

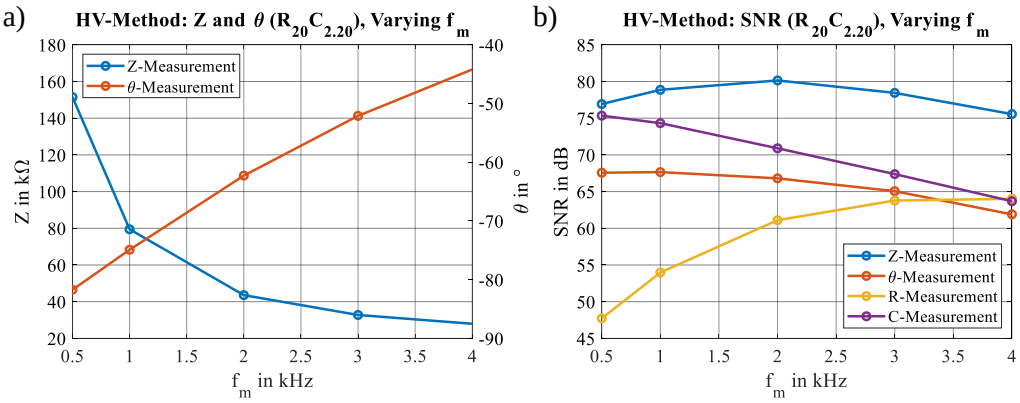

Figure 82: HV-method applied to a test load, varying measurement frequency; with impedance magnitude and phase-shift (a) and the average SNR of all measurands (b).

Varying the measurement voltage U_m, while keeping the remaining measurement settings and the load constant ($f_m = 2$ kHz, $W_m = 20$, sample $R_{20}C_{2.20}$), results in minor changes in Z and θ (Figure 83a). This is probably attributed to the voltage-dependent properties of the capacitor and the resistor of the test sample, which are not further quantified. Neglecting these changes, the trend of the SNR corresponds to the expected behavior for all measurands and increases with increasing U_m, since the measuring current also increases and (quantization) noise decreases. As the curves saturate for $U_m > 20$ V, higher values only result in minor increase in SNR and are thus not meaningful. On the contrary, they can result in an undesired electromechanical actuation response of DETs, which affect the measurement results.

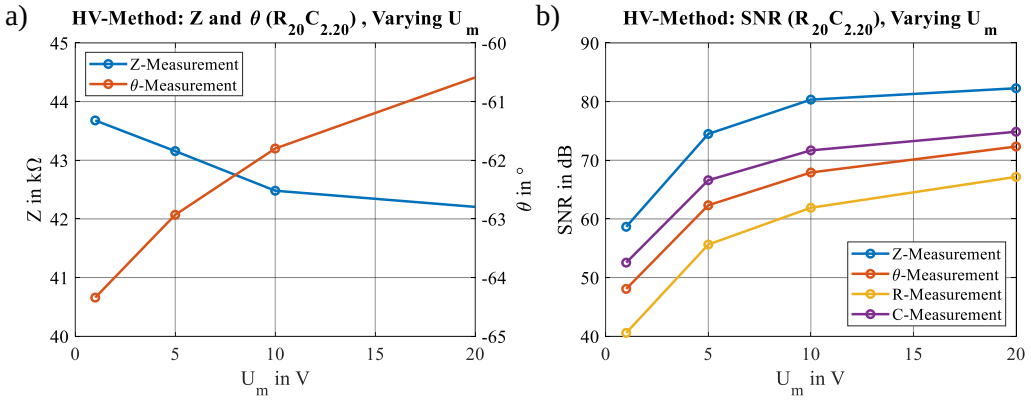

Figure 83: HV-method applied to a test load and varying measurement voltage; with impedance magnitude and phase-shift (a) and the average SNR of all measurands (b).

Varying the measurement window size W_m, while keeping the remaining measurement settings and the test sample constant ($f_m = 2$ kHz, $U_m = 10$ V, $R_{20}C_{2.20}$), results in an increase in SNR for all measurands (Figure 84a). This is expected, as the grouping of several windows (sinusoidal periods) represents a lowpass filter with a decreasing cutoff frequency as the number of windows increases. The filter effect is also evident from the normalized power spectrum (Figure 84b), showing, that the noise attenuation of C increases with increasing W_m. As the filter effect causes phase-shifts in the capacitance and resistance signal, it must be considered for time-dependent experiments.

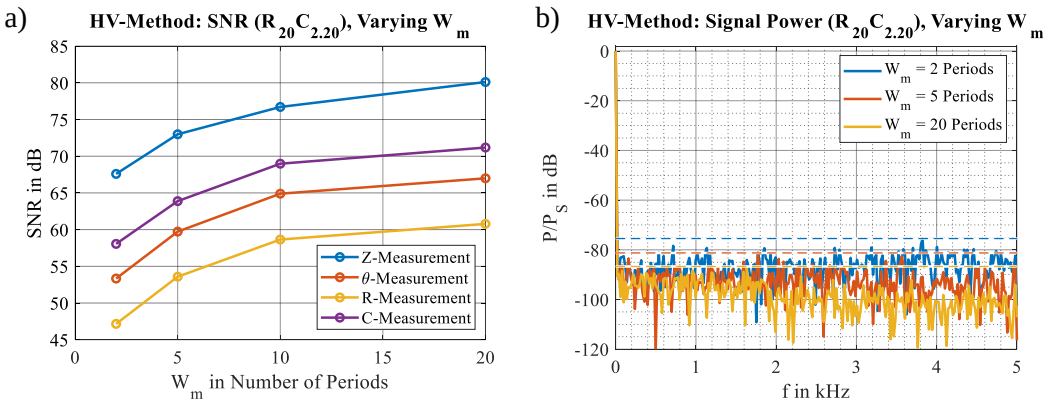

Figure 84: HV-method applied to a test load, varying measurement window size; with the average SNR of all measurands (a) and the capacitance signal power spectrum (b).

High Voltage Impedance Measurement

HV-Method with simultaneous quasi-stationary high voltage control is validated, by using a high voltage ceramic capacitor (Vishay 615R-Z5U) as a test sample (Figure 85a). This features a nominal capacitance of 3.3 nF, and is specified with a typical characteristic capacitance-voltage curve in the data sheet, which is used as validation reference [166]. Identical experiments are conducted once for only this capacitor, and once with an additional resistor in series with a nominal resistance of 23 kΩ. Thereby, high voltage control u_a (0.1 Hz, 10 V ... 2990 V) is applied to the samples, with an overmodulated measuring voltage u_m (1 kHz, −10 ... 10 V) (Figure 85b).

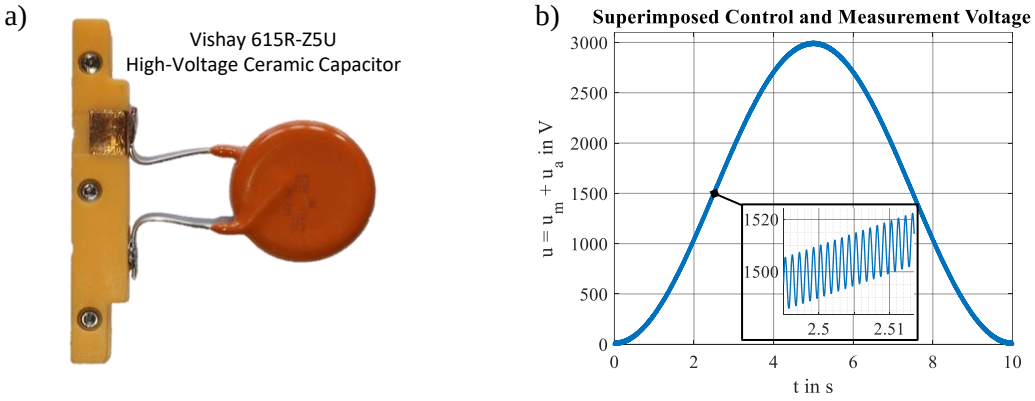

Figure 85: Photo of high voltage ceramic capacitor Vishay 615R-Z5U soldered to a SIP clamp (a), utilized as validation reference sample for testing the HV-method with the measuring voltage superimposed to the high voltage control signal (b).

The results show typical non-linear capacitance over time curves (Figure 86a) and capacitance over voltage curves (Figure 86b).

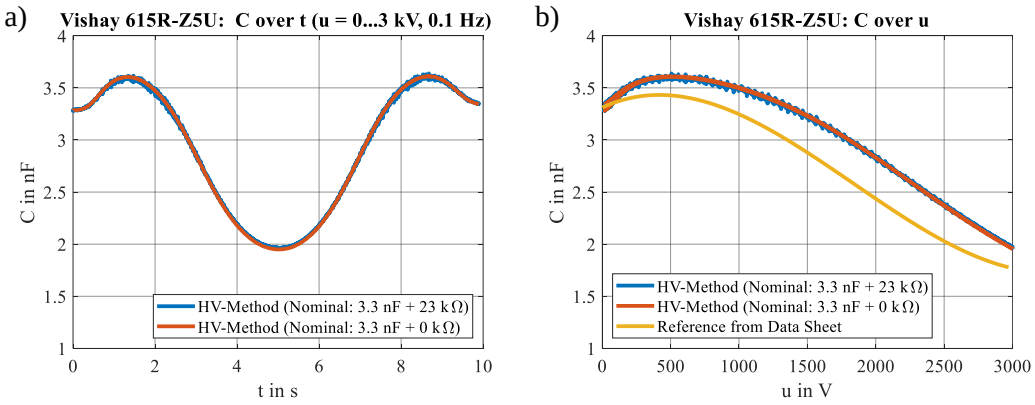

Figure 86: HV-method with quasi-stationary high voltage excitation, applied to high voltage capacitor with and without series resistor; with capacitance-time curves (as), and capacitance-voltage curves in comparison to the validation reference curve (b).

The capacitance curves initially increase slightly with increasing voltage, peaking at $u \approx 500$ V, and then decrease significantly until the maximum voltage is reached. For decreasing voltage, they behave identically on the return path and no hysteresis is observed. Measurement and reference curves show similar qualitative behavior, with less initial increase in capacitance for the reference

curve. However, they agree sufficiently, as the reference curve is derived from the typical curves for this capacitor class and is thus subject to considerable tolerances.

The resistance curves associated to the capacitance measurements show widely constant values over time (Figure 87a) and voltage (Figure 87b) with similar qualitative characteristics and no visible hysteresis.

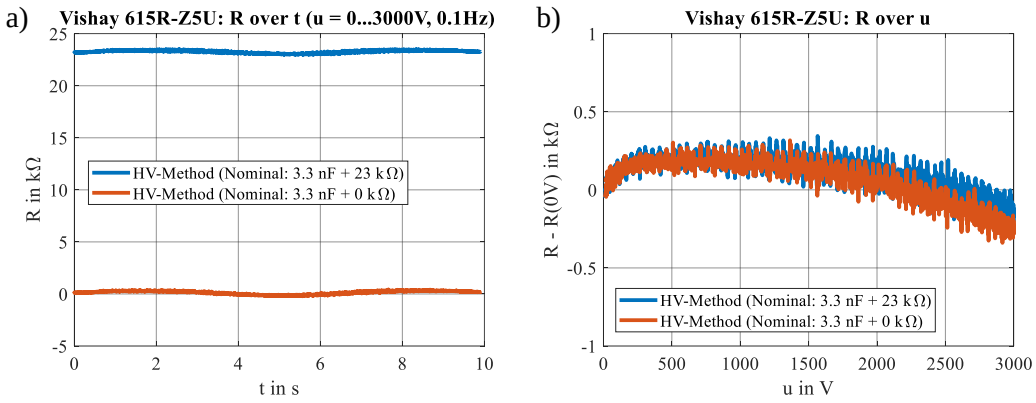

Figure 87: Resistance measurement results associated to the capacitance measurement (refer to Figure 86); with absolute results over time (a) and results over voltage normalized with the respective zero volts resistance for better comparison (b).

The deviation from an exactly constant characteristic curve is thus not attributed to the series resistor, but either to the capacitor or a measuring inaccuracy. Comparison of the capacitance measurement curves in their individual diagrams (refer to Figure 86) shows, that the results for both measurements, with and without series resistor, match. However, the signal noise is higher for the measurements with series resistor. Furthermore, it is not constant, but decreases with decreasing capacitance. In contrast, the resistance curves (refer to Figure 86) show an inverse trend with increasing signal noise over voltage. Hence, these measurements clearly show the change in the measurement signal quality caused by the continuous change of the sample capacitance, which is discussed in Section 3.5.3, and experimentally investigated above (refer to Figure 81). Since DETs increase their capacitance when a high voltage is applied, a similar, but inverse signal quality characteristics, is expected.

3.7.4 Conclusion on Experimental Validation

The individual test rig components and their interaction are validated for accuracy, including assessments of linearity and signal-to-noise ratio (SNR), repeatability, reproducibility, as well as time-, load-, and temperature-dependent characteristics. Since the complex characteristics of DETs makes them unsuitable as a validation reference, simple mechanical and electrical elements such as linear tension springs, resistors, and capacitors are used for this purpose.

The experimental results demonstrate that the test rig incorporated standardized mechanical control and measurement components, i.e. motors and load cells accurately reflect the specifications

outlined in their data sheets. The combination of the test devices demonstrates errors within the same order of magnitude as those observed with individual devices, highlighting a high level of reproducibility across various test stations. Through calibration and sensor characteristic curve adjustment, the accuracy can partially be even further improved, i.e. significantly reducing the linearity error of motor positioning. Positioning can also be customized to optimize either for high test precision or high test rates by employing different controller parameter configurations. Experimental investigations on temperature effects and mechanical compliance of the test rig reveal minor influences, which can be mitigated through derived correction factors.

It is also shown, that the high-voltage amplifier and relays reflect the specifications of their data sheets when used in combination, and that proprietary electronics demonstrate satisfactory functionality and accuracy: The individual current monitors exhibit a typical measuring error of only ± 0.05 %, enabling dynamic measurements with frequencies exceeding 10 kHz. The electrical breakdown detection, coupled with associated high voltage shutdown mechanisms operate within a time frame of ~ 1 ms. Simultaneous use of the devices does not result in significant signal crosstalk, ensuring robust operation without false detections and providing reliably interpretable data. All control and measurement devices support real-time data generation and acquisition rates of at least 1 kS/s with a synchronization error of ~ 1 ms, thus enabling precise synchronization of mechanical and electrical control. Experiments conducted on different test stations show on overall reproducibility error for voltage and current measurement below ± 0.1 %.

For the proprietary impedance measurement methods, namely HV-method and LV-method, similar accuracy levels are demonstrated if their measurement range is limited appropriately. Both methods feature significantly higher data rates in comparison to the standardized LCR-meter. Although the LV-method offers a higher SNR, the HV-method enables accurate measurement during high voltage application to the samples. The experimental confirmation of the dependence of the measurement signal quality on both measurement parameters and the load, as discussed in Chapter 2, validates the qualitative functionality of the measurement methods, complementing the random sample tests.

4 Test Rig Demonstration

This chapter presents a variety of test scenarios that demonstrate the capabilities of the developed test rig for comprehensive electromechanical testing of DETs under controlled environmental conditions. Specifically, experiments conducted on the SIP samples introduced in Section 3.4.1 are discussed, thereby focusing on transducer compounds without physical preload mechanism. For this purpose, an overview of general preparations common to all experiments is given first. Subsequently results of mechanically, electrically, and electromechanically controlled experiments, with an emphasis on short-term and low-cycle experiments are presented and discussed, followed by long-term and high-cycle experiments.

4.1 Test Preparation

The starting conditions are identical for all tests described in the following sections. It is carried out at room ambient conditions (approximately 23 °C and 50 % relative humidity). These environmental conditions are also employed during the tests, unless it is specifically stated that those are carried out under different temperatures or humidity levels. The samples are manually inserted into the sample grips of the respective test stations prior to the tests, where they automatically snap into place on the ball pressure screws, with the sample electrical contact pads connected to the leaf spring contacts. During this procedure, all relays of the test bench are switched to ground for safety reasons, and the motor is locked at 20 mm clamping distance (Figure 88a), resulting in a zero initial pre-strain $\epsilon = 0$ of the SIP (Figure 88b). Using the manual test rig operation mode, the motor can be unlocked, allowing adjustment of the slider position to establish a different starting position before initiating an automatic test routine, resulting in a non-zero pre-strain (Figure 88c).

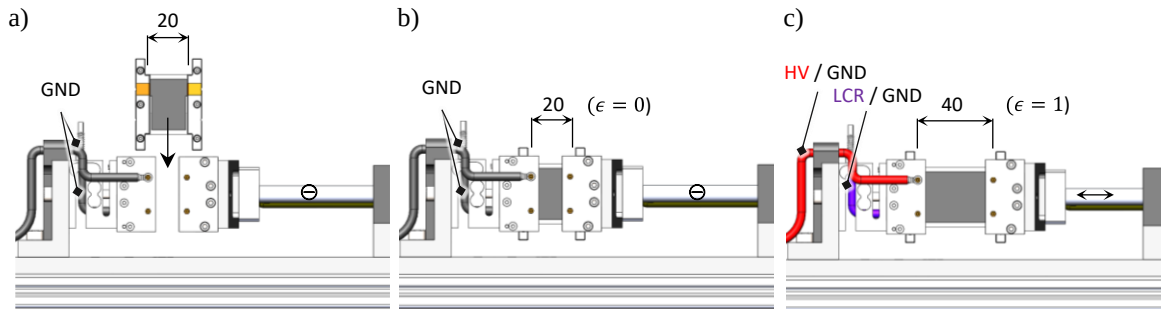

Figure 88: Mounting of a sample on a test station (a), always resulting in a grounded electrode and zero initial strain configuration (b), whereby these initial test conditions can be modified prior to each experiment using manual operation mode of the test rig (c).

Additionally, the electrical connection can be switched to the high voltage amplifier or to the LCR-meter, both of which can be configured and operated manually, i.e. to conduct pre-tests to prove electrical contacting, to identify defective samples, or to identify appropriate impedance measurement parameter configurations.

An appropriate measurement frequency range is determined by measuring impedance and derived quantities of an exemplary SIP with zero pre-strain at varying frequencies using the LCR-meter. For measuring frequencies $f_m = 0.5 \ldots 2.5\,\text{kHz}$, a constant capacitance value $C \approx 0.72\,\text{nF}$ is obtained from the results, with $R \approx 26\,\text{k}\Omega$ (Figure 89a, b). At lower frequencies, the impedance magnitude is in the MΩ-range and the corresponding phase approximately $-90°$ (Figure 89c, d), resulting in inaccurate measurements that underestimate the capacitance value and overestimate the resistance value.

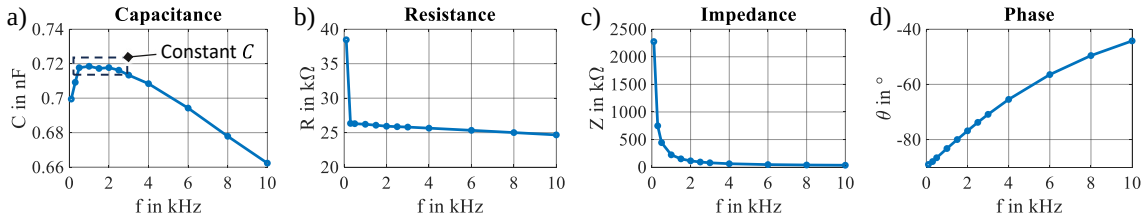

Figure 89: LCR-meter measurements on an exemplary SIP-DET sample, showing measurement results over various increasing measurement frequencies; with capacitance (a), resistance (b), impedance magnitude (c), and phase (d).

At higher frequencies capacitance and resistance decrease systematically. This behavior is attributable to the characteristics of the SIP, which in reality does not behave like an ideal RC-series element, as assumed for these measurements. A more realistic model consists of many RC-series elements connected in series, which corresponds to series of voltage lowpass filter elements (Figure 90).

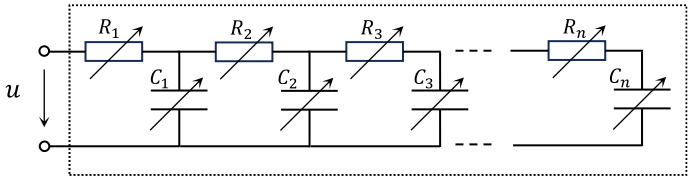

Figure 90: More realistic electric model for a single sided contacted SIP-DET, consisting of a series of RC elements instead of a single RC element, resulting in an attenuation of the measuring voltage over length, so that areas distant from the contacting are no longer present in the measuring signal.

Due to the one-sided contacting of this network, the measuring voltage is attenuated by the filter elements so that it is reduced over the length of the SIP. Therefore, as the measuring frequency increases, distant areas are no longer represented in the measurement signal. Conversely, if the measuring frequency remains constant, increasing resistance or capacitance further increases the attenuation, which distorts the measurement of these variables. Configuring $f_m = f_c$ to achieve a high measurement quality, as discussed in Section 3.5.3, is therefore not suitable for the SIP samples under investigation, as it is too high ($f_c \approx 10\,\text{kHz}$). Instead, for the following tests, measuring frequencies $f_m = 0.5 \ldots 2\,\text{kHz}$ are selected, which are within the lower frequency range, where the capacitance measurement remains constant, and the measurements are less susceptible to the described lowpass filtering effect.

4.2 Mechanically Controlled Experiments

The mechanically controlled experiments demonstrated in the following sections comprise tensile test series with varying strain amplitudes, strain rates, environmental conditions, and complementary applied constant voltages, in which the respective remaining variables are kept constant. Within each test series, all tests are conducted to the same SIP sample. Furthermore, one test is provided, which is applied to multiple SIP samples, to evaluate for their reproducibility.

4.2.1 Tensile Tests with Varying Strain Amplitudes

Equally configured series of low-cycle, constant strain rate tensile tests with varying strain amplitude are conducted on two SIP samples: One pure film sample without electrodes in comparison to one sample provided with electrodes.

Design of Experiments

No pre-strain is applied to both samples prior to the experiments, in which they are subject to cyclic loading and unloading at a constant controlled strain rate ($\dot{\epsilon_c} = 0.05\ 1/\mathrm{s}$), in eight successive experiments (E1-E8). The strain amplitude is gradually increased ($\epsilon = 0.25 \ldots 1.00$ in 0.25-increments), and then decreased, with each strain level undergoing 10 loading cycles (Figure 91).

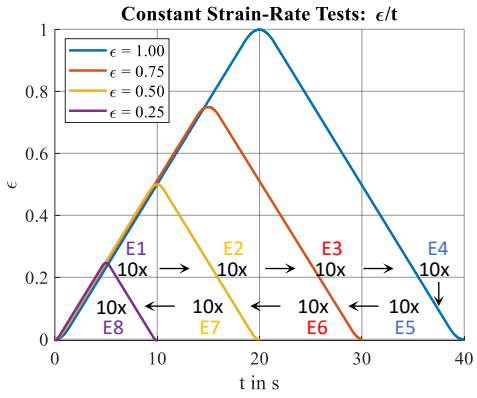

Figure 91: A series of constant strain rate tensile tests consisting of four successive gradually increasing strain experiments, followed by four gradually decreasing strain experiments, with 10 loading and unloading cycles in each experiment.

Pure Film Tests Sample: Stress-Strain Characteristics

The results for the pure-film sample are evaluated in terms of the stress-strain characteristics. In E1-E4, a clear hysteresis is observed in the first loading-unloading cycle, that is not present in the subsequent cycles (Figure 92a). Consequently, the curve-slope, and thus the material stiffness, decreases with increasing strain amplitude. Comparing these results with those of E5-E8 reveals, that the lower stiffness is also maintained for subsequent experiments with lower strains, and all curves follow the same loading-unloading path, which corresponds to the maximum strain curve (Figure 92b). Therefore, the stress-strain curve depends on the previous maximum load, a well-known phenomenon, which is typical for elastomers and called Mullins effect (refer to Section 2.1.7).

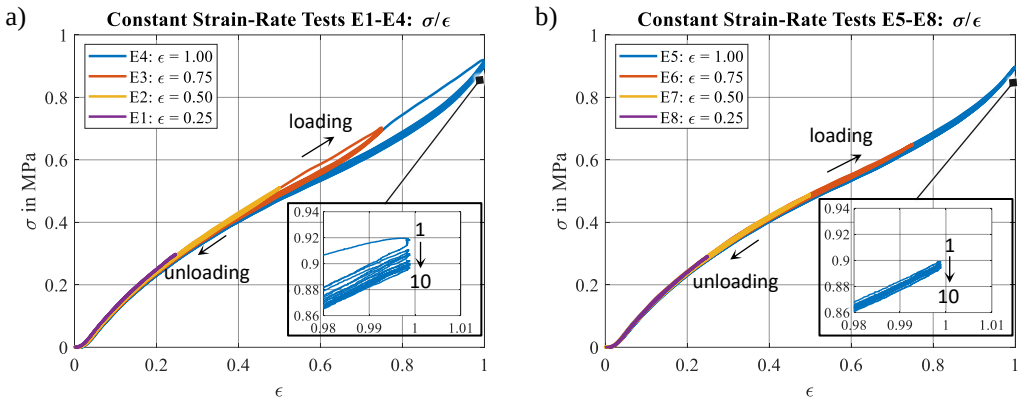

Figure 92: Stress-strain curves of a pure film SIP sample; with E1-E4 showing strain-dependent hysteresis and stress softening for the first loading-unloading cycle (Mullins effect), as well as regressive cyclic stress reduction (a); and E5-E8 showing strain- and cycle-independent characteristics (b).

In addition to this, the experiment results show a generally regressive decrease in stress with increasing number of cycles and a minor noticeable right-shift of the zero crossing on the strain axis, resulting in an irreversible zero-stress plateau for lower strains. There are two possible explanations for this effect, both of which may contribute in combination: One the one hand, it may be due to a run-in behavior, where the film experiences a slight release at the exit area of the clamp. On the other hand, it can be attributed to a permanent set of the PDMS film.

Tests Sample with Electrodes: Stress-Strain Characteristics

The stress-strain curves of the SIP sample provided with electrodes generally exhibit the same qualitative characteristics and a more pronounced Mullins effect (Figure 93a, b).

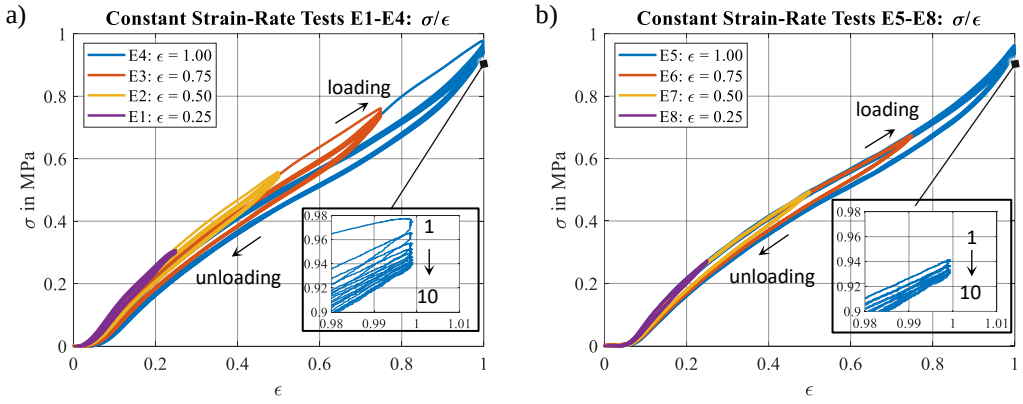

Figure 93: Stress-strain curves of an electrode equipped SIP sample; with E1-E4 showing the Mullins effect, as well as strain-and cycle-dependent hysteresis, and regressive stress reduction over cycles (a); and with E5-E8 showing similar characteristics, but no Mullins effect (b).

However, they also show a significant reproducible strain and cycle-dependent hysteresis, that is barely detectable for the pure film sample, and therefore mainly attributable to the mechanical properties of the electrode. This viscoelastic behavior can be explained by the interaction of the electrode constituents with reorienting and friction processes of the carbon black particles and the polymer chains of the PDMS (refer to Section 2.1.7). It is also noteworthy that the irreversible

zero-stress plateau is significantly more pronounced for the electrode-provided sample, which is an indication of a more pronounced strain-dependent permanent set of the electrode.

Tests Sample with Electrodes: Resistance-Strain Characteristics

Considering the corresponding complementary acquired resistance-strain curves, an effect similar to the Mullins effect is observed from E1-E4, showing a clear hysteresis in the first loading-unloading cycle, that is not observed for the subsequent cycles and results in an increasing slope of the resistance-strain curves (Figure 94a). Comparing the results with E5-E8 shows that this increased slope is also maintained for subsequent lower strains, and all curves follow a similar loading path in particular (Figure 94b).

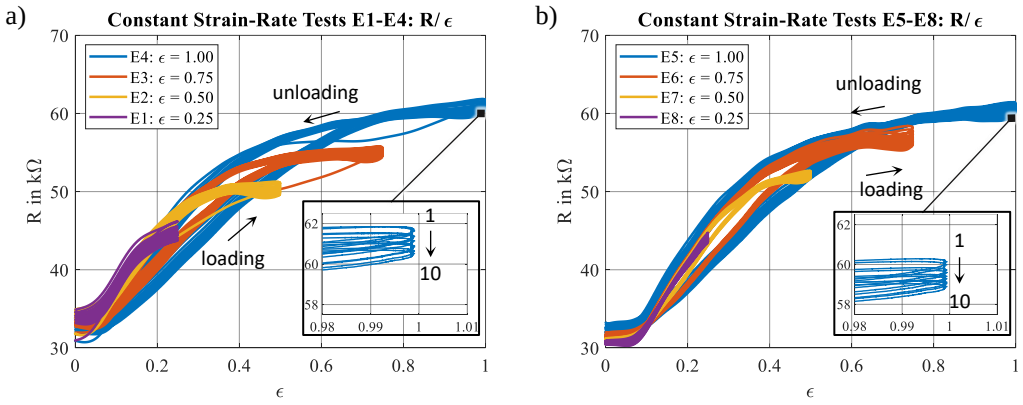

Figure 94: Resistance-strain curves; with E1-E4 showing strain-dependent hysteresis with a strain-dependent increase in curve slope for the first loading-unloading cycle and gradually decreasing resistance over cycles (a), and E5-E8 showing similar characteristics but no initial curve slope increase (b).

Moreover, also in accordance with the stress-strain characteristics, the resistance-strain curves show a significant reproducible hysteresis. As for the stress, these phenomena can be explained by interaction processes of the electrode components, involving reorientation and friction processes of the carbon black particles and the polymer chains. Besides these effects, an overall gradual decrease in resistance over increasing number of cycles is observed, accompanied with a widening of the constant resistance plateau in the lower strain range. Similar to the stress-plateau, the resistance plateau can be explained by permanent set and a run-in characteristic of the clamping.

Tests Sample with Electrodes: Capacitance-Strain Characteristics

A similar plateau is evident in the lower strain range of the capacitance-strain curves, which otherwise show an approximately linear behavior at higher strains, tending to develop an increasing slope with strain (Figure 95a, b). This characteristic is expected because the width of the SIP is too narrow to exhibit a pure shear-like quadratic characteristic, but too wide to exhibit an ideal linear characteristic. Particularly, E1-E4 show an increase in the capacitance plateau with increasing strain (Figure 95a). This increase cannot be attributed to a run-in behavior of the clamping, but only to a permanent deformation of the SIP, resulting in an increased active surface area and a decreased thickness, thus leading to an increased capacitance. No considerable hysteresis can be observed in

the capacitance-strain curves, but a slight decrease in slope for increasing strains. As for the stress and the resistance, this change in slope is maintained for subsequent lower strains, and all curves follow the same loading-unloading path with a regressive cyclic decrease of the overall capacitance (Figure 95b).

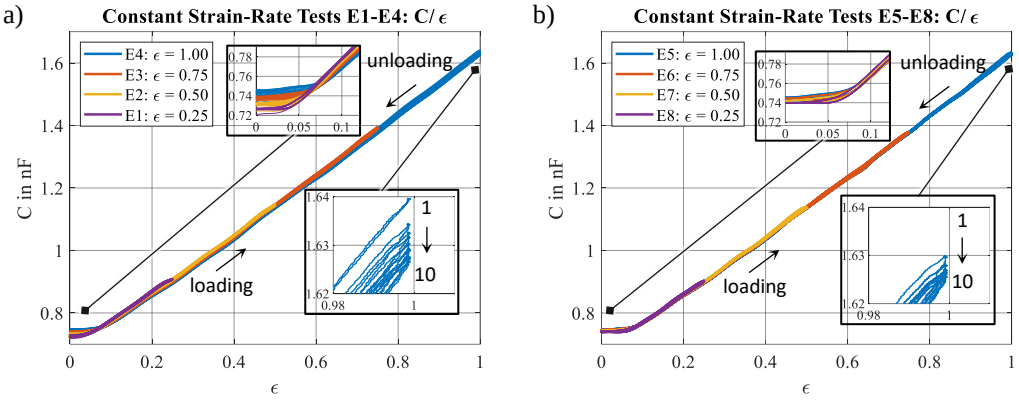

Figure 95: Approximately linear capacitance-strain curves; with E1-E4 showing a strain-dependent increase in zero-strain capacitance for the first loading-unloading cycle, as well as a regressive cyclic capacitance decrease (a); and E5-E8 showing similar characteristics, but no initial capacitance change (b).

However, both effects are small compared to the resistance measurement and it is possible, that the minor observed effects on the capacitance are a result of the coupling of both measurands, which are acquired via common impedance measurement. It is therefore difficult to interpret these effects from a physical perspective.

4.2.2 Tensile Tests on Various Samples

The reproducibility of the SIPs and their manufacturing is evaluated in terms of stress, capacitance, and resistance measurements obtained from identically configured constant strain rate experiments ($\epsilon = 1$, $\dot{\epsilon} = 0.05\ 1/\mathrm{s}$), conducted on five SIP samples, considering the respective first loading-unloading cycle (Figure 96a). The corresponding stress-strain curves show a similar hysteresis behavior with slightly varying stiffness in a range of approximately ± 4 % (Figure 96b). Slopes and offsets of the capacitance-strain curves only deviate within ± 2 % (Figure 96c), whereby the resistance-strain curves show comparatively high deviations within ± 20 % (Figure 96d). There is no systematic correlation observed in the deviations between the individual measurands, which is probably due to the fact that the number of possible causes is large: Deviations in stress can be caused by variations in film and electrode thickness. In addition, a locally varying pre-strain of the film during clamp mounting can result in varying zero-load sample lengths, and discrepancies in sample cutting can result in different sample widths. Deviations in the resistance characteristics are also indicative of varying electrode quality, i.e. in the form of thickness variations. Local effects such as uneven distribution of carbon black particles within the PDMS matrix must also be considered. In particular, the local resistance in the area of the contact points can have a strong influence on the resistance measurement.

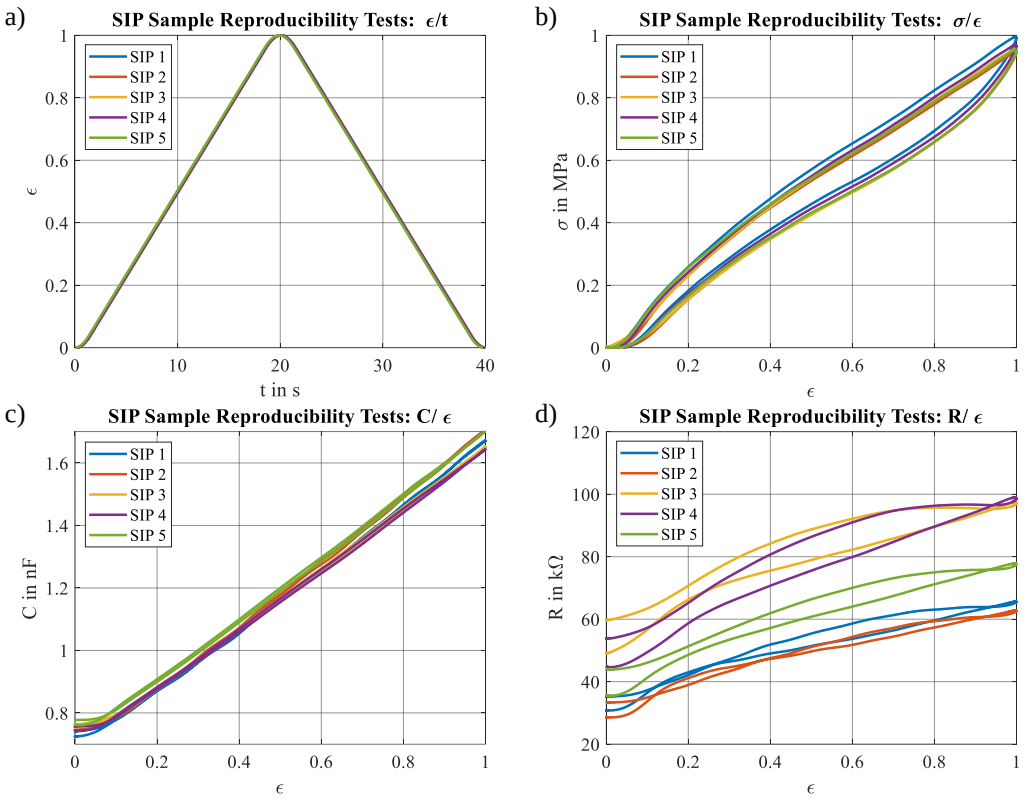

Figure 96: Results of equally configured constant strain-rate experiments conducted on five SIP samples, to evaluate their reproducibility (a), resulting in a reproducibility-error in the lower percentage-range for stress (b) and capacitance (c), as well as a comparatively high reproducibility error for the resistance (d).

The small deviations in the capacitance behavior can also be attributed to varying film thickness, although locally varying permittivity due to imperfections in the film is also conceivable. Another possible source of error may be misalignment of the opposite electrodes, resulting in slight deviations of the active area that forms the capacitor, and thus affects measurement of both quantities, capacitance, and resistance. Furthermore, resistance and capacitance are measured via the common impedance measurement, which is why the deviations of both measurands can be reflected in the respective other variable due to the lowpass filtering effect observed for DETs (refer to Section 4.1). This is particularly important for the SIP samples under consideration, as the corresponding constant measuring range is small and the change in values is high.

4.2.3 Tensile Tests with Varying Environmental Conditions

Investigations on the impact of varying environmental conditions on the properties of DETs are demonstrated, by conducting identically configured tensile experiments with sinusoidal strain control ($\epsilon = 0.5$, $f = 0.1$ Hz) successively on the same SIP sample, thereby applying varying controlled constant temperatures T_c and humidities H_c.

Varying Constant Temperature Tests

For the varying temperature tests, the relative humidity is always fixed at 50 %, and the temperature is gradually increased ($T_c = 1\,°C$, $25\,°C$, and $80\,°C$), with the sample being exposed to the respective settled temperature for at least 10 minutes (Figure 97a). The results show a progressive increase in slope of both, stress-strain (Figure 97b) and capacitance-strain curves (Figure 97c), which additionally show a general increase in capacitance. Conversely, a gradual decrease in resistance is observed (Figure 97d).

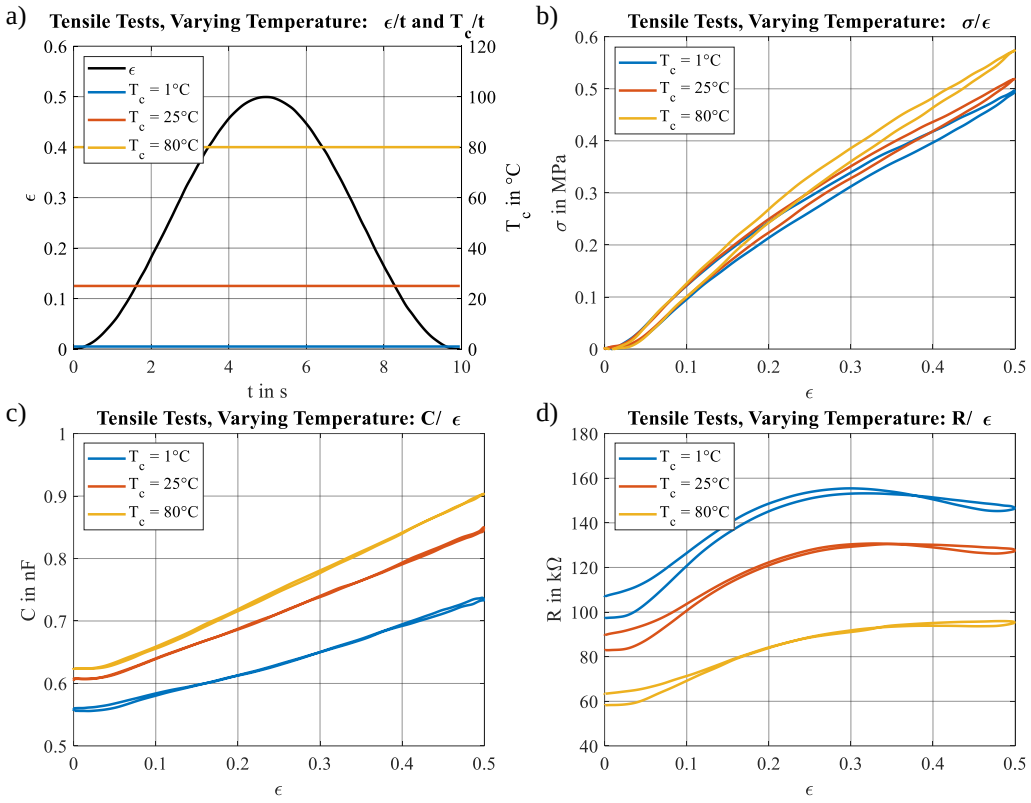

Figure 97: A series of tensile tests complemented with gradually increasing temperatures (a); with results over increasing strain showing increasing stiffness for increasing temperatures (b), along with increasing capacitance (c), and decreasing resistance (d).

Increasing stiffness is a common trend for uniaxially loaded elastomers and can be explained by entropy elasticity (refer to Section 2.1.7). The observed trend of resistance decreasing as temperature increases is a common characteristic of CB-PDMS based electrodes, indicating that the increased mobility of the charge carriers outweighs the resistivity-increasing effect of thermal expansion (refer to Section 2.1.8). Thermal expansion of the DET is expected to increase both its width and thickness. The increase in width would raise capacitance, while the increase in thickness would reduce it. However, the results show a trend with increasing offset and slope with strain. Notably, the relatively large capacitance change systematically decreases with increasing resistance. This correlation indicates that the measurement frequency was set too high for this series of experiments, thereby revealing the lowpass filter effect of DETs as discussed in Section 4.1. Consequently, no meaningful physical interpretation of the capacitance change over

temperature can be drawn from these experiments, and they must either be repeated with samples of lower resistance, or a lower measurement frequency must be selected.

Varying Constant Humidity Tests

For varying constant relative humidity tests, the temperature is always fixed at $25°C$, and the humidity is gradually increased ($H_c = 10\ \%$, $50\ \%$, and $90\ \%$), with the SIP sample being exposed to the respective settled humidity for at least 10 minutes (Figure 98a). Corresponding test results show no significant influence of the humidity regarding stress-strain characteristics (Figure 98b), or capacitance-strain characteristics (Figure 98c). A minor decrease is observed for the resistance (Figure 98d).

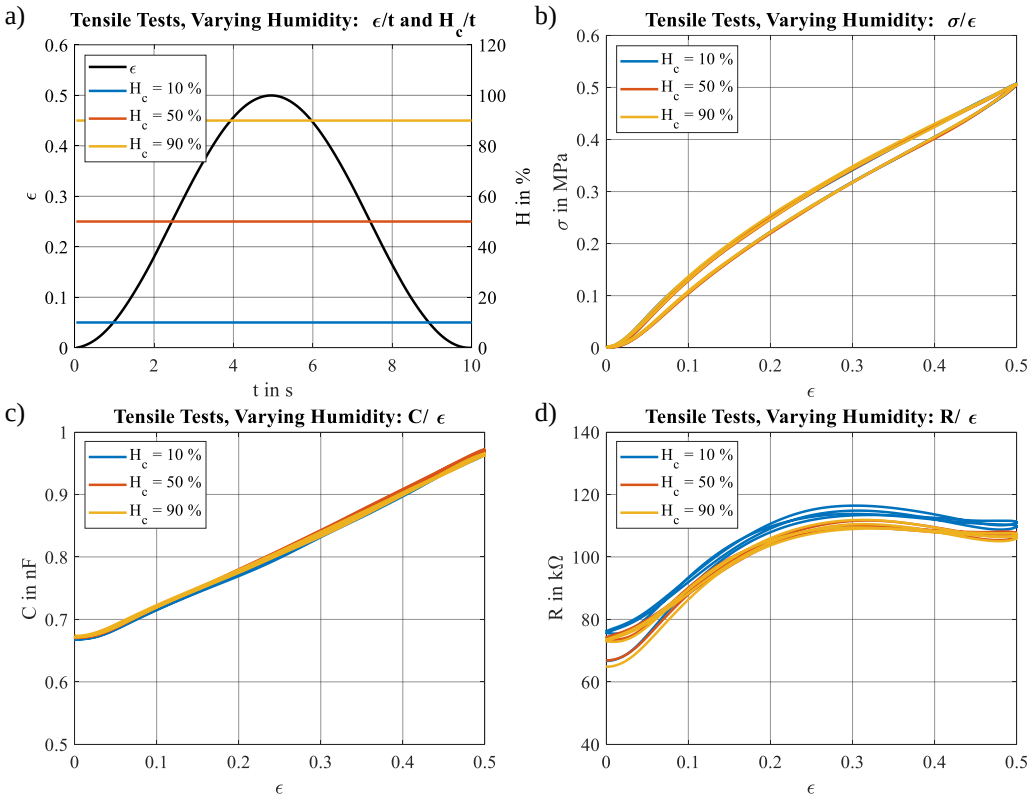

Figure 98: A series of tensile tests complemented with gradually increasing relative humidities (a); with the results showing no significant systematic effects on stress (b), capacitance (c), and resistance (d).

However, the effect is small and could also be due to time-dependent and cyclic effects, making an interpretation as a humidity correlation difficult. Since it is possible that significant changes may occur at higher absolute humidities, it is necessary to repeat the tests at higher temperatures. Although it will be necessary to repeat both sets of experiments and perform additional tests to characterize SIP properties as a function of temperature and humidity, the results demonstrate that the test bench can generally be used to perform systematic testing over a wide temperature and humidity range, yielding plausibly interpretable results.

4.2.4 Tensile Tests with Varying Impedance Measurement Methods

The HV-method can be utilized to acquire capacitance and resistance properties of the DET at high sample rates, especially when the samples are subjected to high voltage simultaneously for actuation. To validate measurement consistency, identically configured constant strain rate tensile experiments ($\epsilon = 1$, $\dot{\epsilon} = 0.2\ 1/\mathrm{s}$) are sequentially conducted on the same SIP sample, once utilizing the LCR-meter and once the HV-method (Figure 99a). The samples are trained prior to these experiments, by applying 10 loading-unloading cycles, to reduce the effect of cyclic changes of the properties and to obtain comparable results. Both measurements are configured with identical measurement frequency $f_m = 1$ kHz, but different amplitudes: $U_m = 1$ V for the LCR-meter, and $U_m = 20$ V for the HV-method, with no superimposed high voltage.

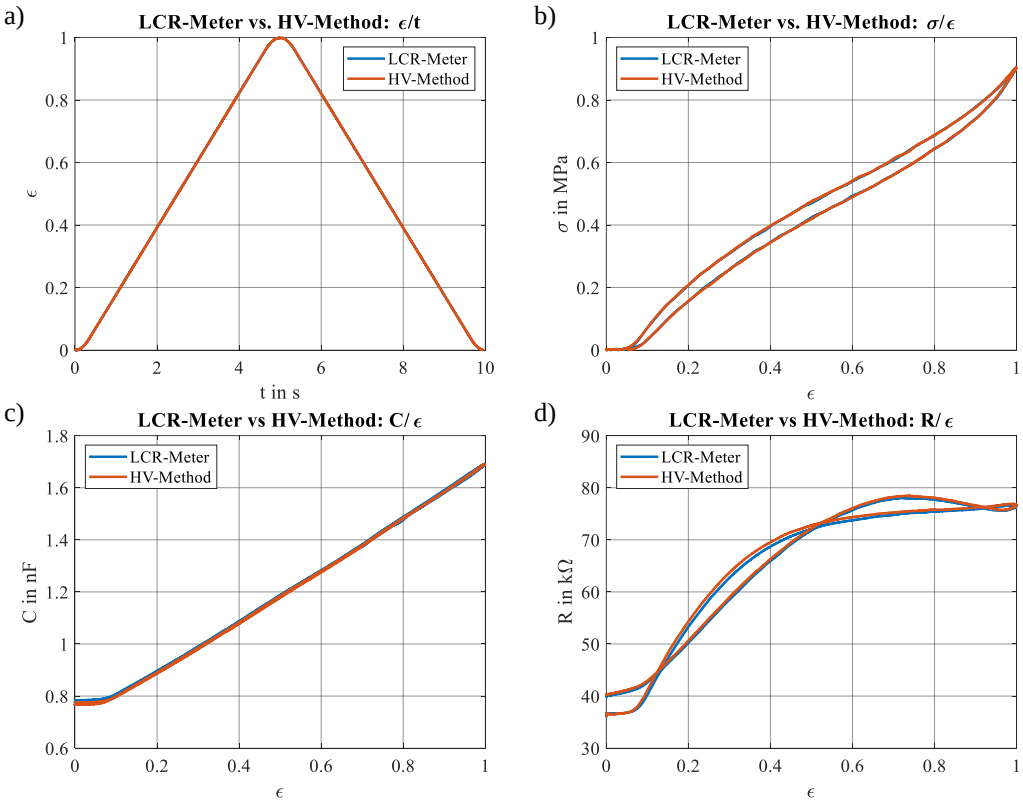

Figure 99: Two identically configured constant strain-rate experiments conducted to the same SIP sample, once using the LCR-meter, and once using the HV-method for complementary impedance measurement (a), showing consistent results for the measurement of force (b), capacitance (c), and resistance (d).

The experiments show satisfactory and consistent measurement results for all measurands, including mechanical stress (Figure 99b), capacitance (Figure 99c) and resistance (Figure 99d), whereby minor deviations are attributable to the cyclic changes in the electro-mechanical properties of the sample. The HV-method can therefore be used to investigate rate-dependent effects, or the influence of superimposed constant controlled high voltages on the electrical DET properties, i.e. during tensile testing.

4.2.5 Tensile Tests with Varying Strain Rate

Varying strain rate experiments at constant strains are used to identify strain rate-dependent characteristics of DETs. A corresponding series of experiments is demonstrated by loading and unloading a single SIP sample with sinusoidal strains of gradually increasing frequency ($\epsilon = 0.5$, $f = 0.01 \dots 10$ Hz, with 10-fold increments), resulting in gradually increasing average strain rates ($\dot{\epsilon} = 0.02 \dots 20\ 1/s$, with 10-fold increments). The choice of sinusoidal strain trajectories thereby enables smooth transitions when changing the motor travel direction (Figure 100a). An increase in slope and hysteresis width is observed from the resulting stress-strain curves, demonstrating the typical viscoelastic characteristics of DETs (Figure 100b).

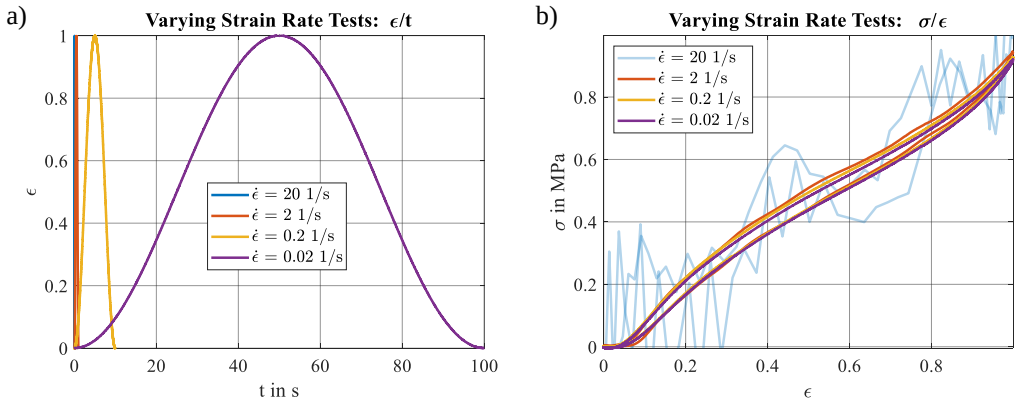

Figure 100: A series of tensile tests with identical strain but different gradually increasing strain rates, sequentially conducted on the same SIP specimen (a), and the resulting stress-strain results showing increasing stiffness and hysteresis for increasing strain rates (b).

The stiffening effect can be attributed to the reduced time available for the polymer chains to realign at higher strain rates. The wider hysteresis can be explained by an increase in frictional effects, such as those caused by the carbon black filler particles. The stress-strain curve for $\dot{\epsilon} = 20\ 1/s$ does not yield an evaluable measurement signal due to the dynamic effects of the test bench, in particular the motor jerk.

However, for complementary measurement of the electrical properties of the SIP, corresponding curves can be examined. The capacitance-strain curves obtained by utilizing the HV-method in a complementary measurement generally show no strain-rate dependent changes in the capacitance curves, except for the highest strain-rate (Figure 101a). Corresponding resistance-strain curves are gradually increasing in slope and hysteresis for increasing strain-rates, similar to the stress-strain curves (Figure 101b). This effect also indicates that the viscoelastic characteristic of the SIP primarily originates from the electrode: The PDMS embedded carbon black particles require time to reorient and redistribute within the electrode material, which affects the electrical conductivity and mechanical properties of the electrode. A homogeneous distribution of carbon black fillers is preferred to achieve low surface resistivity. However, higher strain-rates limit the time available to achieve this condition, thus increasing the resistance. The hysteresis in the capacitance

characteristic curve has no physical meaning but is attributable to synchronization and sampling time error. This becomes particularly evident when comparing an identical test series in which the LCR-meter is used instead of the HV-method for complementary measurement of capacitance (Figure 101c) and resistance (Figure 101d).

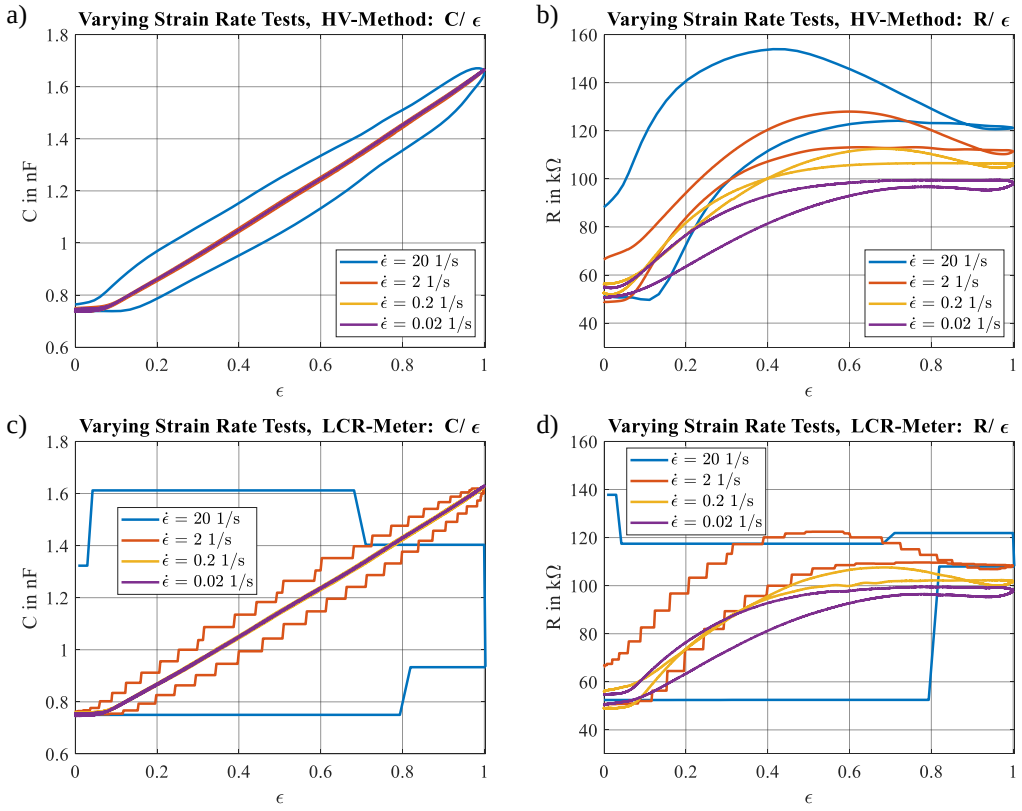

Figure 101: Electrical properties obtained by varying strain rate experiments, showing no strain rate dependence for capacitance (a), but gradually increasing resistance with strain rate (b); demonstrating that the results obtained with the custom implemented HV-method (a, b) generally achieve more reasonable results at higher strain rates compared to the LCR-meter (c, d).

Even at lower strain rates, both sets of measurements exhibit significantly higher hysteresis due to the limited sample transfer rate of the LCR-meter, with non-evaluable results observed at high strain rates. This illustratively demonstrates that the proprietary implemented HV-Method has not only the advantage of providing measurements during applied high voltage and simultaneously on multiple tests samples, but also yields more reliable results for high test rates.

4.2.6 Tensile Tests with Varying Constant Voltage

For demonstration purposes, a series of identically configured constant strain-rate tensile experiments ($\epsilon = 0 \dots 0.5$, $\dot{\epsilon} = 0.05\ 1/\mathrm{s}$) is conducted to the same SIP sample, with gradually increasing complementary constant controlled voltages applied ($u_c = 0 \dots 1.2\ \mathrm{kV}$ in $0.4\ \mathrm{kV}$-increments) (Figure 102a). From the corresponding results, the voltage-induced stress softening demonstrates the typical actuation effect of the SIP, which progressively increases with increasing voltage (Figure 102b). Considering stress at a specific strain (e.g. $\epsilon = 0.5$), approximately

quadratic decrease in stress is observed for increasing voltages. This is expected for both, pure shear and uniaxial DETs, as the Maxwell stress only correlates to the square of the applied voltage, if the uniaxial strain is fixed (refer to Section 2.1.4). Considering the slope of the stress-strain-curves over gradually increasing voltages, an approximately linear decrease is observed, indicating that the SIP sample behaves rather uniaxial, than pure shear, as for pure shear DETs a quadratic decrease over strain is expected (see Section 2.1.4). Furthermore, the zero crossing of the stress with the strain axis shifts to the right, thus widening the zero-stress plateau. This indicates that the Maxwell stress compresses the film at zero-strain, which consequently expands in length. This effect is also evident from the capacitance-strain curves, as the basic capacitance at zero-strain also increases progressively with the applied constant voltage, and the approximately constant capacitance plateau in the lower strain range becomes wider (Figure 102c).

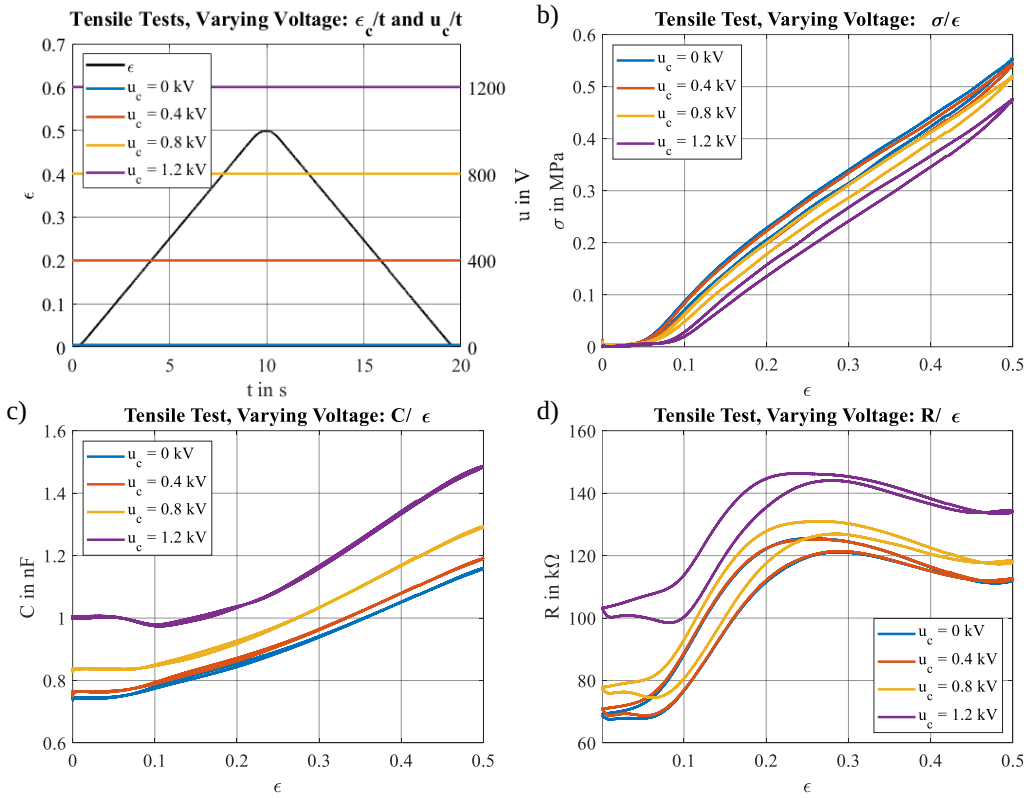

Figure 102: A series of constant strain rate tensile tests complemented with gradually increasing constant voltages (a); and results showing progressive stress softening with increasing voltage (b), as well as increasing magnitudes and slopes of capacitance-strain curves (c), and resistance-strain curves (d).

For ideal pure shear deformation, a consistent capacitance-strain path equal to the 0 kV-curve would be expected for all constant voltages when the curves leave the plateau, since no voltage-induced deformation can occur due to volume consistency (refer to Section 2.1.4). Conversely, for ideally uniaxial samples an increasing capacitance-strain curve is expected for increasing constant voltages, as the Maxwell stress not only applies in the longitudinal direction but also increases the width and simultaneously reduces the thickness. This characteristic is approximately observed from the experiments. However, the considered sample neither behaves pure shear, nor ideally uniaxial.

Instead, it can deform biaxially at zero-strain, and exhibits an inhomogeneous deformation (necking effect) with a trend towards uniaxial deformation. Biaxial deformation generally results in a higher Maxwell stress in comparison to uniaxial deformation, which consequently results in a higher voltage-induced change in capacitance. This explains the non-linear capacitance-strain characteristics in the lower strain range, with the transition from biaxial to uniaxial deformation particularly evident in the 1.2 kV-curve, where the capacitance first decreases from the initial value, and then increases over strain. The resistance measurements also exhibit a progressive increase with increasing voltage (Figure 102d). This can be explained by the voltage induced deformation in width-direction of the SIP. Due to the high charges, it is also conceivable that the distributed conductive electrode particles repel each other. Both effects can lead to an increased distance between the conductive particles and thus increase the resistance.

4.2.7 Conclusion on Mechanically Controlled Experiments

Mechanically controlled experiments comprise strain-controlled tensile tests conducted on both pure film SIP samples and SIP samples equipped with electrodes. Investigations on varying strain amplitudes, strain rates, complementary applied constant voltages, and ambient conditions, are demonstrated. Varying strain amplitudes reveal typical DET properties, including a pronounced Mullins effect, with a similar phenomenon observed for the resistivity-strain characteristics, as well as an approximately uniaxial SIP characteristics resulting in a linear capacitance-strain curve. Experiments with slow strain rates show consistent measurements of the standardized LCR-meter and the proprietary HV-method. Varying strain rates result in an increase in stiffness and electrode resistance, while varying applied constant voltages result in voltage-induced softening, and thus actuation of the DET, accompanied by an increase in capacitance and resistance. These experiments demonstrate that the HV-method provides interpretable results for both, high strain rates and for complementary applied actuation voltage, capabilities that are not achievable with the standardized LCR-meter. Furthermore, testing is conducted under varying ambient conditions to showcase operations within wide temperature and humidity ranges. Thereby, no significant influence of humidity on the electromechanical properties of the SIP is observed, but a noticeable increase in stiffness and conductivity is noted with increasing temperature.

4.3 Electrically Controlled Experiments

The electrically controlled experiments shown in the following sections comprise blocking force experiments and dielectric breakdown experiments. The blocking force experiments are configured as test series with varying pre-strains conducted to one SIP sample. Dielectric breakdown tests are carried out simultaneously on 15 SIP samples, thereby configuring different pre-strains for each module, thus demonstrating simultaneous testing with various operational conditions.

4.3.1 Blocking-Force Tests with Varying Pre-Strains

For the blocking force experiments, one SIP sample is successively subjected to gradually increasing pre-strains ($\epsilon_c = 0 \ldots 0.5$ in 0.125 −increments), and electrically loaded and unloaded with identical voltage ramps ($u = 0 \ldots 1.2\ \mathrm{kV}, \dot{u} = 240\ \mathrm{V/s}$) (Figure 103a). Corresponding stress-voltage curves show similar progressively decreasing characteristics for the non-zero pre-strains (Figure 103b), whereas capacitance- and resistance-voltage curves show increasing behavior for both, increasing pre-strain and increasing voltage (Figure 103c, d).

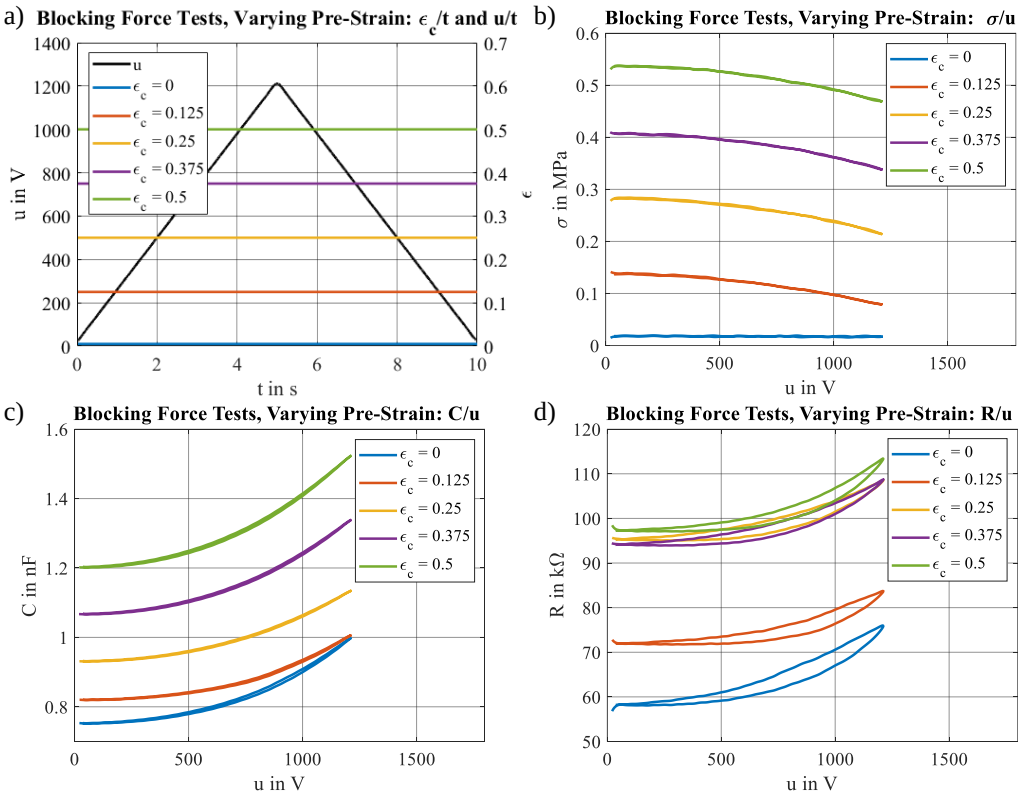

Figure 103: A series of blocking force experiments with complemented gradually increasing pre-strains applied to one SIP sample (a); and results over voltage for stress (b), capacitance (c), and resistance (d).

By only considering the change of stress over voltage, similar approximately quadratically increasing negative stress-softening is observed for all non-zero pre-strains (Figure 104a). A quadratic characteristic is expected for both, ideally uniaxial and ideally pure shear DET samples, as the length of the sample is blocked, and the force only depends on the voltage (refer to Section 2.1.4). Minor deviations and a slightly increasing negative slope of the curves are attributable to the necking effect. To the contrary, the slope of the capacitance-strain curve is gradually increasing with increasing non-zero pre-strains (Figure 104b). This indicates the uniaxial character of the SIP sample, in which width and thickness can change due to voltage induced electric field and resulting Maxwell stress: As those generally increase for increasing pre-strains, higher compression in thickness and a larger expansion in width are obtained, resulting in a larger capacitance change.

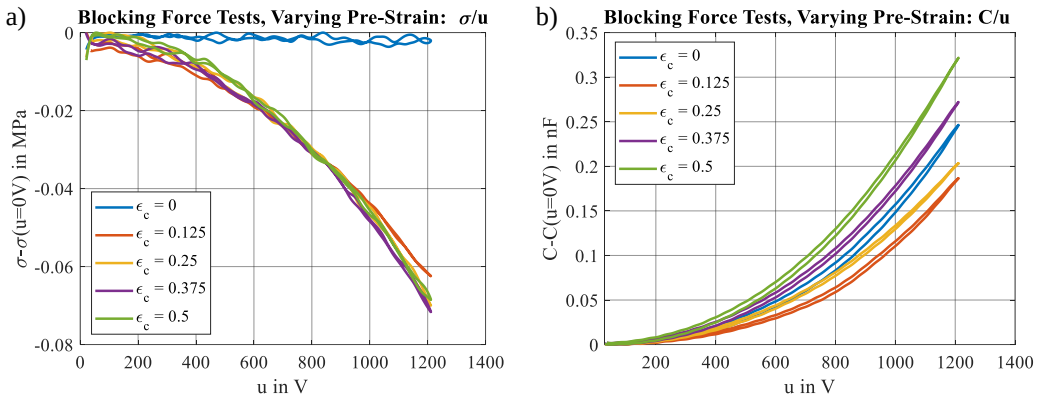

Figure 104: Detailed view of the change in stress and capacitance by subtracting the respective initial values, showing an approximately quadratic characteristic for the stress-voltage curves with decreasing negative slopes for increasing non-zero pre-strains (a), and corresponding increasing positive slopes of the capacitance-voltage curves (b).

The zero-strain curve does not fit into this characteristic, as the SIP deforms biaxially, if it is not constraint by any pre-stretch, resulting in a higher capacitance change in comparison to lower uniaxial pre-strains, but a lower capacitance change when compared to higher pre-strains (refer to Section 2.1.4). A similar behavior is observed from the resistance measurements, which show gradual increase for increasing pre-strains, and a notably higher slope over voltage for the zero-strain curve (Figure 103d).

4.3.2 Dielectric Breakdown Tests with Varying Pre-Strains

For the dielectric breakdown tests, all test stations of the test setup are equipped with SIP samples (Figure 105).

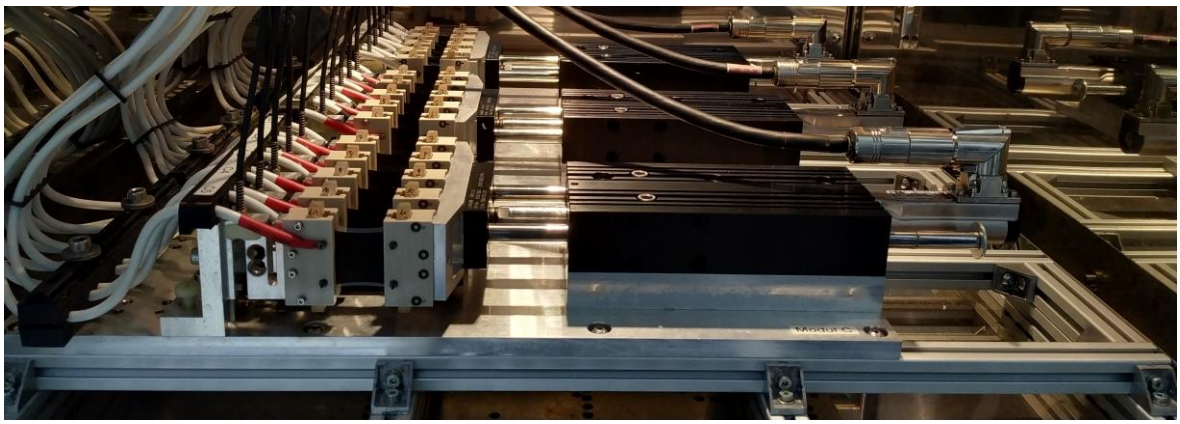

Figure 105: Test bench fully equipped with SIP samples, with different constant slider positions for each module, allowing different pre-strains to be applied to each of the five samples, and dielectric breakdown experiments to be conducted under different operating conditions.

Thereby, the three test modules are configured to apply different constant pre-strains to five samples each ($\epsilon_c = 0, 0.25$, and 0.5). A voltage ramp ($u = 0 \ldots 1.5\,\mathrm{kV}, \dot{u} = 100\,\mathrm{V/s}$) is applied to all samples, thus demonstrating simultaneous testing with varying operational conditions (Figure 106a). The experiments are complemented by an additional similarly configured experiment in

sequence where a pre-strain ϵ_c =1 is applied to five additional SIP samples. From the results, typical stress, capacitance, and resistance curves show a continuous characteristic with increasing voltage until breakdown occurs (Figure 106b). Therefore, failure cannot be predicted by any discernible deviation prior its occurrence. For the present example, the stress curves show that the sample initially undergoes an electrical breakdown, resulting in an initial increase in stress due to the removal of the electric field (Figure 106b, #1). The electrical breakdown results in the formation of a burn hole, which represents a mechanical weak point. This hole serves as the initiation point for a mechanical tear-through of the pre-strained SIP, as evidenced by the subsequent stress reduction (Figure 106b, #2). As the breakdown results in a short-circuiting of the opposing SIP electrodes, no meaningful interpretation can be derived from capacitance and resistance measurements during and after dielectric breakdown.

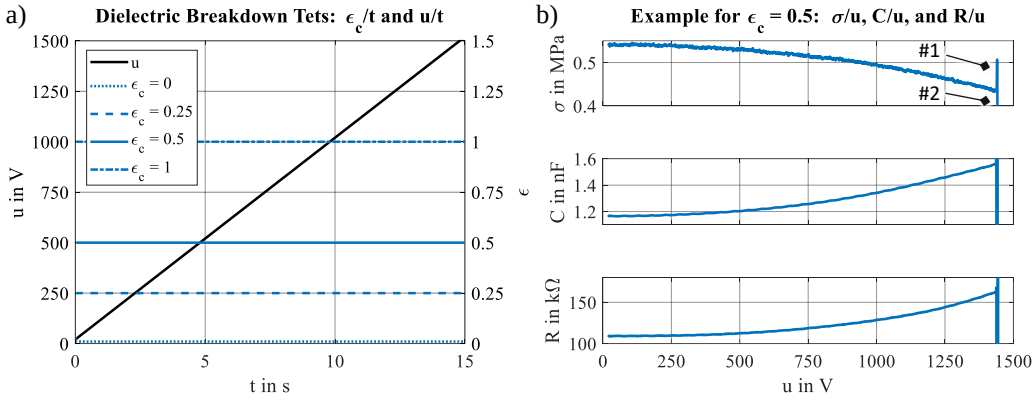

Figure 106: Configuration of dielectric breakdown tests with different pre-strains, with each configuration simultaneously conducted to five SIP samples (a), and corresponding typical characteristics of stress, capacitance, and resistance until breakdown for one exemplary sample (b).

At lower strains, mechanical tear-through of the samples can generally be avoided by switching off the high voltage immediately after breakdown is detected, thus resulting in a smaller burn hole. Therefore, for the presented experiments, the duration of exceeding the short-circuit current limit for detecting a breakdown is set to only 10 ms, with a threshold of 200 µA. On the one hand, this enables reliable breakdown detection, as evidenced by the corresponding current measurements (Figure 107a). On the other hand, except for the highly pre-strained samples, no tear-through is observed, as evidenced by the corresponding stress curves (Figure 107b).

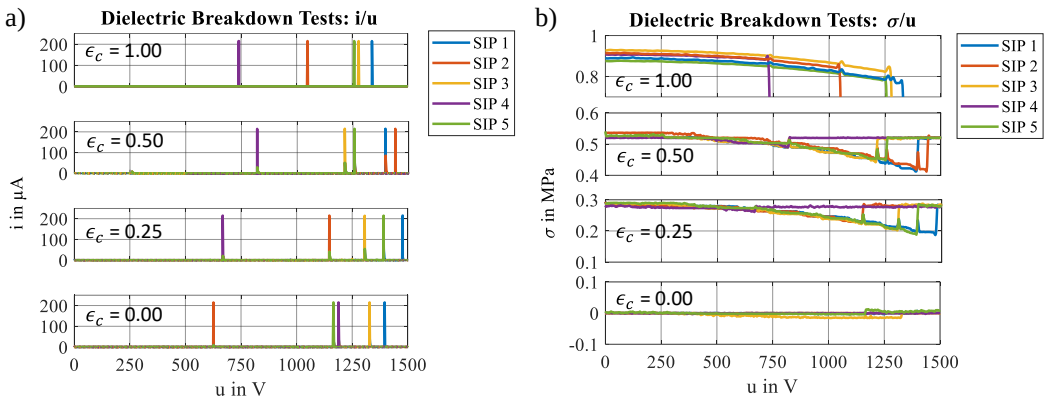

Figure 107: Measurement results of dielectric breakdown tests, with current-voltage curves showing reliable breakdown detection (a), and stress-voltage curves only showing mechanical tear-through for highest pre-strain (b).

A statistical evaluation of the experiments regarding the breakdown voltage as a function of pre-strain, as shown by the corresponding box plots, does not reveal any discernible trends (Figure 108a). However, if the electric field is considered assuming uniaxial deformation, an increase in breakdown strength with increasing pre-strain is observed (Figure 108b), representing a typical trend for (PDMS-based) DETs attributable to the strain-induced reorientation of the polymer chains. The outliers in the statistical analysis predominantly tend towards smaller values, indicating potential early breakdowns due to imperfections in the dielectric film. It is crucial to note that only five samples are considered in each case and a higher number of samples must be investigated to establish more reliable statistical conclusions. However, the experiments presented in this section demonstrate that it is generally possible to reliably collect a substantial amount of statistically relevant data with just a few tests runs by simultaneously testing under either equal or different operating conditions.

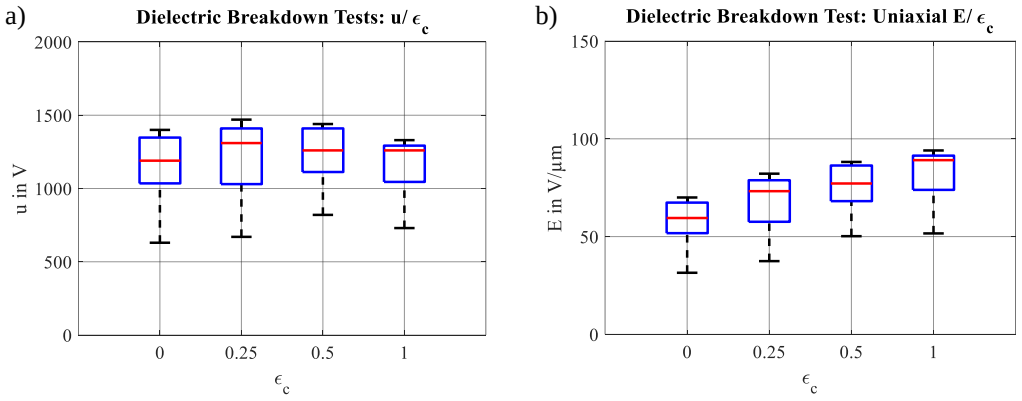

Figure 108: Statistical evaluation of dielectric breakdown experiments, where the breakdown voltage as a function of pre-strain shows no clear trend in the resulting box plots (a), but the corresponding electric field shows a typical increasing dielectric breakdown strength with increasing strain (b).

4.3.3 Conclusion on Electrically Controlled Experiments

Electrically controlled experiments include blocking force tests and dielectric breakdown tests, both with varying constant pre-strains. The blocking force experiments provide physically interpretable results regarding changes in force, capacitance, and resistance over voltage, thus demonstrating the capability of the HV-method. The dielectric breakdown tests are employed to demonstrate simultaneous short-term testing on multiple SIPs, that are subjected to varying pre-strains, and simultaneously exposed to identical voltage ramps until breakdown occurs. From the results it is shown that all breakdowns are reliably detected, and a typical increase in dielectric strength with increasing pre-strains is observed. Thereby capacitance and resistance exhibit continuous increase until failure, while force measurements indicate failure prior to film tearing.

4.4 Electromechanically Controlled Experiments

The experiments shown in the previous sections demonstrate purely mechanically or purely electrically controlled experiments, whereby the respective electrical or mechanical constraints are fixed. However, some test scenarios also require the simultaneous active control of mechanical and electrical variables, such as displacement and voltage. This is generally possible with the experimental test bench presented in this work and is demonstrated in the following using two scenarios: A constantly controlled electric field test, and a simulated DET system test, by configuring voltage and strain-control accordingly.

4.4.1 Electric Field Control Tests

Controlling the electric field applied to a DET can be significant in exploring improvements in the electromechanical response of an actuator. On the one hand dielectric strength of a DET increases with increasing strain, as discussed in Section 4.3.2, enabling to operate corresponding DET actuators with an increasing electric field over strain to enhance their electromechanical output. On the other hand, controlling the electric field instead of the voltage generally enables strain-independent control of the Maxwell stress and thus actuator force, and results in a consistent differential sensor characteristic curve for constantly controlled electric fields. This is demonstrated in a corresponding experiment, in which the voltage and strain curves are configured in such a way that the corresponding electric field is approximately constant ($\epsilon = 0 \dots 0.5, u = 1.20 \dots 0.97\ \mathrm{kV}$, $E_c \approx 60\ \mathrm{V/\mu m}$) assuming uniaxial behavior of the SIP sample (Figure 109a, b). The experiment is compared to two further strain-controlled experiments, one with no voltage applied ($\epsilon = 0 \dots 0.5$, $u_c = 0\ \mathrm{V}, E_c = 0\ \mathrm{V/\mu m}$) and one with constant voltage applied, resulting in an continuously increasing electric field over increasing strain ($\epsilon = 0 \dots 0.5$, $u_c = 1.2\ \mathrm{kV}$, $E_c \approx 60 \dots 75\ \mathrm{V/\mu m}$). For the higher strain ranges ($0.2 < \epsilon < 0.5$), the stress-strain curves exhibit similar slopes for both the constant electric field curves and the zero voltage curves, resulting in consistent stress release over strain, and thus a strain independent Maxwell stress, as expected (Figure 109c). To the contrary, the constant voltage curve exhibits a significantly lower slope, resulting in a continuously

increasing stress release over increasing strain, and thus a strain-dependent Maxwell stress. Similarly, in the capacitance-strain diagram, comparable slopes are observed for the constant electric field curves and zero voltage curves, whereas the constant voltage curve shows a significantly higher slope (Figure 109d).

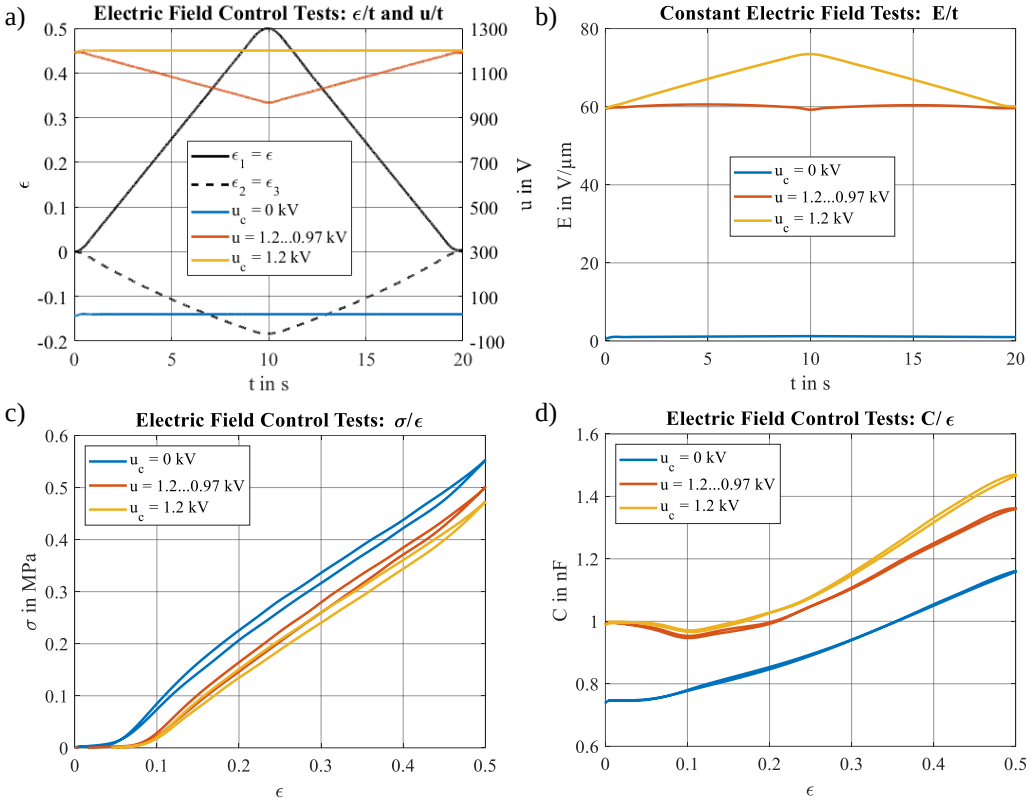

Figure 109: Configuration of voltage and strain control trajectories (a), to obtain an approximately constant electric field applied to a SIP assuming uniaxial characteristics (b). In contrast to a corresponding constant voltage control, this approach yields in an approximately constant stress release (c) and an approximately constant capacitance increase over strain (d), when compared to the non-actuated SIP.

Therefore, for in the higher strain range, approximately consistent sensor characteristic curves over strain are obtained, which only differ by an offset due to the constantly applied electric field. For the lower strain range $(0 < \epsilon < 0.2)$, the results deviate from the expected characteristics, as the SIP does not behave uniaxial in that range but undergoes a transition from biaxial- to uniaxial characteristics.

4.4.2 Simulated DET System Tests

Due to the lack of the respective sensor equipment, it is not possible to carry out free stroke experiments on the test bench, which can be controlled purely electrically and evaluated in terms of stroke over actuation voltage by means of displacement measurements. However, as suggested in Section 3.3.1, a DET actuator system can be installed in such a way, that the force can be measured and used for evaluation purposes, e.g. to investigate the electromechanical response of a SIP-NBS system, which is limited in stroke by hard stops (Figure 110a).

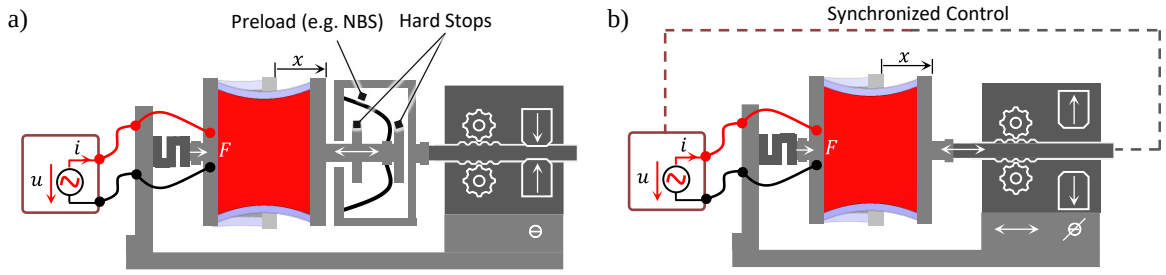

Figure 110: Schematic illustration of the installation of a SIP-NBS actuator system to the test bench in order to conduct free stroke experiments, which can be evaluated in terms of force measurement (a), and alternative configuration with no physical preload mechanism applied, but synchronized control of motor and high voltage amplifier enabling to simulate corresponding strain-voltage system characteristics.

The resulting electromechanical characteristic, although highly non-linear and different from the purely electrically or purely mechanically controlled experiments discussed earlier, accurately reflects the electromechanical load established under realistic operating conditions and closely mirrors the application scenario. It is therefore of particular interest to study the long-term behavior of DETs under these conditions. To draw conclusions from the results that can be attributed to the DET rather than to the preload mechanism, experiments must be conducted in a way that ensures the preload mechanism's characteristics remain constant over time or cycles. Therefore, experiments without a physical preload mechanism can be conducted using a feed-forward HIL-approach, in which voltage and strain are controlled in such a way, to mimic the strain-voltage characteristics that is expected from a free stroke experiment (Figure 110b).

Design of Experiment

To demonstrate this approach, a generic DET actuator system is designed, utilizing the SIP sample combined with a generic linear NBS characteristics and hard stops, enabling the SIP to operate in a stretch range $x = 5 \dots 10$ mm ($\epsilon = 0.25 \dots 0.5$), when subject to high voltage $u = 0 \dots 1.2$ kV (Figure 111a). The corresponding actuator system provides approximately constant actuator force $\Delta F \approx 0.04$ N within a stroke range of $\Delta x = 5$ mm (Figure 111b).

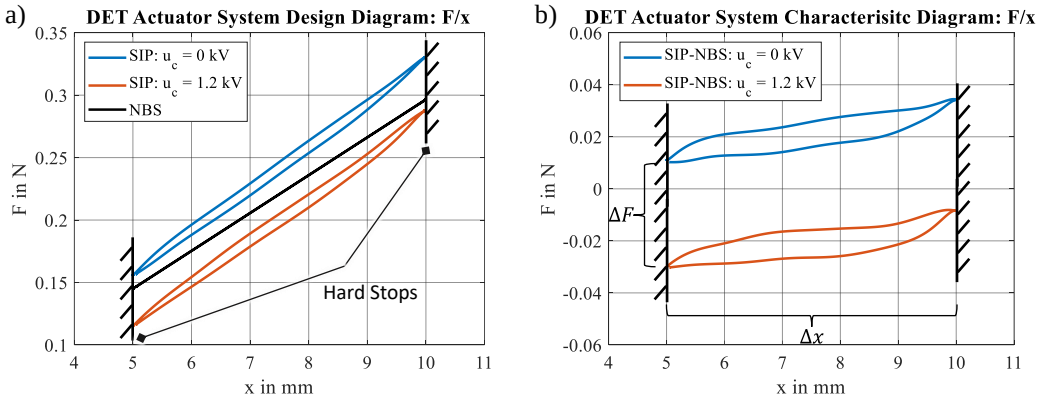

Figure 111: Exemplary system design diagram utilizing the SIP sample combined with a generic linear NBS characteristics and hard stops (a); and resulting actuator system characteristic diagram (b).

To simulate the expected strain-voltage characteristics of this actuator system using the test rig, sinusoidal high voltage waveforms provided by the high voltage amplifier are synchronized to trapezoidal strain trajectories provided by the linear motor (Figure 112a). Thereby, one voltage waveform is configured to be precisely in phase with the strain trajectory in comparison to a second one, which is provided with a constant phase-shift $\phi = -10°$. The resulting strain-voltage curves mimic the expected voltage-controlled system behavior, that is typically observed in free-stroke experiments (Figure 112b). The phase-shifted variant represents the more realistic case, exhibiting typical hysteresis, which is attributable to the hysteresis behavior of the SIP, as well as frictional effects within the overall actuator system (refer to Section 2.1.6).

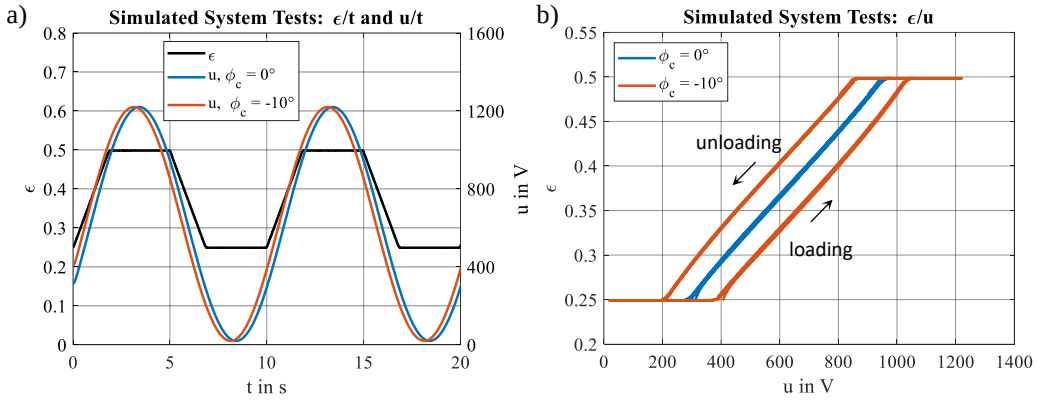

Figure 112: Sinusoidal high voltage waveforms synchronized to a trapezoidal strain trajectory (a); and resulting strain-voltage curves that mimic the expected voltage-controlled system behavior typically observed when conducting free-stroke experiments on an SIP actuator system consisting of a NBS preload mechanism and stroke-limiting hard stops (b).

Experiments conducted to the SIP element with voltage and strain configured in this way can be evaluated in terms of force (stress), capacitance and resistance over voltage (Figure 113a, b, c). In general, similar conclusions can be drawn from this experiment as from corresponding free stroke experiments, provided that the change in properties over time or cycles does not affect the working point of the system.

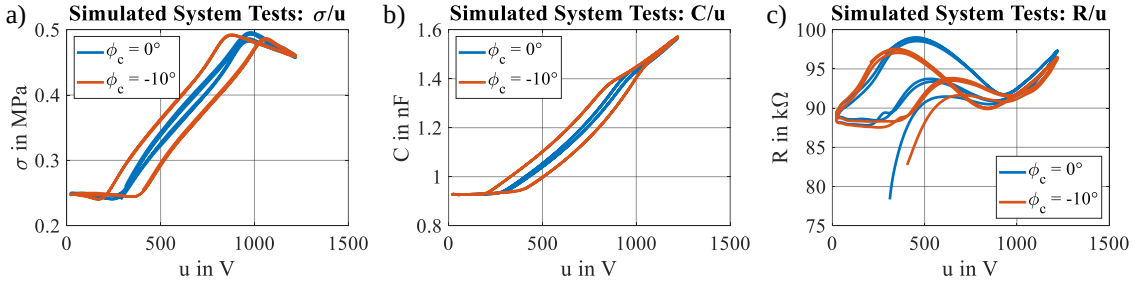

Figure 113: Measurements obtained by the simulated system tests, enabling to evaluate corresponding tests in terms of stress (a), capacitance (b) and resistance (c) as a function of voltage.

A major advantage of this approach is the facilitated test preparation, as no preload mechanism needs to be installed. In addition, especially for the evaluation of long-term tests, the specification

of a constant strain response to the voltage control ensures that the change in the electromechanical properties over time and cycles can only be attributed to the DET.

4.4.3 Conclusion on Electromechanically Controlled Experiments

Electromechanically controlled experiments comprise electric field control tests and simulated DET system tests. These tests showcase the application of flexible control and synchronization of voltage waveforms and displacement trajectories that is possible with the test rig. For the electric field control tests, strain and voltage are configured to ensure a constant electric field across the SIP. As a result, constant actuation force and a consistent sensor characteristic curve are obtained over strain. With the simulated DET system test, voltage and stroke applied to a SIP element are controlled to mimic the stroke-voltage response obtained for a SIP system biased with a preload element. Evaluating the results in terms of force, this test represents a valid alternative for common free-stroke tests, that cannot be carried out on the test rig due to the lack of individual stroke measurements provided for each test station.

4.5 Long-Term and High-Cycle Experiments

Overall, the short-term and low-cycle tests demonstrated previously can be seamlessly extended to uninterrupted long-term and high-cycle tests. This is exemplified in this section by conducting mechanically controlled experiments with a constant applied high voltage to investigate cycle-dependent degradation effects and lifetime characteristics under a variety of environmental conditions.

4.5.1 Degradation Tests

Degradation of the SIP properties is demonstrated by conducting a high strain-rate tensile test with sinusoidal strain control to one SIP with no high voltage applied ($\epsilon = 0 \dots 1,\ f = 5$ Hz for 100,000 cycles). To ensure high-quality measurement results, this procedure is intermittently interrupted at random intervals to perform slower constant strain rate experiments between ($\epsilon = 0 \dots 1,\ \dot{\epsilon} = 0.05\ 1/s$). These experiments provide higher resolution data and less distorted measurements due to dynamic effects, and are evaluated in terms of stress, capacitance, and resistance (Figure 114a-d). The stress-strain curves exhibit a continuous decrease of total stress and hysteresis width in this experiment (Figure 114b). These changes are irreversible and coincide with an increasingly widening zero-stress plateau along the strain axis, indicating cyclic material degradation through permanent deformation.

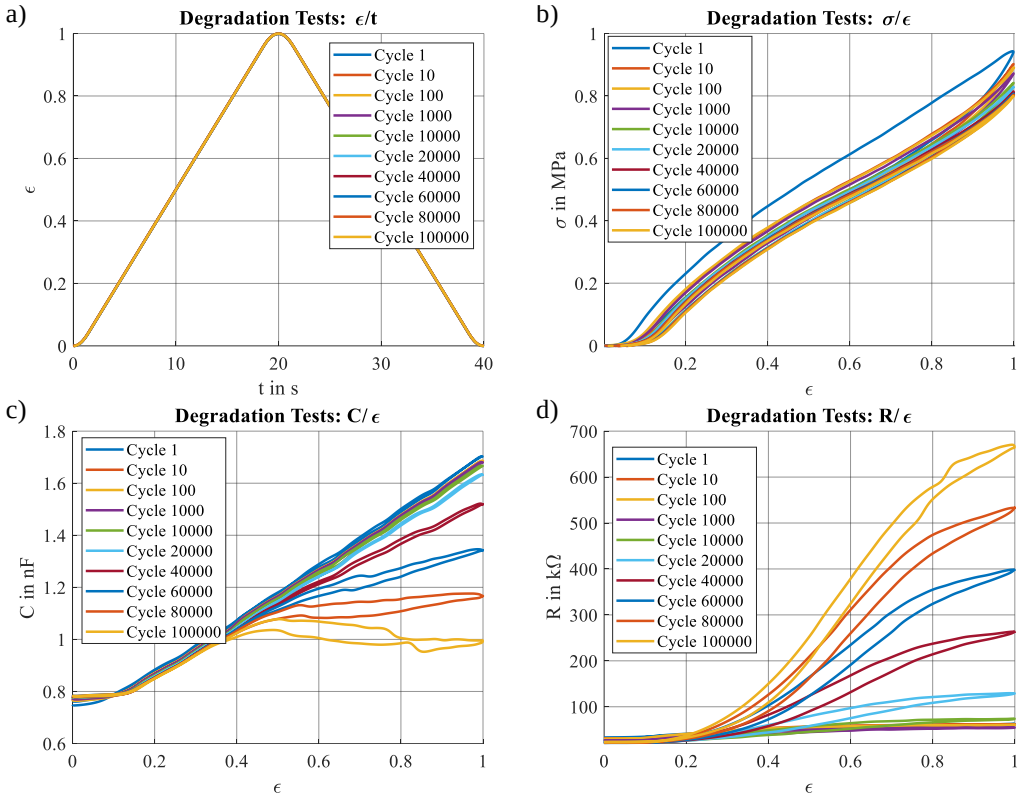

Figure 114: High-cycle strain-controlled degradation test with no complementary voltage applied to the SIP sample (a), showing gradual stress-strain reduction with increasing number of load cycles (b), accompanied by a significant nonlinear decrease in capacitance-strain characteristics (c) and corresponding nonlinear increase in resistance-strain characteristics (d).

From analyzing the reduction of the maximum stress σ_{max} of each stress-strain curve obtained at maximum strain ($\epsilon = 1$), a regressive trend is observed for increasing number of cycles (Figure 115a, top). Examination of the cyclic dissipated energy E_{diss}, associated with the area enclosed by the hysteresis loop of the stress-strain curve shows an approximately linear decrease, if the first cycle is neglected (Figure 115a, bottom).

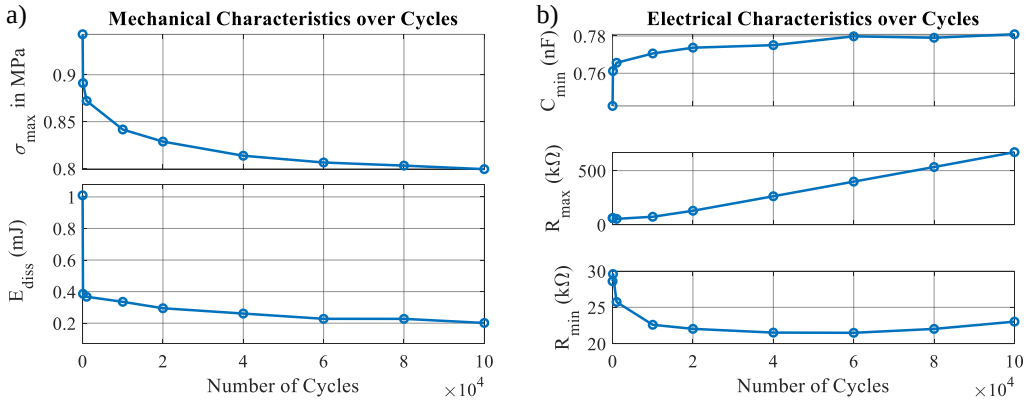

Figure 115: Maximum stress and cyclically dissipated mechanical energy showing decreasing characteristics with increasing number of cycles (a); with minimum capacitance and maximum resistance obtained at maximum strain increasing correspondingly (b), while the minimum resistance obtained at zero-strain shows an initial decreasing trend and increases with increasing number of cycles.

The first cycle typically shows a relatively high energy dissipation, which is attributable to the Mullins effect. From analyzing the evolution of the minimum capacitance C_{min} acquired at zero-strain for each capacitance-strain curve over increasing cycles reveals a degressively increasing trend (Figure 115b, top). This is in accordance with the regressive decrease in stress and allows consistent interpretations regarding permanent deformation, with the capacitance increase attributable to irreversible residual strains after loading and unloading: The residual strains cause an increase in surface area and a decrease in thickness, resulting in an increase in the zero-load capacitance. However, while the slope of the capacitance-strain curves is relatively constant for increasing cycles at low strains, they bend significantly at higher strains and then proceed with a lower slope (refer to Figure 114c). This phenomenon is not indicative of a change in the capacitance properties of the SIP but is rather attributable to a measurement error resulting from the steep increase in electrode resistance over increasing cycles (refer to Figure 114d). Analyzing the evolution of the maximum resistance R_{max} acquired at maximum strain ($\epsilon = 1$) over increasing cycles shows an approximately linear proportional increase, indicating a continuous degradation of the electrode conductivity (Figure 115b, mid). This phenomenon indicates an irreversible rupture of (conductive) connections within the elastomer-filler compound, which becomes particularly evident with large strains, where the destroyed connections and corresponding conductive clusters are pulled apart. Conversely the minimum resistance observed at zero strain first decreases significantly over increasing cycles, until a slight increase is observed in the higher cycle range (Figure 115b, bottom). This phenomenon can be explained by two potential effects with opposing trends, which collectively contribute to the resistivity characteristics: Firstly, the broken connections within the electrode compound may lead to a higher mobility of the conductive clusters, allowing them to be distributed more uniformly. This results in improved conductivity and thus lower resistivity when the electrode is not stretched. Simultaneously, permanent deformation leads to an increase in the electrode surface area, reducing the density of conductive particles within the electrode surface and thus increasing resistivity. Considering that both effects contribute to the resistivity characteristics in combination, the effect of decreasing resistivity dominates in the lower cycle range, while the effect of increasing resistivity dominates in the higher cycle range.

4.5.2 Lifetime Tests with Varying Environmental Conditions

Lifetime tests are demonstrated by conducting tensile tests with sinusoidal strain control ($\epsilon = 0.25 \dots 0.5,\ f = 10$ Hz) and complementary applied constant high voltage ($u_c = 1$ kV) to 15 SIP samples in parallel. The high voltage is selected to be near to the critical dielectric breakdown limit, which is approximately 1.2 kV (refer to Section 4.3.2). In contrast, the constant pre-strain and the cyclic strain range are moderate, aligning with the typical behavior of a large-stroke actuator system designed with an NBS (refer to Section 4.4.2). With this configuration, corresponding DET actuators are tested for their service live when operated close to their maximum electromechanical performance limit. The high cycle rate and simultaneous testing of 15 samples enables accelerated

acquisition of data for statistical evaluation. During the test, samples are monitored for electrical breakdown and mechanical tear-through failure by tracking the exceeding of current and the force thresholds. In both cases, the samples are automatically disconnected from the high voltage amplifier via the respective individual high voltage relay. The test either ends with the mechanical and electrical failure of all samples or is terminated prematurely after reaching five million load cycles, which corresponds to an uninterrupted test duration of six days. As an exemplary study, the test is repeated a total of three times, with each iteration involving new SIP samples and maintaining consistent operational conditions at the same temperature ($T_c = 25$ C) but varying constant humidity levels ($H_c = 10$ %, 50 % and 90 %). The results are evaluated through bar diagrams illustrating the individual electrical and mechanical lifetimes of each SIP sample until failure or premature test termination (Figure 116a, c e).

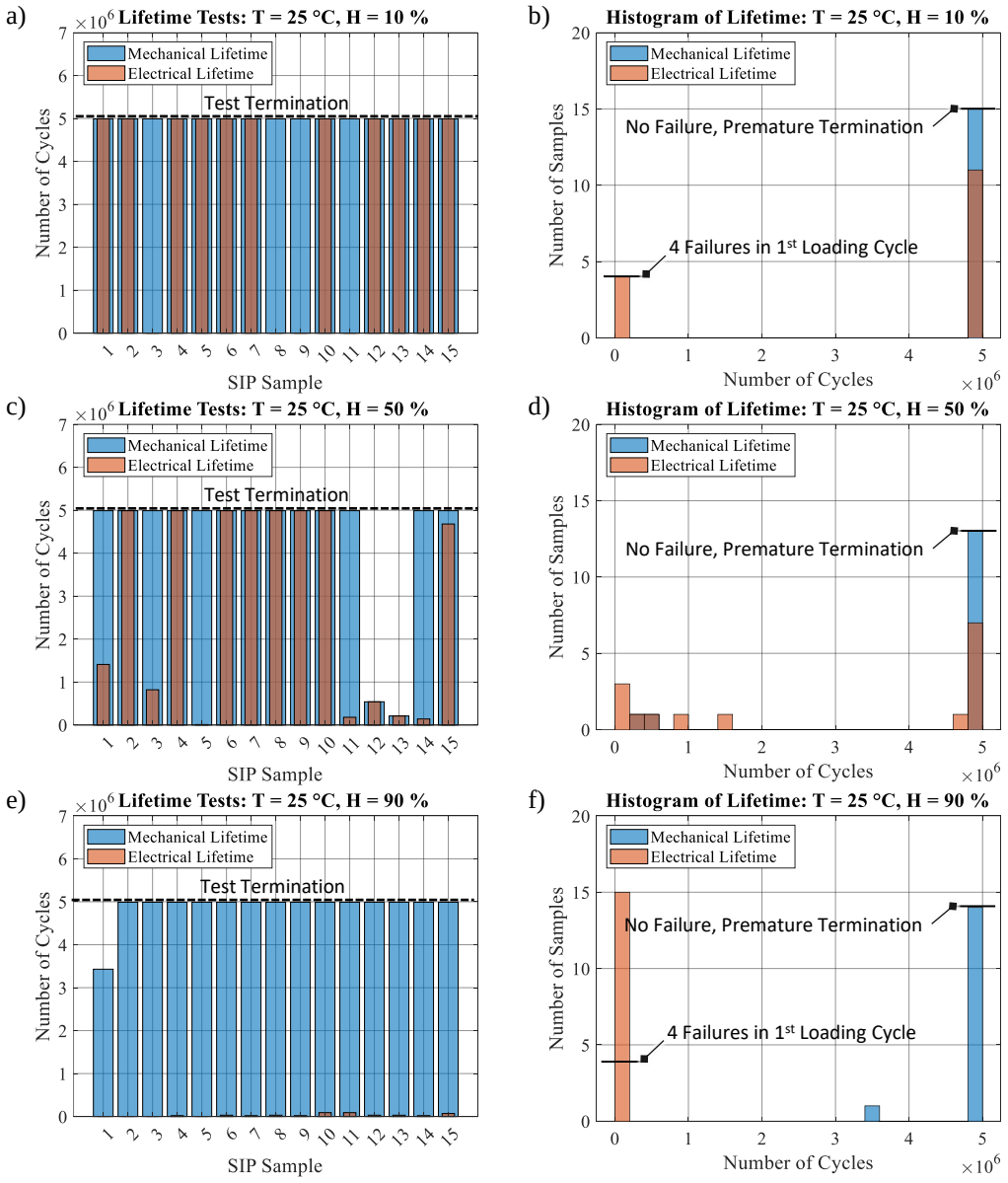

Figure 116: Bar-plots and corresponding histograms showing electromechanical lifetime of SIPs obtained by long-term experiments conducted to 15 SIP samples in parallel within varying humidity conditions respectively; with low humidity level (a, b), moderate humidity level (c, d) and high humidity level (e, f).

Corresponding histograms depict the count of failed or terminated samples relative to the total number of samples (Figure 116b, d f). A clear trend in the dependence of the electrical service life on humidity is obtained, showing a significant decrease in lifetime for higher humidity levels. This observation is particularly evident when excluding samples from the evaluation that fail directly in the initial loading cycle, as these failures are likely attributable to imperfections in the dielectric film, as discussed in the context of dielectric breakdown experiments (refer to Section 4.3.2).

Treating the corresponding samples as outliers, all remaining samples demonstrate a capability to endure a cyclic load of five million cycles without any electrical or mechanical failure at low humidity levels ($H = 10\ \%$) (Figure 116a, b). At moderate humidity ($H = 50\ \%$), no immediate electrical failure occurs, but 7 samples fail within the first 1.5 million cycles, along with one later failure near the end of the test, while seven samples successfully complete the test without any failure (Figure 116c, d). In addition to the electrical breakdown, two samples also undergo mechanical tear-through. At high humidity level ($H = 90\ \%$), all samples experience electrical failure within a maximum of 90,000 cycles (Figure 116e, f), whereby one sample fails mechanically after more than 3.5 million cycles. Since at low and moderate humidity levels electrical failures predominantly occur early, and the remaining samples do not fail until the end of the test, a statistical evaluation of the probability of failure under the given operating and environmental conditions lacks significance. However, neglecting failures in the first loading cycle, it can be stated, that the probability of failure within five million load cycles is 0 % in dry conditions. For moderate humidity approximately 50 % of the sample fail early, whereby the remaining samples survive. In order to be able to make further statistical statements, the test must be run for more than 5 million cycles.

At high humidity levels, the probability of electrical failure is plotted as a function of lifetime and fitted to a Weibull curve using maximum likelihood estimation (MLE), once including initial failures from the first load cycle, and once excluding them (Figure 117). Excluding initial failures results in a significant increase of the characteristic lifetime, which represents the number of cycles, after which 63,2 % of the samples have failed. However, since data in this experiment was only saved randomly every 10,000 cycles, the raw data provides poor resolution for making statements about the lifetime of the samples. To improve statistical accuracy, the experiment must be repeated with higher resolution data collection and more samples.

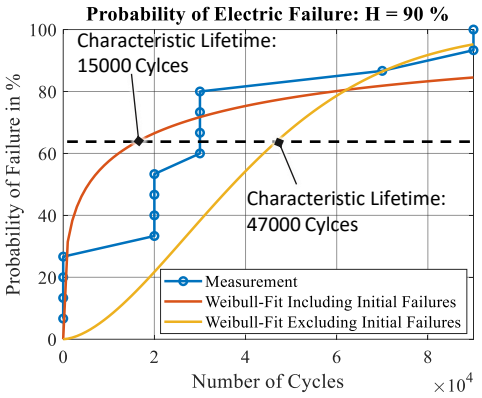

Figure 117: Probability of electrical failure obtained for lifetime tests conducted in high-humidity environments, with corresponding Weibull fits for data including initial failures and excluding initial failures.

To gain deeper insights from the experiments, the samples are removed from the test bench after each long-term test and examined individually with a digital microscope to identify the locations of their electrical or mechanical failure. For a better overview, burn marks resulting from dielectric breakdown and the approximate crack patterns caused by mechanical tear-through for all corresponding samples are highlighted in separate illustrations for each humidity level, thereby color-coding the lifetime in four stages (Figure 118).

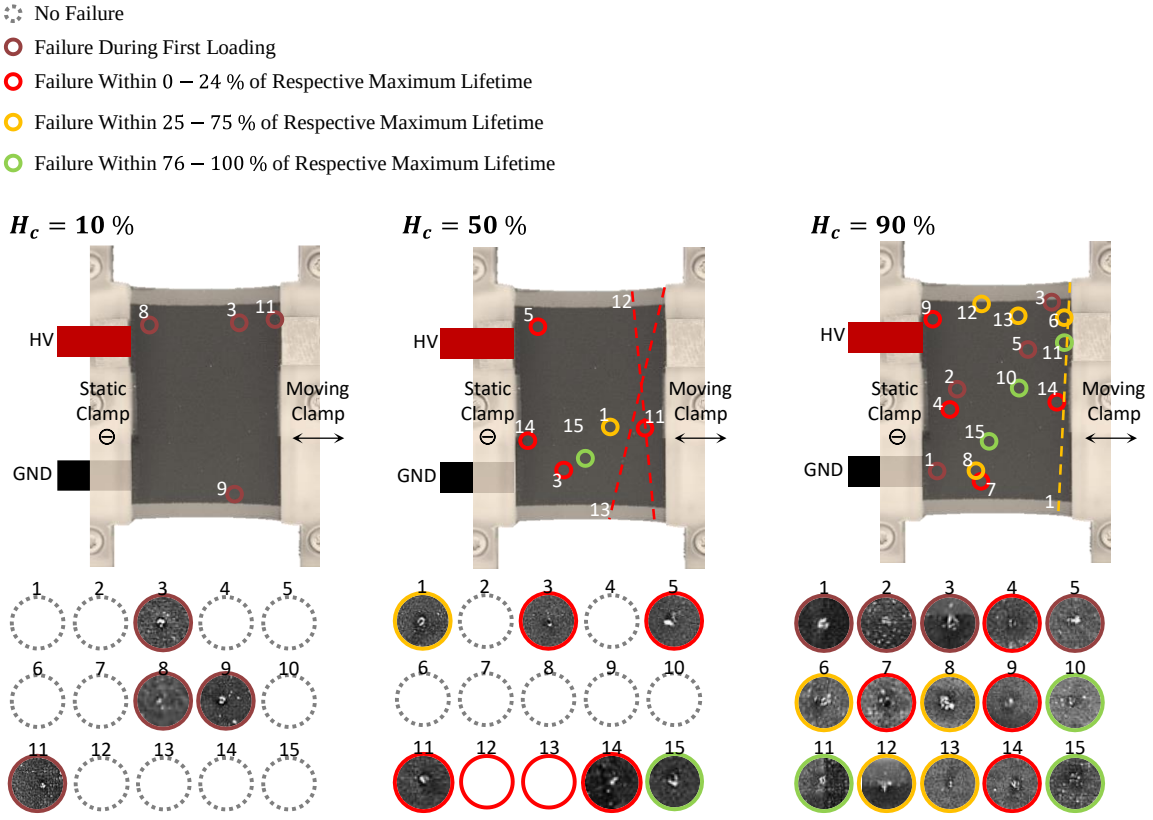

Figure 118: Separate illustrations for each humidity level, highlighting the burn marks resulting from dielectric breakdown and the approximate crack patterns caused by mechanical tear-through for all samples, thereby color-coding the respective lifetimes in four stages, to identify localized defects.

This representation makes it possible to identify potential correlations between localized defects and lifetime of the samples. The absence of burn marks, coupled with a direct tear through from one free SIP edge to the next, suggests that crack initiation due to electrical breakdown can be excluded as a potential cause of mechanical failure. Instead, it can be attributed to minor cutting defects of the respective samples. All mechanical failures occur near the clamping, which is to be expected, as locally increased mechanical shear stresses occur particularly in the corners of the clamping due to the inhomogeneous deformation under uniaxial loading due to the necking effect. Regarding electrical failure, under uniaxial deformation, the highest electric field is expected to be concentrated along the longitudinal axis, especially near the clamps, assuming that the dielectric film has ideally homogeneous properties. However, the breakdown points exhibit distinct concentration patterns across the three test runs and do not adhere to the anticipated failure pattern. This observation suggests that the film lacks homogeneous properties, instead containing localized dielectric weak points that are randomly distributed, leading to dielectric breakdown at various locations. The color coding of the time to failure also shows no clear trend in the local distribution.

4.5.3 Conclusion on Long-Term and High-Cycle Experiments

Long-term experiments demonstrated within this section include degradation tests and lifetime tests within varying environmental conditions.

An exemplary degradation test is conducted to a SIP, by applying 100 % strain (5 Hz) for 100,000 sinusoidal loading-unloading cycles. From the results, permanent set can consistently be observed from all measurands, force, capacitance, and resistance. Additionally, the resistance shows a continuous strain-dependent degradation of the electrode, which is particularly pronounced at high strains.

The lifetime tests demonstrate uninterrupted and accelerated cyclic testing of 15 samples in parallel under long-term conditions. Thereby, sinusoidal strains (10 Hz) and complementary constant voltages are applied while the mechanical and electrical service life is monitored. The test is carried out a total of three times with new samples each time, varying the ambient humidity in the climate chamber. Each test is terminated after 5,000,000 cycles, which corresponds to a duration of approximately six days. These tests demonstrate the durability of the test rig when operated in harsh environmental conditions and provide results that clearly demonstrate the decrease in electrical lifetime of the SIPs with increasing humidity.

4.6 Summary and Discussion on Test Rig Demonstration

To demonstrate the functionality of the test rig developed in the scope of this work, a planar rectangular-shaped DET (SIP) is developed based on an *Elastosil 2030/20* dielectric film, screen-printed with carbon-black-reinforced compliant PDMS-electrodes. Test sample and the test rig sample grips are designed to be compatible and enable facilitated sample mounting by means of snap-in mechanisms and electrical spring contacts. Exemplary tests are conducted on several test samples, including mechanically, electrically, and electromechanically controlled experiments with varying load profiles, and operational as well as environmental conditions.

These tests illustrate the versatility of the test rig and underline its capability to enable comprehensive investigations of the electromechanical characteristics of DETs under various operating and constant environmental conditions. The flexible configurability of the test rig allows a wide range of test scenarios that go beyond those demonstrated, and there is no claim to a complete demonstration of all possibilities in this work. Also, the specification of the general test range considerably exceeds the test range covered by the demonstrated experiments. Both, the specified test ranges, and the corresponding accuracies refer to the test ranges considered and validated within the scope of this thesis. They can generally be further extended by modifying components, i.e. the current monitor shunts, or by replacing series components like motors, load-cells, or high voltage amplifiers, while preserving mechanical, electrical, and program interfaces. Furthermore, the test rig is also not limited to testing of SIP designs and dimensions showcased in this work and can be tailored to various uniaxial operated DET types, i.e. COP, SOP, tubular, and stacked types, with minor adjustments to the sample grips. Generally, the modular test bench design also enables the simultaneous testing of several designs and several operating conditions. Along with testing at high test rates, and within higher environmental temperatures, this underlines its capabilities of accelerated assessment of statistically relevant data.

5 Conclusion and Outlook

5.1 Summary and Conclusion

Dielectric Elastomer Transducers (DETs) have been subject of research for around 30 years. Driven by their promising properties and wide-ranging application, numerous materials, designs, and manufacturing processes have emerged, along with model-based approaches and feasibility studies. Recent trend has increasingly been towards application and process-oriented research and initial efforts have been made to establish the technology on the market. In this context, reliability, and lifetime represent critical factors in assessing the market competitiveness of DET technology, alongside with general DET properties such as sensor accuracy, actuator performance or generator efficiency. These attributes are affected at all product levels, e.g., material, compound, and system, and at all stages of development, e.g., concept, design, and production. Their evaluation and improvement require comprehensive electromechanical testing, including both short-term and particularly long-term testing under various operating and environmental conditions, as well as simultaneous testing of multiple samples for accelerated statistical evaluation.

The literature review conducted in the scope of this thesis shows reveals, that existing test rigs typically focus on specific DET applications and designs, and emphasize either purely mechanical or purely electrical control, with only partial measurement of electromechanical quantities. This applies in particular to test rigs with several test stations for accelerated acquisition of statistically significant data, which are commonly used for long-term testing of DETs. No test rig has been proposed yet, enabling for both, comprehensive short- and uninterrupted long-term testing in parallel on numerous DETs, thereby providing synchronized control on strain and voltage, and simultaneously acquiring force, capacitance, and resistance simultaneously for all test objects within various constant controlled environmental conditions.

This gap is closed by the test rig developed in the scope of this dissertation. It enables for simultaneously electromechanical testing on 15 DETs, thereby providing synchronized control on strain and voltage, and simultaneously acquiring force, capacitance, and resistance for all test objects. The flexible programmability of the setup enables versatile experimental designs under both quasi-static and dynamic conditions. Furthermore, the robust design enables testing within harsh environmental conditions inside a climate chamber, allowing for the investigation of temperature and humidity effects. Along with a high degree of automation and extensive safety features, its functionality is not only limited to short-term investigations, but particularly enables uninterrupted long-term investigations that can also be monitored and controlled remotely. The conducted experimental validation proves high accuracy over a wide testing range, which can generally be further expanded with minor test rig modifications. The versatility of the test rig is

demonstrated in a broad range, by conducting various exemplary experiments on a specially developed rectangular-shaped planar DET (SIP), including variations in strain, voltage, test rate, temperature, humidity, and their combinations. However, the test rig is not limited to testing the demonstrated DET types and dimensions but can generally be adapted to various uniaxial operated DET types and enables the simultaneous testing of several designs and / or several operating conditions.

Due to these properties, the test rig serves a wide range of DET application fields, product levels and R&D phases. It enables DET-based sensors, actuators, and smart actuators to be characterized electromechanically and investigated for the influence of short- and particularly long-term operating conditions and environmental conditions. The test rig is particularly suitable for comprehensive testing of transducer compounds and corresponding systems, including preload mechanisms and external loads. Its versatile configurable test routines can be used to investigate fundamental effects in basic research but can also be utilized in product and production process development, i.e. to evaluate concepts, designs, or production processes.

With this, the test rig developed in this work represents a novel multifunctional tool that serves both research and development of DETs. By supporting scientists and engineers, it can make a significant contribution to the further development and market establishment of the technology.

5.2 Future Work

The hereby introduced test rig will be used at Saarland University to conduct wide-ranging tests on various DET materials, transducer compounds, and systems. Thereby particular emphasis is on the accelerated acquisition of statistically relevant data for the evaluation of failure mechanisms, such as mechanical tearing or dielectric breakdown in short-term experiments, or degradation and fatigue phenomena under long-term operating conditions. Modifications to the test rig that are frequently required in this context include adapting the sample grips and the electrical contacts to the respective test samples.

Although the current test rig capability covers a wide range of relevant tests, it can generally be further expanded and improved in future, buy supplementing additional test hardware, but also by using the existing hardware to implement further functionalities by means of pure software enhancements: For instance, dynamic testing routines can be realized by implementing higher-frequency signals, such as sweep specifications for voltage and displacement control, or force-controlled test routines including closed-loop HIL approaches can be achieved by implementing appropriate controller algorithms. Furthermore, since it has been observed that the implemented capacitance and resistance measurement methods require extensive operator knowledge to achieve meaningful results, the implementation of automated calibration methods can also be pursued.

List of Acronyms

AC	alternating current
AI	analog input
AO	analog output
ASA	acrylnitril-styrol acrylate
CAD	computer aided design
CB	carbon black
CNT	carbon nanotube
COP	cone-out-of-plane (DET)
DC	direct current
DE	dielectric elastomer
DET	dielectric elastomer transducer
DI	digital input
DIO	digital input / output
DIN	deutsches institut für normung
DMA	dynamic mechanical analyses
DO	digital output
EAP	electroactive polymer
EMI	electromechanical instability
FEM	finite element method
FFT	fast fourier transform
FIFO	first-in-first-out
FPGA	field-programmable gate array
GSM	global system for mobile communications
GUI	graphical user interface
GV	global variable
HIL	hardware-in-the-loop
HNBR	hydrogenated nitrile-butadiene rubber
HV	high voltage

IP	internet protocol
LCR	inductance-capacitance-resistance
LV	low voltage
MLE	maximum likelihood estimation
NBS	negative bias stiffness
PBS	positive bias stiffness
PDMS	polydimethylsiloxane
PEEK	polyetheretherketone
PETG	polyethylene terephthalate glycol
PID	proportional-integral-derivative (controller)
RMSE	root mean square error
RT	real-time
R&D	research and development
SBR	styrene-butadiene rubber
SIP	strip-in-plane (DET)
SMA	shape memory alloy
SNR	signal-to-noise ratio
SOP	Strip-Out-of-Plane (DET)
TDMS	technical data management streaming
TPU	thermoplastic polyurethane
UPS	uninterruptible power supply

List of Symbols

ε	permittivity
ε_0	vacuum permittivity
ε_r	material permittivity
ϵ	mechanical strain
$\dot{\epsilon}$	strain rate
ϵ_c	constant strain constraint for experiments
$\epsilon_1, \epsilon_2, \epsilon_3$	spatial strains
η	coefficient of friction
$\lambda_1, \lambda_2, \lambda_3$	principal stretches
ω	circular frequency
ϕ	phase-shift between periodic voltage and displacement signals
ρ_e	specific DET electrode resistance
ρ_l	specific DET leakage resistance
σ	mechanical stress
$\sigma_1, \sigma_2, \sigma_3$	spatial stresses
σ_M	maxwell stress
σ_{nom}	nominal mechanical stress
σ_{true}	true mechanical stress
τ	RC-series time constant
θ	phase-shift between measurement voltage and measurement current
θ_i	zero phase-shift of current measurement
θ_u	zero phase-shift of voltage measurement
θ_L	phase-shift between measurement voltage and current: calibration load
θ_N	phase-shift between measurement voltage and current: overall network
A_{RMS}	root mean square amplitude
C	capacitance
C_0	initial capacitance (undeformed DET)
c_{SP}	stiffness correction factor for mechanical test platform

c_{TLC}	temperature correction factor for load-cells
c_{TM}	temperature correction factor for motors
c_{TP}	temperature correction factor for mechanical platform
E	electric field
E_c	constant electric field constraint for field control test
f	frequency
f_a	acquisition rate
f_c	cutoff-frequency
f_m	measuring frequency
f_s	sample rate
F_B	DET actuator blocking force
F_{D0V}	DET tensile force with no voltage applied
F_{DHV}	DET tensile force with high voltage applied
F_{in}	inertia force
F_{LC}	forced measured by load-cell
F_N	nominal force
F_{NBS}	NBS force
F_{PBS}	PBS force
i	time-dependent current
i_a	large signal actuation current (quasi-stationary)
i_m	small signal measurement current (AC)
i_S	current through shunt resistor
I	current magnitude
$\underline{I}$	complex current (phasor)
k, m, n	count variables
l_1, l_2, l_3	deformed spatial dimensions: length, width, and thickness
l_{3d}	demanded thickness (control)
l_{3e}	electrode thickness
L_1, L_2, L_3	undeformed dimensions: length, width, and thickness
p	pressure
P	power

P_{ea}	active electrical power
P_N	noise power
P_S	signal power
R	electrical resistance
R_a	resistance of connectors and wiring
R_e	electrode resistance of DET
R_{es}	sheet electrode resistance of DET
R_l	leakage resistance of DET
R_P	parasitic resistance
R_S	shunt resistance
t	time
t_c	charging time of RC-series element
t_p	period time (duration)
T_c	constant temperature constraint for experiments
T_G	glass transition temperature
u	time-dependent voltage
$\dot{u}$	voltage slew rate
u_a	large signal actuation voltage (quasi-stationary)
u_m	small signal measurement voltage (AC)
u_c	constant voltage constraint for mechanical controlled experiments
u_C	voltage across capacitor
u_d	demanded voltage
u_R	voltage across resistor
u_S	voltage across shunt
$\underline{U}$	complex voltage (phasor)
U	voltage magnitude
U_N	voltage magnitude across entire electric network
U_P	voltage magnitude across parasitic components
x	position
x_L	position measured with laser position sensor
x_M	position measured with the motor internal encoder

x_{DET}	position, DET coordinate system
x_{NBS}	position, NBS coordinate system
x_{PBS}	position, PBS coordinate system
Y	young's modulus
Y'	tensile storage modulus
Y''	tensile loss modulus
Y^*	complex tensile modulus
$\underline{Z}$	complex impedance (phasor)
Z	impedance magnitude

List of Figures

List of Tables

Bibliography

[1] W. C. Röntgen, “Ueber die durch Electricität bewirkten Form- und Volumenänderungen von dielectrischen Körpern,” *Ann Phys*, vol. 247, no. 13, pp. 771–786, Jan. 1880, doi: https://doi.org/10.1002/andp.18802471304.

[2] R. Pelrine and S. Chiba, “Review of Artificial Muscle Approaches,” 1992. [Online]. Available: https://www.researchgate.net/publication/354343098

[3] Zhenyi, M., Scheinbeim, J. I., Lee, J. W., & Newman, B. A. (1994). High field electrostrictive response of polymers. Journal of Polymer Science Part B: Polymer Physics, 32(16), 2721–2731. doi:10.1002/polb.1994.090321618.

[4] R. K. Q. P. J. E. Ronald Pelrine, “Electroactive polymer sensors ,” US20020130673A1, Sep. 19, 2002

[5] R. Kornbluh, R. Pelrine, J. Eckerle and J. Joseph, "Electrostrictive polymer artificial muscle actuators," *Proceedings. 1998 IEEE International Conference on Robotics and Automation (Cat. No.98CH36146)*, Leuven, Belgium, 1998, pp. 2147-2154 vol.3, doi: 10.1109/ROBOT.1998.680638.

[6] R. E. Pelrine, R. D. Kornbluh, and J. P. Joseph, “Electrostriction of polymer dielectrics with compliant electrodes as a means of actuation,” *Sens Actuators A Phys*, vol. 64, no. 1, pp. 77–85, 1998, doi: https://doi.org/10.1016/S0924-4247(97)01657-9.

[7] R. Pelrine, R. Kornbluh, J. Joseph, R. Heydt, Q. Pei, and S. Chiba, “High-field deformation of elastomeric dielectrics for actuators,” *Materials Science and Engineering: C*, vol. 11, no. 2, pp. 89–100, 2000, doi: https://doi.org/10.1016/S0928-4931(00)00128-4.

[8] R. Pelrine *et al.*, “Dielectric elastomers: Generator mode fundamentals and applications,” *Proceedings of SPIE - The International Society for Optical Engineering*, vol. 4329, Jul. 2001, doi: 10.1117/12.432640.

[9] F. Carpi, D. De Rossi, R. Kornbluh, R. E. Pelrine, and P. Sommer-Larsen, *Dielectric elastomers as electromechanical transducers: Fundamentals, materials, devices, models and applications of an emerging electroactive polymer technology*, Elsevier Publishing, 2011. doi: 10.1016/B978-0-08-047488-5.X0001-9.

[10] F. Carpi, *Electromechanically Active Polymers (A Concise Reference)*, 1st ed., Springer International Publishing, 2016. doi: 10.1007/978-3-319-31530-0.

[11] Y. Guo, L. Liu, Y. Liu, and J. Leng, “Review of Dielectric Elastomer Actuators and Their Applications in Soft Robots,” *Advanced Intelligent Systems*, vol. 3, no. 10, p. 2000282, Oct. 2021, doi: https://doi.org/10.1002/aisy.202000282.

[12] S. Bauer, S. Bauer-Gogonea, I. Graz, M. Kaltenbrunner, C. Keplinger, and R. Schwödiauer, “25th Anniversary Article: A Soft Future: From Robots and Sensor Skin to Energy Harvesters,” *Advanced Materials*, vol. 26, no. 1, pp. 149–162, Jan. 2014, doi: https://doi.org/10.1002/adma.201303349.

[13] R. Kaltseis *et al.*, “Natural rubber for sustainable high-power electrical energy generation,” *RSC Adv*, vol. 4, no. 53, pp. 27905–27913, 2014, doi: 10.1039/C4RA03090G.

[14] Y. Chen, L. Agostini, G. Moretti, M. Fontana, and R. Vertechy, “Dielectric elastomer materials for large-strain actuation and energy harvesting: a comparison between styrenic rubber, natural rubber and acrylic elastomer,” *Smart Mater Struct*, vol. 28, no. 11, p. 114001, 2019, doi: 10.1088/1361-665X/ab3b32.

[15] G. Moretti, L. Sarina, L. Agostini, R. Vertechy, G. Berselli, and M. Fontana, “Styrenic-Rubber Dielectric Elastomer Actuator with Inherent Stiffness Compensation,” *Actuators*, vol. 9, no. 2, 2020, doi: 10.3390/act9020044.

[16] T. Chen, J. Qiu, K. Zhu, and J. Li, “Electro-mechanical performance of polyurethane dielectric elastomer flexible micro-actuator composite modified with titanium dioxide-graphene hybrid fillers,” *Mater Des*, vol. 90, pp. 1069–1076, 2016, doi: https://doi.org/10.1016/j.matdes.2015.11.068.

[17] J. Yao *et al.*, “Thermoplastic Polyurethane Dielectric Elastomers with High Actuated Strain and Good Mechanical Strength by Introducing Ester Group Grafted Polymethylvinylsiloxane,” *Ind Eng Chem Res*, vol. 60, no. 13, pp. 4883–4891, Apr. 2021, doi: 10.1021/acs.iecr.1c00362.

[18] A. L. Skov and L. Yu, “Optimization Techniques for Improving the Performance of Silicone-Based Dielectric Elastomers,” *Adv Eng Mater*, vol. 20, no. 5, p. 1700762, 2018, doi: https://doi.org/10.1002/adem.201700762.

[19] F. B. Madsen, A. E. Daugaard, S. Hvilsted, and A. L. Skov, “The Current State of Silicone-Based Dielectric Elastomer Transducers,” *Macromol Rapid Commun*, vol. 37, no. 5, pp. 378–413, Mar. 2016, doi: https://doi.org/10.1002/marc.201500576.

[20] G. Kofod, R. Kornbluh, R. Pelrine, and P. Sommer-Larsen, “Actuation Response of Polyacrylate Dielectric Elastomers,” *Journal of Intelligent Material Systems and Structures - J INTEL MAT SYST STRUCT*, vol. 14, Dec. 2003, doi: 10.1177/104538903039260.

[21] P. Lotz, M. Matysek, and H. F. Schlaak, “Fabrication and Application of Miniaturized Dielectric Elastomer Stack Actuators,” *IEEE/ASME Transactions on Mechatronics*, vol. 16, no. 1, pp. 58–66, 2011, doi: 10.1109/TMECH.2010.2090164.

[22] H. Zhao, A. Hussain, M. Duduta, D. Vogt, R. Wood, and D. Clarke, “Compact Dielectric Elastomer Linear Actuators,” *Adv Funct Mater*, vol. 28, p. 1804328, Oct. 2018, doi: 10.1002/adfm.201804328.

[23] A. Chortos, E. Hajiesmaili, J. Morales, D. R. Clarke, and J. A. Lewis, “3D Printing of Interdigitated Dielectric Elastomer Actuators,” *Adv Funct Mater*, vol. 30, no. 1, p. 1907375, Jan. 2020, doi: https://doi.org/10.1002/adfm.201907375.

[24] A. Hubracht, O. Cabuk, and J. Maas, “3D printing of elastomer layers for dielectric elastomer transducers,” in *Proc.SPIE*, Apr. 2022, p. 120420V. doi: 10.1117/12.2614828.

[25] D. McCoul, S. Rosset, S. Schlatter, and H. Shea, “Inkjet 3D printing of UV and thermal cure silicone elastomers for dielectric elastomer actuators,” *Smart Mater Struct*, vol. 26, no. 12, p. 125022, 2017, doi: 10.1088/1361-665X/aa9695.

[26] A. J. Cohen, M. Kollosche, M. C. Yuen, D.-Y. Lee, D. R. Clarke, and R. J. Wood, “Batch-Sprayed and Stamp-Transferred Electrodes: A New Paradigm for Scalable Fabrication of Multilayer Dielectric Elastomer Actuators,” *Adv Funct Mater*, vol. 32, no. 43, p. 2205394, Oct. 2022, doi: https://doi.org/10.1002/adfm.202205394.

[27] P. Banet *et al.*, “Evaluation of dielectric elastomers to develop materials suitable for actuation,” *Soft Matter*, p. 10786, Dec. 2021, doi: 10.1039/D1SM00621E.

[28] J. Hubertus, J. Neu, S. Croce, G. Rizzello, S. Seelecke, and G. Schultes, “Nanoscale Nickel-Based Thin Films as Highly Conductive Electrodes for Dielectric Elastomer Applications with Extremely High Stretchability up to 200%,” *ACS Appl Mater Interfaces*, vol. 13, Aug. 2021, doi: 10.1021/acsami.1c10686.

[29] Md. S. S. Faisal, Z. Ye, Z. Chen, and R. Asmatulu, “Electrical properties of nanoscale metallic thin films on dielectric elastomer at various strain rates,” in *Proc.SPIE*, Apr. 2015, p. 943031. doi: 10.1117/12.2179006.

[30] J. Hubertus, B. Fasolt, P. Linnebach, S. Seelecke, and G. Schultes, “Electromechanical evaluation of sub-micron NiCr-carbon thin films as highly conductive and compliant electrodes for dielectric elastomers,” *Sens Actuators A Phys*, vol. 315, p. 112243, 2020, doi: https://doi.org/10.1016/j.sna.2020.112243.

[31] A. Wiranata, Y. Ishii, N. Hosoya, and S. Maeda, “Simple and Reliable Fabrication Method for Polydimethylsiloxane Dielectric Elastomer Actuators Using Carbon Nanotube Powder Electrodes,” *Adv Eng Mater*, vol. 23, no. 6, p. 2001181, 2021, doi: https://doi.org/10.1002/adem.202001181.

[32] J. Yi *et al.*, “Characterizations and Inkjet Printing of Carbon Black Electrodes for Dielectric Elastomer Actuators,” *ACS Appl Mater Interfaces*, vol. 15, no. 35, pp. 41992–42003, Sep. 2023, doi: 10.1021/acsami.3c05444.

[33] B. Fasolt, F. B. Albuquerque, J. Hubertus, G. Schultes, H. Shea, and S. Seelecke, “Electrode Impact on the Electrical Breakdown of Dielectric Elastomer Thin Films,” *Polymers (Basel)*, vol. 15, no. 20, 2023, doi: 10.3390/polym15204071.

[34] J. E. Q. Quinsaat, M. Alexandru, F. A. Nüesch, H. Hofmann, A. Borgschulte, and D. M. Opris, “Highly stretchable dielectric elastomer composites containing high volume fractions of silver nanoparticles,” *J Mater Chem A Mater*, vol. 3, no. 28, pp. 14675–14685, 2015, doi: 10.1039/C5TA03122B.

[35] N. Rosales-Cuello, C. Cárcamo, C. Falcón, and H. Palza, “PDMS composites with carbon grease as reusable compliant electrodes for applications in artificial muscles based on dielectric elastomer actuators,” *Sens Actuators A Phys*, vol. 363, p. 114710, 2023, doi: https://doi.org/10.1016/j.sna.2023.114710.

[36] O. Çabuk, M. Wegener, B. Gruber, S.-O. Seidel, and J. Maas, “Inkjet printing and characterization of applied electrodes for dielectric elastomer transducer,” in *Proc.SPIE*, Jun. 2020, p. 113751V. doi: 10.1117/12.2558545.

[37] S. Rosset, O. A. Araromi, S. Schlatter, and H. R. Shea, “Fabrication Process of Silicone-based Dielectric Elastomer Actuators,” *J Vis Exp*, 2016, [Online]. Available: https://api.semanticscholar.org/CorpusID:6889672

[38] B. Fasolt, M. Hodgins, G. Rizzello, and S. Seelecke, “Effect of screen printing parameters on sensor and actuator performance of dielectric elastomer (DE) membranes,” *Sens Actuators A Phys*, vol. 265, pp. 10–19, 2017, doi: https://doi.org/10.1016/j.sna.2017.08.028.

[39] M. Wissler and E. Mazza, “Modeling and simulation of dielectric elastomer actuators,” *Smart Mater Struct*, vol. 14, p. 1396, Oct. 2005, doi: 10.1088/0964-1726/14/6/032.

[40] S. Croce, J. Neu, G. Moretti, J. Hubertus, G. Schultes, and G. Rizzello, “Finite element modeling and validation of a soft array of spatially coupled dielectric elastomer transducers,” *Smart Mater Struct*, vol. 31, no. 8, p. 084001, 2022, doi: 10.1088/1361-665X/ac78ad.

[41] F. Carpi *et al.*, “Standards for dielectric elastomer transducers,” *Smart Mater Struct*, vol. 24, no. 10, p. 105025, 2015, doi: 10.1088/0964-1726/24/10/105025.

[42] G. Moretti, S. Rosset, R. Vertechy, I. Anderson, and M. Fontana, “A Review of Dielectric Elastomer Generator Systems,” *Advanced Intelligent Systems*, vol. 2, no. 10, p. 2000125, Oct. 2020, doi: https://doi.org/10.1002/aisy.202000125.

[43] D. Orbaugh, C. R. Walker, S. Rosset, and I. A. Anderson, “From New Zealand to Croatia: hand gesture control of an underwater robot using dielectric elastomer sensors,” in *Proc.SPIE*, Apr. 2022, p. 120420K. doi: 10.1117/12.2612682.

[44] D. W. O. Antillon, C. R. Walker, S. Rosset, and I. A. Anderson, “Glove-Based Hand Gesture Recognition for Diver Communication,” *IEEE Trans Neural Netw Learn Syst*, vol. 34, no. 12, pp. 9874–9886, Dec. 2023, doi: 10.1109/TNNLS.2022.3161682.

[45] J. Gao *et al.*, “Smart Insole: Stand-Alone Soft 3-Axis Force Sensing Array in a Shoe,” *2023 IEEE SENSORS*, pp. 1–4, 2023, [Online]. Available: https://api.semanticscholar.org/CorpusID:265500281

[46] J. Gao, Y. Wu, X. Yin, Z. Chen, K. Morton, and J. D. W. Madden, “TouchBand: a modular low-power elastomer-based watchband for touch input and hand gesture recognition,” in *Proc.SPIE*, Apr. 2023, p. 1248202. doi: 10.1117/12.2658198.

[47] B. Huang *et al.*, “Wearable Stretch Sensors for Motion Measurement of the Wrist Joint Based on Dielectric Elastomers,” *Sensors*, vol. 17, no. 12, 2017, doi: 10.3390/s17122708.

[48] D. Orbaugh, C. Walker, S. Rosset, and I Anderson, "Jumping into virtual reality with dielectric elastomer sensors," in Proc. SPIE, Mar 2012, p. 115870A. doi: 10.1117/12.2584971.

[49] S. Chiba and M. Waki, “Dielectric Elastomer Multi-Sensors and Tactile Actuators for Robot Fingers in Human-Robot Interaction,” *Preprints (Basel)*, Jul. 2023, doi: 10.20944/preprints202307.0181.v1.

[50] J. Ziegler, D. Uhl, and H. Böse, “Dielectric elastomer sensors adapted for monitoring compression load of clamped battery cells,” in *Proc.SPIE*, Apr. 2023, p. 124820J. doi: 10.1117/12.2658246.

[51] Z. Suo, “Theory of dielectric elastomers,” *Acta Mechanica Solida Sinica*, vol. 23, no. 6, pp. 549–578, 2010, doi: https://doi.org/10.1016/S0894-9166(11)60004-9.

[52] S. Rosset, B. M. O'Brien, T. Gisby, D. Xu, H. R. Shea, and I. A. Anderson, "Self-sensing dielectric elastomer actuators in closed-loop operation," *Smart Mater Struct*, vol. 22, no. 10, p. 104018, Sep. 2013, doi: 10.1088/0964-1726/22/10/104018.

[53] G. Rizzello, D. Naso, A. York, and S. Seelecke, "Closed loop control of dielectric elastomer actuators based on self-sensing displacement feedback," *Smart Mater Struct*, vol. 25, no. 3, p. 35034, Feb. 2016, doi: 10.1088/0964-1726/25/3/035034.

[54] R. Zhang, P. Iravani, and P. Keogh, "Closed loop control of force operation in a novel self-sensing dielectric elastomer actuator," *Sens Actuators A Phys*, vol. 264, pp. 123–132, 2017, doi: https://doi.org/10.1016/j.sna.2017.08.013.

[55] T. Hoffstadt and J. Maas, "Sensorless force control for dielectric elastomer transducers," *J Intell Mater Syst Struct*, vol. 30, no. 9, pp. 1419–1434, 2019, doi: 10.1177/1045389X17754255.

[56] G. Rizzello, P. Serafino, D. Naso, and S. Seelecke, "Towards Sensorless Soft Robotics: Self-Sensing Stiffness Control of Dielectric Elastomer Actuators," *IEEE Transactions on Robotics*, vol. 36, no. 1, pp. 174–188, 2020, doi: 10.1109/TRO.2019.2944592.

[57] M. Hill, G. Rizzello, and S. Seelecke, "Development and experimental characterization of a pneumatic valve actuated by a dielectric elastomer membrane," *Smart Mater Struct*, vol. 26, no. 8, p. 85023, Jul. 2017, doi: 10.1088/1361-665X/aa746d.

[58] M. Giousouf and G. Kovacs, "Dielectric elastomer actuators used for pneumatic valve technology," *Smart Mater Struct*, vol. 22, no. 10, p. 104010, Sep. 2013, doi: 10.1088/0964-1726/22/10/104010.

[59] D. Bruch, T. P. Willian, H. C. Schäfer, and P. Motzki, "Performance-Optimized Dielectric Elastomer Actuator System with Scalable Scissor Linkage Transmission," *Actuators*, vol. 11, no. 6, 2022, doi: 10.3390/act11060160.

[60] S. Hau, G. Rizzello, M. Hodgins, A. York, and S. Seelecke, "Design and Control of a High-Speed Positioning System Based on Dielectric Elastomer Membrane Actuators," *IEEE/ASME Transactions on Mechatronics*, vol. 22, no. 3, pp. 1259–1267, 2017, doi: 10.1109/TMECH.2017.2681839.

[61] M. Baltes, J. Kunze, J. Prechtl, P. Motzki, S. Seelecke, and G. Rizzello, "Soft Robotic Tentacle Arm Element Actuated by Rolled Dielectric Elastomer Artificial Muscles," in Proc. SPIE, Apr. 2022, p. 1204207. doi: 10.1117/12.2612516.

[62] P. Linnebach, S. Hau, G. Rizzello, S. Seelecke, "Design of a dielectric elastomer actuator driven pneumatic pump," in Proc. SPIE, Mar. 2019, p. 109661S. doi: 10.1117/12.2514034.

[63] P. Lotz, M. Matysek, and H. F. Schlaak, “Peristaltic pump made of dielectric elastomer actuators,” in *Electroactive Polymer Actuators and Devices (EAPAD) 2009*, Y. Bar-Cohen and T. Wallmersperger, Eds., SPIE, 2009, p. 72872D. doi: 10.1117/12.819216.

[64] P. Bakardjiev, A. Richter, E. Altinsoy, U. Marschner, and J. Troge, “Dielectric elastomer loudspeaker driver.” Presented at EuroEAP, 7th international conference on Electromechanically Active Polymer (EAP) transducers and artificial muscles, Cartagena, Spain, 06.-07 June 2017. doi: 10.24406/publica-fhg-399728.

[65] N. Hosoya, H. Masuda, and S. Maeda, “Balloon dielectric elastomer actuator speaker,” *Applied Acoustics*, vol. 148, pp. 238–245, 2019, doi: https://doi.org/10.1016/j.apacoust.2018.12.032.

[66] H. Schlaak, M. Jungmann, M. Matysek, and P. Lotz, “Novel multilayer electrostatic solid state actuators with elastic dielectric (Invited Paper),” *Proc SPIE*, vol. 5759, Jan. 2005, doi: 10.1117/12.604468.

[67] G. Kovacs, L. Düring, S. Michel, and G. Terrasi, “Stacked dielectric elastomer actuator for tensile force transmission,” *Sens Actuators A Phys*, vol. 155, no. 2, pp. 299–307, 2009, doi: https://doi.org/10.1016/j.sna.2009.08.027.

[68] F. Carpi, C. Salaris, and D. de rossi, “Folded dielectric elastomer actuators,” *Smart Mater Struct*, vol. 16, p. S300, Jan. 2007, doi: 10.1088/0964-1726/16/2/S15.

[69] F. Carpi, A. Migliore, G. Serra, and D. de rossi, “Helical dielectric elastomer actuators,” *Smart Mater. Struct*, vol. 14, pp. 1–7, Jan. 2005, doi: 10.1088/0964-1726/14/6/014.

[70] S. Hau, D. Bruch, G. Rizzello, P. Motzki, and S. Seelecke, “Silicone based dielectric elastomer strip actuators coupled with nonlinear biasing elements for large actuation strains,” *Smart Mater Struct*, vol. 27, no. 7, p. 74003, Jun. 2018, doi: 10.1088/1361-665X/aab7d8.

[71] G. Rizzello, P. Loew, D. Naso, and S. Seelecke, “Analytical Modeling of Clamped Dielectric Elastomer Strip Membranes Exhibiting Necking Effect,” *IFAC-PapersOnLine*, vol. 51, no. 2, pp. 701–706, 2018, doi: https://doi.org/10.1016/j.ifacol.2018.03.119.

[72] J.-S. Plante and S. Dubowsky, “On the performance mechanisms of Dielectric Elastomer Actuators,” *Sens Actuators A Phys*, vol. 137, no. 1, pp. 96–109, 2007, doi: https://doi.org/10.1016/j.sna.2007.01.017.

[73] J.Kunze, J. Prechtl, D. Bruch, S. Nalbach, P. Motzki, S. Seelecke, and G. Rizzello, "Design and fabrication of silicone-based dielectric elastomer rolled actuators for soft robotic applications," in Proc. SPIE, Apr. 2020, p. 113752D. doi: 10.1117/12.2558444.

[74] J. Prechtl, J. Kunze, G. Moretti, D. Bruch, S. Seelecke, and G. Rizzello, "Modeling and experimental validation of thin, tightly rolled dielectric elastomer actuators," *Smart Mater Struct*, vol. 31, no. 1, p. 15008, Nov. 2021, doi: 10.1088/1361-665X/ac34be.

[75] R. Sarban, R. W. Jones, B. R. Mace, and E. Rustighi, "A tubular dielectric elastomer actuator: Fabrication, characterization and active vibration isolation," *Mech Syst Signal Process*, vol. 25, no. 8, pp. 2879–2891, 2011, doi: https://doi.org/10.1016/j.ymssp.2011.06.004.

[76] J. Li, L. Liu, Y. Liu, and J. Leng, "Dielectric Elastomer Spring-Roll Bending Actuators: Applications in Soft Robotics and Design," *Soft Robot*, vol. 6, no. 1, pp. 69–81, Oct. 2018, doi: 10.1089/soro.2018.0037.

[77] Q. Pei, M. Rosenthal, S. Stanford, H. Prahlad, and R. Pelrine, "Multiple-degrees-of-freedom electroelastomer roll actuators," *Smart Mater Struct*, vol. 13, p. N86, Jan. 2004, doi: 10.1088/0964-1726/13/5/N03.

[78] P. Loew, M. Brill, G. Rizzello, and S. Seelecke, "Development of a nonintrusive pressure sensor for polymer tubes based on dielectric elastomer membranes," *Sens Actuators A Phys*, vol. 292, pp. 1–10, 2019, doi: https://doi.org/10.1016/j.sna.2019.03.006.

[79] D. McCoul and Q. Pei, "Tubular dielectric elastomer actuator for active fluidic control," *Smart Mater Struct*, vol. 24, no. 10, p. 105016, Sep. 2015, doi: 10.1088/0964-1726/24/10/105016.

[80] S. Hau, A. York, G. Rizzello, and S. Seelecke, "Performance Prediction and Scaling Laws of Circular Dielectric Elastomer Membrane Actuators," *Journal of Mechanical Design*, vol. 140, Jan. 2018, doi: 10.1115/1.4039104.

[81] M. Hill, G. Rizzello, and S. Seelecke, "Development and experimental characterization of a dielectric elastomer membrane strip actuator," *Smart Mater Struct*, vol. 27, no. 2, p. 025019, 2018, doi: 10.1088/1361-665X/aaa695.

[82] P. Loew, G. Rizzello, and S. Seelecke, "Permanent magnets as biasing mechanism for improving the performance of circular dielectric elastomer out-of-plane actuators," Proc. SPIE, Apr. 2017, p. 101630Y. doi: 10.1117/12.2258390

[83] M. Hodgins, " Design of diaphragm dielectric elastomer actuators (DEAs) and experimental characterization techniques," Ph.D. thesis, Naturwissenschaftlich-Technische Fakultät, Universität des Saarlandes, Saarland, Saarbrücken, Germany, 2016.

[84] G. Rizzello, M. Hodgins, D. Naso, A. York, and S. Seelecke, "Dynamic Modeling and Experimental Validation of an Annular Dielectric Elastomer Actuator With a Biasing Mass," *J Vib Acoust*, vol. 137, p. 11005, Feb. 2015, doi: 10.1115/1.4028456.

[85] P. Eyerer, H. Schüle, and P. Elsner, *Polymer Engineering 3 Werkstoff- und Bauteilprüfung, Recycling, Entwicklung, 2nd ed., Springer Verlag*, 2020. doi: 10.1007/978-3-662-59839-9.

[86] M. F. Tassara, K. Grigoriadis, and G. Mavros, "Empirical Models for the Viscoelastic Complex Modulus with an Application to Rubber Friction," *Applied Sciences*, vol. 11, p. 4831, 2021, [Online]. Available: https://api.semanticscholar.org/CorpusID:236373988

[87] D. F. Moore and W. Geyer, "A review of hysteresis theories for elastomers," *Wear*, vol. 30, no. 1, pp. 1–34, 1974, doi: https://doi.org/10.1016/0043-1648(74)90055-6.

[88] A. R. Payne, "The dynamic properties of carbon black-loaded natural rubber vulcanizates. Part I," *J Appl Polym Sci*, vol. 6, no. 19, pp. 57–63, Jan. 1962, doi: https://doi.org/10.1002/app.1962.070061906.

[89] M.-J. Wang, "The Role of Filler Networking in Dynamic Properties of Filled Rubber," *Rubber Chemistry and Technology*, vol. 72, no. 2, pp. 430–448, May 1999, doi: 10.5254/1.3538812.

[90] A. R. Payne, R. E. Whittaker, and J. F. Smith, "Effect of vulcanization on the low-strain dynamic properties of filled rubbers," *J Appl Polym Sci*, vol. 16, pp. 1191–1212, 1972, [Online]. Available: https://api.semanticscholar.org/CorpusID:137415240

[91] P. Eyerer, Elsner, and Hirth, *Elsner, P.; Eyerer, P.; Hirth, Th. (Hrsg.): Kunststoffe – Eigenschaften und Anwendungen (Domininghaus). 8. neu bearbeitete und erweiterte Auflage, Springer Verlag, Januar 2012*. 2012.

[92] J. E. Mark, B. R. Erman, and M. Roland, *The science and technology of rubber*, 3th ed., Elsevir Publishing, 2013. doi: 10.1016/C2011-0-05820-9.

[93] J. E. Mark, "Rubber elasticity," *J Chem Educ*, vol. 58, no. 11, p. 898, Nov. 1981, doi: 10.1021/ed058p898.

[94] Y. Shi, M. Hu, Y. Xing, and Y. Li, "Temperature-dependent thermal and mechanical properties of flexible functional PDMS/paraffin composites," *Mater Des*, vol. 185, p. 108219, 2020, doi: https://doi.org/10.1016/j.matdes.2019.108219.

[95] Y.-C. Sun, B. Leaker, J. J. E. Lee, R. Nam, and H. Naguib, “Shape programming of polymeric based electrothermal actuator (ETA) via artificially induced stress relaxation,” *Sci Rep*, vol. 9, Aug. 2019, doi: 10.1038/s41598-019-47949-0.

[96] M. L. Williams, R. F. Landel, and J. D. Ferry, “The Temperature Dependence of Relaxation Mechanisms in Amorphous Polymers and Other Glass-forming Liquids,” *J Am Chem Soc*, vol. 77, no. 14, pp. 3701–3707, Jul. 1955, doi: 10.1021/ja01619a008.

[97] L. Mullins, “Softening of Rubber by Deformation,” *Rubber Chemistry and Technology*, vol. 42, no. 1, pp. 339–362, Mar. 1969, doi: 10.5254/1.3539210.

[98] J. Diani, B. Fayolle, and P. Gilormini, “A review on the Mullins effect,” *Eur Polym J*, vol. 45, no. 3, pp. 601–612, 2009, doi: https://doi.org/10.1016/j.eurpolymj.2008.11.017.

[99] X. Zhao, S. Koh, and Z. Suo, “Nonequilibrium Thermodynamics of Dielectric Elastomers,” *Int J Appl Mech*, vol. 03, Jun. 2011, doi: 10.1142/S1758825111000944.

[100] L. R. G. Treloar, *The Physics of Rubber Elasticity*. in Monographs on the physics and chemistry of materials. Clarendon Press, 1975. [Online]. Available: https://books.google.de/books?id=qdYmAQAAMAAJ

[101] Y. Takeoka, S. Liu, and F. Asai, “Improvement of mechanical properties of elastic materials by chemical methods,” *Sci Technol Adv Mater*, vol. 21, no. 1, pp. 817–832, Jan. 2020, doi: 10.1080/14686996.2020.1849931.

[102] D. J. Kohls and G. Beaucage, “Rational design of reinforced rubber,” *Curr Opin Solid State Mater Sci*, vol. 6, no. 3, pp. 183–194, 2002, doi: https://doi.org/10.1016/S1359-0286(02)00073-6.

[103] P. Sommer-Larsen, J. C. Hooker, G. Kofod, K. West, M. Benslimane and P Gravesen, "Response of dielectric elastomer actuators," in Proc. SPIE 4329, July 2001. doi: 10.1117/12.432641.

[104] G. Rizzello, D. Naso, A. York and S. Seelecke, "Self-sensing in dielectric electro-active polymer actuator using linear-in-parametes online estimation," *2015 IEEE International Conference on Mechatronics (ICM)*, Nagoya, Japan, 2015, pp. 300-306, doi: 10.1109/ICMECH.2015.7083992.

[105] Wacker Chemie AG, “Datasheet: Wacker Elastosil Film 2030.” Accessed: Mar. 30, 2024. [Online]. Available: https://www.wacker.com/h/de-de/medias/ELASTOSIL-Film-2030-de-2023.04.18.pdf

[106] E. Garnell, C. Rouby, and O. Doaré, “Resistivity-induced coupling between voltage distribution and vibrations in dielectric elastomers,” *Smart Mater Struct*, vol. 30, no. 2, p. 25031, Jan. 2021, doi: 10.1088/1361-665X/abd58f.

[107] A. Tairych, I. Anderson, "A variable R-C transmission line model for resistive stretch sensors," in Proc. SPIE, Mar. 2018, p. 105941L. doi: 10.1117/12.2296805.

[108] T. P. Willian, B. Fasolt, P. Motzki, G. Rizzello, and S. Seelecke, “Effects of Electrode Materials and Compositions on the Resistance Behavior of Dielectric Elastomer Transducers,” *Polymers (Basel)*, vol. 15, no. 2, 2023, doi: 10.3390/polym15020310.

[109] M. Norkhairunnisa, A. Azizan, M. Mariatti, H. Ismail, and L. C. Sim, “Thermal stability and electrical behavior of polydimethylsiloxane nanocomposites with carbon nanotubes and carbon black fillers,” *J Compos Mater*, vol. 46, no. 8, pp. 903–910, Sep. 2011, doi: 10.1177/0021998311412985.

[110] L. Wu *et al.*, “Screen-printed flexible temperature sensor based on FG/CNT/PDMS composite with constant TCR,” *Journal of Materials Science: Materials in Electronics*, vol. 30, no. 10, pp. 9593–9601, 2019, doi: 10.1007/s10854-019-01293-1.

[111] S. Zhang, C. Chen, W. Bin, X. Zheng, H. San, and W. Hofmann, “Dual-axis thermal convective inclinometer based on CNT/PDMS composite,” *Journal of Materials Science: Materials in Electronics*, vol. 29, no. 22, pp. 18997–19004, 2018, doi: 10.1007/s10854-018-0025-x.

[112] S.-H. Jang and Y.-L. Park, “Carbon nanotube-reinforced smart composites for sensing freezing temperature and deicing by self-heating,” *Nanomaterials and Nanotechnology*, vol. 8, p. 1847980418776473, Jan. 2018, doi: 10.1177/1847980418776473.

[113] J. Nagel, T. Hanemann, B. E. Rapp, and G. Finnah, “Negative temperature coefficient and positive temperature coefficient behavior of electrically conductive silicone/carbon black composites,” *J Compos Mater*, vol. 57, no. 26, pp. 4183–4196, 2023, doi: 10.1177/00219983231207357.

[114] C. Karuthedath, U. Fikri, F. Ruf, and N. Schwesinger, “Characterization of Carbon Black Filled PDMS-Composite Membranes for Sensor Applications,” *Key Eng Mater*, vol. 753, pp. 18–27, Aug. 2017, doi: 10.4028/www.scientific.net/KEM.753.18.

[115] K. C. Baby, U. Fikri, and N. Schwesinger, “Resistive characterization of soft conductive PDMS membranes for sensor applications,” in *2016 IEEE Sensors Applications Symposium (SAS)*, 2016, pp. 1–6. doi: 10.1109/SAS.2016.7479870.

[116] J. Won *et al.*, “Highly stretchable wrinkled electrode based on silver ink-elastomer nanocomposite with excellent fatigue resistance,” *Polym Compos*, vol. 41, no. 6, pp. 2210–2223, 2020, doi: https://doi.org/10.1002/pc.25532.

[117] B. Fasolt, F. Welsch, M. Jank, and S. Seelecke, “Effect of actuation parameters and environment on the breakdown voltage of silicone dielectric elastomer films,” *Smart Mater Struct*, vol. 28, no. 9, p. 094002, 2019, doi: 10.1088/1361-665X/ab2f34.

[118] L. Jiang, A. Betts, D. Kennedy, and S. Jerrams, “Eliminating electromechanical instability in dielectric elastomers by employing pre-stretch,” *J Phys D Appl Phys*, vol. 49, p. 265401, May 2016, doi: 10.1088/0022-3727/49/26/265401.

[119] L. R. G. Treloar, “Strains in an Inflated Rubber Sheet, and the Mechanism of Bursting,” *Rubber Chemistry and Technology*, vol. 17, no. 4, pp. 957–967, Dec. 1944, doi: 10.5254/1.3546716.

[120] R. S. Rivlin and D. W. Saunders, “Large Elastic Deformations of Isotropic Materials. VII. Experiments on the Deformation of Rubber,” *Philosophical Transactions of the Royal Society of London. Series A, Mathematical and Physical Sciences*, vol. 243, no. 865, pp. 251–288, 1951, [Online]. Available: http://www.jstor.org/stable/91489

[121] A. Esmaeili, D. George, I. Masters, and M. Hossain, “Biaxial experimental characterizations of soft polymers: A review,” *Polym Test*, vol. 128, p. 108246, 2023, doi: https://doi.org/10.1016/j.polymertesting.2023.108246.

[122] M. Sasso, G. Palmieri, G. Chiappini, and D. Amodio, “Characterization of hyperelastic rubber-like materials by biaxial and uniaxial stretching tests based on optical methods,” *Polym Test*, vol. 27, no. 8, pp. 995–1004, 2008, doi: https://doi.org/10.1016/j.polymertesting.2008.09.001.

[123] A. Schmidt, P. Rothemund, and E. Mazza, “Multiaxial deformation and failure of acrylic elastomer membranes,” *Sens Actuators A Phys*, vol. 174, pp. 133–138, 2012, doi: https://doi.org/10.1016/j.sna.2011.12.004.

[124] L. Jiang, A. Betts, D. Kennedy, and S. Jerrams, “Improving the electromechanical performance of dielectric elastomers using silicone rubber and dopamine coated barium titanate,” *Mater Des*, vol. 85, pp. 733–742, 2015, doi: https://doi.org/10.1016/j.matdes.2015.07.075.

[125] L. Jiang, “The fabrication of dielectric elastomers from silicone rubber and barium titanate: employing equi-biaxial pre-stretch to achieve large deformations,” *J Mater Sci*, vol. 50, Aug. 2015, doi: 10.1007/s10853-015-9357-6.

[126] L. Jiang, A. Betts, D. Kennedy, and S. Jerrams, “Eliminating electromechanical instability in dielectric elastomers by employing pre-stretch,” *J Phys D Appl Phys*, vol. 49, no. 26, p. 265401, 2016, doi: 10.1088/0022-3727/49/26/265401.

[127] S.-J. E *et al.*, “Determination method of constitutive model parameters of dielectric elastomer material,” *AIP Adv*, vol. 10, p. 015208, Jan. 2020, doi: 10.1063/1.5124334.

[128] F. Welsch, B. Fasolt, and S. Seelecke, "Dielectric breakdown test setup for dielectric elastomers: design and validation," Proc. SPIE, Mar. 2018, p.105941A, doi: 10.1117/12.2296995.

[129] E. Taine, T. Andritsch, I. A. Saeedi, and P. H. F. Morshuis, “Dielectric Breakdown Strength of PDMS Elastomers after Mechanical Cycling,” *Energies (Basel)*, vol. 16, no. 21, 2023, doi: 10.3390/en16217424.

[130] M. Hodgins, G. Rizzello, A. York, D. Naso, and S. Seelecke, “A smart experimental technique for the optimization of dielectric elastomer actuator (DEA) systems,” *Smart Mater Struct*, vol. 24, p. 094002, Aug. 2015, doi: 10.1088/0964-1726/24/9/094002.

[131] G. Moretti, G. P. P. Rosati, M. Fontana, and R. Vertechy, “Hardware in the loop simulation of a dielectric elastomer generator for oscillating water column wave energy converters,” in *OCEANS 2015 - Genova*, 2015, pp. 1–7. doi: 10.1109/OCEANS-Genova.2015.7271571.

[132] G. Moretti *et al.*, “Hardware-in-the-loop simulation of wave energy converters based on dielectric elastomer generators,” *Meccanica*, vol. 56, Feb. 2021, doi: 10.1007/s11012-021-01320-8.

[133] W. V Mars and A. Fatemi, “A literature survey on fatigue analysis approaches for rubber,” *Int J Fatigue*, vol. 24, no. 9, pp. 949–961, 2002, doi: https://doi.org/10.1016/S0142-1123(02)00008-7.

[134] W. V Mars and A. Fatemi, “Factors that Affect the Fatigue Life of Rubber: A Literature Survey,” *Rubber Chemistry and Technology*, vol. 77, no. 3, pp. 391–412, Jul. 2004, doi: 10.5254/1.3547831.

[135] X. Qiu, H. Yin, and Q. Xing, “Research Progress on Fatigue Life of Rubber Materials,” *Polymers (Basel)*, vol. 14, no. 21, 2022, doi: 10.3390/polym14214592.

[136] S. M. Cadwell, R. A. Merrill, C. M. Sloman, and F. L. Yost, “Dynamic Fatigue Life of Rubber,” *Industrial & Engineering Chemistry Analytical Edition*, vol. 12, no. 1, pp. 19–23, Jan. 1940, doi: 10.1021/ac50141a006.

[137] G. J. Lake and P. B. Lindley, “The mechanical fatigue limit for rubber,” *J Appl Polym Sci*, vol. 9, no. 4, pp. 1233–1251, Apr. 1965, doi: https://doi.org/10.1002/app.1965.070090405.

[138] B. A. Dogadkin, V. E. Gul, and N. A. Morozova, “The Effect of Electric Charges Formed during Repeated Deformations on the Fatigue Resistance of Vulcanizates,” *Rubber Chemistry and Technology*, vol. 33, no. 4, p. 970, Sep. 1960, doi: 10.5254/1.3542237.

[139] W. Fan, Y. Wang, and S. Cai, “Fatigue fracture of a highly stretchable acrylic elastomer,” *Polym Test*, vol. 61, pp. 373–377, 2017, doi: https://doi.org/10.1016/j.polymertesting.2017.06.005.

[140] A. Iannarelli, M. G. Niasar, and R. Ross, “Assessing Partial Discharge Activity in Dielectric Elastomer Under Cyclic Tensile Stress,” in *2018 IEEE Electrical Insulation Conference (EIC)*, 2018, pp. 562–565. doi: 10.1109/EIC.2018.8481049.

[141] R. Kornbluh, A. Wong-Foy, R. Pelrine, H. Prahlad, and B. McCoy, “Long-lifetime All-polymer Artificial Muscle Transducers,” *MRS Online Proceedings Library*, vol. 1271, no. 1, p. 301, 2010, doi: 10.1557/PROC-1271-JJ03-01.

[142] M. Matysek, P. Lotz, and H. Schlaak, “Lifetime Investigation of Dielectric Elastomer Stack Actuators,” *IEEE Transactions on Dielectrics and Electrical Insulation - IEEE TRANS DIELECT ELECTR IN*, vol. 18, pp. 89–96, Feb. 2011, doi: 10.1109/TDEI.2011.5704497.

[143] P. Lotz, M. Matysek, and H. F. Schlaak, “Lifetime of dielectric elastomer stack actuators,” in *Proc.SPIE*, Mar. 2011, p. 79760P. doi: 10.1117/12.878954.

[144] S. Rosset, C. de Saint-Aubin, A. Poulin, and H. R. Shea, “Assessing the degradation of compliant electrodes for soft actuators,” *Review of Scientific Instruments*, vol. 88, no. 10, p. 105002, Oct. 2017, doi: 10.1063/1.4989464.

[145] D. Kühnel, F. Beco Albuquerque, V. Py, and H. Shea, “Automated test setup to quantify the lifetime of dielectric elastomer actuators under a wide range of operating conditions,” *Smart Mater Struct*, vol. 30, no. 6, p. 065020, 2021, doi: 10.1088/1361-665X/abfb85.

[146] F. B., Albuquerque, “Lifetime of dielectric elastomer actuators under DC electric fields.”," Ph.D. thesis, Faculté des sciences et techniques de l’ingénieur, École polytechnique fédérale de Lausanne, Waadt Waadt, Lausanne, Switzerland, 2022.

[147] A. Iannarelli, M. G. Niasar, and R. Ross, “The effects of static pre-stretching on the short and long-term reliability of dielectric elastomer actuators,” *Smart Mater Struct*, vol. 28, no. 12, p. 125014, 2019, doi: 10.1088/1361-665X/ab4fbe.

[148] S. Rosset, S. Schlatter, C. de Saint-Aubin, A. Poulin, and H. Shea, “The NERD setup: assessing the life time of electrodes for dielectric elastomer transducers,” in *Proc.SPIE*, Mar. 2018, p. 105940N. doi: 10.1117/12.2294408.

[149] C. A. de Saint-Aubin, S. Rosset, S. Schlatter, and H. Shea, “High-cycle electromechanical aging of dielectric elastomer actuators with carbon-based electrodes,” *Smart Mater Struct*, vol. 27, no. 7, p. 074002, 2018, doi: 10.1088/1361-665X/aa9f45.

[150] Y. Chen, L. Agostini, G. Moretti, G. Berselli, M. Fontana, and R. Vertechy, “Fatigue life performances of silicone elastomer membranes for dielectric elastomer transducers: preliminary results,” in *Proc.SPIE*, Mar. 2019, p. 1096616. doi: 10.1117/12.2515312.

[151] C. Yi, L. Agostini, M. Fontana, G. Moretti, and R. Vertechy, “On the Lifetime Performance of a Styrenic Rubber Membrane for Dielectric Elastomer Transducers,” *Volume 1: Development and Characterization of Multifunctional Materials; Modeling, Simulation, and Control of Adaptive Systems; Integrated System Design and Implementation*, 2018, [Online]. Available: https://api.semanticscholar.org/CorpusID:139769614

[152] A. Iannarelli and M. G. Niasar, “Mechanical stretch influence on lifetime of dielectric elastomer films,” in *Electroactive Polymer Actuators and Devices (EAPAD) 2017*, SPIE, Apr. 2017, p. 1016326. doi: 10.1117/12.2258601.

[153] F. B. Albuquerque and H. Shea, “Influence of electric field, temperature, humidity, elastomer material, and encapsulation on the lifetime of dielectric elastomer actuators (DEAs) under DC actuation,” *Smart Mater Struct*, vol. 30, no. 12, p. 125022, 2021, doi: 10.1088/1361-665X/ac3433.

[154] D. Bruch, M. Hill, S. Hau, P. Motzki, and S. Seelecke, “Electromechanical Fatique Testing Device for Dielectric Elastomers under Controllable Environmental Conditions,” in *ACTUATOR 2018; 16th International Conference on New Actuators*, 2018, pp. 1–4.

[155] M. Hill, “Entwicklung bauraumoptimierter dielektrischer Elastomer-Aktoren und eines Prüfstandes zur Charakterisierung ihres Ermüdungsverhaltens”, Ph.D. thesis, Naturwissenschaftlich-Technische Fakultät, Universität des Saarlandes, Saarland, Saarbrücken, Germany, 2018.

[156] M. Hill, G. Rizzello, and S. Seelecke, “Development of a fatigue testing setup for dielectric elastomer membrane actuators,” in *Proc.SPIE*, Apr. 2017, p. 101630X. doi: 10.1117/12.2259867.

[157] M. Hill, G. Rizzello, and S. Seelecke, “Development and validation of a fatigue testing setup for dielectric elastomer membrane actuators,” *Smart Mater Struct*, vol. 28, no. 5, p. 055029, 2019, doi: 10.1088/1361-665X/ab1347.

[158] D. Bruch, S. Nalbach, G. Rizzello, P. Motzki, and S. Seelecke, “Multifunctional fatigue testing setup for in-plane operating DEAs,” in *Proc.SPIE*, Apr. 2020, p. 113800S. doi: 10.1117/12.2558609.

[159] D. Bruch, S. Nalbach, S. Seelecke, P. Motzki, and G. Rizzello, “Fully automatic multi-characterization setup for systematic long-term investigation on dielectric elastomers,” *EuroEAP 2021 International conference on Electromechanically Active Polymer (EAP) transducers & artificial muscles*. Chianciano Terme - Tuscany, Italy, pp. 63–63, Jun. 03, 2021. Accessed: Apr. 29, 2024. [Online]. Available: http://win.euroeap.eu/public/programme/EuroEAP%202021_Programme.pdf

[160] CTS GmbH, “Datasheet: CTS-Klima-Prüfschränke / Serie C-40 und C-70.” 2024. Accessed: Apr. 27, 2024. [Online]. Available: https://www.cts-umweltsimulation.de/images/produkte/ps-baureihe-c/download/CTS_Climatic_Test_Chambers_deu.pdf

[161] NTI AG, “Datasheet: LinMot Linear Guides H01.” 2024. Accessed: Apr. 22, 2024. [Online]. Available: file:///C:/Users/Daniel/Downloads/0185-1025-E_1V2_DS_Linear_Guides_H01.pdf

[162] NTI AG, “Datasheet: LinMot Linear Motors PS01-23x160H-HP-R.” 2024. Accessed: Apr. 20, 2024. [Online]. Available: https://shop.linmot.com/data/import/Dokumente/0185-0048-E_1V2_DS_Linear_Motors_P01-23x160H-HP.pdf

[163] ME-Meßsysteme GmbH, “Datasheet: Me-Meßsysteme KD40s +-10N.” Accessed: Apr. 03, 2024. [Online]. Available: https://www.me-systeme.de/product-pdf?product_id=1732&lang=de

[164] Sensata Technologies Inc., “Datasheet: Sensata Technologies Cynergy3 D Series High Voltage Relays 10kV & 15kV.” 2024. Accessed: Apr. 27, 2024. [Online]. Available: https://www.cynergy3.com/sites/default/files/cynergy3-d-v3.pdf

[165] hivolt.de GmbH & Co. KG, “Datasheet: hivolt.de HA51U Series.” 2024. Accessed: Apr. 03, 2024. [Online]. Available: https://www.hivolt.de/fileadmin/hivolt/pdf/HA51U_HAR-51-4M.pdf

[166] Vishay Intertechnology Inc., “Datasheet: Vishay 615R Series.” 2024. Accessed: Apr. 05, 2024. [Online]. Available: https://www.vishay.com/docs/23119/615rseries.pdf